

AD-A182 399

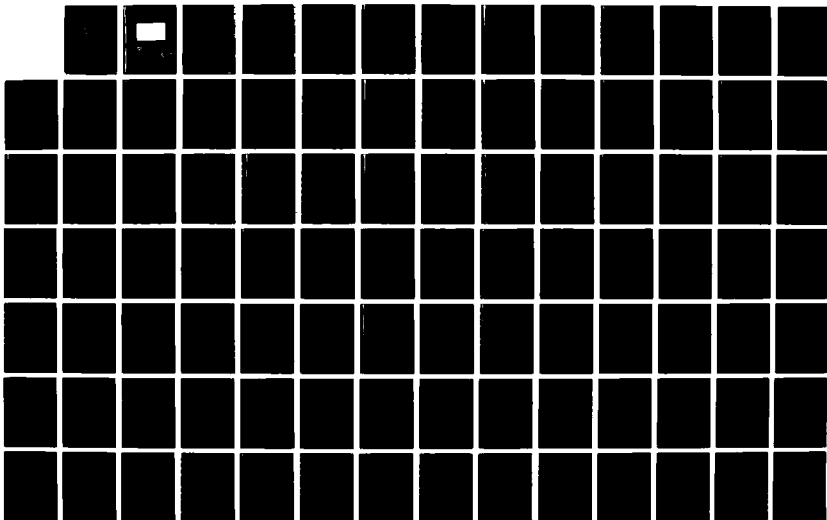
ORGANIZED STRUCTURES IN A SUPERSONIC TURBULENT BOUNDARY
LAYER(U) PRINCETON UNIV NJ DEPT OF MECHANICAL AND
AEROSPACE ENGINEERING E F SPINA ET AL. FEB 86 MAE-1736
AFOSR-85-0126

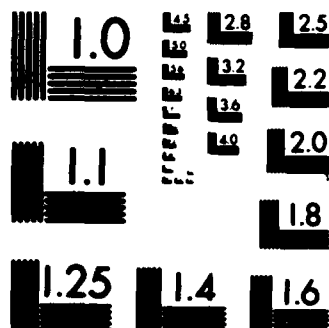
1/2

UNCLASSIFIED

F/G 20/4

NL



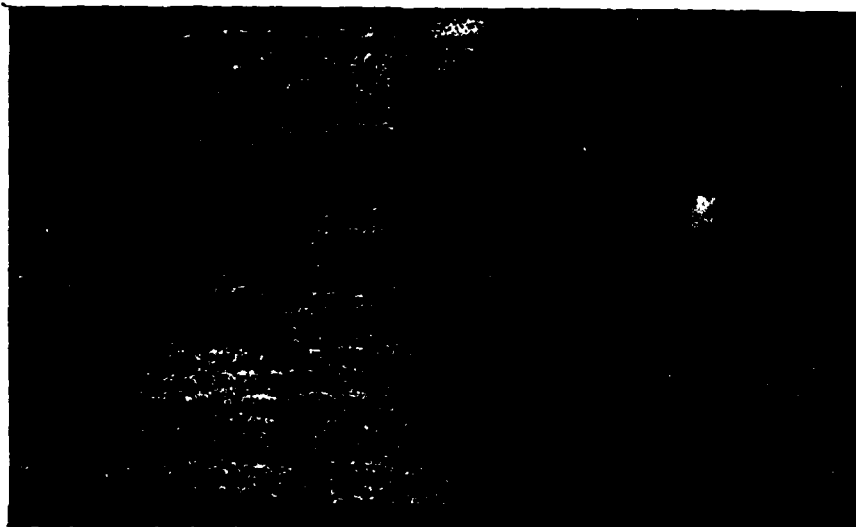


MICROCOPY RESOLUTION TEST CHART
NATIONAL BUREAU OF STANDARDS-1963-A

AD-A182 399

Princeton University

DTIC FILE COPY



Department of
Mechanical and
Aerospace Engineering

DTIC
ELECTE
JUL 09 1987
S A D

This document has been approved
for public release and sale; its
distribution is unlimited.

87 4 21 097

**ORGANIZED STRUCTURES IN A
SUPERSONIC TURBULENT BOUNDARY LAYER**

By

Eric F. Spina & Alexander J. Smits

**MAE Report #1736
February 1986**

**DTIC
S ELECTE
JUL 09 1987
A**

**This work was supported by AFOSR Grant 85-0126
monitored by Dr. James McMichael.**

**This document has been approved
for public release and sale; its
distribution is unlimited.**

TABLE OF CONTENTS

	<u>Page</u>
Chapter 1. INTRODUCTION AND LITERATURE REVIEW	1
1.1 Introduction	1
1.2 Literature Review	3
Chapter 2. EXPERIMENTAL PROGRAM: INSTRUMENTATION AND TECHNIQUE	15
2.1 Overview of Program	15
2.2 Test Environment	16
2.2.1 Wind Tunnel Facility	16
2.2.2 Test Section	17
2.2.3 Test Conditions	17
2.3 Data Acquisition	18
2.3.1 Data Acquisition Hardware	18
2.3.1.1 Preliminary Mean Flow Surveys	18
2.3.1.2 Fluctuating Data Surveys	18
2.3.2 Data Acquisition Procedures	20
2.3.2.1 Preliminary Measurements	20
2.3.2.2 Fluctuating Wall-Pressure Measurements	21
2.3.2.3 Fluctuating Mass-Flow Measurements	24
2.3.2.4 Fluctuating Mass-Flow/ Wall Pressure Measurements	28
2.4 Data Reduction Procedures	30
2.4.1 Time Series Analysis	30
2.4.1.1 Probability Density Function (pdf)	31
2.4.1.2 Power Spectral Density Function	32
2.4.1.3 Autocorrelation Function	33
2.4.1.4 Cross Correlation Function	34
2.4.1.5 Cross Spectral Density Function	36
2.4.2 Conditional Sampling and Averaging Techniques	37
Chapter 3. PRELIMINARY RESULTS: BOUNDARY LAYER OVERVIEW	41
3.1 Mean Flow Survey of the Boundary Layer	41
3.2 Fluctuating Wall-Pressure Measurements	43
3.3 Fluctuating Mass-Flow Measurements	44

Chapter 4. TWO-POINT CORRELATION AND SPECTRUM RESULTS AND DISCUSSION	45
4.1 Pressure-Pressure Results	45
4.2 Mass Flow-Mass Flow Results	47
4.3 Pressure - Mass Flow Results	48
4.4 Summary	49
Chapter 5. CONDITIONAL SAMPLING RESULTS AND DISCUSSION	51
5.1 Introduction	51
5.2 One-Point Pressure	51
5.3 One-Point Mass Flow	55
5.4 Three-Point Mass Flow	58
5.5 Pressure-Mass Flow Two-Point Conditioning	60
5.6 Summary	61
Chapter 6. FINAL DISCUSSION AND CONCLUSIONS	63
ACKNOWLEDGEMENTS	66
BIBLIOGRAPHY	67



Attch on file

A-1

CHAPTER 1

INTRODUCTION AND LITERATURE REVIEW

1.1 Introduction

Great strides have recently been made toward an increased physical knowledge of turbulence, especially in the area of turbulent structure. The older, stochastic approach to the description of turbulent boundary layers is being modified as much new evidence is found to indicate the presence of a complex deterministic hierarchy of structures. Some basic structures have been identified in a variety of shear flows and they appear to evolve through time and space in a quasi-repeatable manner, (see, for example, Acarlar and Smith [1984]). The birth of the structures has been linked to the production of turbulent energy, their movement through the boundary layer has been associated with the diffusion of turbulent energy, and their breakup has been linked with turbulent energy dissipation. The importance of these structures cannot be overemphasized; to gain a fuller understanding of them is essential to gain a fuller understanding of turbulence.

Despite these observations, the actual form the structures take, and how they are manifested through the boundary layer, is still a controversial subject. One of the aims of the present study is to describe experimentally the dynamic behavior of these structures more clearly.

A further aim of this study is to examine the effect of compressibility. Morkovin [1962] hypothesized that the essential dynamics of equilibrium compressible turbulent boundary layers followed the incompressible pattern closely, as long as the fluctuating Mach number remained small. While this hypothesis has been widely accepted in describing the time-averaged behavior,

the effect of compressibility on the organized structures has not been extensively investigated. Do the structures appear the same, and behave in the same way in compressible flow as they do in incompressible flow? Since nearly all the research on coherent structures has been performed in incompressible flows, we intend to extend our knowledge of organized structures to supersonic, compressible flows.

The work was performed in a zero pressure gradient boundary layer. As a preliminary, a complete set of mean flow measurements was taken to characterize the boundary layer used in the study. The instantaneous nature of the turbulence behavior was then investigated, and the primary method of structure eduction used conditional sampling of instantaneously measured flow parameters. Turbulent signals were recorded at several locations simultaneously, providing spatial and temporal information about the structures. Prior to the conditioning of the signals, a complete time series analysis was performed, including cross-correlations and cross-spectra.

The remainder of this chapter discusses the literature pertinent to this experimental program. The equipment, instrumentation, experimental techniques and data reduction methods are described in Chapter 2. An overview of the boundary layer, including mean flow measurements and the basic fluctuating quantities, is given in Chapter 3. The two-point correlation and spectrum results are discussed in Chapter 4 and the conditional sampling results are discussed in Chapter 5. Chapter 6 presents the final discussion and conclusions. A tabulation of the mean flow data is given in the Appendix.

1.2 Literature Review

The review articles by Willmarth [1975], Cantwell [1981], and Wallace [1982] give an excellent account of the recent work on organized structures in turbulence. Willmarth's review deals with the simple case of incompressible flow over a smooth, plane surface with zero pressure gradient. He considers, among other topics, space-time correlation measurements, probe measurements in the intermittent region and the viscous sublayer, and statistical properties of the turbulence field. Cantwell and Wallace both concentrate on the organized motions and flow structure present in turbulent fields. Cantwell deals with boundary layers and free shear flows, while Wallace studies bounded flows (both fully developed and transitional). They both give excellent summaries of the work to date along with their own conceptual models for organized motions.

The "modern" history of organized structures in turbulent flow begins with the bursting cycle first proposed in 1967 by Kline and his colleagues at Stanford (Kline et al. 1967). A hydrogen-bubble wire, placed at various positions near the wall, showed that fluid in the viscous sublayer did not follow straight trajectories; rather, it accumulated into alternating high- and low-speed areas, called streaks. They observed that the streaks had a finite lifetime during which a cycle of events was observed, called the bursting cycle. This process is seen in Figure 1. In more detail, it consists of:

- 1) Accumulation: The formation of low- and high-speed streaks with a uniform spanwise spacing at a y^+ of 3-5.

- 2) Wall Migration: The gradual migration of the low-speed streaks further out into the wall layer.
- 3) Lift-up: The dramatic lift-up of the low-speed streaks until they penetrate the inner portion of the log-law region, thereby creating an unstable inflectional velocity profile.
- 4) Oscillation: The violent, three-dimensional oscillation of the lifted streak for several cycles.
- 5) Breakup: The breakup of the streak into much finer scales, with a broad frequency content, which then becomes chaotic.

Kline et al. also found that the pressure gradient had an effect upon this cycle: a favorable gradient reduced the rate of bursting, and an adverse gradient increased the rate and intensity of the cycle. It was suggested that the pressure gradient either assists or hinders the lift-up of the streak by affecting the inflection in the velocity profile.

Kline et al. conjectured that the bursting phenomenon plays a leading role in the production of turbulent energy and that it controls the diffusion of this energy from the inner layer to the outer layer. Later research supported this claim, most notably the work of Corino and Brodkey [1969], Kim et al. [1971], and Willmarth and Lu [1972]. Corino and Brodkey studied turbulent pipe flow and found a mechanism similar to bursting which they termed "ejections". They noticed that these ejections occurred at a y^+ of approximately 10, and that a "sweep" followed the ejection. The sweep cleans away the fluid from the previous ejection (or burst). They also found that the intensity and number of ejections per burst increases with Reynolds number (a range

from 2,500 to 50,000). Most importantly, they observed, as Kline had suggested, that the bursts account for approximately 70% of the Reynolds stress level in the boundary layer near the wall. Further work by Kim et. al. [1971] showed that virtually all of the net production of turbulent energy in the range $0 < y^+ < 100$ occurs during bursts. Willmarth and Lu [1972] found that significant contributions to the Reynolds stress also occurred during the sweep phase.

These early studies indicated that the bursting process was essentially a wall phenomenon. Further research, however, inferred a stronger level of interaction between the outer layer and the wall layer than a random diffusion of energy from inner to outer layer. Rao et al. [1971] and Grass [1971] showed that the mean bursting period scales with outer-layer parameters (U_∞ and δ), while the spanwise spacing scales with inner-layer parameters (u^* and v). A complex inter-relationship between the inner and outer layers is suggested, not confined to a net flow of fluid during the bursts. Rao et al. suggested that larger eddies from the outer layer move down in the boundary layer and "scour" the slow-moving inner layer, creating regions of intense shear. The shear excites and enlarges local instabilities, thus triggering the burst-sweep cycle. The cycle thus becomes an overall flow phenomenon and can scale on both inner and outer flow variables. Offen and Kline [1974,1975] also showed that the bursting sequence is affected by large-scale motions. These motions appear to stimulate a sequence of low-speed streak lift-up, oscillation, and breakup. Thus from beginning to end the bursting process involves the interaction between inner and outer layers (see Figure 2).

The burst-sweep cycle was modelled by many researchers using hairpin vortices. These vortices take on many forms, but are basically Λ -shaped loops formed from a vortex tube. In fact, Kline derived his bursting model from studies of vortex loop structures developing in turbulent boundary layers. In these models, the mechanism of vortex stretching produces the locally intense shear layers which then cause the oscillation and breakup of the low-speed streaks. The vortex stretching, caused by the interaction of larger eddies from the outer layer with the lifted low-speed streaks, manifests itself as a region of concentrated vorticity just outside the sublayer. These stretched vortex elements undergo a rapid breakup due to their high instability. The models further view the formation of the low-speed streaks as being due to the concentration of low-speed fluid between the legs of the vortex. Two excellent examples of hairpin vortex models for near-wall behavior (bursting) are provided by Hinze [1975] and Smith [1984].

Hinze's model begins with a horseshoe vortex (a horseshoe may be considered as a short hairpin vortex with thicker legs) which is stretched and elongated by the wall velocity gradient. In accordance with the Biot-Savart law, the head of the vortex loop is propelled into higher speed regions because of self-induction. This action stretches the vortex further, increasing the vorticity concentration in the hairpin. Meanwhile, low-speed fluid is forced between the counter-rotating legs of the vortex, producing a concentrated shear layer. The fluid surrounding the tip of the hairpin is subjected to the local inflectional instability caused by this intense shear layer. The tip then breaks down and produces a turbulent burst. The highly energetic turbulent fluid which results from the burst is convected downstream and diffused

outward, thereby increasing in scale and decreasing in frequency content. The pressure waves associated with the burst propagate through the boundary layer, setting up a transient local pressure gradient which aids the movement of "fresh" fluid towards the wall - this is the "sweep". Hinze suggests that the horseshoe vortices are generated during the breakdown of the intense local shear layers created at the interface between the inner and outer layers.

Smith's model is the result of extensive flow visualization studies using side-, top-, and end-views of hydrogen bubble lines. To model the boundary layer structures on a large scale, he created vortex loops by using a hemisphere protruding from the wall of the boundary layer. The hemisphere served as a trip for the vortex sheet to roll-up and form a horseshoe vortex loop; see Figure 3. When seen end-on (looking upstream), a "mushrooming" effect was discovered, which indicates a spreading of fluid in the spanwise direction and infers that the loop is leaning forward. When viewed from the top, a double-loop structure was observed. These double-loop and mushrooming patterns are the result of a connected pair of counter-rotating, streamwise-leaning vortical structures, that is, a horseshoe vortex. While observing these structures, Smith noticed that a horseshoe vortex was always present when a low-speed streak evolved, suggesting that the vortices are either necessary for a burst, or the result of one.

A summary of Smith's synthesized model starts by considering a low-speed streak region. The streak grows until the passage of a disturbance of sufficient size and strength (possibly caused by a large eddy from the outer layer) impresses a local adverse pressure gradient upon a portion of the streak. The resultant local deceleration creates a three-dimensional inflectional profile

at the interface between the low-speed streak and the faster moving fluid in the wall region. Once this inflection develops, the streak is extremely susceptible to local disturbances and instabilities can grow. The instabilities cause the onset of three-dimensional oscillations in the inflection region which then propagate to the vorticity sheet encompassing the low-speed streak. This leads to the roll-up of the sheet into characteristic horseshoe vortices, as we have seen in Figure 3. This full process is shown in Figure 4a and 4b.

Once the formation of the three-dimensional vortex loops has begun, Biot-Savart interactions between various parts of the loop cause a self-induced movement of the hairpin away from the wall. This results in the stretching of the vortex in the streamwise direction, which reinforces hairpin formation farther away from the head of the vortex loop. A pair of counter-rotating legs with a streamwise orientation is created, as seen in Figure 4c. These legs remain close to the wall, but are stretched by the strong velocity gradient there. Two phenomena result: 1) elevated viscous dissipation due to the strongly amplified vorticity concentrations caused by the stretching, and 2) the creation of a lateral pressure gradient, causing accumulation of low speed fluid between the legs, which then acts to perpetuate the low-speed streaks (serving to close the cycle).

As the head of the hairpin vortex is convected downstream, it creates a strong local streamwise pressure gradient, which causes the rapid ejection of low-momentum fluid from the low-speed streak, as seen in the end view of Figure 4c and 4d. As the burst event continues, the Biot-Savart effects cause further distortion of the head of the vortex and the hairpin aligns itself in

two characteristic ways. First, the heads of the hairpin vortices, from those just forming to those near "death" due to viscous dissipation, line up at an angle of about $15-30^\circ$ from the wall. Second, the inclination of an individual hairpin vortex becomes approximately 45° , the angle of the principal axis of strain. These two effects have been seen in many experimental investigations and are shown in Figure 4d. Taken to the limit, the hairpin vortex dissipates, leaving only the low-speed fluid near the wall (once the vortex loop's legs). Perry and Chong [1982] point out that "eddy death" occurs because viscosity always "wins out" when the structures are stretched at less than exponentially increasing rates.

Smith's model is probably the most complete description of near-wall, organized structure behavior. It is a full cycle which is able to account for much of the experimental evidence. Contained in the model are Kline's bursts, Corino and Brodkey's ejections and sweeps, and the typical shape of near-wall structures. Furthermore, the model accounts for turbulent energy production, diffusion, and dissipation.

Researchers from Kline to Smith have concentrated their efforts on the near-wall organized structure. Recently, however, research has indicated that hairpin vortices similar to those connected with the bursting process may extend throughout the major portion of the boundary layer. Head and Bandyopadhyay [1981] used flow visualization to study a zero pressure gradient boundary layer over a wide range of Reynolds numbers ($500 < Re_\theta < 17,500$) and found significant Reynolds number effects on the boundary layer structure. The essential feature which they discovered is the presence of many hairpin

vortices throughout the entire boundary layer, as if the layer consisted exclusively of hairpins "attached" to the wall region.

The effect of the Reynolds number upon the character of the vortex loops which Head and Bandyopadhyay observed is seen in Figure 5. These vortex loops have undergone varying amounts of stretching and elongation, depending on the Reynolds number. Apart from the shape of the vortex loops, they found that the character of the entire boundary layer was Reynolds number dependent. At higher Reynolds numbers ($Re_\theta > 2000$), the elongated hairpin vortices originate in the wall region and extend throughout the boundary layer. Individually, they are inclined to the wall at a characteristic "eddy angle" of 40-50°. Larger motions appear to consist of arrays of these hairpins, with their tips lying along a straight line making a smaller angle with the horizontal (approximately 20°), as shown in Figure 6. This larger-scale behavior was only occasionally observed by Head and Bandyopadhyay, but it suggests that, at times, the hairpins arise from the surface in a systematic fashion. They speculated that as one hairpin leaves the surface it creates conditions which are favorable for the creation of another. At lower Reynolds numbers ($Re_\theta < 800$) the vortex loops are much less elongated and the larger motions consist only of isolated vortex loops or of several loops interacting, not of large arrays of hairpins as found in higher Reynolds number flows.

In summary, Head and Bandyopadhyay introduced a new type of organized structure. Instead of merely controlling the production and diffusion of turbulent energy (as with bursting), their proposed large-scale structure appears to describe the whole of the boundary layer. In many ways, however,

the behavior and characteristics of their structure are similar to the structures used by Hinze, Smith, and others to model the bursting phenomenon.

Perry and Chong [1982] have attempted to model the behavior of the full range of organized structures in the boundary layer by emphasizing the theory of vortex dynamics and their interactions. They proposed several shapes and sizes as well as different systematic alignments of the vortices, ("hierarchies"). A model was considered successful when it predicted the law of the wall, accounted for birth and death of the eddies, and described the general behavior of a turbulent boundary layer (proper p.d.f., power spectra, etc.).

The first model Perry and Chong put forth was a simple model using straight rods of vorticity forming a Λ -vortex. The flow was modelled by a random sampling of these eddies of different sizes, all leaning in the downstream direction at a constant angle ϕ , (see Figure 7). The model further assumed that all of the vorticity in the flow resided in the vortices, with the surrounding fluid completely irrotational. The law of the wall can be recovered in this instance by assuming conservation of circulation in the vortex rods, conservation of heat (in the case of a heated wall), and a "Kline scaling" for the lateral spacing of the vortex loops ($\Lambda = 100\nu/u_\tau$). Each Λ -vortex is stretched under the action of its surrounding neighbors, and the height of the eddy grows uniformly with time. However, as this stretching proceeds, the aspect ratio of the Λ -vortex increases, the legs of the vortex approach each other, and viscous diffusion dominates over the stretching. The resulting vorticity cancellation causes the eddy to die at a fixed height (which also scales on ν/u_τ). However, it has always been accepted that the log-law region grows without limit as $\delta u_\tau/\nu \rightarrow \infty$, and therefore a more advanced

model is required to correctly predict the outer layer behavior.

A more advanced model assumes geometrically similar hierarchies of eddies, as seen in Figure 8. Plane strain (from neighboring eddies) occurs within each hierarchy and the eddies grow from their initial height to a height δ , where δ is the height of the largest contributing eddy in that hierarchy. In a given hierarchy, δ is limited to the height at which the legs of the Λ -vortex begin to merge; thus, eddies larger than δ in a particular hierarchy are of no consequence, since they are undergoing vorticity cancellation. It is assumed that each succeeding hierarchy has a length scale twice that of its predecessor. Since all hierarchies originate from the same sublayer, the characteristic "jump velocity" (across the original vortex sheet) is the same and scales with u_τ . The circulation thus doubles from one hierarchy to the next, which is a necessary condition for producing the correct Reynolds stress distribution.

To make the model work, Perry and Chong assume that no hierarchies, other than the first, have eddy heights less than $\delta/2$, where δ is the scale of the hierarchy under consideration. This implies that the shortest eddy in each hierarchy must appear "out of nowhere". Perry and Chong propose vortex pairing to account for this anomaly; two eddies of the largest height in one hierarchy pair to give the shortest eddy for the next hierarchy. One must further assume that half the eddies in a given hierarchy are paired, while the other half die from vorticity cancellation.

This model can be improved by using a distributed system of hierarchies, as opposed to the discrete system just considered. The discrete system consists of eddies whose length scale goes in geometrical progression with a

factor of two from one hierarchy to the next. This "quantum jump" phenomenon can be smoothed out by introducing randomness into the process through jitter in several quantities. The p.d.f. of the eddies then consists of a continuous distribution of scales. Perry and Chong show that either model fits the law of the wall and predicts other important boundary layer parameters.

Perry and Chong have further discovered, by use of the continuous inverse power law p.d.f., that no matter what shape the eddies have, and no matter how they are stretched, they will always lead to a logarithmic law, as long as all hierarchies are geometrically similar and have the same characteristic velocity scale.

In summary, Perry and Chong have validated, to a certain extent, the work of Head and Bandyopadhyay, Kline, Smith, and others by theoretically predicting the boundary layer behavior using vortical structures similar to those observed in flow visualization studies.

From this review of previous work, it is clear that our knowledge of the existence and behavior of organized structures has greatly increased over the last twenty years. Detailed measurements and visualization of these structures have been performed in the viscous layer, the wall layer, the log-law region, and throughout the entire boundary layer. Complex models have been derived to explain the structures' characteristics. The wall layer has been well documented in regards to the burst-sweep cycle, and the models discussed previously are becoming widely accepted. The major weakness of all models is still the

relationship between the outer-layer and the inner-layer structures, and further work is obviously required.

As mentioned previously, practically all research into organized structures has been confined to subsonic flows. This is not to say that there is no evidence for coherent structures in supersonic flows. For example, Head and Bandyopadhyay [1981] found evidence for their hairpin vortex hypothesis from the schlieren photographs of Decker and Weekes [1976] and Decker [1980]. The photographs show the floor of a duct after the passage of a shock wave. For two different shock strengths, 45° striations may be found close to the wall, supporting the 45° leaning vortex theory. The present authors have discovered similar structures in two shadowgraphs published by Van Dyke [1982]. Plate 1 shows the turbulent boundary layer on a cone cylinder moving through the air at a Mach number of 1.84 (photograph by A. C. Charters, p. 160); Plate 2 shows the turbulent boundary layer on a body of revolution in free flight at Mach 2.58, (photograph from the U. S. Army Ballistic Research Laboratory, p. 161). Evidence for the 45° turbulent boundary layer structures which have been discussed by many researchers can be clearly seen in these close-ups.

Despite this flow-visualization evidence, the study of turbulent boundary layer structure in supersonic flow has been largely neglected. No quantitative measurements describing the instantaneous behavior exist, and the effect of large density gradients and high Reynolds number on boundary layer structure are completely missing. The present study aims to be the first step in the effort to fill this gap in our knowledge of wall turbulence.

Chapter 2

EXPERIMENTAL PROGRAM: INSTRUMENTATION AND TECHNIQUES

2.1 Overview of Program

To fulfill the aims of this study, emphasis was placed on the simultaneous measurement of the time-dependent flow behavior at a number of points in the flow.

From these measurements the usual one-point analyses can be done: root-mean-square values, probability density functions, power spectra, and autocorrelation functions may all be computed. In addition, two-point methods such as cross-correlations, coherence functions, and phase angle functions can be used to find length and time scale information throughout the boundary layer. Furthermore, the simultaneous time histories can be conditionally sampled and examined for the presence of characteristic patterns in the turbulent flow.

The experimental program consisted of four basic parts:

- 1) Mean-flow surveys of the flow field to determine boundary-layer characteristics and to verify the two-dimensionality of the flow. Surveys included: static pressure profiles, pitot pressure profiles, and Preston-tube surveys (to deduce skin-friction).
- 2) Simultaneous, multiple wall-pressure transducer measurements to determine spatially averaged convection velocities and typical pressure signals at the wall.

- 3) Simultaneous, multiple hot-wire anemometer measurements to determine typical eddy shapes, sizes, and angles of inclination and to determine typical mass-flow/velocity signatures.
- 4) Simultaneous, combined wall-pressure and mass-flow measurements to determine the connection between the velocity field and the pressure at the wall.

2.2 Test Environment

2.2.1 Wind Tunnel Facility

The experimental studies were performed in the Princeton University 8-inch by 8-inch high-Reynolds-number, supersonic, blowdown wind tunnel. A detailed description of this facility was given by Vas and Bogdonoff [1971].

Briefly, pressurized air is supplied by four Worthington four-stage compressors (from atmospheric to 3200 psia) and stored in four tanks with a total capacity of 2000 cubic feet. A hydraulically controlled valve releases the pressurized air into the settling chamber at a stagnation pressure preset between 60 and 500 psi. The settling chamber temperature decreases by several degrees Kelvin during each run due to expansion. From the settling chamber, the air is expanded through a convergent-divergent nozzle to a nominal Mach number of 2.9 in the working section. The working section is composed of three interchangeable 35.5 inch long constant area test sections with a cross-section of 8 inch x 8 inch. The air is then exhausted to atmosphere through a diffuser section.

2.2.2 Test Section

Tests were conducted in the floor boundary layer in the second section downstream from the nozzle. For convenience, a coordinate system was referenced to the start of this section with X the streamwise coordinate, Z the spanwise coordinate (with $Z = 0$ on the centerline) and Y the coordinate normal to the wall. The origin of this coordinate system is 68.5 inches downstream from the nozzle throat (see Figure 9), measured along the tunnel wall. To measure the static pressure with a static pressure tap or miniature wall-pressure transducer, a two inch instrumentation plug was inserted on the centerline of the tunnel at $X = 18.5$ inches. To survey the floor boundary layer, probes were inserted from one of two different ceilings. For measurements taken along the tunnel centerline, a ceiling with a streamwise slot was used. For measurements taken off the centerline, a ceiling was used which could access any streamwise location, yet also gave lateral mobility.

2.2.3 Test Conditions

For all tests the stagnation pressure was $100 \text{ psia} \pm 0.5\%$ and the stagnation temperature was nominally 270 Kelvin. For hot-wire measurements, the running time was approximately two minutes, with a stagnation temperature drop of 3-4%; other runs were considerably shorter and the temperature drop was not as great. The flow had a typical freestream Mach number of 2.87 (± 0.01) with a unit Reynolds number of $8.5 \times 10^6/\text{m}$ ($\pm 4\%$). The walls were approximately adiabatic and the freestream turbulence level was 1-1.5%. All of the instantaneous flow measurements were centered about $X = 18.5$ inches, $Z = 0$ inches. Conditions at that point are given in Table 1.

2.3 Data Acquisition

2.3.1 Data Acquisition Hardware

Separate data acquisition systems were used for mean flow surveys and for instantaneous measurements.

2.3.1.1 Preliminary Mean Flow Surveys

For the mean-flow surveys, the data acquisition system consisted of a Hewlett-Packard 1000 minicomputer, a Preston Scientific GMAD-4 analog-to-digital converter, and a Hewlett-Packard 2240 Measurement and Control Processor. The GMAD-4 is a sequential, multi-channel, 14 bit (plus sign) analog-to-digital converter with an input range of ± 10 volts and a maximum sampling frequency of 50 kHz. The Measurement and Control Processor was interfaced with the minicomputer and controlled probe movement during flow surveys.

Very briefly, the output voltage from each transducer (stagnation pressure and temperature, position, and quantity of interest) was digitized by the GMAD-4, converted from counts to real values by the appropriate calibration curve, and then stored on the computer hard disc.

2.3.1.2 Fluctuating Data Surveys

For the fluctuating data collection, a much faster system was used, with sampling rates of up to one million hertz on each of four simultaneous channels. The system used consisted of a VAX 11/750 minicomputer and CAMAC (Computer Automated Measurement and Control) data acquisition system. The CAMAC system, obtained from LeCroy Inc., consisted of a programmable amplifier, an analog-to-digital converter, and memory. All units were designed to handle

from one to four channels of data simultaneously, and they were installed in a Kinetic Systems Crate. Interfacing with the VAX was accomplished through a crate controller.

The analog data signal entered the CAMAC system through the 8100 Dual Programmable Amplifier, equipped with adjustable gains from 0.2 to 100. The D.C. bias was adjusted to zero at the specified gain, and the amplifier roll-off frequency was greater than 1 MHz on each channel. The amplified signals were then sampled simultaneously (less than 5 nanosecond uncertainty) and digitized at a rate of 1 MHz by the TD8210 Waveform Analyzer, with a resolution of 9.8 millivolts/count (10 bits) over an input range of ± 5 volts. All four of the TD8210 channels had slightly different gains, which were accounted for in the data reduction programs. These digitized signals were then temporarily stored in a 96000 word (98304 data points) memory formed by cascading three 8800A Memory Modules. When this memory became full, the data was unloaded (stripping one channel at a time) to disc storage on the VAX (as binary representations of A/D counts). The memory modules allowed a maximum, continuous record length of 24576 data points per channel for each of four channels.

Another integral part of the high-speed data acquisition system was a number of Ithaco Model 4213 analog filters with a roll-off of -80 db/decade (four pole Butterworth filters).

Since much of the experimental analysis required comparisons between channels, no phase shift among the channels could be tolerated. Therefore, each CAMAC channel and, more importantly, each Ithaco filter was checked to ensure a zero relative phase shift in the frequency range of operation. This

was accomplished by inputting a sine wave to two different channels, and monitoring the output for any relative shift of signals. Each of the channels and filters which were used was found to have virtually no relative phase shift.

2.3.2 Data Acquisition Procedures

2.3.2.1 Preliminary Measurements

Each mean-flow data point consisted of four measurements: stagnation pressure and stagnation temperature in the settling chamber, a linear distance (from the floor, for instance) and the quantity of interest (pitot, static, or Preston-tube pressure). At the start of the day, each transducer-A/D converter pair was calibrated by inputting a known signal (from a laboratory standard) for at least five values in the range of interest. Calibration coefficients were deduced from a least-squares linear fit to the data pairs of input signal and corresponding sampled value. Only calibrations with a standard deviation of less than 1% were accepted.

The stagnation pressure was measured with a Pace 500 psi transducer referenced to atmosphere. It was calibrated against a Heise 0-500 psi pressure gauge, accurate to 0.2% of its full scale deflection, in 10 psi increments from 80 to 120 psi. Pitot, static, and Preston-tube pressures were measured with 10, 50, or 100 psi Druck transducers referenced to vacuum and calibrated against a Wallace and Tiernan standard gauge. The stagnation temperature was measured by a chromel-alumel thermocouple with an ice bath reference. The calibration was performed against a Time Electronic millivolt source accurate to 0.05% of full scale (9.99 millivolts). Linear distances were measured

using potentiometers calibrated against dial indicator gauges, marked in .001 inch increments.

All pressure probes were designed to be long and slender in order to minimize local interference. The static pressure probes were small, cone-tipped cylindrical probes made from 0.85 mm diameter hypodermic tubing. Two 0.25 mm orifices were located ten diameters behind the tip, circumferentially opposite each other in the horizontal plane. The pitot pressure probe had a 0.18 mm flattened tip with a 0.08 mm opening. The Preston tube had a circular cross-section with an inner-to-outer diameter ratio of 0.6.

As each probe was traversed, a single pressure measurement was taken at each location. No averaging was done, but a delay of 300 milliseconds was used to allow the pressure transducer to equilibrate. This delay was found to give satisfactory results under all operating conditions encountered in this experiment.

2.3.2.2 Fluctuating Wall-Pressure Measurements

Measurements of the wall-pressure fluctuations were made using four identical miniature differential pressure transducers manufactured by Kulite Semiconductor Products Inc., Model XCQ-062-25-D. Each transducer had a 0.71 mm diameter silicon sensing element on which a fully active Wheatstone bridge was bonded atomically. The transducer emitted a voltage proportional to the difference between the pressure applied to the silicon diaphragm and a reference pressure. For this experiment, the reference pressure was set to the local mean pressure (3.34 psi). Therefore, the mean pressure was eliminated from the signal and the resolution of the fluctuating component could be

increased dramatically. The natural frequency, as quoted by the manufacturer, was 500 KHz. The best estimate for the usable frequency range was approximately 0-80 KHz.

The transducers were calibrated statically every three or four runs at the operating temperature, by applying a known pressure to the transducer diaphragm and monitoring the output. The calibrations were carried out at the operating temperature because it was found that the resulting calibration coefficients had a strong dependence on the stagnation temperature. Once again, only calibrations with a standard deviation of less than one percent were accepted. It should be noted that shock tube tests by Raman [1974] have shown that transducers of this type have dynamic calibrations only a few percent lower than those obtained statically.

Four pressure transducers were mounted in-line in a cylindrical plug (see Fig. 10a), which was then fitted in the test section floor with its center at $X = 18.5$ inches, $Z = 0$ inches. The separation distance between each transducer was 0.2 inches, that is, transducers were located at $X = 18.2, 18.4, 18.6, 18.8$ inches. The plug could be rotated through 360° , yawing the transducers relative to the flow.

Hanly [1975] has shown that the flushness of the transducers is an important parameter in measuring fluctuating surface pressure accurately. Accordingly, the transducers were adjusted to less than 0.002δ under the floor surface using a microscope.

Due to the low output voltage level of the transducers, each signal was amplified by a two-stage amplifier circuit for a total gain of 1000. These amplifiers were found to have roll-off frequencies of at least 400 KHz.

The signals were then band-pass filtered by the Ithaco analog filters. The high-pass was set to 250 Hz to reduce electronic noise and low frequency tunnel noise. The r.m.s. noise in the system (without the tunnel running) was found to be .004 psi, giving a typical signal-to-noise ratio of 12. The low-pass was first set to 500 KHz, which is one-half the sampling rate, to reduce aliasing of the signal. At such a high cut-off frequency, however, a resonance of the Kulite transducers at 480 KHz was producing a very large spike in the energy distribution (as found from the power spectra). Since the gain of the transducers is constant to only 80 KHz, it was decided to low-pass at 125 KHz to reduce the effect of the resonance. Even so, the spectra of the transducers was unreliable down to 40 KHz. The effect of this will be seen in Chapter 3. After the signals were filtered, they were fed into the CAMAC system where they were amplified by another factor of 5, digitized at a rate of 1 MHz, and written to disc on the VAX. See Figure 11 for a flowchart of the pressure data acquisition system. Given a typical pressure fluctuation of 0.05 psi, the combined gain of 5000 results in an A/D resolution of 60 counts for that pressure peak.

Data was obtained in files of three records, each record containing 24,576 points per channel. Convergence of mean pressure, r.m.s. pressure, probability density distribution, and power spectrum was easily achieved under such sampling procedures.

Phase shifts between the transducers were determined indirectly by taking one run with the transducers aligned with the flow, another after rotating the plug 180°, and then comparing the cross-correlations. A maximum shift of 2 micro-seconds was observed between channels; i.e., the location of the

maxima of the cross-correlation differed by a maximum of 2 micro-seconds when the plug was rotated. The implications of this result are discussed further in Chapter 3.

2.3.2.3 Fluctuating Mass-Flow Measurements

A DISA 55M10 Constant Temperature Hot-Wire Anemometer was used to measure the instantaneous mass flux. The hot-wire probes were constructed by electroplating 5 micron diameter tungsten wire with copper and soft-soldering the wire onto the probe prongs (2.5 - 3 mm separation). The wires were then etched using a dilute sulphuric acid solution to expose an active portion of tungsten wire 0.8 - 1.0 mm in length. A small amount of slack was introduced into the active length of the wire to avoid strain-gauging at high frequencies. This type of probe, first recommended by Kovaszny [1950] and then critically examined by Smits et al. [1983], gives reasonable wire lifetimes, minimizes interference from bow shocks emanating from the prongs, and yields a good frequency response.

For multi-wire runs, a special hot-wire support was designed to hold four normal wires in pairs of two, one above the other, and the two pairs of wires could be moved relative to each other vertically (see Fig. 10b). No runs were actually made using all four wires. However, two runs were made with a double normal-wire probe: one with a y-separation of 2.38 mm, the other with 2.58 mm. Two runs were also made with a triple normal-wire probe: the separation distances were 2.58 mm, 3.17 mm, and 5.75 mm.

In a constant temperature anemometer system, the output signal contains contributions from mass-flow fluctuations and stagnation temperature fluct-

tuations. The hot-wire response to both contributions varies with the overheat ratio, τ , defined as:

$$\tau = (T_w - T_e) / T_o$$

where T_w is the wire temperature, T_o is the flow stagnation temperature, and T_e is the wire recovery temperature. The contribution due to mass-flow fluctuations and temperature fluctuations could be separated by operating the wire over a range of overheat ratios. However, the constant temperature system is inherently unsuitable for operation at low overheat ratios, and it is therefore unsuitable for measuring stagnation temperature fluctuations. Smits et al. [1983] have shown that at higher overheat ratios (between 1.0 and 1.3), the contribution of the temperature fluctuations is small enough so that it can be neglected and the hot-wire anemometer is then sensitive only to mass-flow fluctuations. In addition to diminishing the effect of the stagnation temperature fluctuations upon the output signal, increasing the overheat ratio improves the frequency response of the wire. The upper limit of the overheat ratio is determined by the oxidation of the tungsten wire. With a stagnation temperature of 270K, the maximum overheat ratio is approximately 1.0, and this value was used throughout the present series of tests.

A small Mach 3 pilot tunnel was used to calibrate the wires and adjust their frequency response. The frequency response was determined by operating the wire in the freestream of the pilot tunnel (at the prescribed stagnation pressure for all tests, 100 psi) while superimposing a square-wave of small amplitude on the wire voltage. Perry and Morrison [1971] have demonstrated

the usefulness of this method for subsonic flow, while Bonnet [1982] has extended the method to compressible flows. The frequency response is optimized by adjusting the gain of the anemometer, the level of the high frequency filter, and the inductance of the circuit until the transient response of the system is minimized. An acceptance criteria for each wire was that the upper roll-off frequency be at least 120 KHz.

The spatial resolution of the hot-wire probe, as determined by the active length of the wire, restricts the frequencies which can be discerned. Since the active portion is larger than the smallest turbulence scales, the hot wire distorts the contribution of the high frequency end of the spectrum. Wyngaard [1968] suggested that the measured value of the one-dimensional spectra falls to one-half of its value at a wave number of $2.1/\ell$ (where ℓ is the active length of the wire). Under test conditions, for a length of 0.8 mm, this frequency was 250 KHz; since this is greater than the frequency limitation of the entire system, it is not the most restrictive factor.

To calibrate the hot wires for mass-flow sensitivity, the wire temperature (and therefore the overheat ratio) was set by selecting the wire operating resistance, and the mass-flow rate was varied by changing the stagnation pressure over the expected operating range (in practice, from 80 to 170 psi). The wall static pressure, stagnation temperature, and anemometer output voltage were all monitored along with the stagnation pressure. The mass-flow rate was calculated and the calibration data was fitted with the following form of King's Law:

$$E^2 = L + M(\rho u)^n$$

From this relation, the calibration coefficients L and M could be calculated along with the mass-flow exponent, n , simply by fitting a linear curve to E^2 vs. $(pu)^n$. The stagnation temperature usually varied by several degrees during a calibration run, and the coefficients L and M were corrected in an iterative manner (as described by Smits et al. [1983]). The calibration temperature to which all data points were referenced was 270K. A value for n of 0.55 proved to give excellent results for all calibration data. For a typical calibration curve see Figure 12.

Boundary-layer traverses were made at many streamwise and spanwise stations. These traverses were made using single normal wires or multiple normal wires arranged in an array. The voltage output from each anemometer was separated into mean and fluctuating components, by means of the Ithaco analog filters, for increased resolution of the fluctuating signal. The mean component was obtained by low-pass filtering at 10 Hz, digitizing the signal at 50 KHz with the GMAD/4 analog-to-digital converter, and then writing the data to disc on the VAX. The stagnation temperature, stagnation pressure, and a linear measurement of the hot-wire probe from the floor were similarly monitored by the GMAD/4.

The fluctuating component of each anemometer signal was band-pass filtered from 10 Hz to 500 KHz, amplified by a factor of 5 and sampled by the CAMAC system at 1 MHz per channel. The low frequency limit, 10 Hz, was chosen to match the mean signal filter, and the high frequency limit, 500 KHz, was chosen as one-half the sampling rate to avoid aliasing errors of the spectrum. See Figure 13 for a flow chart of the hot-wire data acquisition system. Data from each point in the traverse was written to a separate file containing one record

of 24,576 points per channel. This record length gave adequate convergence of the r.m.s. values (within 1% at $y/\delta = 0.5$), the probability density function, and the power spectrum. The total instantaneous values of the mass flow were found by adding the mean voltage to the fluctuating voltage and inverting the calibration curve directly, thereby avoiding the use of the linearized sensitivity coefficients. Before inverting the calibration curve, however, both the total voltage and the time-averaged mean voltage had to be corrected for changes in the stagnation temperature between the actual run and the calibration according to

$$E_{\text{corr}} = E + \left. \frac{\partial E}{\partial T_0} \right|_{(\rho u)} (T_c - T_0) ,$$

where T_c is the reference calibration stagnation temperature (270K) and T_0 is the stagnation temperature during the run. The instantaneous values of the mass-flow fluctuations were then obtained by subtracting the time-averaged mass flow from the total instantaneous mass flow.

2.3.2.4 Fluctuating Mass-Flow/Wall-Pressure Measurements

By combining the use of wall-pressure transducers and hot wires, simultaneous measurements of the instantaneous wall pressure and instantaneous mass flow were made. The hot wires were placed at different points in the flow (relative to the wall-pressure transducers) to obtain a wide spatial resolution of the flow field.

Several different configurations of pressure transducers and hot wires were used:

1) Three Kulites aligned with the flow (separation distances of 0.2 and 0.4 inches) and single normal hot-wire surveys at four upstream stations (ranging to -1.0 inch from the farthest upstream Kulite) and ten downstream stations (ranging to 2.0 inches downstream of the farthest downstream Kulite).

2) Kulites aligned as above, but hot-wire traverses at five spanwise stations (ranging to 0.75 inches laterally away from the line of pressure transducers).

3) Two Kulites aligned with the flow and double normal wire traverses at several downstream stations.

Once again, the matter of relative phase shift between the signals is an important consideration. The best way to determine the phase shift would involve having a step input measured simultaneously by both a hot wire and pressure transducer. By performing a Fourier transform on the output signals to determine frequency content, and examining this spectra, the limit of the response can be found. Alternatively, by examining the frequency limitations of both systems, this limit can be found approximately. As we saw previously, the frequency response of the hot-wire system was always flat to at least 120 KHz, whereas the Kulite's maximum frequency response was limited to approximately 80 KHz. However, the spectra of the Kulites above 40 KHz was found to be unreliable (this will be seen in Chapter 3). Hence, the upper limit on the combined measurements is approximately 40 KHz.

2.4 Data Reduction Procedures

2.4.1 Time Series Analysis

Once the mean and r.m.s. were determined for the mass-flow and the wall pressure, time series analysis was used to further examine the data. This analysis included the probability density function, the power spectrum, and for multi-channel analysis the cross-correlation, the cospectrum, the coherence, and the phase angle.

Before any data analysis was performed, sine waves and square waves were used to determine that all routines were operating correctly.

The reduced fluctuating data was analyzed as 1024 point ensembles in the time series programs. There were several reasons for choosing this record length, including the amount of computation time required to calculate Fourier transforms on the ensemble. Another reason came from considerations involving the cross-correlation function. The cross-correlation program was tested (on all three types of data: pressure/pressure, mass flow/mass flow, and pressure/mass flow) using record lengths of 256, 512, 1024, 2048, 4096, 8192, and 24,576 points. The maximum value of the cross-correlation always occurred at the same value of the time delay (regardless of the ensemble length) yet the peak value varied by $\pm 15\%$. The trend was for lower peak values at small record lengths, a maximum at 1024 points, followed by lower peak values again at larger ensemble lengths. This is probably caused by "phase jitter", which effectively smears the peak value due to the large number of realizations in longer ensemble lengths. Since the maximum value of the peak occurred at a record length of 1024 points, this minimized the phase jitter yet was long enough to achieve a smooth, well-averaged peak value. Also considered was the

fact that the length of the ensemble determines the lowest frequency for the time series analysis. With a record length of 1024 points, this lower limit is approximately 1 KHz. For the present boundary layer, very limited energy is contained below 1 KHz, and therefore a record length of 1024 points was considered to be acceptable.

In each time series analysis, except for the probability density function, fast Fourier transforms were used to improve the speed of the computation. To compute the Fourier coefficients a program called FOURT (written by Norman Brenner, Charles Rader, and Ralph Alter, MIT Lincoln Laboratory, August 1967), was used, which employs the Cooley-Tukey fast Fourier transform method.

2.4.1.1 Probability Density Function (pdf)

The probability density function provides information on the amplitude of the fluctuating data; it describes the probability that the data will lie within a defined range of values at each instant in time. We define the pdf as

$$p(x) = \lim_{\Delta x \rightarrow 0} \frac{\text{Prob}[x < x(t) < x + \Delta x]}{\Delta x}$$

If the data is normally distributed, the pdf will have a Gaussian distribution. The wall pressure followed this closely, as shown in Figure 14. Effects such as intermittency produce a skewed pdf, as is evident near the edge of the boundary layer with the mass-flow data (see Figure 15).

In determining the pdf, 100 cells (or classes) of data were chosen over six standard deviations, giving a cell width of 0.06 σ . The probability density function was then estimated by:

$$p(x) = \frac{N_x}{N.W} ,$$

where N is the total number of data points, W is the cell width, and N_x is the number of data points which fall within the range $X \pm W/2$.

2.4.1.2 Power Spectral Density Function

The power spectral density function gives information as to the frequency composition of the signal; that is, how much of the energy of the signal is contained in each different frequency band. Finding the power spectral density can be thought of as a process in which the data is filtered over a very narrow frequency band (as $\Delta f \rightarrow 0$) and then the mean square value of that band is computed. In exact form:

$$G_X(f) = \lim_{\Delta f \rightarrow 0} \frac{1}{\Delta f} \left[\lim_{T \rightarrow \infty} \frac{1}{T} \int_0^T X^2(t, f, \Delta f) dt \right]$$

Often, the power spectral density function is defined as the Fourier transform of the autocorrelation function:

$$G_X(f) = 2 \int_{-\infty}^{+\infty} R_X(\tau) e^{-j2\pi f\tau} d\tau ,$$

where $R_X(\tau)$ is the autocorrelation defined in 2.4.1.3. The function $G_X(f)$ is a positive, real-valued function.

To estimate the power spectral density function, the data were analyzed using a forward fast Fourier transform. The first and last 10% of each data record was cosine-tapered to avoid the Gibbs phenomenon (Bendat and Piersol

[1971]). This phenomenon is seen as a large spike near the upper and lower cut-off frequencies. These large overshoots are common near digital filter cut-offs, and the Fourier transform behaves as a filter. The power spectrum estimate was computed according to:

$$G_k = \frac{2h}{N} |X_k|^2 ,$$

where X_k is the Fourier coefficient, h is the sampling interval, and N is the total number of data points.

2.4.1.3 Autocorrelation Function

The autocorrelation function describes the dependence of data at a given point at one instant in time to data at a different time. The exact autocorrelation function, for a given separation time between data points, is given by:

$$R_X(\tau) = \lim_{T \rightarrow \infty} \frac{1}{T} \int_0^T x(t) x(t+\tau) dt .$$

The quantity $R_X(\tau)$ is real-valued and may be positive or negative. $R_X(\tau)$ has a maximum at $\tau = 0$ and is symmetric about that point, i.e., $R(\tau_0) = R(-\tau_0)$.

The autocorrelation estimate is computed by determining the power spectral density function, and then computing the inverse Fourier transform to recover the time domain and the autocorrelation function. This estimate of the autocorrelation actually yields a "circular" function, giving spurious results at larger values of τ . However, the autocorrelations of the wall-pressure and the mass-flow signals die out very quickly, and the circular part of the function is therefore not in the region of interest. Finally, the auto-

correlation function was normalized by the value at $\tau = 0$, giving $R_x(0) = 1.0$.

2.4.1.4 Cross Correlation Function

The cross-correlation function describes the dependence which one signal has on another, as a function of the delay time between the two signals. It is determined by taking the average product of $x(t)$ at a time t_0 and of $y(t)$ at a time $t_0 + \tau$ over a total period T , as T approaches infinity. In exact form:

$$R_{xy}(\tau) = \lim_{T \rightarrow \infty} \frac{1}{T} \int_0^T x(t) y(t+\tau) dt .$$

The function $R_{xy}(\tau)$ is a real-valued function which may be positive or negative. Unlike the autocorrelation function, it does not necessarily have a maximum at $\tau = 0$ nor is it an even function. However, $R_{xy}(\tau)$ is symmetric about the ordinate when x and y are interchanged; i.e., $R_{xy}(\tau) = R_{yx}(-\tau)$. The value of the cross-correlation was normalized by the product of the standard deviations of the two signals. Thus, if $x(t)$ and $y(t)$ were completely similar at a specified τ , then $R_{xy}(\tau) = 1$; likewise if $R_{xy}(\tau) = 0$, then the two signals are said to be independent at that time delay.

One of the most important applications for the cross-correlation function is to determine the time required for a signal source (that is, an organized structure) to pass from one point in space to another. If, for example, two signals are measured in a flow at different locations and a peak occurs in the crosscorrelation function at a certain τ_0 , it can be said that, averaged over time, this "event" is likely to take τ_0 seconds to go from one point to the

other. If these two points are aligned with the flow direction, a convection velocity for this event can be found by taking the ratio of the distance between the points and the time delay at which the maximum of the cross-correlation occurs.

To estimate the cross-correlation function, two different methods were used: fast Fourier transforms and a direct calculation via sums and products. Both methods yielded similar results, with the Fourier method having values approximately 5% higher, due in part to a circular definition of the cross-correlation function. Since the computation time for the Fourier transform was much less, it was used almost exclusively.

As discussed previously, a 10% end taper was applied before transforming the data. One signal was packed into the real part of a complex array, the other signal into the imaginary part, and then a forward fast Fourier transform was performed. A raw cross-spectral density estimate was determined as follows:

$$G_{xy}(f_k) = \frac{2h}{N} |X_k^* Y_k| ,$$

where Y_k is the transform of $y(t)$ and X_k is the complex conjugate of the transform of $x(t)$. Similarly to the calculation of the autocorrelation, an inverse Fourier transform of $G_{xy}(f_k)$ was computed and normalized by the product of the signal's standard deviations to determine the normalized cross-correlation function, $R_{xy}(\tau)$.

2.4.1.5 Cross Spectral Density Function

Just as the power spectral density function evolves from the autocorrelation, so the cross-spectral density function evolves from the cross-correlation. The most interesting aspect of the cross-spectral density is not the cross-spectrum but rather the two functions which result from it: the coherence function and the phase function. Since the cross-correlation is not an even function, its Fourier transform (the cross-spectral density) is a complex number:

$$G_{xy}(f) = C_{xy}(f) - j Q_{xy}(f).$$

The real part of the cross-spectral density (the coincident spectral density function) can be thought of as the average product of the two signals within a narrow frequency band, divided by the frequency interval. The imaginary part (the quadrature spectral density function) is the same except that either input signal (but not both) is shifted in time to produce a 90° phase shift at the frequency, f . In polar notation, the cross-spectral density becomes:

$$G_{xy}(f) = |G_{xy}(f)| e^{-j\theta_{xy}(f)},$$

where

$$|G_{xy}(f)| = [C_{xy}^2(f) + Q_{xy}^2(f)]^{1/2}$$

$$\theta_{xy}(f) = \tan^{-1}[Q_{xy}(f)/C_{xy}(f)]$$

The coherence function is then defined as:

$$\gamma_{xy}^2(f) = \frac{|G_{xy}(f)|^2}{G_x(f)G_y(f)} \leq 1$$

Physically, the coherence function tells us how correlated two signals are as a function of frequency. This is an extremely valuable tool, since it contains correlation values for each different frequency; at a glance, the frequencies which contribute to a correlation and the frequencies which die out before being detected at the second location can be determined.

The phase angle, $\theta_{xy}(f)$, constitutes the phase shift between the two signals at a particular frequency. From the phase angle, the time delay in which an organized event moves from one location to another can be determined as a function of frequency:

$$\tau(f) = \theta_{xy}(f)/2\pi f .$$

Furthermore, if the separation distance between measuring locations is known, the convection velocity can be determined as a function of frequency also.

2.4.2 Conditional Sampling and Averaging Techniques

Conditional sampling and averaging was utilized to better determine the existence of organized structures in the boundary layer. Conditional sampling is a technique under which special consideration is given to segments of the signal where certain conditions are fulfilled. The total number of consecutive points satisfying these conditions make up an "event". It is believed that

these "events" are associated with particular fluid dynamic phenomena and are the signature of characteristic structures. The conditional average is then defined as an average taken over all the events.

There are two types of conditional sampling, one-point and two-point. In one-point conditional sampling, the same signal is processed twice; once to define the conditions under which averaging will occur (detection) and once to actually average over the detected events (averaging). In two-point conditional sampling, the detection and averaging are done upon signals acquired at different spatial locations. Two point conditional sampling, therefore, allows time and length scales of the events to be explored.

For this experiment, the following conditional averages were done: 1) one-point on the wall-pressure signal, 2) one-point on the mass flow signal at various points through the boundary layer, 3) two-point on the mass flow (one wire directly above the other), 4) two-point with the wall-pressure signal conditioned on the mass flow at different points (both spanwise and streamwise separations).

Two methods of conditional averaging were utilized: a zero-crossing technique and the variable-interval time-averaging (VITA) method. The zero-crossing technique was a simple first-attempt to find a typical event. Very briefly, a positive event was detected when N negative data points were followed by N positive data points (and vice-versa for negative events). The number of points, N , was dependent upon how stringent a detection criteria was desired. In this series of tests, N varied from two to ten. The events were all summed about the first positive point (in the case of the positive event) and then averaged over the number of detections.

The VITA technique, first developed by Blackwelder and Kaplan [1976], uses the intermittent character of the short-time variance of the detection signal to detect common patterns in the boundary layer. It is assumed that peaks in the short-time variance signal correspond to regions of higher turbulent energy and therefore indicate the existence of organized structures. The short-time variance of a fluctuating signal, $Q(x_1, t)$, is defined by:

$$\text{var}(x_1, t, T) = \frac{1}{T} \int_{t-\frac{1}{2}T}^{t+\frac{1}{2}T} Q^2(x_1, s) ds - \left[\frac{1}{T} \int_{t-\frac{1}{2}T}^{t+\frac{1}{2}T} Q(x_1, s) ds \right]^2$$

where T is the averaging period for the short time variance. As the variance period, T , goes to infinity, the short-time approaches the long-time mean square level. As Johansson and Alfredsson [1982] noted, there is a close relation between the short-time variance period and the time-scales contributing to the short-time variance. A type of band-pass filter behavior is observed, with the center frequency nearly equal to the inverse of the short-time variance period.

The VITA technique assumes that an event occurs when the short-time variance exceeds kQ_{rms}^2 where k is the chosen threshold level. The reference point for the conditional averaging is taken as the midpoint of the event. Once the reference points have been calculated, the averaging can be done as follows:

$$\langle Q(\tau) \rangle = \frac{1}{M} \sum_{j=1}^M Q(t_j + \tau) ,$$

where M is the number of events, t_j is the reference point for the individual event, and τ is the relative time from the reference (so that the signals can be examined upstream and downstream of the center of the event). The events were classified as either positive or negative depending upon the slope of the signal at the midpoint of the event.

In the VITA technique, two important parameters can be varied to optimize results: the period of the short-time variance and the detection threshold. Optimization implies that the average event that results from this process is representative of frequently occurring events, and not a rare event or an atypical one. For each type of data, both parameters were adjusted so that the detection criterion would be "switched on" for all the major events and "switched off" for regions of lesser activity. These judgements were rather subjective but the major conclusions drawn from this conditional sampling were not critically affected by the choice of sampling criteria.

CHAPTER 3

PRELIMINARY RESULTS: BOUNDARY LAYER OVERVIEW

3.1 Mean-Flow Survey of the Boundary Layer

Prior to taking turbulence measurements, several mean-flow surveys were taken in the floor boundary layer. One of the major goals of this part of the experiment was to determine the extent of the two-dimensionality of the flow.

Previous surveys of the tunnel floor boundary layer (Settles [1975], Taylor [1984]) illustrated that the static pressure was constant across the boundary layer in the y-direction. To measure the spanwise and longitudinal variations in static pressure, a four inch spanwise (z-direction) region and a twenty inch streamwise (x-direction) region were surveyed. The static probe was calibrated against the wall static pressure, with a resulting calibration coefficient of 0.91. The spanwise survey was taken at $x = 14.125$ inches, $y = 1.625$ inches. As can be seen in Figure 16, the maximum peak-to-peak variation was less than 5%. The streamwise survey on the centerline at $y = 2.0$ inches revealed a peak-to-peak variation of 6% (corresponding to 1.4% variations in Mach number) and a slight adverse pressure gradient (see Figure 17). The pressure gradient was caused by the growth of the displacement thickness, and it was considered small enough to be neglected.

Pitot pressure profiles (y-direction) were taken at five spanwise and nine streamwise locations; a typical profile is seen in Figure 18. The pitot and static pressure data were used in the Rayleigh-Pitot formula (1) to derive the Mach number profile. A 4% stagnation temperature gradient was assumed through the boundary layer ($T_{o_{wall}} = 1.04 T_{o_{\infty}}$). This was shown to be a good

approximation for this boundary layer by Taylor [1984]. The stagnation temperature profile was used along with the Mach number profile to yield the static temperature distribution (2), which in turn gave the sonic velocity (3). Finally, the product of the local sonic velocity and the Mach number resulted in the local flow velocity. All velocity profiles were found to be similar, and a typical profile is shown in Figure 19.

$$(1) \quad P_{\infty}/P_0 = \frac{\left\{ [2\gamma/(\gamma+1)] M_1^2 - \left(\frac{\gamma-1}{\gamma+1} \right) \right\}^{\gamma/(\gamma-1)}}{\left\{ [(\gamma+1)/2] M_1^2 \right\}^{\gamma/(\gamma-1)}}$$

$$(2) \quad T = T_0 (1 + (\gamma-1)/2 M^2)^{-1}$$

$$(3) \quad a = \sqrt{\gamma RT}$$

Using the Van Driest [1951] transformation, the velocity profiles were mapped onto the incompressible plane, and an extensive logarithmic region was found, as can be seen from the typical profile reproduced in Figure 20.

To investigate the two-dimensionality, two spanwise pitot pressure surveys were taken at points inside the boundary layer. These profiles were taken at the same x position, $x = 18.5$ inches, at two different y positions, $y = 0.4$ and 0.15 inches. A 10% variation in Pitot pressure (see Figure 21). This three-dimensionality is most probably due to the constriction of the side wall boundary layers through the converging-diverging nozzle; however, for the purpose of studying the boundary-layer structure, these effects may not be too significant and they were discounted in this study.

Preston tube measurements were taken at 43 streamwise locations and the skin-friction was deduced according to the method of Hopkins and Keener [1966].

All mean flow results are tabulated in the Appendix.

3.2 Fluctuating Wall-Pressure Measurements

The r.m.s. wall-pressure fluctuation, when normalized by the mean wall static pressure of 3.34 psi, was 0.015. The r.m.s. can also be non-dimensionalized by the dynamic pressure or the wall shear stress; this results in values of 0.0025 and 2.2, respectively. These values are approximately one-half of Kistler and Chen's [1963] values at Mach 3, but are in good agreement with those of Speaker and Ailman [1966], Chyu and Hanly [1968], and Coe [1969]. While it is true that high-pass filtering at 250 Hz reduces the r.m.s. intensity by almost 10%, a significant portion of that is noise associated with tunnel operation. The low values are probably caused by the lack of resolution at high frequencies due to the finite size of the transducers. According to Shewe [1983], the "ideal" transducer (one which would measure 100% of the r.m.s. pressure) has a non-dimensional diameter, $\frac{2\tau_w}{V_{wall}}$, of 20. The transducers used in this experiment have a non-dimensional diameter of about 200. According to Shewe, our transducers should give an r.m.s. pressure which is 60% of that given by the ideal transducer, and this result seems borne out by the present experiment.

As mentioned previously, a resonance was found in the Kulite spectra at 480 KHz. In addition to that spike, however, other abnormalities were found in the spectra all the way down to 40 KHz. The energy distribution, seen in Figure 22, shows the effect of these transducer resonances. It is clear that

the spectrum beyond 40 KHz is inaccurate. However, most of the energy appears to be contained at lower frequencies so the effect of these resonances on the r.m.s. level is probably small.

The probability density function of the wall-pressure fluctuations (Figure 14) has a Gaussian shape, as expected.

3.3 Fluctuating Mass-Flow Measurements

The r.m.s. mass-flow fluctuation level, normalized by the local mass flow, for a typical boundary-layer traverse is shown in Figure 23 along with results from previous work. The profiles show good agreement and were very repeatable. A typical power spectral density plot, taken at $y/\delta = 0.15$ (Figure 24), shows a spectrum without any large spikes or abnormalities well past the region of interest. Normalized probability density distributions for different locations within the boundary layer are shown in Figure 15. These appear as expected; with the edge of the boundary layer approaching, the negative skewness indicates an increased intermittency resulting from one-sided mass-flow spikes (or a mass-flow deficit from the mean) and the positive skewness near the wall indicates intermittency of the opposite sign.

As in the case of multi-pressure transducer runs, an important factor in multi-wire runs is the relative phase shift between the channels. The hot-wire anemometers were all identical DISA 55M10 systems and the wires were only used if they had similar frequency responses. Hence, the relative phase shift through the frequency range of interest was minimized.

CHAPTER 4

TWO-POINT CORRELATION AND SPECTRUM RESULTS AND DISCUSSION

Length and time scale information was determined using two-point correlations and spectrum functions. These two-point measurements reveal a substantial amount of information concerning turbulent scales. Nevertheless, the results are still time-averaged and they are not indicative of the instantaneous properties of the flow field.

4.1 Pressure-Pressure Results

As discussed previously, the four wall-pressure transducers were mounted in a rotatable plug with fixed separation distances, ξ , and measurements were taken with a variety of yaw angles between the flow direction and the line of transducers. Space-time correlations, $R(\xi_1, \xi_2, \tau)$, are shown in Figure 25 for three different yaw angles. Two trends should be noted: 1) the maxima of the space-time correlations decrease with increasing separation distance, and 2) the maxima of the space-time correlations decrease as the alignment of the transducers changes from streamwise to spanwise.

Broad-band convection velocities were deduced from the maxima of the space-time correlations when $\xi_2 = 0$ (streamwise alignment), and they are shown along with previous results in Figure 26. The trend of higher convection velocity for larger transducer separation may be explained by the proposed hierarchical structure of the boundary layer. This states that higher frequency motions (smaller scales) are found closer to the wall, and lower frequency motions (larger scales) are found toward the edge of the boundary

layer, with an appropriate distribution of scales in-between. Thus, the larger structures convect downstream faster than the small-scale structures. When the transducers are moved farther apart, only the large-scale structures move fast enough to be detected by both transducers and therefore a higher convection velocity is computed.

The space correlation pattern, $R(\xi_1, \xi_2, 0)$, of the wall-pressure fluctuations can be mapped out as a set of isocorrelation contours as in Figure 27. The results compare favorably to those obtained by Tan et al. [1985] in a similar boundary layer and by Bull [1967] in a subsonic flow. These contours give an indication of the spatial scales of the pressure-producing structures. From a nearly isotropic pressure field at small spacings, the transverse scale quickly becomes much more significant than the longitudinal scale.

Figure 28 shows a set of isocorrelation contours of the space-time correlation maxima, $R_{\max}(\xi_1, \xi_2, \tau)$. These contours give information on the decay rates of the pressure producing structures, and it may be seen that the decay is much faster in the transverse direction than in the longitudinal.

After the cross-spectrum between pressure signals was computed, several related functions were determined. The coherence, phase angle, time delay, and convection speed functions are shown in Figures 29, 30, 31, and 32 for zero yaw angle. The coherence function, Figure 29, indicates that the higher frequency pressure structures do not retain their shape as well, or for as long, as the lower frequency (larger-scale) pressure structures. This trend is expected, since the larger structures span a greater distance than the high frequency structures and are readily sampled by both transducers. Note that the lack of resolution (limited number of spectral points) is responsible for

the "peaky" nature of the coherence function. The phase angle function, Figure 30, gives similar results. It is worth noting that the phase angle seems to increase linearly over the range from 0 to 40 KHz. The time delay, Figure 31, and the convection speed, Figure 32, again show that the higher frequency structures are moving more slowly than their low frequency counterparts.

4.2 Mass Flow - Mass Flow Results

Two hot wires, one directly above the other at a fixed separation distance, were traversed through the boundary layer. The calculated space-time correlations at different distances from the wall are shown in Figure 33. The peak values of the correlations are quite high, reaching a maximum of 0.65 near the middle of the boundary layer. More importantly, the delay time corresponding to the peak of the space-time correlation, τ_{\max} , decreases from 20 microseconds at the floor to nearly zero at the edge of the boundary layer. The value of τ_{\max} along with the wire separation distance Δ and the local mean velocity can be used to define an angle θ . From the diagrams in Figure 34, we see that:

$$\theta = \tan^{-1} \left[\frac{\bar{U} \tau_{\max}}{\Delta} \right]$$

The angle θ may be called a "structure angle," in that it is associated with an average large-scale motion. The results from three different traverses can be seen in Figure 35 as a function of position in the boundary layer. The angle is small near the floor, increases quickly to about 45°, and it remains

constant at this value throughout 70% of the boundary layer. Finally, the angle shows a rapid increase at the edge of the boundary layer. Note that the distribution of the structure angle seems to be independent of the two different separation distances chosen.

The distribution of θ is in accordance with Head and Bandyopadhyay's [1981] observations in a subsonic boundary layer at low Reynolds numbers. They observed that the hairpin vortices displayed small angles near the floor and 45° through the central portion of the boundary layer, followed by a slight increase near the edge.

The coherence function between two wires (separated by 0.1δ) is shown in Figure 36 for various positions in the boundary layer. Due to the relatively large separation between the wires, information about the higher frequency motions in the flow (above approximately 50 KHz) was not obtained. Therefore Figure 36 describes the behavior of the low frequency (large-scale) structures. Near the floor, these structures do not have a high coherence, as expected from the low space-time correlation values seen near the floor in Figure 33. However, from $y/\delta = 0.2$ to the edge of the boundary layer, the coherence over the low frequency range is quite high and remarkably similar in shape, indicating that they scale upon the boundary-layer thickness.

4.3 Pressure - Mass Flow Results

Cross-correlations were computed between pressure fluctuations at the wall and mass-flow fluctuations measured at various points within the boundary layer. Figure 37a shows the correlations with the hot wire located 0.45δ

downstream of the pressure transducer, while Figure 37b shows them for a streamwise separation of 0.916.

The first point of interest is the rather low level of correlation, with a maximum peak of 0.22. This level of correlation was observed for even the smallest transducer separations and can be ascribed to the differences in the frequency content of the pressure and mass-flow signals. This reduces the correlations, as can easily be demonstrated by calculating the correlation between two sine waves of differing frequencies.

Secondly, although the separation of the transducers is doubled between Figures 37a and 37b, the level of the correlation remains nearly the same. Furthermore, the general shape of the correlation is retained (the small peak at a negative value of τ , followed by a sharp rise to the major peak). Hence, the structures appear to retain their shape and coherence as they are convected downstream.

Figures 37c and 37d show correlations for spanwise separations between the transducers of 0.116 and 0.456 respectively (both also have a streamwise separation of 0.096). We see that Figure 37c shows a slight decrease in correlation level when compared to the previous figures which had no spanwise separation. In addition, in Figure 37d we observe that, with an increased spanwise displacement, the correlation has broken down completely, suggesting that the structures have a very limited spanwise extent.

4.4 Summary

These two-point, time-averaged methods have revealed the existence of organized motions in the boundary layer. They appear to scale on outer-

layer variables and convect downstream a significant distance. At the same time, they have a very limited extent in the transverse direction. Furthermore, these average structures show traits which are similar to motions found in subsonic boundary layers.

Chapter 5

CONDITIONAL SAMPLING RESULTS AND DISCUSSION

5.1 Introduction

The time averaged measurements given in Chapter 4 showed the presence of 45° structures in a high Reynolds number, supersonic boundary layer similar to the structures observed in subsonic flows at low Reynolds number. To investigate the detailed instantaneous structure of these organized motions, conditional sampling techniques were used. Two different schemes were used, and the details were given in Chapter 2. The measurements were confined to the outer layer for two fundamental reasons: 1) we were not able to access the y^+ values at which the bursting process occurs, since the minimum y^+ value was about 1000, and 2) the time scale needed to identify the bursting process ($10\nu/u_\tau^2$) was too small to resolve with our current instrumentation.

Although the shape of these outer-layer structures and their frequency of occurrence strongly suggests that the bursting process is intimately involved in their development, we have not been afforded the opportunity to try to link the two events. Therefore the words "event", "organized structure", "organized motion", "large-scale structure", etc. will refer to the outer-layer motions which we have identified; while the word "burst" will refer exclusively to the bursting process in the inner portion of the boundary layer.

5.2 One-Point Pressure

In this section, a single record length of pressure data, consisting of 25,000 points (0.025 seconds), was examined. The results are virtually

independent of the length of the record and the particular record chosen.

The wall-pressure signal was initially conditioned upon itself using the VITA technique. Here, detection and sampling occur at the same spatial location. In Figure 38, a typical pressure signal is shown, along with its short-time variance with a period, T , of 30 microseconds. When scaled with outer-layer variables, this period corresponds to a non-dimensionalized "decision time", $T^* = TU_\infty/\delta$, of 0.6. It appears that, with an appropriate threshold value k , the short-time variance signal functions quite well as a detection scheme; it is "switched on" for the more energetic and sudden events and "switched off" for quiescent periods and more gradual events.

A number of individual positive events are shown in Figure 39. These events were detected with $T^* = 0.2$ and $k = 0.8$, and it will later be seen that these values optimized the average event. The similarity of the events is remarkable. Note that the "downside" of the major peak in most events does not return to the level at the beginning of the cycle. That is, the positive pressure event is slightly one-sided. Also, the major rise in pressure is always preceded by a decrease, whether it is sharp or gradual. These two observations are reinforced in Figure 40, which shows a number of positive events superimposed. The significant features are: 1) the very sharp rise about which the event is centered, 2) the elevated pressure level after the cycle is over, and 3) the dip in pressure prior to the steep rise.

After identifying the individual events, an ensemble average was computed. The threshold dependence is seen in Figure 41. The major features of the positive event seem to be essentially independent of threshold value; the steep rise, and the size of all three averages are approximately the same. The major

difference is found in the secondary peak on the downside of the cycle, where the pressure falls off as the threshold decreases and the number of events increases. This trend is due to the summation of random signals, and as the number of events increase some "washout" occurs. The frequency of these events, non-dimensionalized with outer-layer variables, $f^* = f\delta/U_\infty$, can be seen in Table 2. We see that, as the threshold increases from 0.7 to 1.0, the number of events falls off by one-half.

The effect of changing the period of the decision time for the short-time variance is seen in Figure 42. Again, the most significant portion of the average event, the steep rise, is virtually unaffected by changing the detection parameters. The secondary peaks, however, increase with the length of the decision time. For the short-time variance to remain above the threshold level with an increasing decision time, there must be activity over a longer period of time, and the individual events are more apt to have an additional peak. It is interesting to note that as the decision time goes from 0.4 to 1.0, the number of events stays roughly constant. We will see later that this trend is the opposite to that observed for the mass-flow events.

The threshold and the decision time were chosen to give the most energetic average event while retaining a significant number of realizations. The average positive event, Figure 43, and the average negative event, Figure 44, were detected with $k = 0.8$ and $T^* = 0.2$ (10 microseconds). The character of these average events is, of course, similar to the individual events from which they evolve. Therefore, we see the characteristic strong rise about which the event is centered, the decrease in pressure before and after this "wave front", and the presence of the secondary peaks.

From peak-to-peak the positive event is 2.2 times the pressure r.m.s. level, while the negative event is 2.5 times the r.m.s. level. These average events are significantly larger than those in Figures 41 and 42 where the detection parameters were not optimized. The non-dimensionalized frequency of occurrence for the positive events is 0.16 and for the negative events it is 0.21. The period of each of the average events is approximately 40 microseconds, and when this is combined with their frequency of occurrence and the length of the total record, it appears that these typical events (positive and negative combined) occupy about 25% of the total signal time. It seems that we are looking at a relatively common event. Considering the high level of activity associated with the events, we can state that they contain the majority of the turbulent energy in the flow. Presumably, they will also carry most of the turbulent shear stress.

For comparison, a conditional average using a different detection scheme, the zero-crossing technique, was also performed. In this case, there was a single detection parameter N , where N is the number of consecutive negative data points followed by the same number of positive data points. Figure 45 shows the average positive zero crossing ($N = 5, 8, 10$) and Figure 46 shows the average negative zero crossing ($N = 10$). The effect of varying N can be seen in Figure 45. As the criterion becomes less stringent (N decreasing) the number of events increase and the secondary peaks drop off more quickly. Once again, this demonstrates the wash-out due to the summation of random signals. As with the VITA technique, however, varying the detection parameter does not effect the basic character of the average event.

Most importantly, the zero-crossing and VITA methods give approximately the same shape for the average events. Also, the frequency of occurrence is very similar to that deduced using VITA: $f^+ = 0.17$ for the positive events and $f^- = 0.16$ for the negative events (as compared to 0.16 and 0.21 with the VITA technique). The standard deviation from the event frequency was computed to be 0.21 for the positive events. That the standard deviation is greater than the mean implies that this is not a Gaussian event; rather, the distribution of the frequency of events is one-sided, biased towards higher frequencies.

Overall, it appears that the wall-pressure events deduced by conditional sampling do not depend strongly on the sampling method or criteria, and it also appears that the events are reasonably common and contain significant turbulence activity.

5.3 One-Point Mass Flow

The VITA technique was used to condition the streamwise mass-flow signal at several points throughout the boundary layer. Initially only one hot wire was used, so that detection and sampling occurred at the same spatial location.

Before examining the results, we need to consider the effect of the sampling criteria on the nature of the deduced positive and negative mass-flow events.

In Figure 47 a mass-flow time trace and its corresponding short-time variance are shown for a y/δ value of 0.03 ($y^+ = 350$, or $y = 0.8$ mm). The decision time is $T^* = 0.2$ (10 microseconds) and the marked threshold is 0.8. Nearly all of the positive events which were detected show a feature

which was also seen on the positive pressure events; namely, once the event is over, the velocity is at a higher level than before the cycle began. This observation is reinforced by Figure 48, which shows a number of individual events superimposed. The similarity of the events along the steep velocity rise and the uniformity in width of the peaks is particularly striking.

Three interesting trends appear in Figure 49, which shows the frequency of positive events and total events (positive plus negative) against position in the boundary layer. First, as one might expect, the frequency of events decreases as the edge of the boundary layer is approached. Lower frequency (larger) motions are expected in the outer regions of the boundary layer, and therefore fewer events will be detected. Also, no events occur in the free-stream, so a drop-off is imperative.

Second, the number of total events and positive events falls off drastically near the wall. This is caused by the band-pass filter characteristics of the short-time variance, with the inverse of the short-time variance period being the center frequency. With a hierarchical structure of frequencies in the boundary layer (as discussed in Chapter 4), fewer events will be detected near the floor since the frequencies of the most prevalent structures will be too high to contribute to the short-time variance.

Third, the total events near the floor consist almost exclusively of positive events, while further from the wall the split between positive and negative events becomes more equal. Again referring to the hierarchical structure of the boundary layer, it would appear that the negative events are slower events; i.e., they have a lower frequency content. Since there are fewer low frequency structures near the wall, the number of negative events

detected there will be less than that detected elsewhere. This explanation is given further credence by Figure 50, which shows the frequency of total events, positive events, and negative events versus the short-time variance period for the station nearest the floor. We see that the number of negative events increases as the short-time variance period increases. Referring to the band-pass filter nature of this technique, we can say that as the detection scheme becomes exclusively a lower frequency detection scheme, the number of negative events increases. Hence, to detect more representative negative events near the floor (that is, more common) a longer short-time variance period should be used, such as 50 microseconds ($T^* = 1.0$).

If we examine the distribution of positive events in Figure 50, it appears that a period of 10 microseconds ($T^* = 0.2$) would most nearly represent the true character of a positive event near the floor. Thus, positive events have a higher frequency content than negative events. It appears that when using the VITA technique, different decision times should be used to detect positive and negative events. This result is in contrast to the great similarity between positive and negative wall-pressure events. Furthermore, the detection criteria for the mass-flow events may have to be varied from point to point within the boundary layer.

Figure 51 displays the threshold effect at $y/\delta = 0.33$ with a decision time of $T^* = 0.2$. The gradual decrease in events as the threshold increases is as expected.

Figures 52 and 53 illustrate the optimum conditionally averaged positive and negative mass-flow events for three positions in the boundary layer. For both the positive and negative events a threshold of 0.8 was acceptable. The

decision times were based upon Figure 50 for $y/\delta = 0.03$ and were chosen to be $T^* = 0.2$ for the positive event and $T^* = 1.0$ for the negative event. Ideally, a plot of occurrence-frequency versus decision time should be consulted for each point in the boundary layer.

Table 3 shows the non-dimensionalized occurrence frequencies for various points in the boundary layer. In subsonic flow, Willmarth and Sharma [1984] computed $f^* = 0.13$ at $y/\delta = 0.01$; which compares favorably to that computed here at $y/\delta = 0.03$.

Now that the question of sampling criteria has been discussed, consider the results. From Figures 52 and 53, it is clear that the typical positive mass-flow event is stronger and more energetic than the typical negative event since its peak-to-peak value is much greater. It can also be seen that the "wave front" of the positive event is steeper than for the negative event, implying that the positive event contains higher frequency motions.

The shape of the average positive event at the lowest position in the boundary layer can be interpreted as an organized structure moving down in the boundary layer and bringing faster-moving fluid with it. The shape of the positive event at the edge of the boundary layer implies that faster-moving fluid still moves down, but the dip prior to the steep rise suggests that a large-scale structure containing slower fluid is moving up through the boundary layer.

5.4 Three-Point Mass Flow

Two-point conditional sampling was performed on the data taken with the three hot-wire probe. The three wires were located at $y/\delta = 0.37, 0.46$, and

0.57 and the detection signal was the short-time variance of either the middle wire or the lowest wire. When an event was detected, all three signals were sampled simultaneously.

The three mass-flow signals and the short-time variance of the lowest wire are shown in Figure 54 for a decision time of $T^* = 0.2$ and a marked threshold of 0.8. The similarity of the three mass-flow signals, especially in the proximity of detected events, is remarkable and gives strong indication of an organized structure. The inclination of these structures, previously discussed in the context of the cross-correlation, is also evident here by the shifting of the peaks from position to position. The organized structures and their angles of inclination are even more evident in Figure 55. Here individual events from all three channels, conditioned upon the middle signal, are plotted. For each series of detected events, the time delay of the peak between positions is slightly different, implying that the angle of inclination and the convection velocity vary from structure to structure.

Figure 56 depicts the average positive events from the three wires, all conditioned upon the middle wire ($k = 0.8$, $T^* = 0.2$). As expected, the average event from the conditioning signal is much more distinct than those events which are two-point conditioned averages. However, the existence of an average organized structure spanning the distance between the three wires is clearly indicated.

A structure angle can also be determined from the average positive events by using the time delay between the points where each event crosses zero during its steep rise. The angles which result (45° from bottom to middle, 63° from middle to top, and 51° from bottom to top) are very similar to

those deduced from the cross-correlation. This is not surprising, and it illustrates that the deduced structures are indeed typical of the boundary layer and important in characterizing it.

5.5 Pressure-Mass Flow Two-Point Conditioning

Two-point conditional sampling was performed on the data taken with a single normal hot wire and three wall-pressure transducers. At all times, the short-time variance of the mass flow signal was used as the detection signal.

The height and streamwise extent of the organized structures was investigated by placing the hot wire directly downstream of the three wall-pressure transducers (aligned in the streamwise direction) at four different y/δ values in the boundary layer. For a hot wire/pressure transducer separation of 0.09δ , Figure 57a shows the average positive conditioned wall-pressure events for each of the y/δ values of the hot wire. Likewise, Figure 57b shows the average pressure events for a streamwise separation of 0.27δ and Figure 57c depicts the average pressure events for a separation of 0.45δ . All of these pressure events were conditioned upon the mass flow ($k = 0.8$, $T^* = 0.2$) and the average positive mass-flow event is shown for each y/δ value in Figure 57d.

The first feature to notice is the excellent average pressure event which is extracted by conditioning upon the mass-flow signal; this is best illustrated in Figure 57a for a y/δ value of 0.03. This average event is almost as large as when the pressure was conditioned upon itself, although slightly different in shape. The difference in shape is most probably because, in the latter case, all pressure events were summed about a point on the steep rise, accentuating that part of the event and neglecting the downside of the peak.

Looking at Figures 57a, b, and c independently, it can be seen that while the structure deteriorates slightly as y/δ increases, the strong correlation between events at different y/δ values indicates an organized structure of significant height (at least 0.3δ). When the three figures are taken together, we see that over a streamwise distance of 0.45δ the structures have retained much of their original coherence. This is further supported by Figure 58, which shows the average pressure and mass-flow events for a streamwise separation of 1.4δ . At this distance, a lot of background noise has appeared, but the organized structure has clearly preserved its basic identity.

The spanwise extent of the organized structures was explored by introducing a spanwise separation between the hot wire and the wall-pressure transducer (in addition to the hot wire being 0.09δ downstream) and measuring the mass flow at four values of y/δ . Figure 59 shows the average positive events for a spanwise separation of 0.11δ and Figure 60 shows them for a separation of 0.23δ . It is readily seen that the organized structure which retained its shape in the streamwise direction has lost its correlation within a very short spanwise distance.

5.6 Summary

These conditional sampling and averaging methods have reinforced our ideas from Chapter 4 about the average large-scale structures in the boundary layer. We have seen that they fill the height of the boundary layer, they retain their shape as they convect downstream, and that they are of limited spanwise extent. The instantaneous character of this technique showed that the individual events are very frequent, similar in shape and size to each other

and to the average event, and that positive events are much more energetic than negative events.

Chapter 6

FINAL DISCUSSION AND CONCLUSIONS

This experimental investigation has extended our knowledge of organized structures in turbulent boundary layers by examining their behavior in a compressible flow. Large-scale structures, inclined at 45° to the wall, were found to fill the height of the boundary layer. As they were convected downstream, these structures retained a great deal of their shape and character, and preserved their identity for at least 1.56. *However, the spanwise extent of the structures was limited.*

The individual events, whether pressure or mass flow, were similar to each other and to the average event, and they were very energetic. In general the positive mass-flow events had a higher frequency content and were larger in amplitude than the negative events.

It would appear that the effect of compressibility on the large-scale motions is very small. Certainly, there are more similarities than differences between the events found in this compressible flow and those observed in incompressible boundary layers. These similarities are clearly shown by comparing the structure angles and the conditionally-averaged results.

For example, the deduced structure angles from this investigation are consistent with Head and Bandyopadhyay's [1981] observations in incompressible flow. The eddy angle is low near the floor, increases quickly to 45° (where it remains throughout 70% of the boundary layer), and increases again near the edge of the boundary layer.

Furthermore, Johansson and Alfredsson [1982] used VITA conditional sampling in fully developed turbulent water-channel flow. Figure 61 shows a number of individual positive streamwise velocity events from their flow. Qualitatively, this figure compares quite favorably to Figure 48, which are individual positive mass-flow events from this investigation. Both figures show the individual events possessing a uniform steep rise and having a higher level at the end of the event than the beginning. In addition, the average amplitude of the events in both cases seems to be approximately four times the r.m.s. level.

The frequency of the events in this flow also compare favorably to incompressible flow. For instance, Willmarth and Sharma [1984]. Normalized with outer flow variables, the frequency of events is approximately .15 close to the wall ($y/\delta \approx .01$).

Several examples of average positive velocity events in incompressible flows were examined and found to be strikingly similar to the mass flow events from this investigation (Fig. 52). Thomas and Bull [1983] performed the most extensive measurements, from $y/\delta = .05$ to .91, as seen in Figure 62. The character of the average event changes (with increasing height in the boundary layer) in a manner similar to that of the compressible flow investigated here. As position in the boundary layer increases, the drop prior to the steep rise (or burst) becomes more significant in both cases.

Johansson and Alfredsson [1982] and Blackwelder and Kaplan [1976] both present VITA average positive events from positions nearer the wall, and the results are reproduced in Figure 63 and 64, respectively. Despite the difference in position ($y^+ = 15$ in Figures 63 and 64), the incompressible events

are nearly identical to those events from the center of the compressible boundary layer. The amplitudes of the incompressible and compressible events are also very similar.

In summary, the organized structures in compressible flow have a large number of similarities to their counterparts in incompressible flow. The large-scale structures are similar in both flows and more surprisingly, the incompressible small-scale structures have some characteristics of the compressible large-scale structures. While a much more intensive study is called for, this preliminary investigation indicates that the effect of compressibility on organized structures in a turbulent boundary layer is small.

ACKNOWLEDGEMENTS

This work was supported by AFOSR Grant 85-0126, monitored by Dr. James McMichael.

We wish to mention the time, support and sanity provided by friends and colleagues at the Gas Dynamics Lab. Special thanks are due Dr. Yiannis Andreopoulos, Emerick Fernando, John Donovan, Michael Smith, Roger Kimmel, Amy Alving and Laura Sabadell. Furthermore, the assistance of the Lab staff is greatly appreciated, especially Bob Bogart, Dick Gilbert, Sharon Matarese and Bill Stokes. A special note of thanks is reserved for Dr. David Tan, who provided great moral support for this study.

BIBLIOGRAPHY

Acarlar, M. S. and Smith, C. R. [1984], "An Experimental Study of Hairpin-Type Vortices as a Potential Flow Structure of Turbulent Boundary Layers," Report FM-5, Dept. of Mech. Engrg. and Mechanics, Lehigh University.

Bendat, J. S. and Persol, A. G. [1971], Random Data: Analysis and Measurement Procedures, John Wiley and Sons.

Blackwelder, R. F. and Kaplan, R. E. [1976], "On the Wall Structure of the Turbulent Boundary Layer," Journal of Fluid Mechanics, Vol. 76, p. 89.

Bonnet, J. P. [1982], "Etude Theorique et Experimentale de la Turbulence dans un Sillage Supersonique," Ph.D. Thesis, L'Universite de Poitiers, Poitiers, France.

Bull, M. K. [1967], "Wall Pressure Fluctuations Associated with Subsonic Turbulent Boundary Layer Flow," Journal of Fluid Mechanics, Vol. 28, p.719.

Cantwell, B. J. [1981], "Organized Motion in Turbulent Flow," Annual Review of Fluid Mechanics, Vol. 13, p. 457.

Chyu, W. J. and Hanly, R. D. [1968], "Power and Cross Spectra and Space-Time Correlations of Surface Fluctuating Pressures at Mach Numbers Between 1.6 and 2.6," AIAA Paper 68-77, AIAA 6th Aerospace Sciences Meeting, New York.

Coe, C. F. [1969], "Surface-Pressure Fluctuations Associated with Aerodynamic Noise," NASA SP-207, p. 409.

Coles, D. E. [1962], "The Turbulent Boundary Layer in a Compressible Fluid," Rand Corporation Report R-403-PR.

Corino, E. R. and Brodkey, R. S. [1969], "A Visual Investigation of the Wall Region in Turbulent Flow," Journal of Fluid Mechanics, Vol. 37, p.1.

Deckker, B.E.L. [1980], "An Investigation of Some Unsteady Boundary Layers by the Schlieren Method," International Symposium on Flow Visualization, Ruhr-Universitat.

Deckker, B.E.L. and Weekes, M. E. [1976], "The Unsteady Boundary Layer in a Shock Tube," Proc. I. Mech. Eng., Vol. 190, p. 287.

Grass, A. J. [1971], "Structural Features of Turbulent Flow Over Smooth and Rough Boundaries," Journal of Fluid Mechanics, Vol. 50, p. 233.

Hanly, R. D. [1975], "Effects of Transducer Flushness on Fluctuating Surface Pressure Measurements," AIAA Paper 75-534, AIAA 22nd Aero-Acoustics Conference, Hampton, VA.

Head, M. R. and Bandyopadhyay, P. [1981], "New Aspects of Turbulent Boundary-Layer Structure," Journal of Fluid Mechanics, Vol. 107, p. 297.

Hinze, J. O. [1975], Turbulence, 2nd Edition, McGraw Hill, p. 682.

Hopkins, E. J. and Keener, E. R. [1966], "Study of Surface Pitots for Measuring Turbulent Skin Friction at Supersonic Mach Numbers - Adiabatic Wall," NASA TN D-3478.

Johansson, A. V. and Alfredsson, p. H. [1982], "On the Structure of Turbulent Channel Flow," Journal of Fluid Mechanics, Vol. 122, p. 295.

Kim, H. T., Kline, S. J. and Reynolds, W. C. [1971], "The Production of Turbulence Near a Smooth Wall in a Turbulent Boundary Layer," Journal of Fluid Mechanics, Vol. 50, p. 133.

Kistler, A. L. [1959], "Fluctuation Measurements in a Supersonic Turbulent Boundary Layer," Physics of Fluids, Vol. 2, p. 290.

Kistler, A. L. and Chen, W. S. [1963], "The Fluctuating Pressure Field in a Supersonic Turbulent Boundary Layer," Journal of Fluid Mechanics, Vol. 16, p. 41.

Kline, S. J., Reynolds, W. C., Schraub, F. A. and Runstadler, P. W. [1967], "The Structure of Turbulent Boundary Layers," Journal of Fluid Mechanics, Vol. 30, p. 741.

Kovaszny, L. S. G [1950], "The Hot-Wire Anemometer in Supersonic Flow," Journal of the Aeronautical Sciences, Vol. 17, p. 565.

Morkovin, M. V. [1962], "Effects of Compressibility on Turbulent Flows," International Symposium on the "Mechanique de la Turbulence", Centre National de la Recherche Scientifique, Paris, p. 367.

Offen, G. R. and Kline, S. J. [1975], "A Proposed Model of the Bursting Process in Turbulent Boundary Layers," Journal of Fluid Mechanics, Vol. 70, p. 209.

Offen, G. R. and Kline, S. J. [1974], "Combined Dye Streak and Hydrogen Bubble Visual Observations of a Turbulent Boundary Layer," Journal of Fluid Mechanics, Vol. 62, p. 223.

Owen, F. K. and Horstman, C. C. [1974], "Turbulent Measurements in an Equilibrium Hypersonic Boundary Layer," AIAA Paper 74-93.

Perry, A. E. and Chong, M. S. [1982], "The Mechanism of Wall Turbulence," Journal of Fluid Mechanics, Vol. 119, p. 173.

Perry, A. E., Lim, T. T., and Teh, E. W. [1981], "A Visual Study of Turbulent Spots," Journal of Fluid Mechanics, Vol. 104, p. 387.

Perry, A. E. and Morrison, G. L. [1971], "A Study of the Constant Temperature Hot-Wire Anemometer," Journal of Fluid Mechanics, Vol. 47, p. 577.

Raman, K. R. [1974], "A Study of Surface Pressure Fluctuations in Hypersonic Turbulent Boundary Layers," NASA CR-2386.

Rao, K. N., Narasimha, R. and Narayanan, M.A.B. [1971], "The 'Bursting' Phenomenon in a Turbulent Boundary Layer," Journal of Fluid Mechanics, Vol. 48, p. 339.

Settles, G. S. [1975], "An Experimental Study of Compressible Turbulent Boundary Layer Separation at High Reynolds Number," Ph.D. Thesis, Mechanical and Aerospace Engineering Department, Princeton University.

Shewe, G. [1983], "On the Structure and Resolution of Wall-Pressure Fluctuations Associated with Turbulent Boundary-Layer Flows," Journal of Fluid Mechanics, Vol. 134, p. 311.

Smith, C. R. [1984], "A Synthesized Model of the Near-Wall Behavior in Turbulent Boundary Layers," Proceedings of Eighth Symposium on Turbulence, (Ed. G. K. Patterson and J. L. Zakin), Department of Chemical Engineering, University of Missouri-Rolla.

Smits, A. J., Hayakawa, K. and Muck, K. C. [1983], "Constant-Temperature Hot-Wire Anemometer Practice in Supersonic Flows. Part I - The Normal Wire," Experiments in Fluids, Springer-Verlag.

Speaker, W. V. and Ailman, C. M. [1966], "Spectra and Space-Time Correlations of the Fluctuating Pressures at a Wall Beneath a Supersonic Turbulent Boundary Layer Perturbed by Steps and Shock Wave," NASA CR-486.

Tan, D.K.M., Tran, T. T. and Bogdonoff, S. M. [1985], "Surface Pressure Fluctuations in a Three-Dimensional Shock Wave/Turbulent Boundary Layer Interaction," AIAA Paper 85-0125, AIAA 23rd Aerospace Sciences Meeting, Reno, Nevada.

Taylor, M. W. [1984], "A Supersonic Turbulent Boundary Layer on Concavely Curved Surfaces," M.S.E. Thesis, Mechanical and Aerospace Engineering Department, Princeton University.

Thomas, A.S.W. and Bull, M. K. [1983], "On the Role of Wall-Pressure Fluctuations in Deterministic Motions in the Turbulent Boundary Layer," Journal of Fluid Mechanics, Vol. 128, p. 283.

Van Driest, E. R. [1951], "Turbulent Boundary Layer in Compressible Fluids," Journal of Aeronautical Science, Vol. 18, p. 145.

Van Dyke, M. [1982], An Album of Fluid Motion, The Parabolic Press, Stanford, CA.

Vas, I. E. and Bogdonoff, S. M. [1971], "A Preliminary Report on the Princeton University High Reynolds Number 8" x 8" Supersonic Tunnel," Internal Memorandum No. 39, Gas Dynamics Laboratory, MAE Department, Princeton University.

Wallace, J. M. [1982], "On the Structure of Bounded Turbulent Shear Flow: A Personal View," Developments in Theoretical and Applied Mechanics, Vol. XI, (Ed. T. J. Chung and G. R. Karr), Department of Mechanical Engineering, University of Alabama-Huntsville, p. 509.

Willmarth, W. W. [1975], "Structure of Turbulence in Boundary Layers," Advances in Applied Mechanics, Vol. 15, (Ed. C. S. Yih), Academic Press, p. 159.

Willmarth, W. W. and Lu, S. S. [1971], "Structure of the Reynolds Stress Near the Wall," Journal of Fluid Mechanics, Vol. 55, p. 481.

Willmarth, W. W. and Sharma, L. K. [1984], "Study of Turbulent Structure with Hot-Wires Smaller than the Viscous Length," Journal of Fluid Mechanics, Vol. 142, p. 121.

Wyngaard, J. C. [1968], "Measurements of Small-Scale Turbulence with Hot-Wires," J. Phys. E: Sci. Instr., Vol. 1, p. 1105.

APPENDIX A MEAN FLOW DATA TABULATION

NOTE: All pressures are in N/m² and all temperatures are in Kelvin

SPANWISE STATIC PRESSURE PROFILE

X= 35.88 cm.

Y= 4.13 cm.

Average Stagnation Pressure= .6886E+06

Average Stagnation Temperature= 257.2

Z(cm.)	Static Pressure	Z(cm.)	Static Pressure
5.080	.2268E+05	1.812	.2313E+05
5.083	.2265E+05	1.743	.2297E+05
5.019	.2267E+05	1.674	.2281E+05
4.947	.2266E+05	1.603	.2277E+05
4.874	.2269E+05	1.530	.2280E+05
4.802	.2261E+05	1.458	.2281E+05
4.733	.2267E+05	1.389	.2283E+05
4.661	.2261E+05	1.317	.2284E+05
4.587	.2264E+05	1.244	.2282E+05
4.518	.2266E+05	1.174	.2285E+05
4.446	.2259E+05	1.101	.2283E+05
4.376	.2264E+05	1.029	.2284E+05
4.304	.2264E+05	.9582	.2286E+05
4.234	.2259E+05	.8867	.2285E+05
4.160	.2261E+05	.8163	.2285E+05
4.086	.2251E+05	.7451	.2294E+05
4.014	.2255E+05	.6717	.2300E+05
3.946	.2259E+05	.6027	.2304E+05
3.873	.2254E+05	.5304	.2315E+05
3.802	.2265E+05	.4626	.2320E+05
3.728	.2264E+05	.3896	.2315E+05
3.656	.2273E+05	.3173	.2310E+05
3.587	.2274E+05	.2454	.2300E+05
3.514	.2280E+05	.1720	.2287E+05
3.442	.2279E+05	.1015	.2276E+05
3.372	.2274E+05	.3256E-01	.2269E+05
3.301	.2272E+05	0.000	.2269E+05
3.229	.2268E+05	-.6347E-01	.2259E+05
3.159	.2280E+05	-.1332	.2267E+05
3.088	.2302E+05	-.2077	.2275E+05
3.014	.2307E+05	-.2803	.2292E+05
2.945	.2312E+05	-.3500	.2309E+05
2.871	.2307E+05	-.4197	.2312E+05
2.802	.2296E+05	-.4938	.2320E+05
2.730	.2293E+05	-.5643	.2315E+05
2.657	.2286E+05	-.6369	.2304E+05
2.586	.2282E+05	-.7081	.2294E+05
2.515	.2277E+05	-.7804	.2277E+05
2.445	.2271E+05	-.8490	.2265E+05
2.374	.2274E+05	-.9184	.2253E+05
2.306	.2273E+05	-.9932	.2252E+05
2.238	.2280E+05	-1.067	.2253E+05
2.165	.2286E+05	-1.137	.2253E+05
2.092	.2294E+05	-1.208	.2255E+05
2.022	.2305E+05	-1.279	.2260E+05
1.950	.2314E+05	-1.351	.2261E+05
1.880	.2319E+05	-1.422	.2269E+05

Z(cm.)	Static Pressure
-1. 494	. 2282E+05
-1. 567	. 2284E+05
-1. 638	. 2283E+05
-1. 710	. 2282E+05
-1. 781	. 2276E+05
-1. 852	. 2280E+05
-1. 922	. 2287E+05
-1. 994	. 2294E+05
-2. 068	. 2304E+05
-2. 139	. 2303E+05
-2. 209	. 2292E+05
-2. 284	. 2278E+05
-2. 352	. 2256E+05
-2. 421	. 2234E+05
-2. 499	. 2222E+05
-2. 568	. 2212E+05
-2. 641	. 2209E+05
-2. 710	. 2218E+05
-2. 781	. 2224E+05
-2. 849	. 2231E+05
-2. 920	. 2230E+05
-2. 992	. 2235E+05
-3. 065	. 2244E+05
-3. 136	. 2251E+05
-3. 208	. 2260E+05
-3. 278	. 2273E+05
-3. 346	. 2280E+05
-3. 417	. 2284E+05
-3. 489	. 2290E+05
-3. 559	. 2295E+05
-3. 634	. 2308E+05
-3. 703	. 2329E+05
-3. 774	. 2347E+05
-3. 845	. 2362E+05
-3. 914	. 2369E+05
-3. 986	. 2363E+05
-4. 059	. 2348E+05
-4. 128	. 2337E+05
-4. 202	. 2326E+05
-4. 276	. 2324E+05
-4. 346	. 2325E+05
-4. 417	. 2326E+05
-4. 489	. 2329E+05
-4. 559	. 2325E+05
-4. 631	. 2326E+05
-4. 702	. 2327E+05
-4. 773	. 2325E+05
-4. 847	. 2330E+05
-4. 919	. 2330E+05
-4. 991	. 2331E+05
-5. 064	. 2332E+05
-5. 135	. 2330E+05

SPANWISE PITOT PRESSURE PROFILE

X= 46.99 cm

Y= 1.02 cm

Average Stagnation Pressure= 6880E+06

Average Stagnation Temperature= 254.0

Z(cm.)	Pitot Pressure	Z(cm.)	Pitot Pressure
5.080	1584E+06	1.455	1441E+06
5.077	1587E+06	1.385	1427E+06
5.020	1584E+06	1.316	1397E+06
4.950	1573E+06	1.242	1431E+06
4.874	1587E+06	1.168	1435E+06
4.803	1581E+06	1.100	1432E+06
4.730	1586E+06	1.028	1444E+06
4.659	1578E+06	.9562	1440E+06
4.586	1589E+06	.8845	1443E+06
4.515	1568E+06	.8160	1439E+06
4.444	1576E+06	.7414	1441E+06
4.372	1562E+06	.6696	1446E+06
4.300	1560E+06	.5990	1453E+06
4.229	1565E+06	.5272	1453E+06
4.159	1557E+06	.4533	1450E+06
4.089	1561E+06	.3608	1454E+06
4.019	1572E+06	.3116	1455E+06
3.949	1562E+06	.2410	1468E+06
3.875	1551E+06	.1700	1454E+06
3.802	1533E+06	.9679E-01	1454E+06
3.731	1551E+06	.2321E-01	1468E+06
3.661	1544E+06	.3311E-02	1472E+06
3.589	1549E+06	0.000	1477E+06
3.516	1557E+06	- .4705E-01	1477E+06
3.445	1545E+06	- .6401E-01	1497E+06
3.374	1549E+06	- .1354	1483E+06
3.302	1554E+06	- .2093	1501E+06
3.231	1545E+06	- .2803	1493E+06
3.161	1537E+06	- .3539	1486E+06
3.089	1562E+06	- .4290	1506E+06
3.019	1541E+06	- .4985	1497E+06
2.948	1545E+06	- .5688	1526E+06
2.875	1561E+06	- .6420	1519E+06
2.803	1533E+06	- .7100	1510E+06
2.735	1556E+06	- .7818	1515E+06
2.662	1544E+06	- .8543	1557E+06
2.589	1530E+06	- .9227	1539E+06
2.516	1519E+06	- .9933	1545E+06
2.445	1531E+06	-1.066	1555E+06
2.374	1497E+06	-1.142	1552E+06
2.303	1530E+06	-1.214	1544E+06
2.232	1497E+06	-1.282	1539E+06
2.162	1485E+06	-1.356	1555E+06
2.091	1495E+06	-1.427	1551E+06
2.022	1475E+06	-1.497	1555E+06
1.952	1460E+06	-1.569	1555E+06
1.881	1457E+06	-1.641	1561E+06
1.808	1456E+06	-1.713	1571E+06
1.735	1431E+06	-1.785	1576E+06
1.668	1430E+06	-1.854	1557E+06
1.595	1438E+06	-1.925	1564E+06
1.526	1445E+06	-1.998	1560E+06

Z(cm)	Pitot Pressure
-2 069	1575E+06
-2 142	1564E+06
-2 214	1572E+06
-2 283	1569E+06
-2 358	1554E+06
-2 427	1567E+06
-2 499	1550E+06
-2 573	1564E+06
-2 644	1554E+06
-2 714	1558E+06
-2 784	1564E+06
-2 857	1547E+06
-2 923	1555E+06
-2 993	1541E+06
-3 066	1555E+06
-3 138	1552E+06
-3 212	1545E+06
-3 281	1541E+06
-3 351	1535E+06
-3 421	1522E+06
-3 492	1540E+06
-3 561	1532E+06
-3 629	1529E+06
-3 702	1542E+06
-3 776	1533E+06
-3 844	1516E+06
-3 917	1532E+06
-3 987	1518E+06
-4 056	1516E+06
-4 129	1516E+06
-4 201	1512E+06
-4 275	1507E+06
-4 343	1513E+06
-4 416	1508E+06
-4 489	1529E+06
-4 560	1519E+06
-4 630	1517E+06
-4 701	1529E+06
-4 773	1523E+06
-4 843	1530E+06
-4 914	1531E+06
-4 989	1540E+06
-5 062	1565E+06
-5 133	1587E+06

SPANWISE PITOT PRESSURE PROFILE

X= 46.99 cm.

Y= 0.38 cm

Average Stagnation Pressure= .6880E+06

Average Stagnation Temperature= 253.0

Z(cm)	Pitot Pressure	Z(cm)	Pitot Pressure
5.080	.1146E+06	1.452	.1041E+06
5.082	.1144E+06	1.383	.1039E+06
5.019	.1147E+06	1.311	.1035E+06
4.945	.1132E+06	1.240	.1051E+06
4.874	.1139E+06	1.171	.1039E+06
4.800	.1135E+06	1.100	.1057E+06
4.728	.1149E+06	1.027	.1037E+06
4.656	.1134E+06	.9573	.1048E+06
4.583	.1133E+06	.8845	.1056E+06
4.513	.1145E+06	.8109	.1051E+06
4.441	.1139E+06	.7410	.1061E+06
4.369	.1146E+06	.6681	.1055E+06
4.299	.1136E+06	.5993	.1051E+06
4.228	.1118E+06	.5276	.1044E+06
4.156	.1122E+06	.4559	.1056E+06
4.089	.1117E+06	.3823	.1047E+06
4.016	.1118E+06	.3142	.1044E+06
3.943	.1121E+06	.2429	.1050E+06
3.869	.1116E+06	.1722	.1039E+06
3.798	.1121E+06	.9753E-01	.1054E+06
3.728	.1113E+06	.2469E-01	.1055E+06
3.657	.1115E+06	0.000	.1057E+06
3.582	.1113E+06	-.6549E-01	.1060E+06
3.513	.1126E+06	-.1369	.1078E+06
3.441	.1117E+06	-.2097	.1060E+06
3.369	.1124E+06	-.2825	.1058E+06
3.298	.1129E+06	-.3561	.1064E+06
3.224	.1125E+06	-.4293	.1066E+06
3.155	.1120E+06	-.4978	.1069E+06
3.085	.1122E+06	-.5736	.1085E+06
3.014	.1125E+06	-.6435	.1087E+06
2.940	.1134E+06	-.7123	.1093E+06
2.869	.1123E+06	-.7833	.1096E+06
2.797	.1131E+06	-.8561	.1087E+06
2.728	.1114E+06	-.9238	.1101E+06
2.654	.1120E+06	-.9959	.1102E+06
2.584	.1116E+06	-.1.069	.1103E+06
2.511	.1111E+06	-.1.144	.1099E+06
2.439	.1101E+06	-.1.217	.1108E+06
2.368	.1085E+06	-.1.286	.1107E+06
2.295	.1082E+06	-.1.358	.1114E+06
2.228	.1075E+06	-.1.430	.1114E+06
2.158	.1082E+06	-.1.501	.1109E+06
2.090	.1069E+06	-.1.574	.1106E+06
2.019	.1066E+06	-.1.645	.1106E+06
1.948	.1056E+06	-.1.717	.1114E+06
1.876	.1049E+06	-.1.788	.1106E+06
1.803	.1036E+06	-.1.859	.1116E+06
1.733	.1035E+06	-.1.929	.1101E+06
1.664	.1045E+06	-.2.001	.1110E+06
1.592	.1030E+06	-.2.072	.1101E+06
1.525	.1057E+06	-.2.146	.1106E+06

Z(cm.)	Pitot Pressure
-2 216	1112E+06
-2 284	1101E+06
-2 357	1116E+06
-2 430	1099E+06
-2 500	1100E+06
-2 574	1107E+06
-2 645	1101E+06
-2 716	1104E+06
-2 785	1091E+06
-2 856	1098E+06
-2 924	1095E+06
-2 997	1097E+06
-3 067	1099E+06
-3 138	1089E+06
-3 213	1091E+06
-3 282	1083E+06
-3 351	1097E+06
-3 422	1095E+06
-3 491	1095E+06
-3 564	1095E+06
-3 629	1095E+06
-3 703	1088E+06
-3 775	1075E+06
-3 843	1088E+06
-3 914	1078E+06
-3 986	1083E+06
-4 057	1080E+06
-4 128	1076E+06
-4 200	1080E+06
-4 269	1078E+06
-4 343	1074E+06
-4 414	1061E+06
-4 486	1061E+06
-4 558	1072E+06
-4 628	1069E+06
-4 699	1074E+06
-4 771	1080E+06
-4 841	1087E+06
-4 916	1098E+06
-4 989	1092E+06
-5 061	1102E+06
-5 134	1111E+06

VERTICAL PITOT PRESSURE PROFILE AT A SPANWISE STATION

X= 46.99 cm

Z= 3.02 cm

Average Stagnation Pressure= .6874E+06

Average Stagnation Temperature= 260.9

Y(cm.)	Pitot Pressure	Static Pressure	U(m/s)	M
2540E-01	6097E+05	2306E+05	366.4	1.276
7681E-01	7324E+05	2306E+05	399.1	1.437
1222	8347E+05	2306E+05	421.1	1.554
1725	9236E+05	2306E+05	437.9	1.650
2212	9836E+05	2306E+05	447.9	1.710
2674	1034E+06	2306E+05	455.8	1.759
3218	1083E+06	2306E+05	462.6	1.804
3672	1112E+06	2306E+05	466.8	1.832
4136	1161E+06	2306E+05	473.0	1.874
4654	1191E+06	2306E+05	477.0	1.903
5089	1224E+06	2306E+05	480.9	1.931
6045	1292E+06	2306E+05	489.5	1.995
7066	1358E+06	2306E+05	496.7	2.051
8026	1420E+06	2306E+05	502.7	2.101
8971	1479E+06	2306E+05	507.7	2.143
9901	1533E+06	2306E+05	512.5	2.186
1.090	1591E+06	2306E+05	518.0	2.235
1.189	1673E+06	2306E+05	524.0	2.292
1.285	1738E+06	2306E+05	529.1	2.342
1.381	1798E+06	2306E+05	533.2	2.384
1.476	1863E+06	2306E+05	537.2	2.427
1.671	2004E+06	2306E+05	546.1	2.526
1.867	2108E+06	2306E+05	551.9	2.597
2.059	2251E+06	2306E+05	559.2	2.689
2.251	2340E+06	2306E+05	562.5	2.738
2.443	2420E+06	2306E+05	565.7	2.788
2.637	2462E+06	2306E+05	567.2	2.816
2.833	2486E+06	2306E+05	568.3	2.830
3.028	2496E+06	2306E+05	568.8	2.837
3.218	2496E+06	2306E+05	568.8	2.837
3.414	2498E+06	2306E+05	568.8	2.837
3.613	2496E+06	2306E+05	568.8	2.837
3.807	2511E+06	2306E+05	569.4	2.844
4.001	2502E+06	2306E+05	568.8	2.837
4.191	2513E+06	2306E+05	569.4	2.844
4.389	2499E+06	2306E+05	568.8	2.837
4.583	2530E+06	2306E+05	570.5	2.859
4.780	2520E+06	2306E+05	569.9	2.851
4.974	2530E+06	2306E+05	570.5	2.859
5.169	2524E+06	2306E+05	569.9	2.851

VERTICAL PITOT PRESSURE PROFILE AT A SPANWISE STATION

X= 46.99 cm.

Z= 1.51 cm.

Average Stagnation Pressure= .6873E+06

Average Stagnation Temperature= 257.7

Y(cm.)	Pitot Pressure	Static Pressure	U(m/s)	M
.2540E-01	.5856E+05	.2280E+05	358.8	1.253
.7681E-01	.6959E+05	.2280E+05	389.7	1.402
.1218	.7890E+05	.2280E+05	410.7	1.512
.1728	.8569E+05	.2280E+05	424.7	1.589
.2208	.9106E+05	.2280E+05	434.5	1.646
.2677	.9517E+05	.2280E+05	441.5	1.689
.3218	.9960E+05	.2280E+05	448.9	1.735
.3652	.1043E+06	.2280E+05	456.3	1.782
.4166	.1070E+06	.2280E+05	459.4	1.804
.4631	.1096E+06	.2280E+05	463.6	1.832
.5085	.1124E+06	.2280E+05	466.6	1.853
.5071	.1197E+06	.2280E+05	476.6	1.924
.7047	.1274E+06	.2280E+05	485.1	1.988
.8007	.1330E+06	.2280E+05	491.4	2.037
.8948	.1361E+06	.2280E+05	494.8	2.066
.9908	.1452E+06	.2280E+05	503.4	2.136
1.091	.1494E+06	.2280E+05	507.3	2.172
1.189	.1583E+06	.2280E+05	515.2	2.243
1.284	.1618E+06	.2280E+05	517.3	2.264
1.379	.1673E+06	.2280E+05	521.6	2.306
1.476	.1748E+06	.2280E+05	527.3	2.363
1.669	.1862E+06	.2280E+05	534.5	2.441
1.867	.1965E+06	.2280E+05	540.6	2.512
2.060	.2090E+06	.2280E+05	547.7	2.597
2.253	.2257E+06	.2280E+05	556.1	2.703
2.443	.2308E+06	.2280E+05	558.2	2.738
2.632	.2395E+06	.2280E+05	561.5	2.788
2.832	.2434E+06	.2280E+05	563.7	2.816
3.029	.2469E+06	.2280E+05	565.3	2.837
3.220	.2480E+06	.2280E+05	565.9	2.844
3.415	.2485E+06	.2280E+05	565.9	2.844
3.608	.2504E+06	.2280E+05	567.0	2.859
3.805	.2516E+06	.2280E+05	567.5	2.866
4.003	.2514E+06	.2280E+05	567.5	2.866
4.196	.2508E+06	.2280E+05	567.0	2.859
4.397	.2518E+06	.2280E+05	567.5	2.866
4.580	.2510E+06	.2280E+05	567.0	2.859
4.780	.2535E+06	.2280E+05	568.0	2.873
4.976	.2530E+06	.2280E+05	568.0	2.873
5.171	.2555E+06	.2280E+05	569.1	2.887

VERTICAL PITOT PRESSURE PROFILE AT A SPANWISE STATION

X= 46.99 cm

Z= 0.0 cm

Average Stagnation Pressure= .6873E+06

Average Stagnation Temperature= 251.0

Y(cm.)	Pitot Pressure	Static Pressure	U(m/s)	M
3334E-01	5916E+05	2252E+05	358.6	1.274
8739E-01	7186E+05	2252E+05	392.1	1.441
1297	8046E+05	2252E+05	410.5	1.540
1819	8738E+05	2252E+05	424.1	1.618
2299	9368E+05	2252E+05	435.2	1.685
2734	9813E+05	2252E+05	442.6	1.731
3304	1024E+06	2252E+05	449.4	1.775
3735	1050E+06	2252E+05	452.5	1.797
4238	1090E+06	2252E+05	458.7	1.839
4711	1130E+06	2252E+05	463.8	1.874
5172	1160E+06	2252E+05	467.7	1.903
6166	1225E+06	2252E+05	475.3	1.959
7156	1286E+06	2252E+05	482.5	2.016
8090	1363E+06	2252E+05	490.4	2.080
9020	1399E+06	2252E+05	493.6	2.108
9991	1481E+06	2252E+05	501.0	2.172
1.101	1557E+06	2252E+05	508.0	2.235
1.197	1607E+06	2252E+05	511.6	2.271
1.292	1675E+06	2252E+05	517.4	2.328
1.386	1741E+06	2252E+05	521.5	2.370
1.483	1792E+06	2252E+05	525.5	2.412
1.676	1915E+06	2252E+05	533.0	2.497
1.873	2014E+06	2252E+05	538.1	2.561
2.070	2163E+06	2252E+05	546.0	2.660
2.262	2275E+06	2252E+05	551.1	2.731
2.450	2342E+06	2252E+05	553.7	2.774
2.641	2374E+06	2252E+05	554.7	2.795
2.839	2439E+06	2252E+05	557.9	2.837
3.038	2450E+06	2252E+05	558.5	2.844
3.229	2477E+06	2252E+05	559.5	2.859
3.423	2465E+06	2252E+05	559.0	2.851
3.618	2498E+06	2252E+05	560.6	2.873
3.812	2491E+06	2252E+05	560.1	2.866
4.010	2515E+06	2252E+05	561.1	2.880
4.202	2505E+06	2252E+05	560.6	2.873
4.393	2516E+06	2252E+05	561.1	2.880
4.586	2509E+06	2252E+05	561.1	2.880
4.787	2523E+06	2252E+05	561.6	2.887
4.985	2513E+06	2252E+05	561.1	2.880
5.178	2523E+06	2252E+05	561.1	2.887

VERTICAL PITOT PRESSURE PROFILE AT A SPANWISE STATION

X= 46.99 cm.

Z= -1.51 cm.

Average Stagnation Pressure= .6877E+06

Average Stagnation Temperature= 257.0

Y(cm.)	Pitot Pressure	Static Pressure	U(m/s)	M
2540E-01	.6396E+05	.2281E+05	374.1	1.327
7000E-01	.7462E+05	.2281E+05	401.0	1.462
1191	.8425E+05	.2281E+05	421.2	1.572
1679	.9172E+05	.2281E+05	435.3	1.653
2125	.9813E+05	.2281E+05	445.7	1.717
2669	.1038E+06	.2281E+05	454.9	1.775
3119	.1074E+06	.2281E+05	460.3	1.811
3641	.1120E+06	.2281E+05	466.5	1.853
4117	.1151E+06	.2281E+05	470.5	1.881
4537	.1188E+06	.2281E+05	475.5	1.917
5077	.1237E+06	.2281E+05	481.3	1.959
6022	.1297E+06	.2281E+05	487.7	2.009
6937	.1366E+06	.2281E+05	494.9	2.066
7920	.1407E+06	.2281E+05	499.0	2.101
8944	.1490E+06	.2281E+05	506.5	2.165
9908	.1565E+06	.2281E+05	513.7	2.228
1.085	.1629E+06	.2281E+05	518.1	2.271
1.179	.1709E+06	.2281E+05	524.8	2.335
1.276	.1771E+06	.2281E+05	528.9	2.377
1.378	.1824E+06	.2281E+05	532.9	2.420
1.475	.1933E+06	.2281E+05	539.5	2.490
1.667	.2038E+06	.2281E+05	545.4	2.561
1.858	.2173E+06	.2281E+05	552.8	2.653
2.051	.2277E+06	.2281E+05	557.4	2.717
2.249	.2415E+06	.2281E+05	563.4	2.802
2.443	.2453E+06	.2281E+05	564.2	2.823
2.632	.2502E+06	.2281E+05	565.7	2.851
2.824	.2493E+06	.2281E+05	565.7	2.851
3.019	.2512E+06	.2281E+05	566.2	2.859
3.215	.2499E+06	.2281E+05	565.7	2.851
3.414	.2513E+06	.2281E+05	566.2	2.859
3.608	.2502E+06	.2281E+05	565.7	2.851
3.796	.2510E+06	.2281E+05	566.2	2.859
3.993	.2498E+06	.2281E+05	565.7	2.851
4.193	.2514E+06	.2281E+05	566.7	2.866
4.387	.2505E+06	.2281E+05	566.2	2.859
4.575	.2524E+06	.2281E+05	566.7	2.866
4.775	.2529E+06	.2281E+05	567.2	2.873
4.972	.2548E+06	.2281E+05	567.8	2.880
5.166	.2549E+06	.2281E+05	567.8	2.880

VERTICAL PITOT PRESSURE PROFILE AT A SPANWISE STATION

X= 46.99 cm.

Z= -3.04 cm.

Average Stagnation Pressure= .6877E+06

Average Stagnation Temperature= 250.9

Y(cm.)	Pitot Pressure	Static Pressure	U(m/s)	M
2351E-01	.6054E+05	.2239E+05	363.1	1.296
7945E-01	.7436E+05	.2239E+05	398.8	1.476
1195	.8442E+05	.2239E+05	419.9	1.593
1717	.9195E+05	.2239E+05	433.6	1.674
2197	.9750E+05	.2239E+05	442.7	1.731
2651	1.017E+06	.2239E+05	449.5	1.775
3199	1.066E+06	.2239E+05	455.9	1.816
3622	1.116E+06	.2239E+05	463.0	1.867
4159	1.147E+06	.2239E+05	466.9	1.896
4609	1.175E+06	.2239E+05	470.8	1.924
5058	1.212E+06	.2239E+05	474.6	1.952
6060	1.293E+06	.2239E+05	483.2	2.023
7035	1.354E+06	.2239E+05	490.7	2.060
7973	1.417E+06	.2239E+05	496.5	2.129
8922	1.484E+06	.2239E+05	503.0	2.186
9889	1.546E+06	.2239E+05	508.3	2.235
1.089	1.616E+06	.2239E+05	513.5	2.285
1.187	1.691E+06	.2239E+05	519.2	2.342
1.281	1.762E+06	.2239E+05	524.7	2.393
1.377	1.841E+06	.2239E+05	530.0	2.455
1.473	1.899E+06	.2239E+05	533.0	2.490
1.666	2.045E+06	.2239E+05	541.4	2.589
1.864	2.175E+06	.2239E+05	548.6	2.682
2.058	2.344E+06	.2239E+05	556.3	2.788
2.252	2.430E+06	.2239E+05	559.3	2.837
2.440	2.473E+06	.2239E+05	560.6	2.866
2.632	2.503E+06	.2239E+05	561.5	2.887
2.829	2.500E+06	.2239E+05	561.0	2.880
3.028	2.506E+06	.2239E+05	561.5	2.887
3.217	2.496E+06	.2239E+05	561.0	2.880
3.414	2.484E+06	.2239E+05	560.5	2.873
3.607	2.498E+06	.2239E+05	561.0	2.880
3.804	2.502E+06	.2239E+05	561.0	2.880
4.001	2.522E+06	.2239E+05	562.0	2.894
4.192	2.530E+06	.2239E+05	562.5	2.901
4.384	2.525E+06	.2239E+05	562.0	2.894
4.580	2.544E+06	.2239E+05	563.0	2.908
4.778	2.553E+06	.2239E+05	563.6	2.915
4.975	2.567E+06	.2239E+05	564.1	2.922
5.167	2.567E+06	.2239E+05	564.1	2.922

STREAMWISE STATIC PRESSURE PROFILE

Y= 5.08 cm.

Z= 0.0 cm.

Average Stagnation Pressure= .6890E+06

Average Stagnation Temperature= 254.0

X(cm.)	Static Pressure	X(cm.)	Static Pressure
16.51	.2198E+05	19.90	.2214E+05
16.55	.2201E+05	19.96	.2214E+05
16.59	.2205E+05	20.02	.2214E+05
16.73	.2199E+05	20.09	.2222E+05
16.81	.2196E+05	20.16	.2220E+05
16.86	.2198E+05	20.22	.2222E+05
16.92	.2202E+05	20.29	.2223E+05
17.00	.2206E+05	20.35	.2217E+05
17.06	.2203E+05	20.42	.2214E+05
17.13	.2204E+05	20.49	.2218E+05
17.20	.2201E+05	20.55	.2211E+05
17.26	.2198E+05	20.62	.2212E+05
17.32	.2199E+05	20.69	.2216E+05
17.40	.2200E+05	20.76	.2215E+05
17.46	.2202E+05	20.81	.2217E+05
17.52	.2206E+05	20.90	.2212E+05
17.59	.2204E+05	20.95	.2211E+05
17.66	.2202E+05	21.01	.2211E+05
17.72	.2201E+05	21.08	.2212E+05
17.78	.2197E+05	21.15	.2210E+05
17.85	.2196E+05	21.22	.2209E+05
17.92	.2199E+05	21.28	.2213E+05
17.96	.2200E+05	21.35	.2213E+05
18.04	.2200E+05	21.40	.2208E+05
18.11	.2206E+05	21.47	.2210E+05
18.17	.2201E+05	21.55	.2210E+05
18.25	.2202E+05	21.61	.2203E+05
18.30	.2202E+05	21.67	.2212E+05
18.37	.2201E+05	21.74	.2202E+05
18.44	.2202E+05	21.81	.2207E+05
18.51	.2205E+05	21.88	.2211E+05
18.57	.2204E+05	21.94	.2206E+05
18.63	.2199E+05	22.02	.2214E+05
18.71	.2197E+05	22.09	.2219E+05
18.76	.2195E+05	22.14	.2226E+05
18.84	.2199E+05	22.21	.2227E+05
18.91	.2207E+05	22.28	.2230E+05
18.95	.2210E+05	22.35	.2224E+05
19.03	.2218E+05	22.41	.2217E+05
19.10	.2214E+05	22.49	.2214E+05
19.17	.2210E+05	22.54	.2209E+05
19.22	.2215E+05	22.61	.2210E+05
19.29	.2220E+05	22.68	.2208E+05
19.37	.2219E+05	22.74	.2210E+05
19.43	.2224E+05	22.81	.2209E+05
19.49	.2227E+05	22.86	.2215E+05
19.57	.2222E+05	22.94	.2220E+05
19.64	.2215E+05	23.01	.2219E+05
19.70	.2217E+05	23.06	.2223E+05
19.76	.2222E+05	23.13	.2225E+05
19.82	.2217E+05	23.20	.2225E+05

X(cm)	Static Pressure	X(cm)	Static Pressure
23 27	2222E+05	27 58	2311E+05
23 35	2224E+05	27 66	2305E+05
23 41	2224E+05	27 73	2295E+05
23 46	2235E+05	27 79	2298E+05
23 54	2243E+05	27 87	2328E+05
23 61	2244E+05	27 95	2301E+05
23 68	2245E+05	28 02	2298E+05
23 74	2242E+05	28 08	2276E+05
23 81	2233E+05	28 15	2253E+05
23 88	2243E+05	28 23	2246E+05
23 94	2249E+05	28 30	2256E+05
23 99	2249E+05	28 37	2263E+05
24 08	2253E+05	28 48	2255E+05
24 15	2250E+05	28 55	2238E+05
24 20	2243E+05	28 62	2227E+05
24 27	2241E+05	28 69	2222E+05
24 35	2248E+05	28 76	2211E+05
24 45	2261E+05	28 83	2204E+05
24 50	2256E+05	28 91	2199E+05
24 57	2251E+05	28 98	2200E+05
24 63	2253E+05	29 06	2200E+05
24 71	2257E+05	29 12	2195E+05
24 78	2257E+05	29 19	2198E+05
24 86	2255E+05	29 27	2209E+05
24 92	2249E+05	29 33	2204E+05
25 00	2243E+05	29 41	2193E+05
25 06	2250E+05	29 48	2191E+05
25 14	2254E+05	29 56	2184E+05
25 22	2268E+05	29 62	2180E+05
25 29	2262E+05	29 70	2178E+05
25 36	2280E+05	29 77	2176E+05
25 44	2285E+05	29 84	2176E+05
25 50	2274E+05	29 91	2176E+05
25 58	2272E+05	29 98	2171E+05
25 66	2273E+05	30 06	2174E+05
25 75	2285E+05	30 12	2178E+05
25 80	2304E+05	30 20	2170E+05
25 88	2312E+05	30 27	2162E+05
25 93	2311E+05	30 34	2166E+05
26 02	2310E+05	30 40	2170E+05
26 09	2319E+05	30 48	2177E+05
26 16	2326E+05	30 55	2178E+05
26 23	2325E+05	30 63	2178E+05
26 30	2300E+05	30 70	2179E+05
26 42	2302E+05	30 77	2176E+05
26 45	2299E+05	30 84	2174E+05
26 54	2292E+05	30 91	2172E+05
26 60	2280E+05	30 98	2173E+05
26 64	2279E+05	31 05	2175E+05
26 72	2274E+05	31 13	2182E+05
26 79	2278E+05	31 19	2194E+05
26 85	2284E+05	31 25	2202E+05
26 94	2290E+05	31 32	2205E+05
27 02	2284E+05	31 40	2218E+05
27 08	2282E+05	31 47	2222E+05
27 15	2284E+05	31 53	2241E+05
27 23	2290E+05	31 61	2262E+05
27 30	2296E+05	31 67	2268E+05
27 36	2304E+05	31 74	2273E+05
27 44	2314E+05	31 82	2291E+05
27 51	2318E+05	31 88	2292E+05

X(cm.)	Static Pressure	X(cm.)	Static Pressure
31.94	2292E+05	35.52	2265E+05
32.00	2292E+05	35.58	2258E+05
32.06	2294E+05	35.64	2254E+05
32.14	2302E+05	35.69	2255E+05
32.18	2290E+05	35.76	2260E+05
32.25	2285E+05	35.81	2261E+05
32.30	2283E+05	35.87	2264E+05
32.36	2281E+05	35.92	2266E+05
32.42	2275E+05	35.99	2265E+05
32.48	2274E+05	36.06	2262E+05
32.53	2279E+05	36.10	2256E+05
32.59	2275E+05	36.16	2256E+05
32.65	2274E+05	36.21	2259E+05
32.71	2274E+05	36.28	2266E+05
32.76	2275E+05	36.33	2266E+05
32.82	2276E+05	36.39	2265E+05
32.88	2277E+05	36.45	2262E+05
32.95	2276E+05	36.51	2259E+05
32.99	2276E+05	36.56	2256E+05
33.06	2280E+05	36.63	2264E+05
33.11	2281E+05	36.68	2265E+05
33.17	2280E+05	36.75	2270E+05
33.23	2283E+05	36.80	2269E+05
33.29	2287E+05	36.87	2273E+05
33.35	2287E+05	36.92	2270E+05
33.41	2287E+05	36.98	2267E+05
33.47	2284E+05	37.04	2267E+05
33.52	2285E+05	37.10	2267E+05
33.59	2284E+05	37.16	2268E+05
33.64	2285E+05	37.22	2268E+05
33.70	2280E+05	37.27	2274E+05
33.75	2280E+05	37.33	2271E+05
33.81	2282E+05	37.39	2266E+05
33.88	2280E+05	37.45	2262E+05
33.93	2277E+05	37.51	2258E+05
33.99	2280E+05	37.56	2259E+05
34.05	2281E+05	37.63	2261E+05
34.10	2283E+05	37.68	2257E+05
34.16	2285E+05	37.73	2253E+05
34.22	2289E+05	37.80	2255E+05
34.28	2296E+05	37.87	2256E+05
34.34	2305E+05	37.91	2253E+05
34.40	2314E+05	37.97	2251E+05
34.46	2316E+05	38.03	2253E+05
34.52	2319E+05	38.09	2252E+05
34.58	2318E+05	38.15	2254E+05
34.64	2319E+05	38.20	2253E+05
34.69	2317E+05	38.27	2247E+05
34.75	2316E+05	38.32	2246E+05
34.81	2316E+05	38.38	2248E+05
34.87	2315E+05	38.44	2251E+05
34.94	2316E+05	38.50	2245E+05
34.99	2304E+05	38.55	2253E+05
35.05	2299E+05	38.62	2253E+05
35.11	2295E+05	38.66	2258E+05
35.17	2286E+05	38.73	2262E+05
35.22	2280E+05	38.79	2259E+05
35.29	2277E+05	38.84	2259E+05
35.34	2274E+05	38.91	2261E+05
35.40	2274E+05	38.95	2261E+05
35.46	2270E+05	39.01	2260E+05

X(cm)	Static Pressure	X(cm)	Static Pressure
39 07	2258E+05	42 91	2280E+05
39 13	2262E+05	42 98	2281E+05
39 19	2268E+05	43 05	2280E+05
39 24	2268E+05	43 12	2277E+05
39 24	2272E+05	43 17	2276E+05
39 35	2275E+05	43 25	2277E+05
39 42	2281E+05	43 32	2264E+05
39 47	2287E+05	43 38	2269E+05
39 53	2286E+05	43 45	2267E+05
39 60	2300E+05	43 52	2268E+05
39 65	2311E+05	43 58	2268E+05
39 70	2324E+05	43 65	2265E+05
39 76	2334E+05	43 71	2265E+05
39 82	2343E+05	43 79	2262E+05
39 88	2353E+05	43 85	2261E+05
39 94	2364E+05	43 93	2259E+05
40 00	2375E+05	43 99	2253E+05
40 06	2384E+05	44 05	2251E+05
40 12	2383E+05	44 12	2247E+05
40 17	2387E+05	44 18	2246E+05
40 24	2385E+05	44 26	2249E+05
40 29	2383E+05	44 32	2248E+05
40 34	2376E+05	44 40	2245E+05
40 40	2377E+05	44 46	2251E+05
40 46	2372E+05	44 53	2251E+05
40 52	2371E+05	44 59	2249E+05
40 58	2371E+05	44 66	2251E+05
40 64	2368E+05	44 72	2252E+05
40 70	2361E+05	44 79	2251E+05
40 74	2347E+05	44 86	2251E+05
40 82	2343E+05	44 92	2253E+05
40 88	2340E+05	44 99	2256E+05
40 95	2338E+05	45 06	2255E+05
41 01	2338E+05	45 13	2253E+05
41 08	2332E+05	45 20	2253E+05
41 15	2330E+05	45 27	2251E+05
41 24	2325E+05	45 33	2239E+05
41 29	2320E+05	45 40	2235E+05
41 36	2312E+05	45 46	2231E+05
41 42	2310E+05	45 54	2225E+05
41 49	2307E+05	45 59	2222E+05
41 56	2305E+05	45 66	2222E+05
41 63	2306E+05	45 73	2223E+05
41 71	2311E+05	45 80	2219E+05
41 76	2310E+05	45 86	2216E+05
41 83	2309E+05	45 93	2213E+05
41 90	2308E+05	46 00	2210E+05
41 97	2305E+05	46 06	2209E+05
42 03	2302E+05	46 13	2205E+05
42 10	2294E+05	46 21	2202E+05
42 17	2296E+05	46 29	2205E+05
42 23	2294E+05	46 33	2208E+05
42 30	2293E+05	46 39	2209E+05
42 37	2288E+05	46 46	2212E+05
42 45	2290E+05	46 53	2212E+05
42 50	2292E+05	46 59	2213E+05
42 57	2288E+05	46 66	2220E+05
42 64	2280E+05	46 73	2224E+05
42 72	2283E+05	46 79	2230E+05
42 77	2282E+05	46 86	2239E+05
42 85	2276E+05	46 93	2249E+05

X(cm.)	Static Pressure	X(cm.)	Static Pressure
47 00	2253E+05	50 93	2232E+05
47 06	2261E+05	50 99	2228E+05
47 14	2271E+05	51 05	2222E+05
47 20	2277E+05	51 11	2222E+05
47 26	2282E+05	51 18	2229E+05
47 33	2291E+05	51 24	2237E+05
47 40	2301E+05	51 31	2238E+05
47 46	2310E+05	51 37	2241E+05
47 53	2320E+05	51 44	2239E+05
47 60	2322E+05	51 51	2236E+05
47 65	2327E+05	51 57	2239E+05
47 72	2325E+05	51 63	2246E+05
47 81	2326E+05	51 69	2258E+05
47 86	2325E+05	51 75	2269E+05
47 92	2325E+05	51 82	2277E+05
47 99	2322E+05	51 89	2286E+05
48 07	2325E+05	51 95	2297E+05
48 13	2322E+05	52 02	2307E+05
48 19	2320E+05	52 08	2315E+05
48 26	2319E+05	52 13	2322E+05
48 33	2317E+05	52 20	2322E+05
48 39	2311E+05	52 26	2319E+05
48 46	2307E+05	52 32	2310E+05
48 53	2304E+05	52 40	2301E+05
48 60	2303E+05	52 46	2296E+05
48 66	2304E+05	52 53	2297E+05
48 72	2300E+05	52 58	2297E+05
48 79	2300E+05	52 65	2296E+05
48 85	2295E+05	52 71	2295E+05
48 88	2278E+05	52 78	2290E+05
48 95	2276E+05	52 84	2284E+05
49 01	2273E+05	52 91	2283E+05
49 07	2266E+05	52 97	2281E+05
49 14	2262E+05	53 04	2283E+05
49 21	2257E+05	53 11	2281E+05
49 26	2254E+05	53 17	2281E+05
49 33	2256E+05	53 23	2281E+05
49 40	2261E+05	53 29	2281E+05
49 45	2258E+05	53 37	2280E+05
49 52	2251E+05	53 42	2280E+05
49 58	2246E+05	53 49	2279E+05
49 65	2242E+05	53 55	2279E+05
49 71	2239E+05	53 61	2281E+05
49 77	2240E+05	53 66	2282E+05
49 84	2241E+05	53 74	2283E+05
49 90	2243E+05	53 80	2284E+05
49 97	2235E+05	53 87	2285E+05
50 04	2228E+05	53 93	2284E+05
50 10	2224E+05	53 99	2284E+05
50 15	2223E+05	54 05	2285E+05
50 22	2227E+05	54 12	2289E+05
50 28	2227E+05	54 17	2285E+05
50 35	2229E+05	54 24	2284E+05
50 41	2229E+05	54 31	2286E+05
50 48	2225E+05	54 38	2286E+05
50 54	2220E+05	54 44	2284E+05
50 60	2220E+05	54 50	2284E+05
50 67	2225E+05	54 56	2284E+05
50 73	2226E+05	54 63	2288E+05
50 81	2230E+05	54 69	2284E+05
50 85	2233E+05	54 75	2283E+05

X(cm)	Static Pressure	X(cm)	Static Pressure
54 81	2285E+05	58 75	2357E+05
54 88	2284E+05	58 80	2362E+05
54 94	2283E+05	58 90	2357E+05
55 01	2284E+05	58 93	2355E+05
55 07	2286E+05	59 01	2350E+05
55 13	2289E+05	59 08	2346E+05
55 19	2292E+05	59 15	2348E+05
55 32	2295E+05	59 23	2345E+05
55 32	2300E+05	59 31	2341E+05
55 39	2310E+05	59 36	2334E+05
55 45	2313E+05	59 45	2324E+05
55 51	2316E+05	59 51	2316E+05
55 58	2325E+05	59 60	2316E+05
55 64	2331E+05	59 65	2318E+05
55 70	2340E+05	59 73	2310E+05
55 77	2352E+05	59 81	2311E+05
55 82	2360E+05	59 86	2305E+05
55 89	2368E+05	59 93	2299E+05
55 96	2373E+05	60 00	2294E+05
56 02	2378E+05	60 09	2295E+05
56 08	2382E+05	60 14	2294E+05
56 15	2385E+05	60 20	2294E+05
56 21	2385E+05	60 29	2284E+05
56 27	2388E+05	60 35	2278E+05
56 33	2390E+05	60 43	2275E+05
56 40	2396E+05	60 48	2271E+05
56 47	2391E+05	60 52	2267E+05
56 53	2387E+05	60 64	2265E+05
56 60	2383E+05	60 71	2261E+05
56 66	2379E+05	60 76	2254E+05
56 73	2375E+05	60 85	2241E+05
56 77	2372E+05	60 92	2240E+05
56 85	2372E+05	60 99	2235E+05
56 90	2363E+05	61 04	2240E+05
56 97	2348E+05	61 10	2241E+05
57 03	2353E+05	61 16	2243E+05
57 12	2344E+05	61 26	2242E+05
57 19	2341E+05	61 30	2238E+05
57 23	2341E+05	61 39	2235E+05
57 30	2336E+05	61 45	2237E+05
57 38	2346E+05	61 51	2252E+05
57 42	2334E+05	61 60	2265E+05
57 52	2326E+05	61 65	2287E+05
57 57	2328E+05	61 72	2304E+05
57 64	2328E+05	61 80	2312E+05
57 69	2330E+05	61 86	2323E+05
57 79	2326E+05	61 95	2341E+05
57 85	2328E+05	62 00	2355E+05
57 89	2334E+05	62 10	2371E+05
57 96	2333E+05	62 15	2383E+05
58 00	2334E+05	62 20	2394E+05
58 08	2338E+05	62 30	2393E+05
58 15	2336E+05	62 34	2397E+05
58 21	2341E+05	62 44	2388E+05
58 28	2343E+05	62 48	2392E+05
58 33	2346E+05	62 54	2393E+05
58 40	2355E+05	62 64	2390E+05
58 46	2355E+05	62 69	2388E+05
58 53	2346E+05	62 76	2380E+05
58 60	2346E+05	62 84	2373E+05
58 66	2353E+05	62 91	2369E+05

X(cm.)

Static Pressure

62 98	2370E+05
63 06	2371E+05
63 11	2373E+05
63 18	2372E+05
63 25	2373E+05
63 31	2369E+05
63 38	2365E+05
63 45	2361E+05
63 51	2356E+05
63 58	2352E+05
63 65	2348E+05
63 71	2344E+05
63 78	2340E+05
63 84	2333E+05
63 91	2324E+05
63 97	2315E+05
64 04	2308E+05
64 11	2305E+05
64 18	2303E+05
64 24	2298E+05
64 30	2293E+05
64 36	2288E+05
64 43	2284E+05
64 49	2281E+05
64 56	2277E+05
64 64	2271E+05
64 70	2269E+05
64 76	2268E+05
64 83	2267E+05
64 88	2266E+05
64 96	2264E+05
65 01	2264E+05
65 09	2264E+05
65 15	2266E+05
65 21	2268E+05
65 28	2272E+05
65 34	2274E+05
65 42	2274E+05
65 47	2274E+05
65 54	2275E+05
65 60	2282E+05
65 66	2291E+05
65 72	2300E+05
65 80	2311E+05
65 86	2319E+05
65 92	2325E+05
65 98	2329E+05
66 06	2333E+05

VERTICAL PITOT PRESSURE PROFILE AT A STREAMWISE STATION

Y= 16.51 cm

Z= 0.0 cm

Average Stagnation Pressure= .6900E+06

Average Stagnation Temperature= 255.0

Y(cm)	Pitot Pressure	Static Pressure	U(m/s)	M
8890E-02	4831E+05	2190E+05	329.1	1.129
5503E-01	6547E+05	2190E+05	384.2	1.354
9890E-01	7202E+05	2190E+05	400.0	1.406
1416	7998E+05	2190E+05	417.2	1.511
1862	8602E+05	2190E+05	425.2	1.529
2422	9139E+05	2190E+05	439.3	1.657
2872	9398E+05	2190E+05	443.6	1.717
3383	1009E+06	2190E+05	455.1	1.789
3832	1033E+06	2190E+05	458.2	1.811
4317	1063E+06	2190E+05	462.3	1.837
4843	1119E+06	2190E+05	470.5	1.891
5751	1163E+06	2190E+05	475.2	1.921
6704	1245E+06	2190E+05	485.6	2.009
7666	1353E+06	2190E+05	497.2	2.101
8666	1395E+06	2190E+05	501.2	2.136
9616	1490E+06	2190E+05	510.1	2.214
1.056	1546E+06	2190E+05	514.6	2.257
1.150	1600E+06	2190E+05	519.0	2.299
1.246	1671E+06	2190E+05	524.7	2.356
1.345	1745E+06	2190E+05	530.2	2.412
1.442	1833E+06	2190E+05	536.1	2.476
1.639	1962E+06	2190E+05	544.0	2.566
1.823	2061E+06	2190E+05	548.9	2.632
2.018	2169E+06	2190E+05	554.2	2.703
2.212	2268E+06	2190E+05	559.1	2.774
2.411	2367E+06	2190E+05	562.7	2.830
2.599	2403E+06	2190E+05	564.0	2.859
2.791	2422E+06	2190E+05	564.5	2.866
2.982	2446E+06	2190E+05	565.6	2.890
3.177	2440E+06	2190E+05	565.6	2.890
3.370	2465E+06	2190E+05	566.6	2.894
3.571	2447E+06	2190E+05	565.6	2.892
3.764	2473E+06	2190E+05	567.1	2.901
3.952	2464E+06	2190E+05	566.6	2.894
4.153	2469E+06	2190E+05	566.6	2.894
4.342	2465E+06	2190E+05	566.6	2.894
4.534	24.7E+06	2190E+05	565.6	2.890
4.734	2473E+06	2190E+05	567.1	2.901
4.930	2446E+06	2190E+05	565.6	2.890
5.119	2460E+06	2190E+05	566.6	2.894

VERTICAL PITOT PRESSURE PROFILE AT A STREAMWISE STATION

X = 24.13 cm

Z = 0.0 cm

Average Stagnation Pressure = 6904E+06

Average Stagnation Temperature = 250.7

Y (cm)	Pitot Pressure	Static Pressure	U (m/s)	M
8890E-02	5316E+05	2209E+05	342.3	1.200
8108E-01	7052E+05	2209E+05	392.0	1.441
1027	8050E+05	2209E+05	414.1	1.561
1468	8704E+05	2209E+05	426.4	1.632
1938	9222E+05	2209E+05	435.7	1.689
2362	9487E+05	2209E+05	443.6	1.738
2876	1034E+06	2209E+05	453.6	1.804
3360	1061E+06	2209E+05	457.7	1.832
3814	1100E+06	2209E+05	462.8	1.867
4254	1147E+06	2209E+05	468.7	1.910
4609	1177E+06	2209E+05	472.5	1.938
5028	1254E+06	2209E+05	479.0	1.988
5715	1294E+06	2209E+05	486.1	2.044
7732	1386E+06	2209E+05	495.6	2.122
8448	1438E+06	2209E+05	500.4	2.165
9586	1523E+06	2209E+05	507.4	2.228
1.053	1585E+06	2209E+05	512.7	2.278
1.153	1657E+06	2209E+05	518.4	2.335
1.249	1755E+06	2209E+05	525.4	2.405
1.340	1816E+06	2209E+05	529.9	2.455
1.442	1879E+06	2209E+05	533.6	2.497
1.631	2085E+06	2209E+05	545.7	2.639
1.824	2206E+06	2209E+05	551.4	2.717
2.020	2331E+06	2209E+05	556.8	2.795
2.215	2450E+06	2209E+05	561.9	2.873
2.407	2475E+06	2209E+05	562.1	2.887
2.596	2497E+06	2209E+05	562.3	2.901
2.787	2514E+06	2209E+05	562.8	2.908
2.983	2543E+06	2209E+05	564.3	2.929
3.180	2546E+06	2209E+05	564.3	2.929
3.374	2544E+06	2209E+05	564.3	2.929
3.567	2544E+06	2209E+05	564.3	2.929
3.758	2541E+06	2209E+05	564.3	2.929
3.954	2539E+06	2209E+05	563.8	2.922
4.152	2565E+06	2209E+05	565.3	2.943
4.343	2585E+06	2209E+05	565.8	2.951
4.533	2593E+06	2209E+05	566.3	2.958
4.727	2574E+06	2209E+05	565.3	2.943
4.924	2556E+06	2209E+05	564.8	2.936
5.122	2531E+06	2209E+05	563.8	2.922

VERTICAL PITOT PRESSURE PROFILE AT A STREAMWISE STATION

X= 31.75 cm

Z= 0.0 cm

Average Stagnation Pressure= 6913E+06

Average Stagnation Temperature= 250.0

Y(cm.)	Pitot Pressure	Static Pressure	U(m/s)	M
8890E-02	5145E+05	2191E+05	357.1	1.179
6486E-01	7326E+05	2191E+05	399.5	1.432
1076	8098E+05	2191E+05	415.4	1.572
1579	8795E+05	2191E+05	428.7	1.650
2074	9302E+05	2191E+05	437.9	1.708
2494	9705E+05	2191E+05	444.0	1.755
3031	1021E+06	2191E+05	451.2	1.797
3478	1051E+06	2191E+05	455.0	1.825
3965	1106E+06	2191E+05	464.1	1.891
4487	1152E+06	2191E+05	470.0	1.924
4926	1179E+06	2191E+05	472.8	1.945
5894	1243E+06	2191E+05	481.1	2.019
6897	1307E+06	2191E+05	488.1	2.068
7846	1382E+06	2191E+05	495.7	2.127
8780	1429E+06	2191E+05	499.6	2.157
9737	1479E+06	2191E+05	504.2	2.207
1.071	1544E+06	2191E+05	509.5	2.257
1.169	1653E+06	2191E+05	516.4	2.343
1.263	1685E+06	2191E+05	520.2	2.363
1.356	1794E+06	2191E+05	523.4	2.448
1.452	1836E+06	2191E+05	529.8	2.478
1.647	2004E+06	2191E+05	541.1	2.567
1.844	2160E+06	2191E+05	549.4	2.702
2.036	2252E+06	2191E+05	553.2	2.758
2.226	2379E+06	2191E+05	558.4	2.857
2.418	2446E+06	2191E+05	560.8	2.880
2.609	2504E+06	2191E+05	562.5	2.915
2.808	2523E+06	2191E+05	563.6	2.928
3.001	2528E+06	2191E+05	563.6	2.928
3.189	2546E+06	2191E+05	564.6	2.942
3.382	2529E+06	2191E+05	563.6	2.927
3.583	2534E+06	2191E+05	564.1	2.936
3.779	2539E+06	2191E+05	564.1	2.936
3.971	2524E+06	2191E+05	563.6	2.929
4.162	2532E+06	2191E+05	564.1	2.936
4.354	2521E+06	2191E+05	563.6	2.928
4.551	2519E+06	2191E+05	563.6	2.928
4.748	2528E+06	2191E+05	563.6	2.928
4.940	2522E+06	2191E+05	563.6	2.928
5.129	2542E+06	2191E+05	564.1	2.936

VERTICAL PITOT PRESSURE PROFILE AT A STREAMWISE STATION

x = 39.37 cm.

z = 0.0 cm.

Average Stagnation Pressure = .6903E+06

Average Stagnation Temperature = 251.1

Y (cm.)	Pitot Pressure	Static Pressure	U (m/s)	M
339E-02	5269E+05	2267E+05	336.3	1.172
545E-01	7151E+05	2267E+05	390.3	1.430
9701E-01	7865E+05	2267E+05	406.2	1.515
1473	8481E+05	2267E+05	418.7	1.586
1916	8973E+05	2267E+05	427.8	1.639
2434	9710E+05	2267E+05	439.9	1.713
2888	1015E+06	2267E+05	447.1	1.759
3379	1045E+06	2267E+05	451.6	1.789
3909	1077E+06	2267E+05	455.8	1.818
4332	1084E+06	2267E+05	456.7	1.825
4850	1127E+06	2267E+05	462.8	1.867
5319	1224E+06	2267E+05	474.5	1.952
5723	1319E+06	2267E+05	485.6	2.037
6713	1347E+06	2267E+05	488.0	2.058
8651	1412E+06	2267E+05	494.7	2.115
9657	1500E+06	2267E+05	502.1	2.179
1066	1547E+06	2267E+05	506.6	2.221
1154	1571E+06	2267E+05	507.9	2.235
1249	1683E+06	2267E+05	516.9	2.320
1344	1740E+06	2267E+05	521.0	2.363
1447	1785E+06	2267E+05	524.3	2.398
1635	1870E+06	2267E+05	529.2	2.455
1827	2087E+06	2267E+05	542.2	2.604
2022	2243E+06	2267E+05	549.9	2.703
2222	2342E+06	2267E+05	554.2	2.766
2412	2409E+06	2267E+05	556.7	2.809
2597	2467E+06	2267E+05	558.6	2.844
2791	2490E+06	2267E+05	559.6	2.859
2997	2506E+06	2267E+05	560.2	2.866
3196	2495E+06	2267E+05	559.6	2.859
3373	2512E+06	2267E+05	560.7	2.873
3574	2503E+06	2267E+05	560.2	2.866
3767	2520E+06	2267E+05	560.7	2.873
3956	2544E+06	2267E+05	561.7	2.887
4155	2539E+06	2267E+05	561.7	2.887
4342	2556E+06	2267E+05	562.2	2.894
4540	2559E+06	2267E+05	562.8	2.901
4731	2542E+06	2267E+05	561.7	2.887
4929	2544E+06	2267E+05	561.7	2.887
5123	2538E+06	2267E+05	561.7	2.887

AD-A102 399

ORGANIZED STRUCTURES IN A SUPERSONIC TURBULENT BOUNDARY 2/2

LAYER(U) PRINCETON UNIV NJ DEPT OF MECHANICAL AND
AEROSPACE ENGINEERING E F SPINA ET AL. FEB 86 MAE-1736

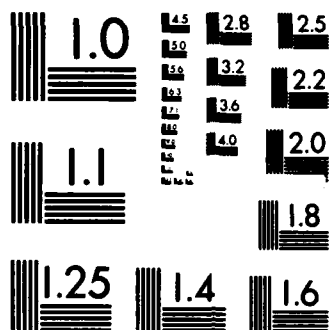
UNCLASSIFIED

AFOSR-85-0126

F/G 20/4

NL

END
P: 87
D: 11



MICROCOPY RESOLUTION TEST CHART
NATIONAL BUREAU OF STANDARDS-1963-A

VERTICAL PITOT PRESSURE PROFILE AT A STREAMWISE STATION
X= 43.18 cm
Z= 0.0 cm

Average Stagnation Pressure= .6897E+06
Average Stagnation Temperature= 252.3

Y(cm.)	Pitot Pressure	Static Pressure	U(m/s)	M
.8890E-02	.5251E+05	.2276E+05	335.5	1.165
.5806E-01	.7111E+05	.2276E+05	367.8	1.423
.1019	.8078E+05	.2276E+05	411.0	1.536
.1579	.8798E+05	.2276E+05	424.6	1.614
.1995	.9410E+05	.2276E+05	435.3	1.678
.2494	.9923E+05	.2276E+05	443.8	1.731
.2971	.9964E+05	.2276E+05	444.2	1.735
.3409	.1054E+06	.2276E+05	452.7	1.785
.3977	.1085E+06	.2276E+05	456.8	1.819
.4423	.1128E+06	.2276E+05	463.0	1.850
.4937	.1175E+06	.2276E+05	469.0	1.903
.5879	.1252E+06	.2276E+05	478.5	1.974
.6817	.1307E+06	.2276E+05	484.8	2.023
.7751	.1345E+06	.2276E+05	488.2	2.051
.8716	.1444E+06	.2276E+05	498.5	2.136
.9707	.1481E+06	.2276E+05	501.6	2.165
1.070	.1549E+06	.2276E+05	507.0	2.214
1.166	.1567E+06	.2276E+05	508.3	2.228
1.257	.1680E+06	.2276E+05	517.4	2.313
1.349	.1714E+06	.2276E+05	520.0	2.342
1.451	.1805E+06	.2276E+05	526.2	2.405
1.643	.1979E+06	.2276E+05	537.2	2.526
1.837	.2088E+06	.2276E+05	542.8	2.597
2.027	.2146E+06	.2276E+05	545.8	2.639
2.222	.2346E+06	.2276E+05	555.5	2.764
2.420	.2410E+06	.2276E+05	557.5	2.802
2.609	.2442E+06	.2276E+05	558.3	2.823
2.802	.2523E+06	.2276E+05	562.0	2.873
2.993	.2526E+06	.2276E+05	562.0	2.873
3.185	.2519E+06	.2276E+05	561.5	2.864
3.385	.2546E+06	.2276E+05	563.1	2.887
3.579	.2534E+06	.2276E+05	562.6	2.880
3.772	.2535E+06	.2276E+05	562.6	2.880
3.960	.2531E+06	.2276E+05	562.0	2.873
4.155	.2505E+06	.2276E+05	561.0	2.857
4.353	.2529E+06	.2276E+05	562.0	2.873
4.548	.2543E+06	.2276E+05	562.6	2.880
4.738	.2541E+06	.2276E+05	562.6	2.880
4.931	.2553E+06	.2276E+05	563.1	2.887
5.126	.2559E+06	.2276E+05	563.6	2.894

VERTICAL PITOT PRESSURE PROFILE AT A STREAMWISE STATION
 $x = 46.99$ cm.
 $z = 0.0$ cm.

Average Stagnation Pressure= $6901E+06$
Average Stagnation Temperature= 292 K

Y(cm.)	Pitot Pressure	Static Pressure	U(m/s)	M
8890E-02	4621E+05	2252E+05	313.6	1.069
5228E-01	6690E+05	2252E+05	381.1	1.377
9096E-01	7522E+05	2252E+05	401.0	1.480
1242	8359E+05	2252E+05	418.3	1.575
1624	8788E+05	2252E+05	426.9	1.629
2010	9183E+05	2252E+05	434.0	1.667
2445	9502E+05	2252E+05	439.1	1.699
2816	9850E+05	2252E+05	444.7	1.735
3156	1050E+06	2252E+05	454.3	1.797
3519	1093E+06	2252E+05	460.6	1.839
3921	1092E+06	2252E+05	460.5	1.839
4229	1146E+06	2252E+05	467.5	1.889
3524	1205E+06	2252E+05	475.2	1.945
5250	1246E+06	2252E+05	479.8	1.981
7035	1296E+06	2252E+05	485.2	2.023
7755	1349E+06	2252E+05	490.5	2.066
7557	1403E+06	2252E+05	496.4	2.115
8340	1466E+06	2252E+05	502.2	2.165
1006	1536E+06	2252E+05	508.6	2.221
1088	1549E+06	2252E+05	509.1	2.228
1165	1641E+06	2252E+05	516.7	2.299
1316	1704E+06	2252E+05	521.4	2.349
1473	1851E+06	2252E+05	531.6	2.455
1627	1918E+06	2252E+05	535.1	2.497
1777	1999E+06	2252E+05	539.8	2.554
1929	2078E+06	2252E+05	543.6	2.604
2089	2220E+06	2252E+05	551.5	2.703
2247	2265E+06	2252E+05	553.1	2.731
2400	2348E+06	2252E+05	556.4	2.781
2548	2370E+06	2252E+05	556.9	2.795
2698	2439E+06	2252E+05	559.9	2.837
2860	2439E+06	2252E+05	559.9	2.837
3017	2502E+06	2252E+05	562.6	2.873
3171	2505E+06	2252E+05	562.6	2.873
3321	2501E+06	2252E+05	562.6	2.873
3477	2519E+06	2252E+05	563.6	2.887
3637	2534E+06	2252E+05	564.1	2.894
3792	2529E+06	2252E+05	563.6	2.887
3944	2530E+06	2252E+05	564.1	2.894
4098	2573E+06	2252E+05	564.1	2.894
4250	2530E+06	2252E+05	564.1	2.894
4406	2532E+06	2252E+05	564.1	2.894
4559	2562E+06	2252E+05	565.2	2.908
4715	2580E+06	2252E+05	566.2	2.922

VERTICAL PITOT PRESSURE PROFILE AT A STREAMWISE STATION.
 X= 50 8 cm
 Z= 0 0 cm

Average Stagnation Pressure= 6903E+06
 Average Stagnation Temperature= 251 8

Y(cm)	Pitot Pressure	Static Pressure	U(m/s)	M
8890E-02	4737E+05	2304E+05	313 0	1 066
9390E-01	4879E+05	2304E+05	373 2	1 342
9285E-01	7590E+05	2304E+05	398 1	1 469
1265	8288E+05	2304E+05	412 4	1 547
1632	8736E+05	2304E+05	421 1	1 592
2052	9184E+05	2304E+05	428 9	1 643
2472	9643E+05	2304E+05	437 1	1 692
2827	9851E+05	2304E+05	440 4	1 713
3183	1046E+06	2304E+05	449 0	1 768
3561	1078E+06	2304E+05	454 4	1 802
3965	1092E+06	2304E+05	456 4	1 810
4745	1120E+06	2304E+05	459 3	1 835
5550	1187E+06	2304E+05	465 2	1 902
6246	1237E+06	2304E+05	474 0	1 945
7067	1260E+06	2304E+05	476 7	1 962
7785	1296E+06	2304E+05	480 2	1 992
8545	1353E+06	2304E+05	486 5	2 044
9393	1387E+06	2304E+05	489 6	2 072
1 011	1474E+06	2304E+05	492 4	2 142
1 090	1531E+06	2304E+05	503 1	2 162
1 163	1572E+06	2304E+05	507 0	2 211
1 311	1652E+06	2304E+05	512 8	2 275
1 469	1747E+06	2304E+05	519 8	2 345
1 630	1896E+06	2304E+05	529 4	2 452
1 793	2001E+06	2304E+05	534 1	2 521
1 932	2089E+06	2304E+05	540 7	2 562
2 087	2203E+06	2304E+05	546 2	2 653
2 242	2341E+06	2304E+05	553 2	2 742
2 401	2385E+06	2304E+05	554 6	2 762
2 584	2456E+06	2304E+05	557 4	2 812
2 703	2493E+06	2304E+05	558 8	2 837
2 857	2590E+06	2304E+05	561 0	2 852
3 012	2667E+06	2304E+05	562 0	2 857
3 171	2681E+06	2304E+05	562 5	2 857
3 326	2681E+06	2304E+05	562 5	2 857
3 482	2682E+06	2304E+05	562 5	2 857
3 634	2678E+06	2304E+05	562 0	2 857
3 786	2672E+06	2304E+05	562 0	2 857
3 946	2663E+06	2304E+05	561 5	2 872
4 104	2655E+06	2304E+05	561 5	2 872
4 256	2648E+06	2304E+05	561 0	2 852
4 367	2644E+06	2304E+05	561 0	2 852
4 575	2641E+06	2304E+05	561 0	2 852
5 182	2551E+06	2304E+05	561 0	2 826

VERTICAL PITOT PRESSURE PROFILE AT A STREAMWISE STATION

z = 54.61 cm

z = 0.0 cm

Average Stagnation Pressure = 6903E+06

Average Stagnation Temperature = 251.4

Y(cm)	Pitot Pressure	Static Pressure	U(m/s)	M
859E-02	5534E+05	2310E+05	342.0	1.196
3377E-01	6606E+05	2310E+05	373.6	1.345
8359E-01	7136E+05	2310E+05	387.0	1.412
8566E-01	7714E+05	2310E+05	399.9	1.480
1118	8113E+05	2310E+05	408.3	1.526
1303	8458E+05	2310E+05	415.3	1.565
1609	8891E+05	2310E+05	423.3	1.611
1791	9074E+05	2310E+05	426.2	1.628
2044	9500E+05	2310E+05	433.9	1.674
2332	9725E+05	2310E+05	437.3	1.696
2509	9804E+05	2310E+05	439.0	1.706
2790	1035E+06	2310E+05	447.3	1.759
3170	1066E+06	2310E+05	451.9	1.789
3203	1104E+06	2310E+05	457.1	1.825
3139	1134E+06	2310E+05	461.1	1.853
3275	1204E+06	2310E+05	470.1	1.917
3459	1228E+06	2310E+05	473.0	1.938
3713	1257E+06	2310E+05	475.7	1.959
3801	1284E+06	2310E+05	478.5	1.981
3978	1325E+06	2310E+05	483.0	2.016
4331	1351E+06	2310E+05	485.6	2.037
4300	1395E+06	2310E+05	490.7	2.080
4253	1440E+06	2310E+05	494.8	2.115
4625	1523E+06	2310E+05	502.1	2.179
4119	1558E+06	2310E+05	505.1	2.207
4214	1668E+06	2310E+05	513.5	2.285
4311	1727E+06	2310E+05	517.8	2.328
4409	1773E+06	2310E+05	521.1	2.363
4506	1845E+06	2310E+05	525.8	2.412
4596	1921E+06	2310E+05	531.0	2.469
4592	2002E+06	2310E+05	535.4	2.519
4768	2060E+06	2310E+05	538.9	2.561
4889	2144E+06	2310E+05	543.5	2.618
4987	2178E+06	2310E+05	545.0	2.639
5083	2291E+06	2310E+05	550.5	2.710
5181	2301E+06	2310E+05	550.7	2.717
5277	2418E+06	2310E+05	556.0	2.788
5368	2382E+06	2310E+05	553.9	2.766
5466	2413E+06	2310E+05	554.6	2.781
5564	2456E+06	2310E+05	556.4	2.809
5659	2452E+06	2310E+05	556.2	2.809
5850	2518E+06	2310E+05	558.9	2.844
5940	2548E+06	2310E+05	560.5	2.866
6238	2566E+06	2310E+05	561.0	2.873
6434	2584E+06	2310E+05	562.1	2.887
6623	2592E+06	2310E+05	562.1	2.887
6815	2591E+06	2310E+05	562.1	2.887
7014	2607E+06	2310E+05	563.1	2.901
7207	2626E+06	2310E+05	563.6	2.908
7397	2656E+06	2310E+05	565.1	2.929
7591	2655E+06	2310E+05	564.6	2.922
7787	2616E+06	2310E+05	563.1	2.901
7983	2603E+06	2310E+05	562.6	2.894
8173	2591E+06	2310E+05	562.1	2.887

VERTICAL PITOT PRESSURE PROFILE AT A STREAMWISE STATION:

X= 62.23 cm

Z= 0.0 cm.

Average Stagnation Pressure= .6906E+06

Average Stagnation Temperature= 250.3

Y(cm.)	Pitot Pressure	Static Pressure	U(m/s)	M
.8890E-02	.9640E+05	.2298E+05	346.0	1.212
.3536E-01	.6888E+05	.2298E+05	380.7	1.364
.6184E-01	.7455E+05	.2298E+05	394.4	1.455
.8415E-01	.7987E+05	.2298E+05	405.6	1.515
.1008	.8129E+05	.2298E+05	408.7	1.523
.1326	.8409E+05	.2298E+05	418.1	1.564
.1549	.8903E+05	.2298E+05	423.6	1.618
.1787	.8909E+05	.2298E+05	423.5	1.618
.2037	.9164E+05	.2298E+05	428.2	1.646
.2267	.9720E+05	.2298E+05	437.5	1.703
.2525	.9715E+05	.2298E+05	436.9	1.699
.2975	.1062E+06	.2298E+05	451.0	1.784
.3421	.1075E+06	.2298E+05	453.0	1.804
.3977	.1150E+06	.2298E+05	463.4	1.874
.4408	.1137E+06	.2298E+05	461.2	1.860
.4941	.1157E+06	.2298E+05	463.0	1.874
.5391	.1224E+06	.2298E+05	471.9	1.932
.5841	.1222E+06	.2298E+05	471.8	1.932
.6375	.1273E+06	.2298E+05	477.4	1.981
.6791	.1314E+06	.2298E+05	482.0	2.016
.7320	.1364E+06	.2298E+05	487.3	2.055
.8250	.1436E+06	.2298E+05	494.1	2.115
.9226	.1464E+06	.2298E+05	496.3	2.134
1.018	.1538E+06	.2298E+05	502.7	2.193
1.112	.1626E+06	.2298E+05	510.4	2.264
1.213	.1674E+06	.2298E+05	514.0	2.299
1.311	.1713E+06	.2298E+05	516.6	2.328
1.404	.1791E+06	.2298E+05	522.2	2.384
1.498	.1870E+06	.2298E+05	527.5	2.441
1.594	.1888E+06	.2298E+05	527.8	2.446
1.694	.2008E+06	.2298E+05	535.5	2.523
1.791	.2084E+06	.2298E+05	539.6	2.562
1.883	.2123E+06	.2298E+05	541.8	2.611
1.980	.2230E+06	.2298E+05	546.8	2.674
2.075	.2234E+06	.2298E+05	547.0	2.682
2.174	.2298E+06	.2298E+05	549.5	2.717
2.274	.2377E+06	.2298E+05	553.1	2.766
2.368	.2406E+06	.2298E+05	554.4	2.788
2.462	.2424E+06	.2298E+05	554.5	2.795
2.556	.2498E+06	.2298E+05	557.9	2.844
2.658	.2538E+06	.2298E+05	559.3	2.866
2.844	.2575E+06	.2298E+05	560.8	2.887
3.039	.2630E+06	.2298E+05	563.4	2.922
3.233	.2653E+06	.2298E+05	563.9	2.929
3.434	.2652E+06	.2298E+05	563.9	2.929
3.627	.2668E+06	.2298E+05	564.9	2.943
3.815	.2642E+06	.2298E+05	563.9	2.925
4.009	.2618E+06	.2298E+05	562.9	2.915
4.206	.2609E+06	.2298E+05	562.4	2.908
4.401	.2605E+06	.2298E+05	561.9	2.901
4.594	.2610E+06	.2298E+05	562.4	2.908
4.782	.2636E+06	.2298E+05	563.4	2.922
4.979	.2643E+06	.2298E+05	563.9	2.926
5.174	.2642E+06	.2298E+05	563.9	2.929

STREAMWISE PRESTON TUBE MEASUREMENTS

(determined from Hopkins-Keener calibration scheme)

0.0 cm.

0.0 cm

Preston Tube Diameter = 1.65 mm.

cm	Stag. Pressure	Stag. Temp.	Stat. Pressure	Preston Pressure	Cf
51	6900E+06	259 6	2190E+05	6864E+05	0010845
18	6900E+06	254 8	2192E+05	6884E+05	0010822
45	6900E+06	251 5	2203E+05	6993E+05	0010943
02	6900E+06	249 3	2196E+05	6912E+05	0010739
31	6900E+06	247 6	2213E+05	6986E+05	0010826
13	6902E+06	255 4	2209E+05	6994E+05	0010992
79	6900E+06	246 0	2222E+05	6956E+05	0010699
08	6900E+06	244 5	2210E+05	6981E+05	0010784
02	6902E+06	251 5	2209E+05	6993E+05	0010935
50	6902E+06	248 7	2268E+05	6953E+05	0010536
19	6902E+06	246 7	2288E+05	7004E+05	0010523
51	6902E+06	245 2	2242E+05	6964E+05	0010656
41	6902E+06	243 6	2179E+05	6961E+05	0010862
02	6898E+06	248 0	2182E+05	6898E+05	0010784
12	6902E+06	242 1	2273E+05	6881E+05	0010382
59	6898E+06	244 6	2276E+05	6874E+05	0010368
04	6902E+06	240 7	2280E+05	6917E+05	0010353
41	6898E+06	242 5	2284E+05	6927E+05	0010375
59	6898E+06	240 8	2261E+05	6909E+05	0010384
37	6898E+06	239 5	2267E+05	6888E+05	0010313
71	6898E+06	238 2	2250E+05	6823E+05	0010268
09	6898E+06	236 7	2302E+05	6760E+05	0009908
13	6889E+06	251 7	2300E+05	6944E+05	0010526
42	6898E+06	235 4	2330E+05	6783E+05	0009850
57	6889E+06	248 2	2288E+05	7067E+05	0010685
20	6889E+06	246 0	2259E+05	6912E+05	0010462
54	6889E+06	244 3	2224E+05	6857E+05	0010486
64	6889E+06	242 6	2296E+05	6456E+05	0009549
07	6889E+06	241 2	2274E+05	6716E+05	0010093
07	6890E+06	250 6	2240E+05	6797E+05	0010456
94	6889E+06	239 6	2224E+05	6732E+05	0010235
07	6889E+06	238 3	2229E+05	6750E+05	0010211
18	6890E+06	247 5	2240E+05	6728E+05	0010320
13	6890E+06	245 5	2284E+05	6774E+05	0010188
9	6890E+06	243 8	2284E+05	6793E+05	0010164
12	6890E+06	242 1	2387E+05	6851E+05	0009910
14	6890E+06	240 5	2328E+05	6921E+05	0010151
50	6890E+06	239 0	2317E+05	6938E+05	0010233
23	6891E+06	252 2	2297E+05	7058E+05	0010638
57	6890E+06	237 5	2239E+05	6999E+05	0010638
71	6891E+06	249 5	2236E+05	7002E+05	0010820
04	6891E+06	247 6	2390E+05	7096E+05	0010351
50	6891E+06	245 7	2323E+05	7104E+05	0010554

HOT WIRE ANEMOMETER MEASUREMENTS (NORMAL WIRE)

X=165.1 mm												
UT= 2.2430E+01 RNDM= 2.8306E-01 TM= 2.6936E+02 D= 2.4840E-02 Uinf=5.6660E+02												
Y (M)	Y/D	(RND U)' RND U	(RND U)' RNDM+UT	U Uinf	M	R-U'2 R-U+2	<RNDU>/RNDUE	<U>/ILOC				
2.7800E-03	1.1192E-01	1.5140E-01	5.2198E+00	7.8164E-01	1.7113E+00	1.9134E-03	6.9334E-02	7.3471E-02				
4.0490E-03	1.6300E-01	1.4140E-01	5.1844E+00	8.1191E-01	1.8233E+00	1.6438E-03	6.8846E-02	6.3897E-02				
5.2743E-03	2.1233E-01	1.4620E-01	5.6373E+00	8.3433E-01	1.9126E+00	1.7265E-03	7.7535E-02	6.2440E-02				
6.3418E-03	2.5531E-01	1.4320E-01	6.0310E+00	8.5007E-01	1.9794E+00	1.6301E-03	8.0108E-02	5.8641E-02				
7.6220E-03	3.0684E-01	1.4310E-01	6.2725E+00	8.7654E-01	2.0964E+00	1.5764E-03	8.3315E-02	5.4458E-02				
8.9720E-03	3.6119E-01	1.4040E-01	6.5143E+00	8.8963E-01	2.1611E+00	1.4873E-03	8.6531E-02	5.1338E-02				
1.0284E-02	4.1401E-01	1.3950E-01	6.8397E+00	9.0590E-01	2.2444E+00	1.4283E-03	9.0850E-02	4.8466E-02				
1.1729E-02	4.7218E-01	1.3470E-01	7.0817E+00	9.1839E-01	2.3126E+00	1.3004E-03	9.4065E-02	4.4902E-02				
1.3188E-02	5.3092E-01	1.3840E-01	7.7078E+00	9.3319E-01	2.3972E+00	1.3314E-03	1.0238E-01	4.3851E-02				
1.4329E-02	5.7685E-01	1.3780E-01	8.2983E+00	9.4519E-01	2.4700E+00	1.2844E-03	1.0969E-01	4.1815E-02				
1.5405E-02	6.2017E-01	1.2700E-01	7.8150E+00	9.5314E-01	2.5220E+00	1.0693E-03	1.0381E-01	4.1739E-02				
1.6207E-02	6.5246E-01	1.2440E-01	7.8079E+00	9.5882E-01	2.5995E+00	1.0117E-03	1.0371E-01	3.5824E-02				
1.7087E-02	6.8788E-01	1.1620E-01	7.4781E+00	9.6339E-01	2.5922E+00	8.7120E-04	9.9329E-02	3.2833E-02				
1.8167E-02	7.3136E-01	1.1160E-01	7.3525E+00	9.6846E-01	2.6298E+00	7.9165E-04	9.7662E-02	3.0859E-02				
1.9597E-02	7.8893E-01	1.0080E-01	6.8837E+00	9.7532E-01	2.6818E+00	6.3204E-04	9.1437E-02	2.7058E-02				
2.0897E-02	8.4126E-01	8.7720E-02	6.1598E+00	9.8131E-01	2.7292E+00	4.6944E-04	8.1554E-02	2.2922E-02				
2.2047E-02	8.8754E-01	6.8740E-02	4.8947E+00	9.8644E-01	2.7713E+00	2.8334E-04	6.5015E-02	1.7543E-02				
2.2857E-02	9.2017E-01	6.0130E-02	4.3299E+00	9.8912E-01	2.7947E+00	2.1471E-04	5.7513E-02	1.5147E-02				
2.4797E-02	9.7814E-01	4.6090E-02	3.3705E+00	9.9335E-01	2.8329E+00	1.2415E-04	4.4769E-02	1.1367E-02				
2.5747E-02	1.0365E+00	3.0270E-02	2.2346E+00	9.9511E-01	2.8553E+00	5.2984E-05	2.9681E-02	7.1373E-02				
2.7197E-02	1.0949E+00	2.0520E-02	1.5222E+00	9.9597E-01	2.8634E+00	2.4286E-05	2.0219E-02	4.9763E-03				
2.8627E-02	1.1525E+00	1.6330E-02	1.1400E+00	9.9702E-01	2.8713E+00	1.5351E-05	1.6125E-02	3.9432E-03				
3.0077E-02	1.2108E+00	1.4270E-02	1.0629E+00	9.9824E-01	2.8800E+00	1.1697E-05	1.4118E-02	3.4294E-03				
3.1547E-02	1.2700E+00	1.1280E-02	8.4300E-01	9.9824E-01	2.8800E+00	7.3142E-06	1.1197E-02	2.7107E-02				
3.2987E-02	1.3289E+00	1.2200E-02	9.1310E-01	9.9935E-01	2.8888E+00	8.5352E-06	1.2129E-02	2.9177E-03				
3.4447E-02	1.3868E+00	1.1740E-02	8.8240E-01	9.9934E-01	2.8888E+00	7.9345E-06	1.1721E-02	2.8122E-03				
3.5907E-02	1.4455E+00	1.1440E-02	8.6145E-01	9.9851E-01	2.8821E+00	7.5402E-06	1.1442E-02	2.7462E-03				
3.7357E-02	1.5039E+00	1.2020E-02	9.0493E-01	1.0005E+00	2.8979E+00	8.2771E-06	1.2020E-02	2.6604E-03				

HOT WIRE ANEMOMETER MEASUREMENTS (NORMAL WIRE)

X-241 3 mm UT= 2 2375E+01 RNDU= 2 8447E-01 TM= 2 7071E+02 D= 2 5030E-02 Uinf=3.6450E+02

Y (M)	Y/D	(RND U)' RND U	(RND U)' RNDU	U Uinf	M	R-U'2 R-U'2	<RNDU>/RNDUE	<U>/ULOC
2 7800E-03	1 1107E-01	1 4820E-01	4 9805E+00	8 0023E-01	1 7917E+00	1 8027E-03	6 6597E-02	6 8336E-02
4 0600E-03	1 6221E-01	1 4260E-01	5 1328E+00	8 2469E-01	1 8870E+00	1 6411E-03	6 8634E-02	6 1899E-02
5 5018E-03	2 1981E-01	1 4650E-01	5 6184E+00	8 4570E-01	1 9757E+00	1 6969E-03	7 5127E-02	6 0130E-02
6 9250E-03	2 7667E-01	1 4290E-01	5 9451E+00	8 6459E-01	2 0601E+00	1 5780E-03	7 9496E-02	5 5632E-02
8 3470E-03	3 3348E-01	1 3790E-01	6 0989E+00	8 8365E-01	2 1509E+00	1 4303E-03	8 1552E-02	5 0744E-02
9 7850E-03	3 9093E-01	1 4250E-01	6 6875E+00	9 0083E-01	2 2385E+00	1 4845E-03	8 9422E-02	4 9688E-02
1 1236E-02	4 4890E-01	1 3830E-01	6 7598E+00	9 1537E-01	2 3182E+00	1 3603E-03	9 0389E-02	4 5945E-02
1 2689E-02	5 0695E-01	1 3570E-01	7 0804E+00	9 3248E-01	2 4159E+00	1 2646E-03	9 4676E-02	4 2518E-02
1 4133E-02	5 6464E-01	1 3330E-01	7 3364E+00	9 4342E-01	2 4852E+00	1 1883E-03	9 8099E-02	4 0090E-02
1 5571E-02	6 2209E-01	1 3210E-01	7 6232E+00	9 5832E-01	2 5835E+00	1 1228E-03	1 0193E-01	3 7515E-02
1 7034E-02	6 8054E-01	1 2400E-01	7 5354E+00	9 7048E-01	2 6683E+00	9 5705E-04	1 0076E-01	3 3542E-02
1 8484E-02	7 3847E-01	1 1560E-01	7 3630E+00	9 7798E-01	2 7267E+00	8 1204E-04	9 8454E-02	3 0251E-02
1 9914E-02	7 9561E-01	1 0310E-01	6 8762E+00	9 8496E-01	2 7836E+00	6 3088E-04	9 1945E-02	2 6132E-02
2 1354E-02	8 5314E-01	9 0160E-02	6 2908E+00	9 9168E-01	2 8409E+00	4 7125E-04	8 4118E-02	2 2137E-02
2 2804E-02	9 1107E-01	7 5630E-02	5 3625E+00	9 9551E-01	2 8777E+00	3 2633E-04	7 1706E-02	1 8198E-02
2 4244E-02	9 6860E-01	5 7310E-02	4 0978E+00	9 9578E-01	2 8883E+00	1 8639E-04	5 4794E-02	1 3710E-02
2 5694E-02	1 0265E+00	4 6010E-02	3 3173E+00	9 9605E-01	2 8990E+00	1 1949E-04	4 4357E-02	1 0942E-02
2 7144E-02	1 0845E+00	3 3450E-02	2 4511E+00	9 9665E-01	2 9053E+00	6 3043E-05	3 2775E-02	7 9279E-03
2 8564E-02	1 1412E+00	2 5520E-02	1 8849E+00	9 9793E-01	2 9154E+00	3 6588E-05	2 5204E-02	6 0152E-03
3 0014E-02	1 1991E+00	1 5470E-02	1 1533E+00	9 9965E-01	2 9290E+00	1 3387E-05	1 5421E-02	3 6196E-03
3 1494E-02	1 2582E+00	1 3020E-02	9 7146E-01	9 9965E-01	2 9290E+00	9 4901E-06	1 2990E-02	3 0464E-03
3 2924E-02	1 3154E+00	1 3480E-02	1 0085E+00	9 9965E-01	2 9290E+00	1 0184E-05	1 3486E-02	3 1540E-03
3 4384E-02	1 3737E+00	1 3320E-02	9 9510E-01	9 9965E-01	2 9290E+00	9 9556E-06	1 3306E-02	3 1166E-03
3 5844E-02	1 4320E+00	1 2650E-02	9 4465E-01	9 9965E-01	2 9290E+00	8 9897E-06	1 2631E-02	2 9598E-03
3 7304E-02	1 4904E+00	1 3370E-02	9 9799E-01	9 9965E-01	2 9290E+00	1 0050E-05	1 3345E-02	3 1283E-03
3 8774E-02	1 5491E+00	1 3120E-02	9 8077E-01	9 9911E-01	2 9247E+00	9 7054E-06	1 3114E-02	3 0769E-03
4 0254E-02	1 6082E+00	1 3330E-02	1 0036E+00	9 9972E-01	2 9296E+00	1 0011E-05	1 3420E-02	3 1179E-03
4 1704E-02	1 6662E+00	1 4280E-02	1 0810E+00	1 0015E+00	2 9438E+00	1 1432E-05	1 4434E-02	3 3145E-03
4 3184E-02	1 7253E+00	1 4730E-02	1 1273E+00	1 0022E+00	2 9500E+00	1 2146E-05	1 5073E-02	3 4075E-03

HOT WIRE ANEMOMETER MEASUREMENTS (NORMAL WIRE)

X=317.5 mm UT= 2.2044E+01 RHO= 2.8521E-01 TW= 2.6733E+02 D= 2.7120E-02 Uinf=5.6400E+02

Y (M)	Y/D	(RHO U)' RHO U	(RHO U)' RHO*UT	U Uinf	M	R-U'2 R-U*2	<RHO>/RHOUE	<U>/ULOC
2.7800E-03	1.0291E-01	1.4840E-01	5.1172E+00	7.9440E-01	1.7727E+00	1.8203E-03	6.7733E-02	6.9258E-02
4.0360E-03	1.4936E-01	1.4120E-01	5.1699E+00	8.2470E-01	1.8885E+00	1.6143E-03	6.8430E-02	6.1232E-02
5.4959E-03	2.0265E-01	1.4350E-01	5.5713E+00	8.4694E-01	1.9827E+00	1.6305E-03	7.3744E-02	5.8641E-02
6.9210E-03	2.5520E-01	1.4280E-01	6.0120E+00	8.6577E-01	2.0674E+00	1.5777E-03	7.9577E-02	5.5334E-02
8.3440E-03	3.0767E-01	1.4270E-01	6.3188E+00	8.8239E-01	2.1482E+00	1.5370E-03	8.3637E-02	5.2597E-02
9.7810E-03	3.6066E-01	1.3810E-01	6.4709E+00	8.9440E-01	2.2093E+00	1.4109E-03	8.5631E-02	4.9024E-02
1.1224E-02	4.1384E-01	1.3700E-01	6.8007E+00	9.1165E-01	2.3016E+00	1.3450E-03	9.0016E-02	4.5974E-02
1.2686E-02	4.6777E-01	1.3530E-01	7.0391E+00	9.2322E-01	2.3681E+00	1.2804E-03	9.3172E-02	4.3620E-02
1.4127E-02	5.2091E-01	1.3580E-01	7.4539E+00	9.3939E-01	2.4645E+00	1.2448E-03	9.8662E-02	4.1341E-02
1.5569E-02	5.7408E-01	1.3170E-01	7.6204E+00	9.5096E-01	2.5411E+00	1.1354E-03	1.0087E-01	3.8333E-02
1.7037E-02	6.2821E-01	1.2400E-01	7.5833E+00	9.6363E-01	2.6275E+00	9.7295E-04	1.0037E-01	3.4333E-02
1.8477E-02	6.8131E-01	1.1320E-01	7.5482E+00	9.7424E-01	2.7041E+00	8.5716E-04	9.9910E-02	3.1329E-02
1.9907E-02	7.3403E-01	1.0940E-01	7.1933E+00	9.7926E-01	2.7458E+00	7.2168E-04	9.5213E-02	2.8323E-02
2.1347E-02	7.8713E-01	9.6180E-02	6.5933E+00	9.8544E-01	2.7995E+00	5.4522E-04	8.7271E-02	2.4163E-02
2.2797E-02	8.4060E-01	8.4340E-02	5.9138E+00	9.9126E-01	2.8490E+00	4.1064E-04	7.8303E-02	2.0614E-02
2.4247E-02	8.9406E-01	6.5740E-02	4.4925E+00	9.9443E-01	2.8812E+00	2.4594E-04	6.2861E-02	1.5788E-02
2.5687E-02	9.4716E-01	5.1200E-02	3.7590E+00	9.9670E-01	2.9076E+00	1.4746E-04	4.9756E-02	1.2129E-02
2.7137E-02	1.0004E+00	4.1340E-02	3.0680E+00	9.9837E-01	2.9224E+00	9.5599E-05	4.0609E-02	9.7075E-03
2.8567E-02	1.0534E+00	2.4070E-02	1.8081E+00	9.9929E-01	2.9290E+00	3.2353E-05	2.3933E-02	5.6318E-03
3.0017E-02	1.1068E+00	2.1200E-02	1.5984E+00	9.9930E-01	2.9291E+00	2.5127E-05	2.1160E-02	4.9401E-03
3.1487E-02	1.1610E+00	1.7830E-02	1.3383E+00	1.0007E+00	2.9400E+00	1.7710E-05	1.7714E-02	4.1470E-03
3.2937E-02	1.2141E+00	1.4470E-02	1.0730E+00	1.0001E+00	2.9355E+00	1.1699E-05	1.4203E-02	3.3738E-03
3.4387E-02	1.2680E+00	1.2520E-02	9.3015E-01	9.9954E-01	2.9310E+00	8.7843E-06	1.2312E-02	2.9267E-03
3.5847E-02	1.3218E+00	1.1000E-02	9.7241E-01	1.0002E+00	2.9360E+00	9.6052E-06	1.2871E-02	3.0539E-03
3.7297E-02	1.3753E+00	1.2510E-02	9.2921E-01	1.0007E+00	2.9360E+00	8.7664E-06	1.2797E-02	2.9159E-03
3.8767E-02	1.4295E+00	1.2280E-02	9.1252E-01	9.9973E-01	2.9324E+00	8.4690E-06	1.2078E-02	2.8479E-03
4.0247E-02	1.4840E+00	1.1170E-02	8.3092E-01	9.9954E-01	2.9310E+00	7.0164E-06	1.0998E-02	2.6107E-03
4.1697E-02	1.5375E+00	1.1900E-02	8.8674E-01	1.0001E+00	2.9357E+00	7.9582E-06	1.1737E-02	2.7742E-03
4.3177E-02	1.5921E+00	1.2160E-02	9.0611E-01	9.9944E-01	2.9307E+00	8.3374E-06	1.1994E-02	2.8471E-03

X=393.7 mm UT= 2.1734E+01 RHON= 2.9745E-01 TW= 2.6536E+02 D= 2.7750E-02 UINF=5.6200E+02

Y	(M)	Y/D	(RMO U)' RMO U	(RMO U)' RMO+UT	U Uinf	M	R-U/2 R-U+2	<RMO>/<RMOUE	<U>/<ULOC
2	7800E-03	1.0018E-01	1.4300E-01	4.5722E+00	7.9250E-01	1.7481E+00	1.7925E-03	6.2228E-02	6.7791E-02
4	0400E-03	1.4559E-01	1.4210E-01	4.8556E+00	8.1153E-01	1.8202E+00	1.7490E-03	6.6084E-02	6.4349E-02
5	4854E-03	1.9767E-01	1.4130E-01	5.1823E+00	8.3714E-01	1.9227E+00	1.6927E-03	7.0531E-02	5.9963E-02
2	4908E-01	1.4480E-01	1.4480E-01	5.4444E+00	8.6487E-01	2.0410E+00	1.7924E-03	7.6820E-02	5.7048E-02
3	0018E-01	3.0018E-01	1.4030E-01	5.7577E+00	8.7617E-01	2.0935E+00	1.5927E-03	7.8361E-02	5.3429E-02
9	7670E-03	3.5196E-01	1.3830E-01	6.1206E+00	8.9429E-01	2.1836E+00	1.5057E-03	8.3300E-02	4.9875E-02
4	0400E-01	4.0400E-01	1.3710E-01	6.4577E+00	9.0287E-01	2.2598E+00	1.4540E-03	8.7888E-02	4.8042E-02
1	2665E-02	5.5640E-01	1.3420E-01	6.6117E+00	9.2109E-01	2.3279E+00	1.3477E-03	8.9985E-02	4.4324E-02
1	4110E-02	5.0847E-01	1.3560E-01	7.0834E+00	9.3087E-01	2.3858E+00	1.3449E-03	9.6404E-02	4.3258E-02
5	6036E-01	5.6036E-01	1.3290E-01	7.0369E+00	9.3793E-01	2.4307E+00	1.2712E-03	9.5772E-02	4.1276E-02
6	1359E-01	6.1359E-01	1.2340E-01	6.8699E+00	9.4979E-01	2.5075E+00	1.0435E-03	9.3498E-02	3.6629E-02
1	1467E-02	6.548E-01	1.2030E-01	7.0155E+00	9.6615E-01	2.6140E+00	9.6761E-04	9.5480E-02	3.3568E-02
1	9887E-02	7.1665E-01	1.1570E-01	7.0837E+00	9.7613E-01	2.6861E+00	8.7098E-04	9.6409E-02	3.0981E-02
2	1337E-02	7.6890E-01	1.0430E-01	6.6632E+00	9.8274E-01	2.7382E+00	6.9258E-04	9.0686E-02	2.7118E-02
8	2115E-01	8.2115E-01	9.0290E-02	5.9260E+00	9.8745E-01	2.7788E+00	5.1024E-04	8.0653E-02	2.2947E-02
2	4237E-02	8.7341E-01	7.4720E-02	5.110E+00	9.9078E-01	2.8112E+00	3.4444E-04	6.9560E-02	1.8650E-02
2	5687E-02	9.2566E-01	5.9890E-02	4.1355E+00	9.9343E-01	2.8386E+00	2.1864E-04	5.6284E-02	1.4723E-02
2	7127E-02	9.7755E-01	5.2580E-02	3.6722E+00	9.9501E-01	2.8529E+00	1.6760E-04	4.9979E-02	1.2825E-02
2	8557E-02	1.0291E+00	3.6090E-02	2.5635E+00	9.9608E-01	2.8613E+00	7.8752E-05	3.4890E-02	8.7623E-03
3	0017E-02	1.0817E+00	2.6040E-02	1.8553E+00	9.9672E-01	2.8653E+00	4.0984E-05	2.5251E-02	6.3078E-03
3	1497E-02	1.1350E+00	1.9230E-02	1.3707E+00	9.9592E-01	2.8603E+00	2.2411E-05	1.8655E-02	4.6715E-03
1	1869E+00	1.1869E+00	1.6890E-02	1.2094E+00	9.9683E-01	2.8669E+00	1.7258E-05	1.6460E-02	4.0883E-03
3	2937E-02	1.2395E+00	1.5280E-02	1.0941E+00	9.9741E-01	2.8708E+00	1.4121E-05	1.4891E-02	3.6905E-03
3	3497E-02	1.2921E+00	1.3300E-02	9.568E-01	9.9685E-01	2.8644E+00	1.0726E-05	1.3023E-02	3.2200E-03
3	7307E-02	1.3444E+00	1.3130E-02	9.4950E-01	9.9752E-01	2.8717E+00	1.0439E-05	1.2923E-02	3.1697E-03
3	8767E-02	1.3970E+00	1.2440E-02	9.0499E-01	9.9872E-01	2.8811E+00	9.3460E-06	1.2317E-02	2.9874E-03
4	0257E-02	1.4507E+00	1.3370E-02	9.7658E-01	9.9947E-01	2.8870E+00	1.0778E-05	1.3291E-02	3.2007E-03
1	5022E+00	1.5022E+00	1.2800E-02	9.7693E-01	9.9953E-01	2.8875E+00	9.5884E-06	1.2751E-02	3.0634E-03
4	1687E-02	1.5022E+00	1.2800E-02	9.7693E-01	9.9953E-01	2.8875E+00	9.5884E-06	1.2751E-02	3.0634E-03
4	3167E-02	1.5536E+00	1.3570E-02	9.9791E-01	1.0003E+00	2.8931E+00	1.1098E-05	1.3581E-02	3.2378E-03

HOT WIRE ANEMOMETER MEASUREMENTS (NORMAL WIRE)

X=469.9 mm UT= 2.1899E+01 RHOW= 3.0226E-01 TW= 2.5906E+02 D= 2.8150E-02 Uinf=5.6400E+02

Y (M)	Y/D	(RHO U)' RHO U	(RHO U)' RHOWUT	U Uinf	N	R-U'2 R-U+2	<RHOU>/RHOWE	<U>/ULOC
2.7800E-03	9.8757E-02	1.3970E-01	4.5798E+00	7.8751E-01	1.7315E+00	1.7348E-03	6.3288E-02	6.6927E-02
4.2320E-03	1.5034E-01	1.4240E-01	5.0061E+00	8.2117E-01	1.8579E+00	1.7668E-03	6.9178E-02	6.2962E-02
5.6980E-03	2.0242E-01	1.4170E-01	5.3219E+00	8.4451E-01	1.9536E+00	1.7123E-03	7.3542E-02	5.8973E-02
7.1142E-03	2.5273E-01	1.3980E-01	5.4552E+00	8.6108E-01	2.0266E+00	1.5440E-03	7.5385E-02	5.3985E-02
8.5550E-03	3.0391E-01	1.3440E-01	5.7259E+00	8.8012E-01	2.1149E+00	1.4739E-03	7.9125E-02	5.0570E-02
9.9960E-03	3.5510E-01	1.3400E-01	5.9963E+00	9.0076E-01	2.2160E+00	1.4197E-03	8.2862E-02	4.7372E-02
1.1455E-02	4.0693E-01	1.3370E-01	6.3060E+00	9.1272E-01	2.2810E+00	1.3823E-03	8.7142E-02	4.5429E-02
1.2849E-02	4.5645E-01	1.3510E-01	6.7027E+00	9.2275E-01	2.3387E+00	1.3822E-03	9.2624E-02	4.4332E-02
1.4223E-02	5.0526E-01	1.2900E-01	6.7684E+00	9.3671E-01	2.4208E+00	1.2226E-03	9.3532E-02	4.0303E-02
1.5671E-02	5.5670E-01	1.2560E-01	6.8215E+00	9.4635E-01	2.4807E+00	1.1336E-03	9.4266E-02	3.7875E-02
1.7078E-02	6.0668E-01	1.2400E-01	6.9632E+00	9.5325E-01	2.5277E+00	1.0846E-03	9.6223E-02	3.6375E-02
1.8528E-02	6.5819E-01	1.1660E-01	6.8330E+00	9.6045E-01	2.5789E+00	9.3949E-04	9.4424E-02	3.3201E-02
1.9668E-02	6.9869E-01	1.1120E-01	6.7417E+00	9.6714E-01	2.6274E+00	8.3811E-04	9.3162E-02	3.0791E-02
2.1128E-02	7.5055E-01	1.0610E-01	6.5783E+00	9.7826E-01	2.7072E+00	7.3945E-04	9.0905E-02	2.8072E-02
2.1978E-02	7.8146E-01	1.0110E-01	6.4699E+00	9.7983E-01	2.7226E+00	6.6721E-04	8.9407E-02	2.6517E-02
2.3308E-02	8.2799E-01	8.9120E-02	5.8541E+00	9.8388E-01	2.7984E+00	5.1070E-04	8.0896E-02	2.2910E-02
2.4768E-02	8.7986E-01	7.8080E-02	5.2256E+00	9.8698E-01	2.7883E+00	3.8701E-04	7.2212E-02	1.9739E-02
2.6218E-02	9.3137E-01	5.6780E-02	3.8593E+00	9.9003E-01	2.8137E+00	2.0231E-04	5.3331E-02	1.4134E-02
2.7688E-02	9.8359E-01	5.1190E-02	3.5118E+00	9.9273E-01	2.8370E+00	1.6324E-04	4.8529E-02	1.2594E-02
3.0588E-02	1.0344E+00	3.7170E-02	2.5741E+00	9.9431E-01	2.8489E+00	8.5731E-05	3.5571E-02	9.0864E-03
3.2058E-02	1.0866E+00	2.8060E-02	1.9636E+00	9.9752E-01	2.8730E+00	4.8448E-05	2.7134E-02	6.7691E-03
3.3498E-02	1.1388E+00	2.3390E-02	1.6629E+00	9.9752E-01	2.8730E+00	3.3705E-05	2.2980E-02	5.6425E-03
3.4978E-02	1.1900E+00	1.8810E-02	1.3464E+00	9.9752E-01	2.8736E+00	2.1792E-05	1.8606E-02	4.5313E-03
3.6458E-02	1.2426E+00	1.8110E-02	1.3026E+00	9.9941E-01	2.8879E+00	2.0123E-05	1.8000E-02	4.3333E-03
3.7898E-02	1.2951E+00	1.6460E-02	1.1886E+00	1.0001E+00	2.8936E+00	1.6603E-05	1.6424E-02	3.9268E-03
3.9378E-02	1.3467E+00	1.6530E-02	1.1959E+00	9.9930E-01	2.8971E+00	1.6812E-05	1.6527E-02	3.9570E-03
	1.3987E+00	1.5130E-02	1.0988E+00	1.0001E+00	2.8937E+00	1.4058E-05	1.5104E-02	3.6092E-03

INUT WIRE ANEMOMETER MEASUREMENTS (NORMAL WIRE)

X=546 1 mm UT= 2 2149E+01 RHOM= 2 9806E-01 TW= 2 6983E+02 D= 2 9500E-02 Uinf=5 6200E+02

Y (M)	Y/D	(RHO U)' RHO U	(RHO U)' RHOM*UT	U Uinf	M	R-U'2 R-Ur2	<RHOU>/RHOU	<U>/ULDC
2 7800E-03	9 4237E-02	1 4630E-01	4 3457E+00	7 8946E-01	1 7359E+00	1 0805E-03	6 2477E-02	6 9896E-02
4 0403E-03	1 3696E-01	1 3990E-01	4 4226E+00	8 1388E-01	1 8271E+00	1 6962E-03	6 3583E-02	6 3074E-02
5 4799E-03	1 8576E-01	1 4160E-01	4 7402E+00	8 4186E-01	1 9390E+00	1 6973E-03	6 8148E-02	5 9479E-02
6 9089E-03	2 3420E-01	1 3620E-01	4 0854E+00	8 5975E-01	2 0174E+00	1 5388E-03	7 0236E-02	5 4457E-02
8 3239E-03	2 8217E-01	1 3590E-01	5 1237E+00	8 7331E-01	2 0809E+00	1 5039E-03	7 3662E-02	5 2226E-02
9 7659E-03	3 3105E-01	1 3890E-01	5 5082E+00	8 8711E-01	2 1479E+00	1 5394E-03	7 9190E-02	5 1205E-02
1 1213E-02	3 8010E-01	1 4020E-01	5 8783E+00	8 9911E-01	2 2089E+00	1 5377E-03	8 4511E-02	4 9781E-02
1 2677E-02	4 2973E-01	1 3510E-01	5 9162E+00	9 1794E-01	2 3088E+00	1 3796E-03	8 5055E-02	4 5139E-02
1 4118E-02	4 7857E-01	1 3520E-01	6 2994E+00	9 2746E-01	2 3644E+00	1 3538E-03	9 0565E-02	4 3685E-02
1 5568E-02	5 2773E-01	1 3110E-01	6 2653E+00	9 4081E-01	2 4442E+00	1 2356E-03	9 0074E-02	4 0394E-02
1 7038E-02	5 7756E-01	1 2970E-01	6 5972E+00	9 5343E-01	2 5242E+00	1 1728E-03	9 4846E-02	3 8126E-02
1 8478E-02	6 2637E-01	1 2610E-01	6 7369E+00	9 6374E-01	2 5947E+00	1 0779E-03	9 6854E-02	3 5579E-02
1 9908E-02	6 7484E-01	1 2120E-01	6 8000E+00	9 7014E-01	2 6418E+00	9 7712E-04	9 7762E-02	3 3284E-02
2 1358E-02	7 2400E-01	1 1680E-01	6 7301E+00	9 7973E-01	2 7138E+00	8 8086E-04	9 6757E-02	3 0789E-02
2 2818E-02	7 7349E-01	1 0820E-01	6 5640E+00	9 8913E-01	2 7868E+00	7 3345E-04	9 4369E-02	2 7376E-02
2 4258E-02	8 2230E-01	9 4560E-02	5 8554E+00	9 8632E-01	2 7748E+00	5 6244E-04	8 4181E-02	2 4085E-02
2 5718E-02	8 7179E-01	8 3770E-02	5 2786E+00	9 9001E-01	2 8090E+00	4 3487E-04	7 5889E-02	2 0935E-02
2 7168E-02	9 2095E-01	6 8950E-02	4 4513E+00	9 9113E-01	2 8196E+00	2 9352E-04	6 3995E-02	1 7130E-02
2 8598E-02	9 6942E-01	5 7350E-02	3 7534E+00	9 9463E-01	2 8451E+00	2 0126E-04	5 3990E-02	1 4049E-02
3 0058E-02	1 0189E+00	4 4750E-02	2 9568E+00	9 9682E-01	2 8620E+00	1 2180E-04	4 2509E-02	1 0861E-02
3 1528E-02	1 0687E+00	3 4490E-02	2 2997E+00	9 9784E-01	2 8700E+00	7 2171E-05	3 3063E-02	8 3340E-03
3 2968E-02	1 1176E+00	2 5290E-02	1 6917E+00	9 9881E-01	2 8772E+00	3 8754E-05	2 4321E-02	6 0848E-03
3 4428E-02	1 1670E+00	2 3170E-02	1 5607E+00	1 0002E+00	2 8870E+00	3 2433E-05	2 2438E-02	5 5467E-03
3 5898E-02	1 2169E+00	1 7850E-02	1 2070E+00	1 0002E+00	2 8870E+00	1 9264E-05	1 7352E-02	4 2732E-03
3 7348E-02	1 2660E+00	1 3470E-02	9 1449E-01	1 0002E+00	2 8870E+00	1 0983E-05	1 3147E-02	3 2246E-03
3 8808E-02	1 3155E+00	1 3970E-02	9 5287E-01	1 0008E+00	2 8916E+00	1 1805E-05	1 3699E-02	3 3359E-03
4 0288E-02	1 3657E+00	1 4390E-02	9 8523E-01	1 0020E+00	2 9015E+00	1 2485E-05	1 4164E-02	3 4176E-03
4 1728E-02	1 4145E+00	1 4300E-02	9 9466E-01	1 0027E+00	2 9068E+00	1 2317E-05	1 4300E-02	3 3866E-03
4 3208E-02	1 4647E+00	1 3960E-02	9 7101E-01	1 0044E+00	2 9206E+00	1 1683E-05	1 3960E-02	3 2813E-03

HOT WIRE ANEMOMETER MEASUREMENTS (NORMAL WIRE)

X=622.3 mm UT= 2.1308E+01 RH04= 2.9963E-01 TM= 2.6718E+02 D= 3.0210E-02 Uinf=5.6350E+02

Y (M)	Y/D	(RHO U)' RHO U	(RHO U)' RHO*UT	U Uinf	M	R-U'2 R-U+2	<RHOU>/RHOUE	<U>/ULOC
2.7800E-03	9.2023E-02	1.4710E-01	4.5063E+00	7.8931E-01	1.7500E+00	1.8931E-03	6.2684E-02	6.9649E-02
3.9584E-03	1.3104E-01	1.4420E-01	4.7133E+00	8.2175E-01	1.8717E+00	1.7831E-03	6.5563E-02	6.3202E-02
5.4090E-03	1.7909E-01	1.3460E-01	4.7684E+00	8.3744E-01	1.9380E+00	1.5296E-03	6.6332E-02	5.6573E-02
6.8360E-03	2.2628E-01	1.3680E-01	5.1313E+00	8.5617E-01	2.0196E+00	1.5473E-03	7.1380E-02	5.4624E-02
8.2520E-03	2.7315E-01	1.4160E-01	5.6374E+00	8.7685E-01	2.1150E+00	1.6121E-03	7.8420E-02	5.3274E-02
9.6900E-03	3.2075E-01	1.4100E-01	5.9403E+00	8.8627E-01	2.1637E+00	1.5732E-03	8.2634E-02	5.1475E-02
1.1145E-02	3.6892E-01	1.3790E-01	6.1229E+00	9.0593E-01	2.2649E+00	1.4544E-03	8.5174E-02	4.7319E-02
1.2607E-02	4.1731E-01	1.3600E-01	6.4304E+00	9.1440E-01	2.3131E+00	1.3905E-03	8.7452E-02	4.5321E-02
1.4048E-02	4.6501E-01	1.3880E-01	6.8867E+00	9.2679E-01	2.3845E+00	1.4109E-03	9.5799E-02	4.4312E-02
1.5488E-02	5.1268E-01	1.3390E-01	6.9204E+00	9.3640E-01	2.4447E+00	1.2832E-03	9.6268E-02	4.1244E-02
1.6968E-02	5.6167E-01	1.2870E-01	6.7928E+00	9.5052E-01	2.5344E+00	1.1449E-03	9.4492E-02	3.7604E-02
1.8408E-02	6.0933E-01	1.2550E-01	7.0661E+00	9.5970E-01	2.5977E+00	1.0618E-03	9.8295E-02	3.5349E-02
1.9838E-02	6.5667E-01	1.2180E-01	7.0867E+00	9.7038E-01	2.6743E+00	9.6945E-04	9.8581E-02	3.2833E-02
2.1288E-02	7.0467E-01	1.1660E-01	6.9997E+00	9.7313E-01	2.7010E+00	8.7806E-04	9.7370E-02	3.0959E-02
2.2748E-02	7.5300E-01	1.0570E-01	6.6300E+00	9.8156E-01	2.7662E+00	7.0250E-04	9.2228E-02	2.7054E-02
2.4198E-02	8.0099E-01	9.5290E-02	6.1338E+00	9.8395E-01	2.7919E+00	5.6423E-04	8.5325E-02	2.4042E-02
2.5648E-02	8.4899E-01	8.5960E-02	5.6880E+00	9.9028E-01	2.8459E+00	4.4882E-04	7.9124E-02	2.1049E-02
2.7098E-02	8.9699E-01	7.5830E-02	5.1163E+00	9.9329E-01	2.8719E+00	3.4564E-04	7.1171E-02	1.8305E-02
2.8528E-02	9.4432E-01	6.2060E-02	4.2941E+00	9.9542E-01	2.8886E+00	2.3021E-04	5.9734E-02	1.4844E-02
2.9988E-02	9.9265E-01	4.9190E-02	3.4768E+00	9.9887E-01	2.9149E+00	1.4325E-04	4.8365E-02	1.1599E-02
3.1468E-02	1.0416E+00	3.6950E-02	2.6244E+00	1.0003E+00	2.9257E+00	8.0571E-05	3.6507E-02	8.6609E-03
3.2908E-02	1.0897E+00	2.8060E-02	1.9987E+00	1.0007E+00	2.9290E+00	4.6444E-05	2.7803E-02	6.5654E-03
3.4358E-02	1.1373E+00	2.2030E-02	1.5733E+00	1.0002E+00	2.9291E+00	2.8659E-05	2.1884E-02	5.1541E-03
3.5828E-02	1.1860E+00	1.7220E-02	1.2365E+00	1.0021E+00	2.9399E+00	1.7450E-05	1.7201E-02	4.0051E-03
3.7268E-02	1.2336E+00	1.4870E-02	1.0613E+00	1.0015E+00	2.9356E+00	1.4763E-05	1.4763E-02	3.4464E-03
3.8738E-02	1.2823E+00	1.3160E-02	9.3408E-01	1.0002E+00	2.9248E+00	1.0273E-05	1.2994E-02	3.0862E-03
4.0218E-02	1.3313E+00	1.2440E-02	8.8103E-01	9.9888E-01	2.9145E+00	9.2247E-06	1.2554E-02	2.7136E-03
4.1658E-02	1.3789E+00	1.1740E-02	1.1024E+00	9.9820E-01	2.9024E+00	1.4811E-05	1.2034E-02	2.3774E-03
4.3138E-02	1.4275E+00	1.1290E-02	8.9866E-01	9.9756E-01	2.9041E+00	9.9721E-06	1.1593E-02	2.0520E-03

HOT WIRE ANEMOMETER MEASUREMENTS (NORMAL WIRE)

NOTE: The mean flow data for this station is the same as for X= 622.3 mm.

X=660.4 mm U1= 2.1269E+01 RHOW= 3.0076E-01 TW= 2.6619E+02 D= 3.1000E-02 Uinf=5.6350E+02

Y (M)	Y/D	(RHO U)' RHO U	(RHO U)' RHOWUT	U Uinf	M	R-U' ² R-U ²	<RHOU>/RHOWE	<U>/ULOC
2.7800E-03	8.9677E-02	1.4710E-01	4.5371E+00	7.8931E-01	1.7500E+00	1.9004E-03	6.3507E-02	6.9649E-02
3.9853E-03	1.2856E-01	1.4400E-01	4.7363E+00	8.2229E-01	1.8737E+00	1.7843E-03	6.6297E-02	6.3032E-02
5.4350E-03	1.7532E-01	1.3840E-01	4.8507E+00	8.3743E-01	1.9380E+00	1.6228E-03	6.7898E-02	5.8170E-02
6.8650E-03	2.2145E-01	1.4360E-01	5.3360E+00	8.5668E-01	2.0219E+00	1.7097E-03	7.4691E-02	5.7256E-02
8.2850E-03	2.6726E-01	1.4210E-01	5.5735E+00	8.7698E-01	2.1158E+00	1.6293E-03	7.8015E-02	5.3438E-02
9.7230E-03	3.1365E-01	1.4030E-01	5.8319E+00	8.8666E-01	2.1657E+00	1.5620E-03	8.1632E-02	5.1157E-02
1.1179E-02	3.6061E-01	1.3760E-01	5.9670E+00	9.0614E-01	2.2660E+00	1.4531E-03	8.3524E-02	4.7182E-02
1.2634E-02	4.0755E-01	1.3910E-01	6.4453E+00	9.1453E-01	2.3139E+00	1.4592E-03	9.0217E-02	4.6332E-02
1.4073E-02	4.5397E-01	1.3580E-01	6.5344E+00	9.2704E-01	2.3860E+00	1.3550E-03	9.1464E-02	4.3315E-02
1.5513E-02	5.0042E-01	1.3160E-01	6.6553E+00	9.3641E-01	2.4449E+00	1.2437E-03	9.3157E-02	4.0531E-02
1.6993E-02	5.4816E-01	1.2660E-01	6.7329E+00	9.5071E-01	2.5357E+00	1.1111E-03	9.4244E-02	3.6965E-02
1.8443E-02	5.9494E-01	1.2320E-01	6.8063E+00	9.5985E-01	2.5988E+00	1.0259E-03	9.5271E-02	3.4679E-02
1.9873E-02	6.4106E-01	1.2240E-01	7.0185E+00	9.7039E-01	2.6746E+00	9.8228E-04	9.8241E-02	3.2990E-02
2.1323E-02	6.8784E-01	1.1770E-01	6.9864E+00	9.7329E-01	2.7023E+00	8.9702E-04	9.7791E-02	3.1229E-02
2.2773E-02	7.3461E-01	1.0980E-01	6.7732E+00	9.8162E-01	2.7668E+00	7.6021E-04	9.4808E-02	2.8094E-02
2.4213E-02	7.8106E-01	1.0350E-01	6.5302E+00	9.8395E-01	2.7920E+00	6.6794E-04	9.1406E-02	2.6112E-02
2.5663E-02	8.2784E-01	8.9480E-02	5.8121E+00	9.9031E-01	2.8462E+00	4.8797E-04	8.1354E-02	2.1906E-02
2.7113E-02	8.7461E-01	7.7440E-02	5.1329E+00	9.9331E-01	2.8720E+00	3.6172E-04	7.1848E-02	1.8691E-02
2.8543E-02	9.2074E-01	6.3360E-02	4.2750E+00	9.9545E-01	2.8888E+00	2.4068E-04	5.9838E-02	1.5153E-02
3.0003E-02	9.6784E-01	5.2800E-02	3.5988E+00	9.9891E-01	2.9151E+00	1.6562E-04	5.0374E-02	1.2448E-02
3.1483E-02	1.0156E+00	4.0740E-02	2.8207E+00	1.0003E+00	2.9259E+00	9.8253E-05	3.9483E-02	9.5480E-03
3.2923E-02	1.0620E+00	3.2590E-02	2.2778E+00	1.0007E+00	2.9290E+00	6.2847E-05	3.1884E-02	7.6253E-03
3.4373E-02	1.1088E+00	2.5270E-02	1.7729E+00	1.0007E+00	2.9292E+00	3.7826E-05	2.4817E-02	5.9118E-03
3.5833E-02	1.1559E+00	1.8010E-02	1.2701E+00	1.0021E+00	2.9398E+00	1.9148E-05	1.7777E-02	4.1892E-03
3.7283E-02	1.2027E+00	1.5490E-02	1.0948E+00	1.0015E+00	2.9355E+00	1.4200E-05	1.5324E-02	3.6116E-03
3.8743E-02	1.2498E+00	1.4630E-02	1.0434E+00	1.0002E+00	2.9247E+00	1.2737E-05	1.4064E-02	3.4310E-03
4.0223E-02	1.2975E+00	1.4060E-02	1.0047E+00	9.9888E-01	2.9145E+00	1.1821E-05	1.4063E-02	3.3157E-03
4.1663E-02	1.3440E+00	1.3910E-02	9.9332E-01	9.9823E-01	2.9094E+00	1.1608E-05	1.3904E-02	3.2895E-03
4.3143E-02	1.3917E+00	1.4030E-02	1.0017E+00	9.9756E-01	2.9041E+00	1.1844E-05	1.4021E-02	3.3274E-03

HOT WIRE ANEMOMETER MEASUREMENTS (NORMAL WIRE)

X=660.4 mm UT= 2.0990E+01 RHOW= 3.0731E-01 TM= 2.6619E+02 D= 3.1000E-02

Y (M)	Y/D	(RHO U)' RHO U	(RHO U)' RHO*UT	U Uinf	H	R-U' ² R-U*2	CRHOU>/RHOU	<U>/ULOC
2.7800E-03	8.9677E-02	1.4710E-01	4.4993E+00	*****	*****	*****	6.3507E-02	*****
3.9833E-03	1.2856E-01	1.4400E-01	4.6969E+00	*****	*****	*****	6.6297E-02	*****
5.4330E-03	1.7532E-01	1.3840E-01	4.8103E+00	*****	*****	*****	6.7898E-02	*****
6.8630E-03	2.2143E-01	1.4360E-01	5.2916E+00	*****	*****	*****	7.4691E-02	*****
8.2830E-03	2.6726E-01	1.4210E-01	5.7834E+00	*****	*****	*****	7.8013E-02	*****
9.7230E-03	3.1363E-01	1.4030E-01	5.9174E+00	*****	*****	*****	8.1632E-02	*****
1.1179E-02	3.6061E-01	1.3760E-01	5.9174E+00	*****	*****	*****	8.3524E-02	*****
1.2634E-02	4.0753E-01	1.3910E-01	6.3916E+00	*****	*****	*****	9.0217E-02	*****
1.4073E-02	4.5397E-01	1.3580E-01	6.4800E+00	*****	*****	*****	9.1464E-02	*****
1.5513E-02	5.0042E-01	1.3160E-01	6.5999E+00	*****	*****	*****	9.3157E-02	*****
1.6993E-02	5.4816E-01	1.2660E-01	6.6769E+00	*****	*****	*****	9.4244E-02	*****
1.8443E-02	5.9494E-01	1.2320E-01	6.7497E+00	*****	*****	*****	9.5271E-02	*****
1.9873E-02	6.4106E-01	1.2240E-01	6.9601E+00	*****	*****	*****	9.8241E-02	*****
2.1323E-02	6.8784E-01	1.1770E-01	6.9282E+00	*****	*****	*****	9.7791E-02	*****
2.2773E-02	7.3461E-01	1.0980E-01	6.7168E+00	*****	*****	*****	9.4808E-02	*****
2.4213E-02	7.8106E-01	1.0350E-01	6.4758E+00	*****	*****	*****	9.1406E-02	*****
2.5663E-02	8.2784E-01	8.9480E-02	5.7637E+00	*****	*****	*****	8.1354E-02	*****
2.7113E-02	8.7461E-01	7.7440E-02	5.0903E+00	*****	*****	*****	7.1848E-02	*****
2.8543E-02	9.2074E-01	6.3360E-02	4.2394E+00	*****	*****	*****	5.9838E-02	*****
3.0003E-02	9.6784E-01	5.2800E-02	3.5688E+00	*****	*****	*****	5.0374E-02	*****
3.1483E-02	1.0136E+00	4.0740E-02	2.7972E+00	*****	*****	*****	3.9483E-02	*****
3.2923E-02	1.0620E+00	3.2590E-02	2.2589E+00	*****	*****	*****	3.1884E-02	*****
3.4373E-02	1.1088E+00	2.5270E-02	1.7587E+00	*****	*****	*****	2.4817E-02	*****
3.5833E-02	1.1599E+00	1.8010E-02	1.2595E+00	*****	*****	*****	1.7777E-02	*****
3.7283E-02	1.2027E+00	1.5490E-02	1.0857E+00	*****	*****	*****	1.5324E-02	*****
3.8743E-02	1.2498E+00	1.4630E-02	1.0347E+00	*****	*****	*****	1.4604E-02	*****
4.0223E-02	1.2974E+00	1.4040E-02	9.9632E-01	*****	*****	*****	1.4043E-02	*****
4.1663E-02	1.3440E+00	1.3910E-02	9.8505E-01	*****	*****	*****	1.3904E-02	*****
4.3143E-02	1.3917E+00	1.4030E-02	9.9337E-01	*****	*****	*****	1.4021E-02	*****

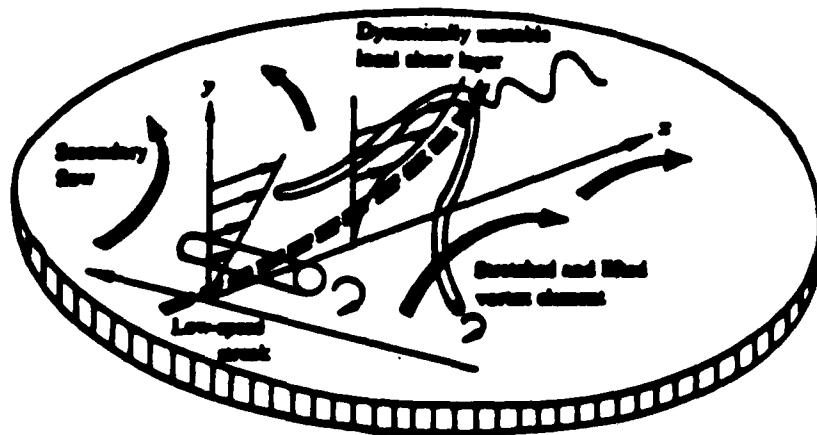


FIGURE 1. The mechanics of streak breakup; adapted from Kline et. al (1967)

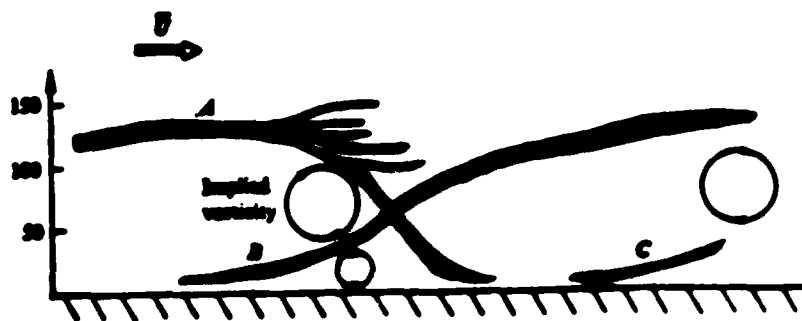


FIGURE 2. Side view of the interactions between bursting flow modules(model interpretation) (Offen and Kline, 1975)

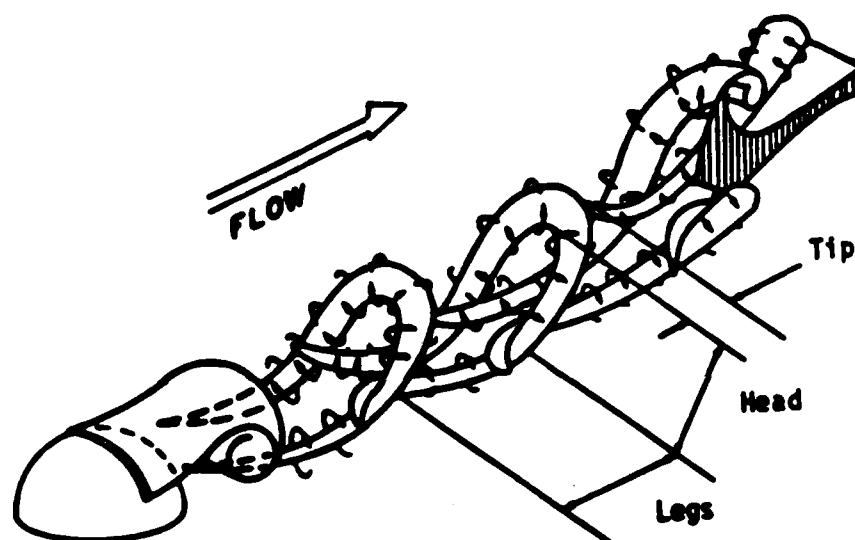


FIGURE 3.

Schematic showing the development and interaction of hairpin vortices created by the three-dimensional separation of the flow over a hemisphere (Acarlar and Smith, 1984)

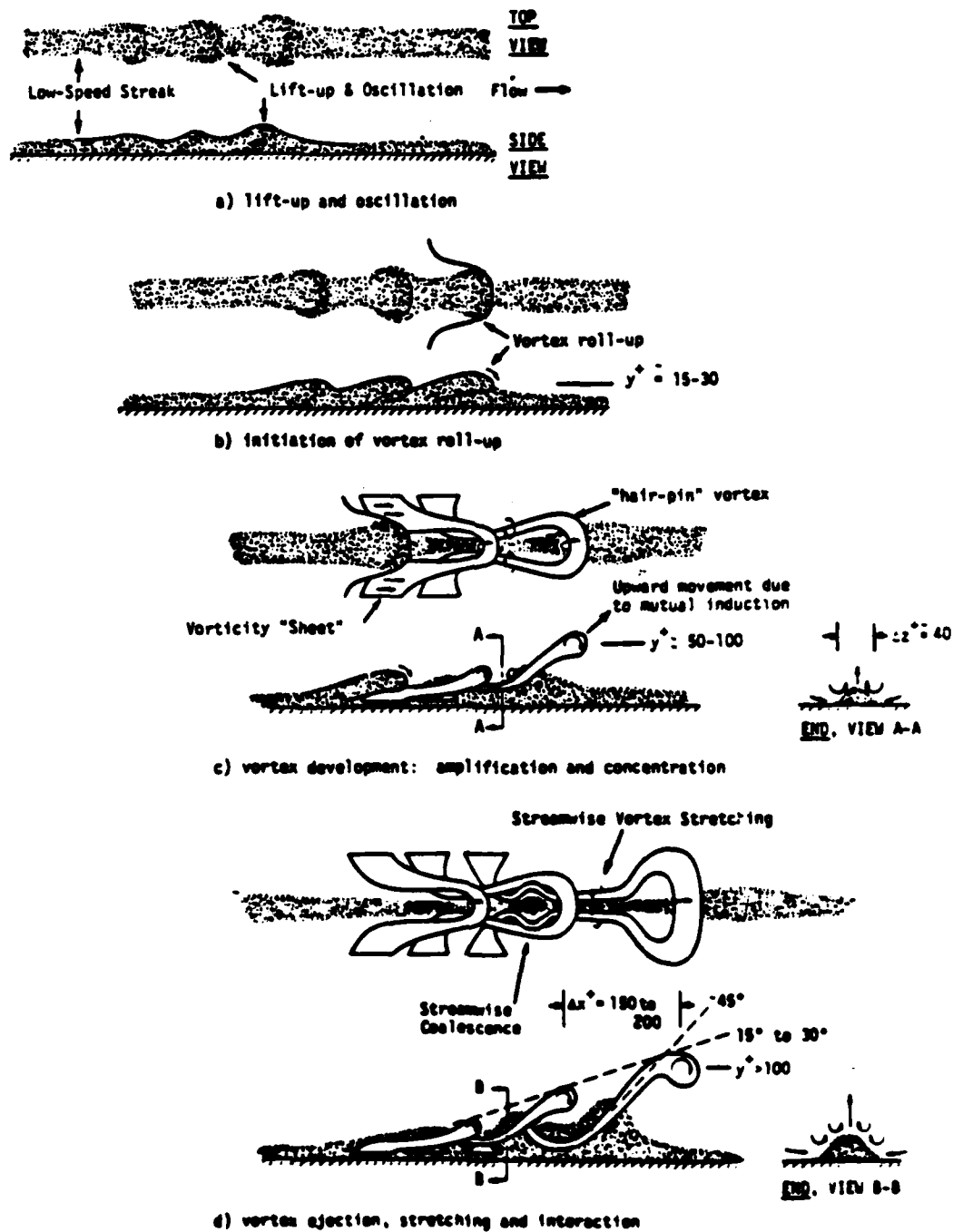


FIGURE 4.

Illustration of the breakdown and formation of hairpin vortices during the bursting process. Low-speed streak regions are indicated by shading (Smith, 1984)

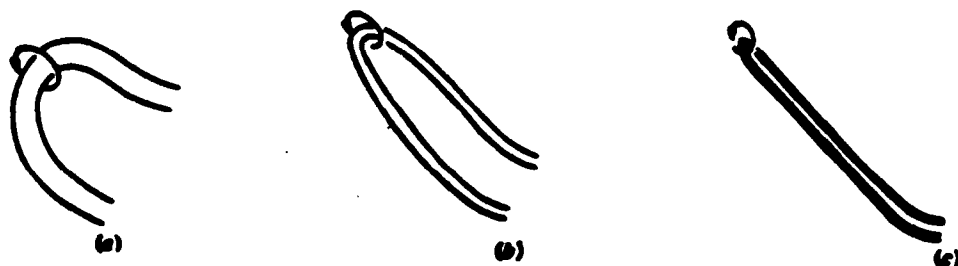


FIGURE 5. Effect of Reynolds number on eddies: (a) very low Re (vortex loops), (b) low-moderate Re (horseshoes), (c) moderate-high Re (hairpins) (Head and Bandyopadhyay, 1981)

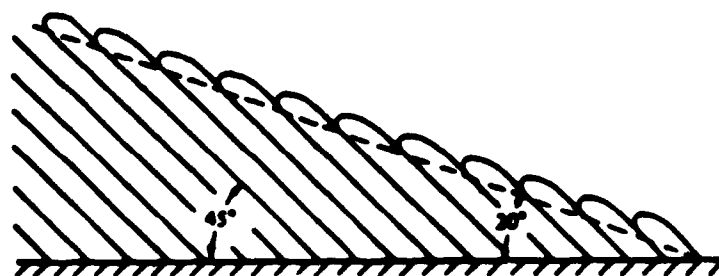


FIGURE 6. 20° interface caused by 45° structures (Head and Bandyopadhyay, 1981)

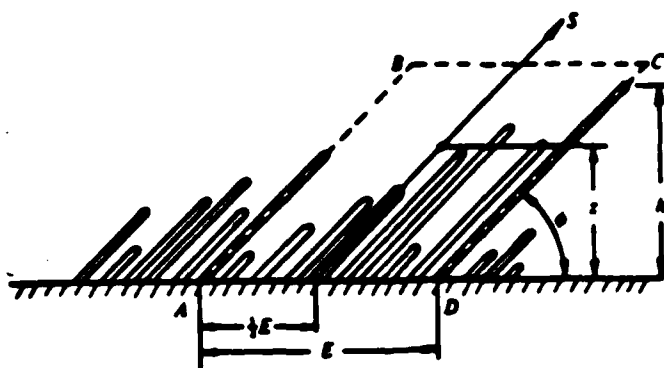


FIGURE 7. Random array of eddies at a constant angle ϕ . The sampling volume for the p.d.f. is ABCD (Perry and Chong, 1982)

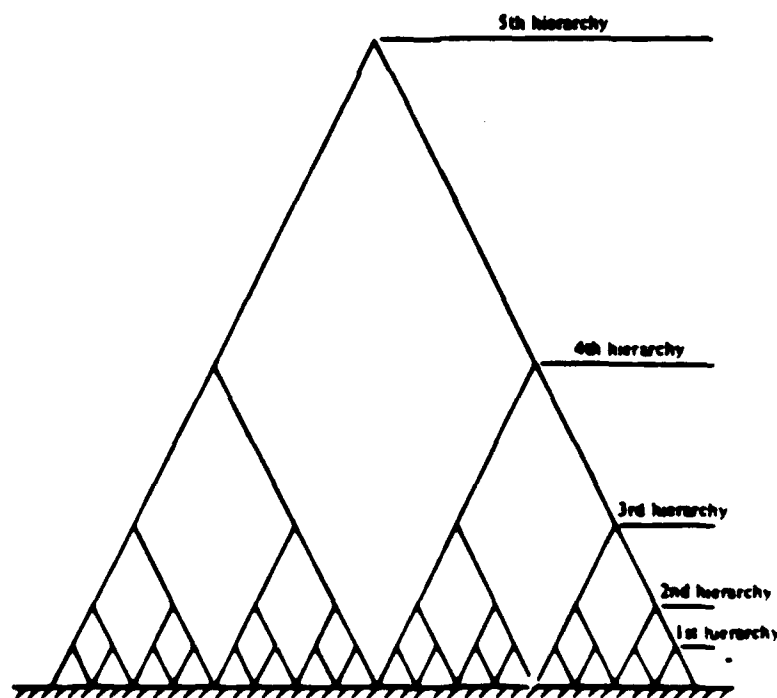


FIGURE 8. Symbolic representation of a discrete system of geometrically similar hierarchies (Perry and Chong, 1982)

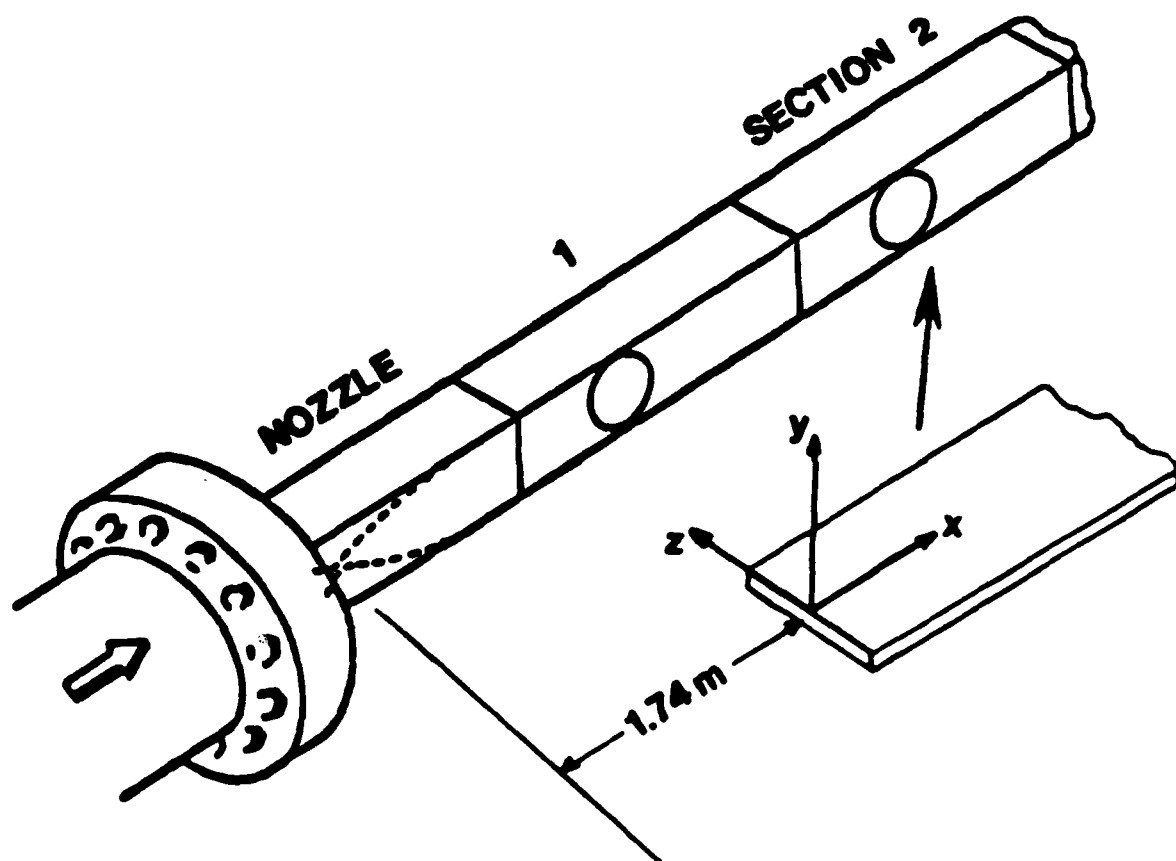


FIGURE 9.

Sketch of the wind tunnel, test surface, and coordinate system

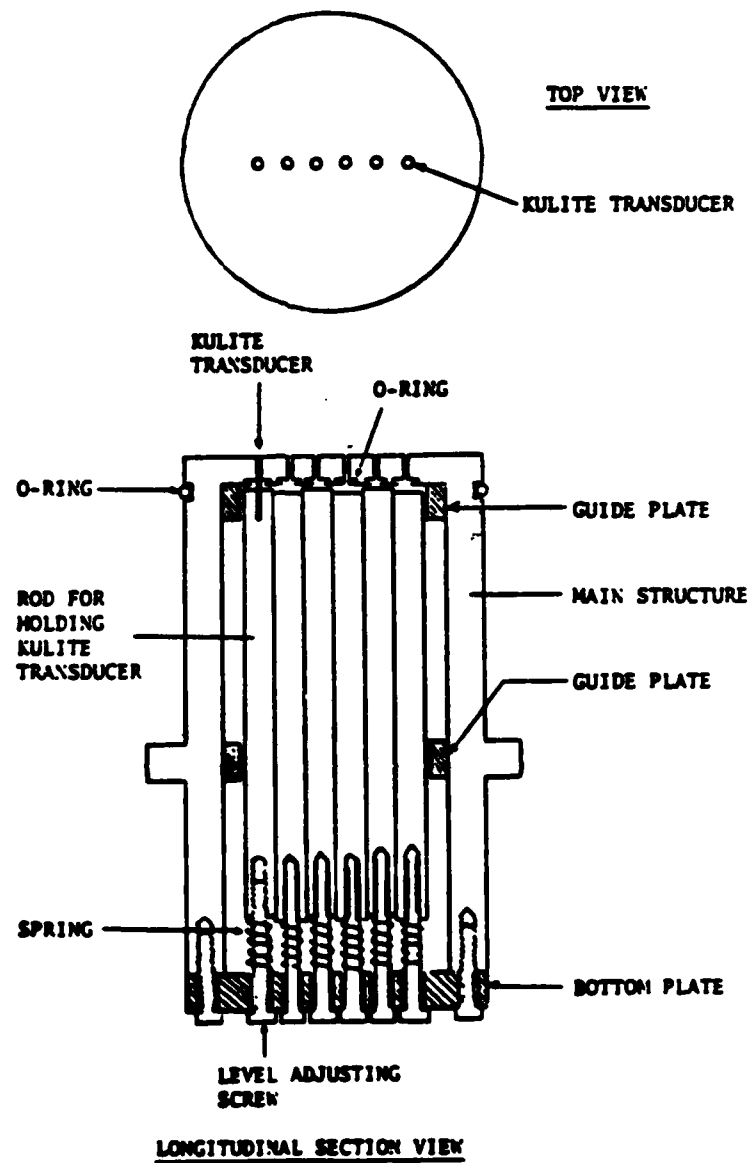


FIGURE 10 a

Sketch of the Kulite pressure transducer plug

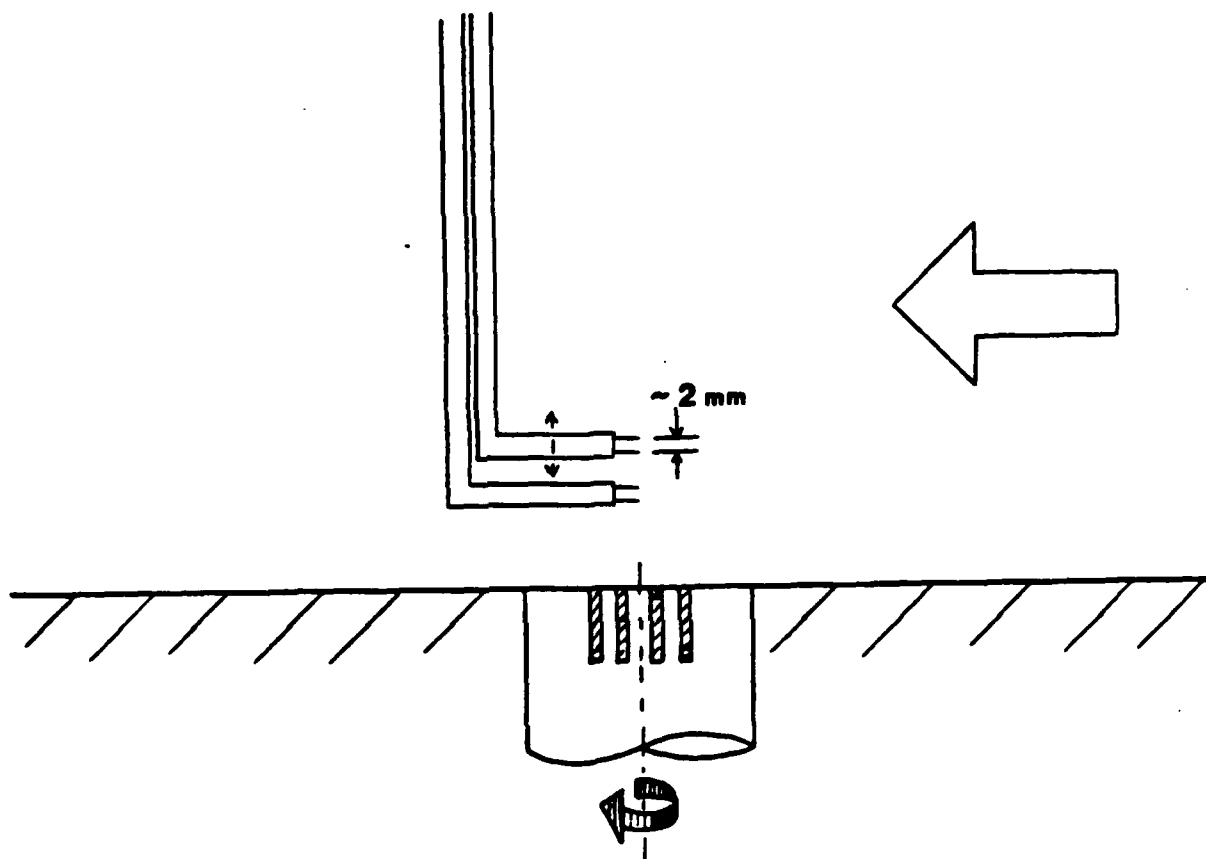


FIGURE 10 b Arrangement of hot wire probes and wall pressure transducers

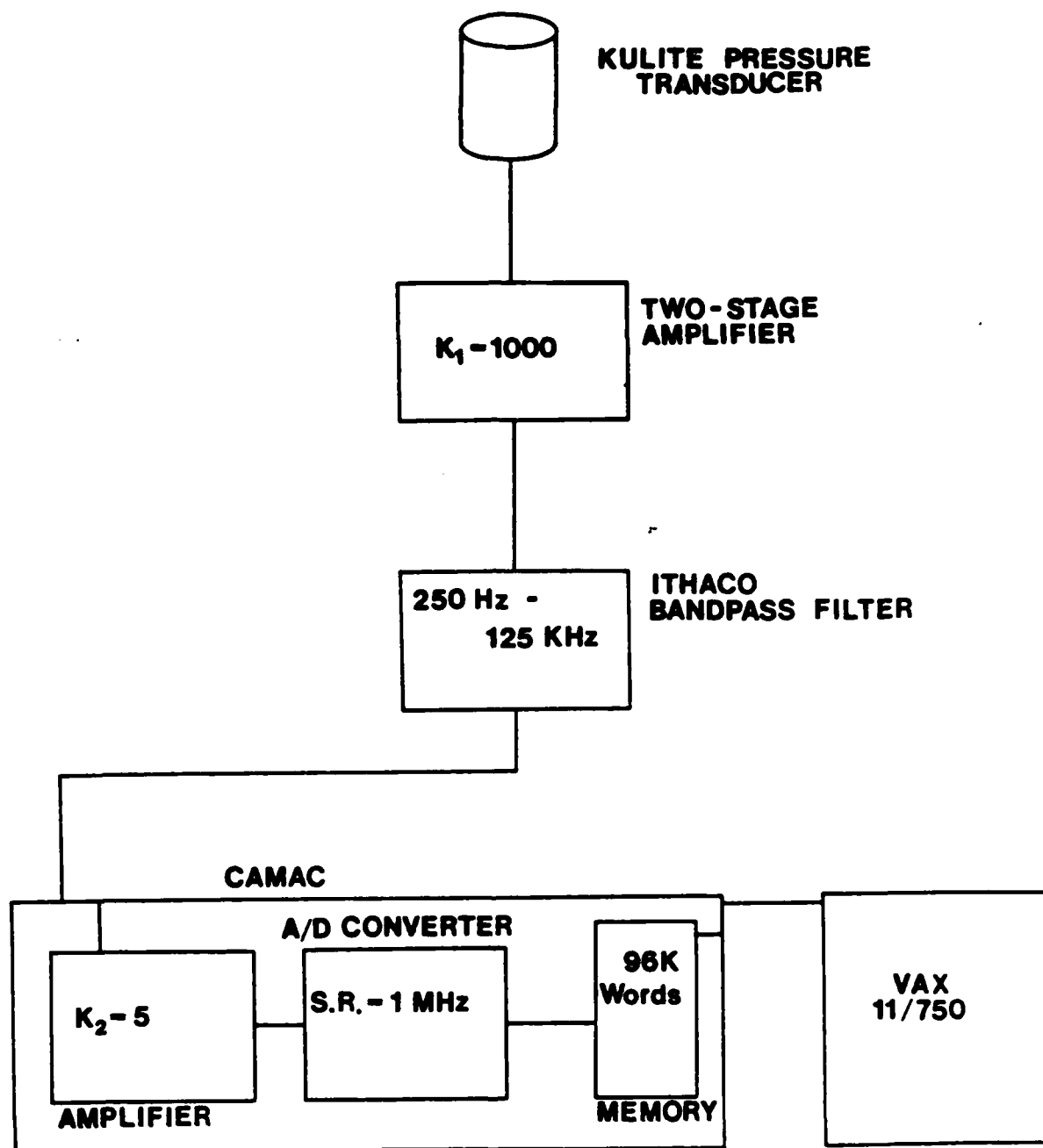


FIGURE 11.

Flowchart of the fluctuating pressure data acquisition system

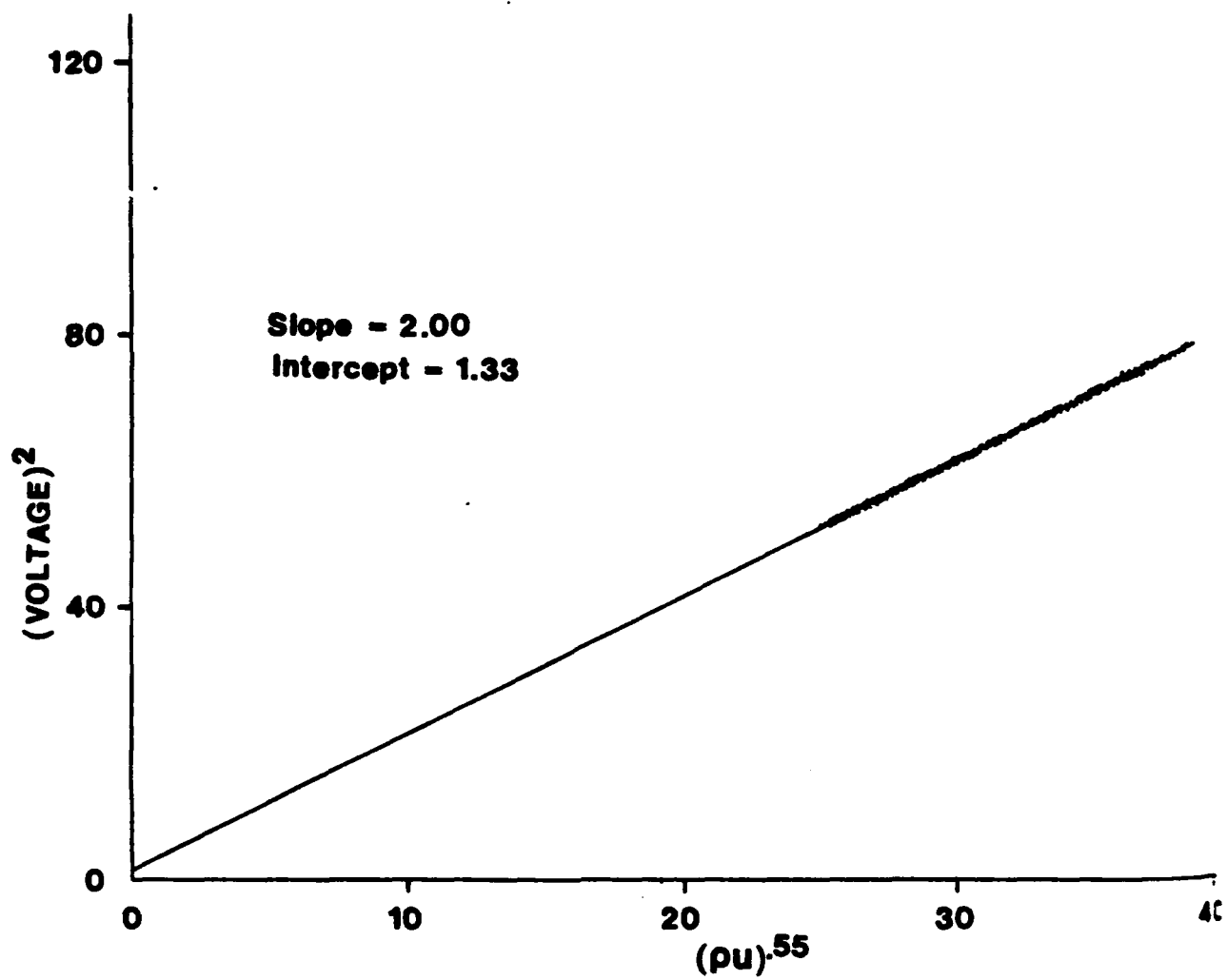


FIGURE 12. Typical normal hot-wire calibration

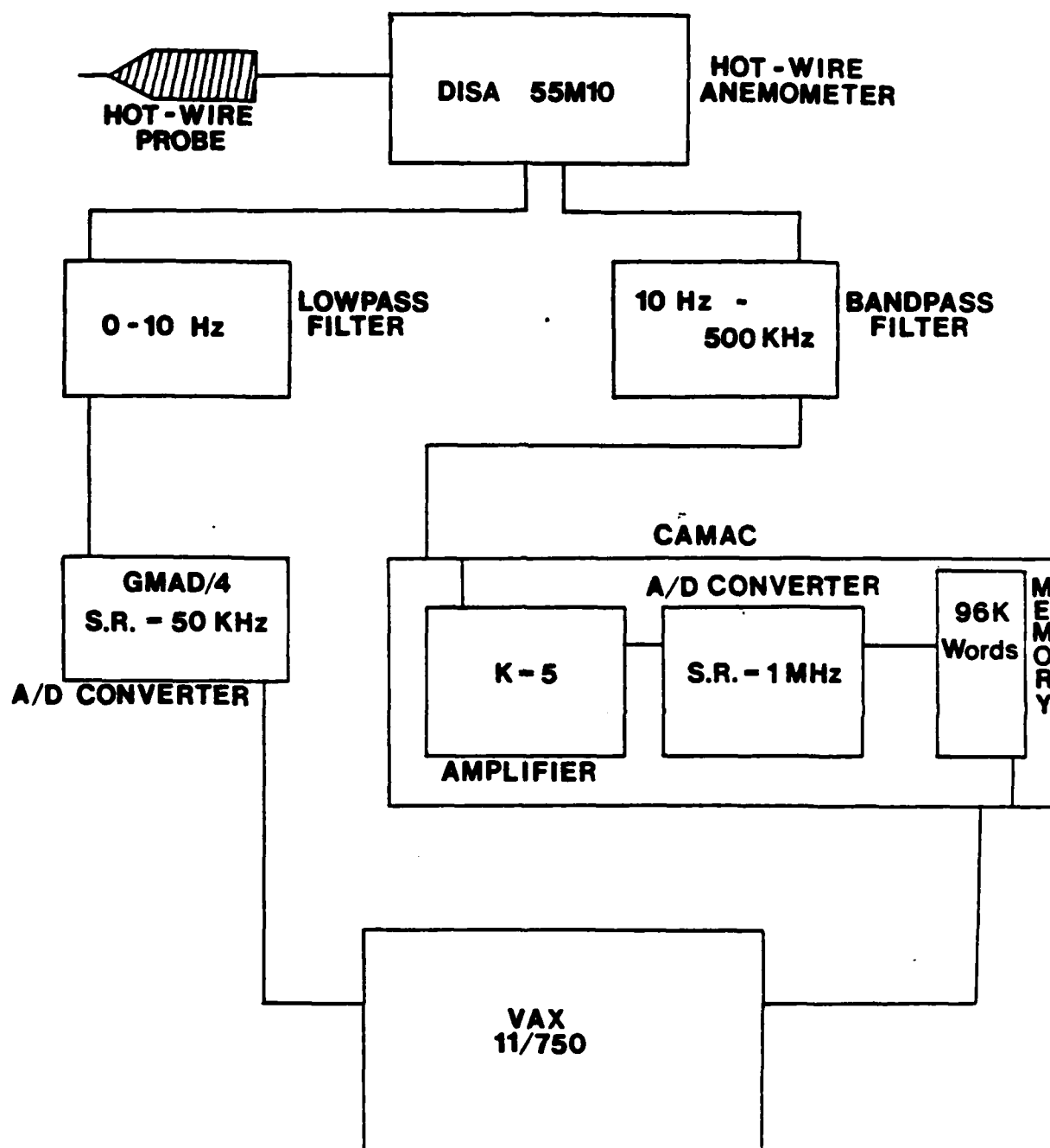


FIGURE 13. Flowchart of the hot-wire data acquisition system

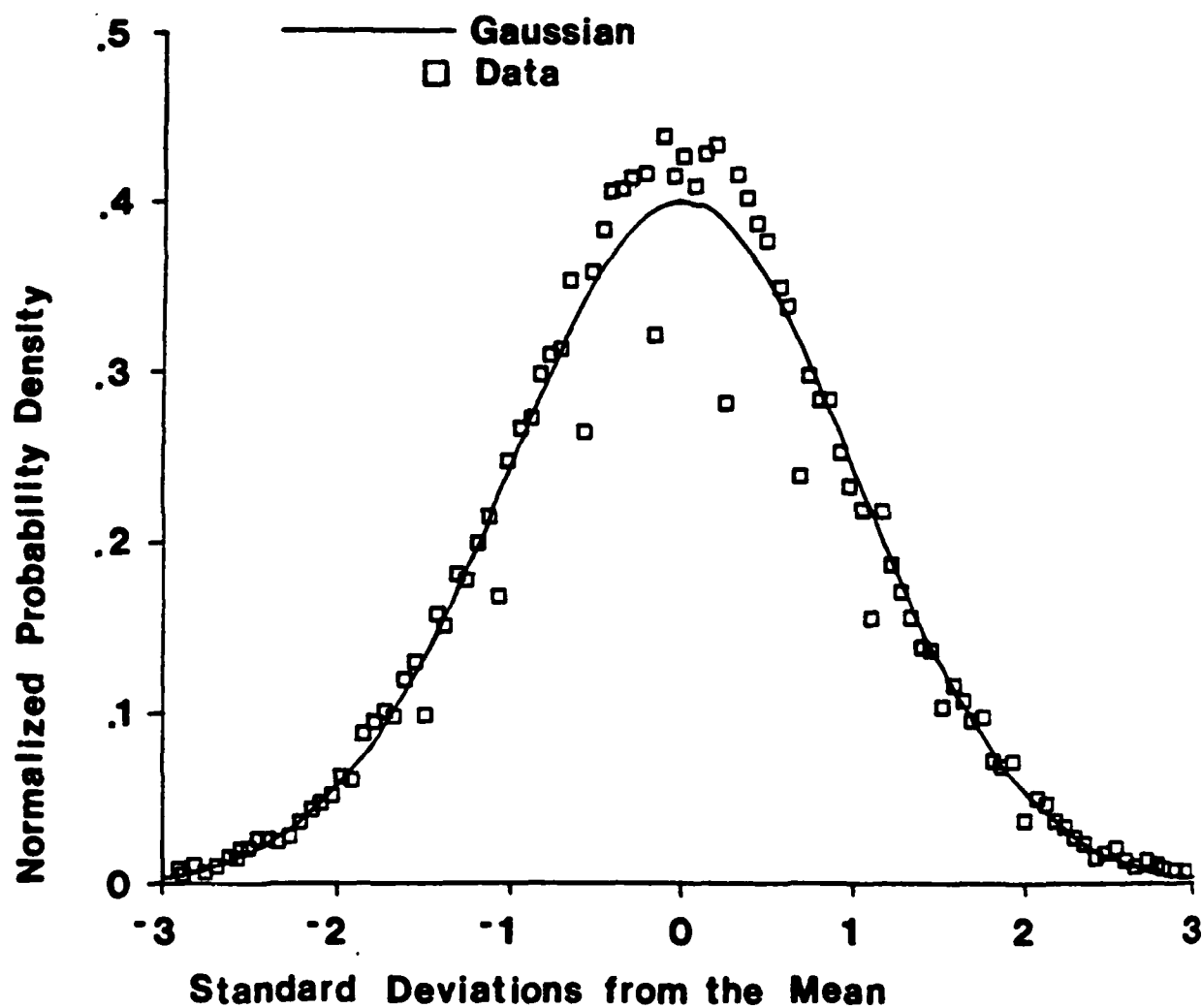


FIGURE 14. Typical wall-pressure probability density function

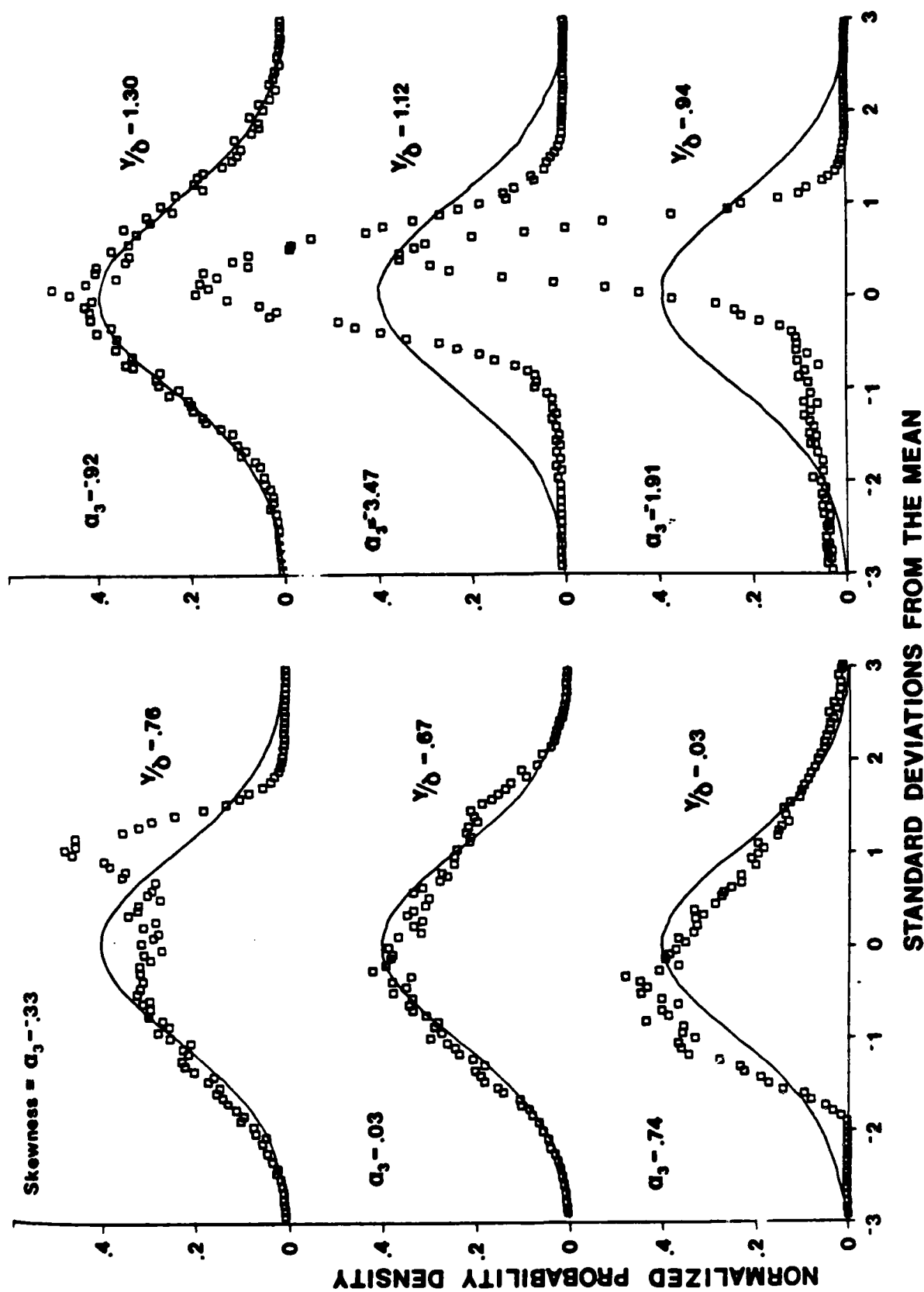


FIGURE 15. The mass-flow probability density function at several points in the boundary layer

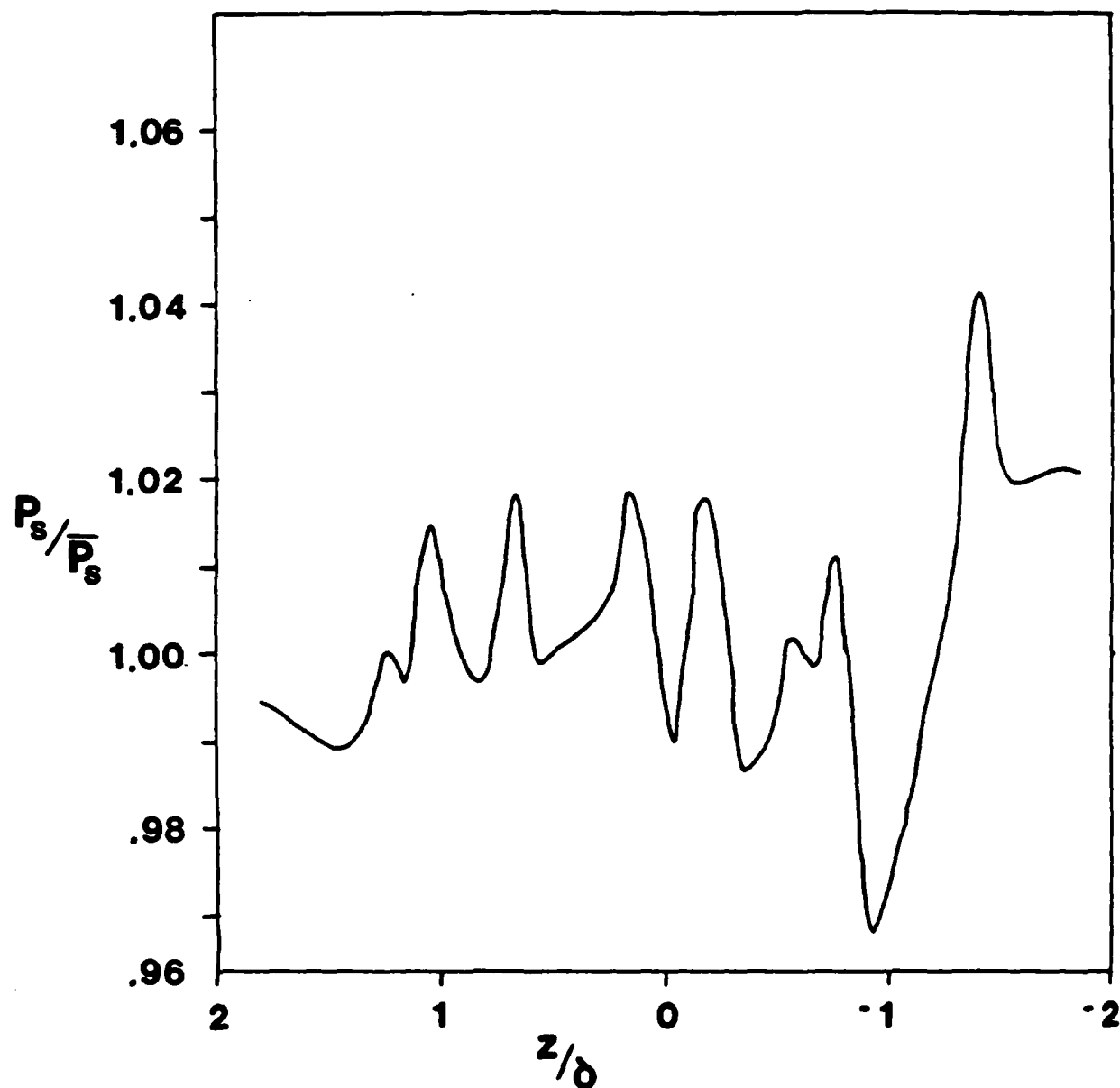


FIGURE 16.

Spanwise static pressure distribution at $x = 14.125$ inches, $y = 1.625$ inches

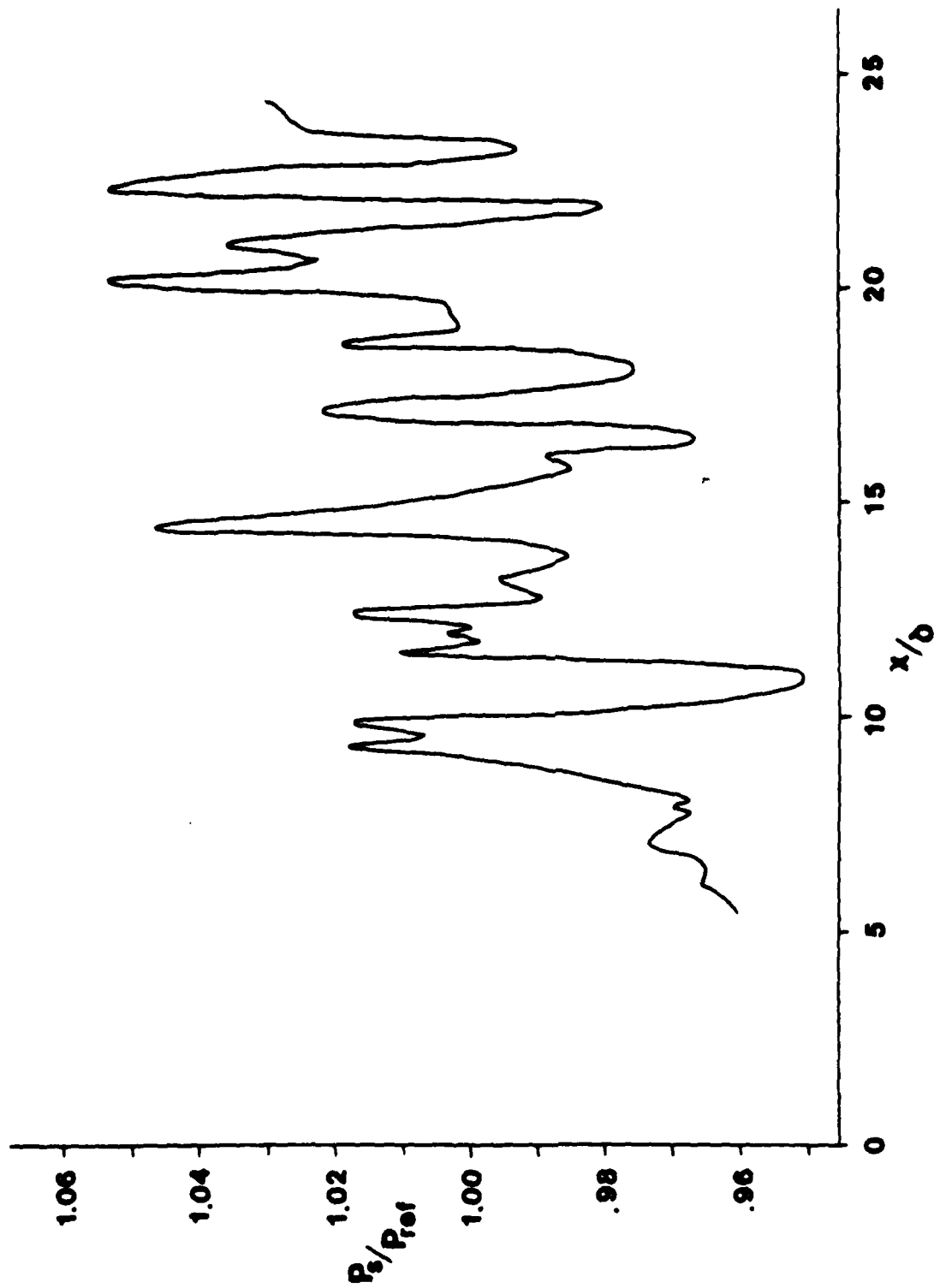


FIGURE 17. Streamwise static pressure distribution of the tunnel centerline at $y = 2.0$ inches

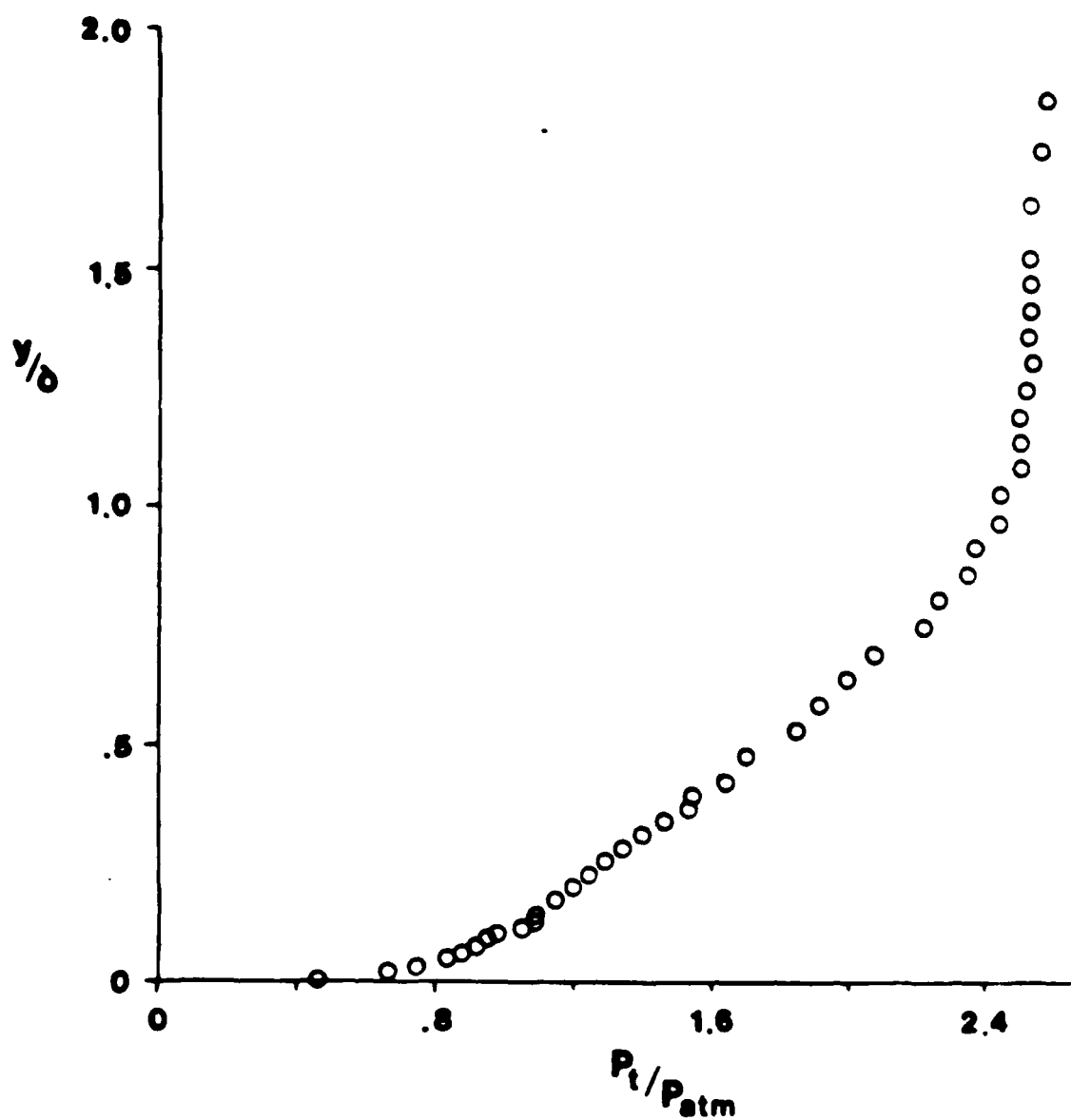


FIGURE 18. Typical Pitot pressure profile

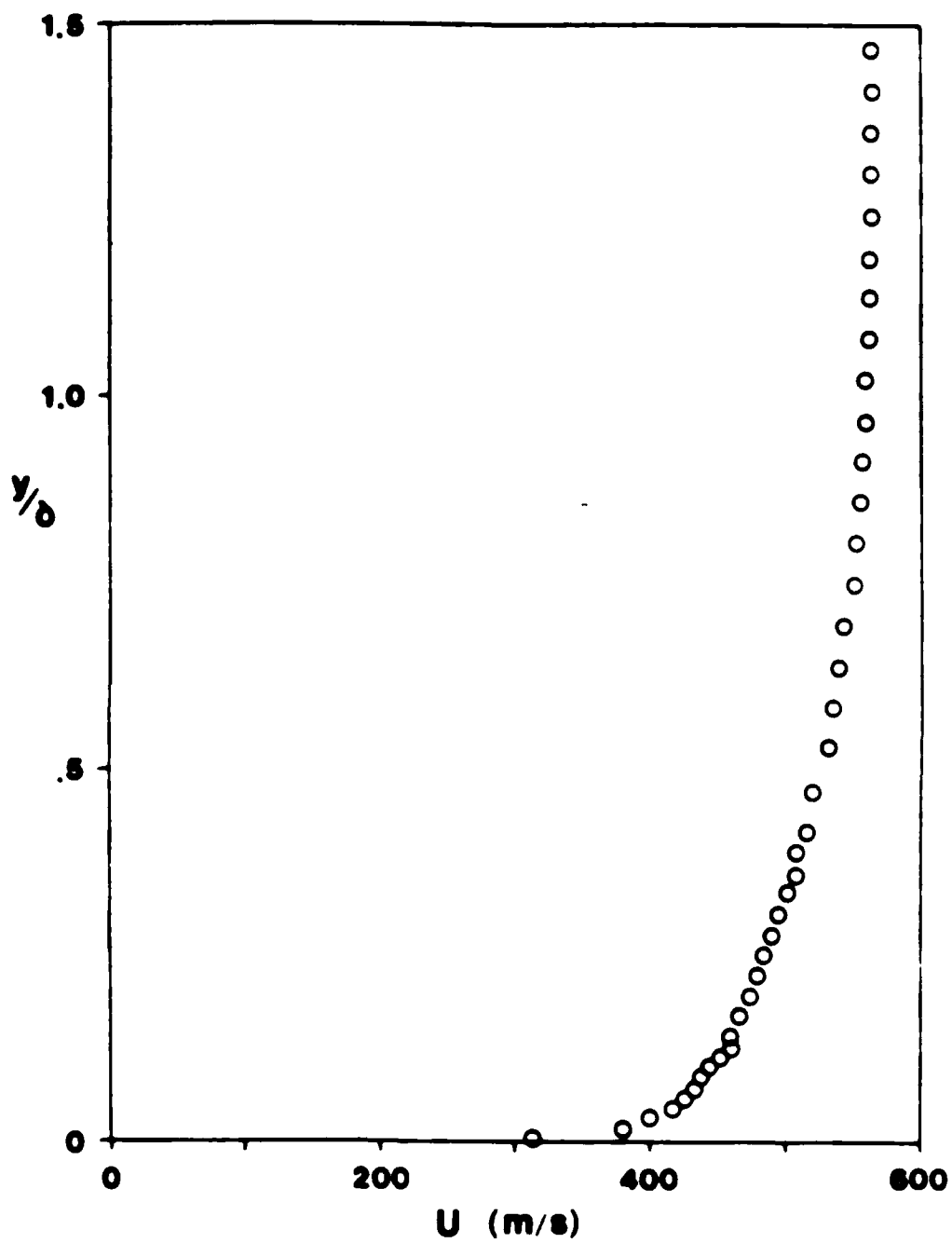


FIGURE 19. Typical mean velocity profile

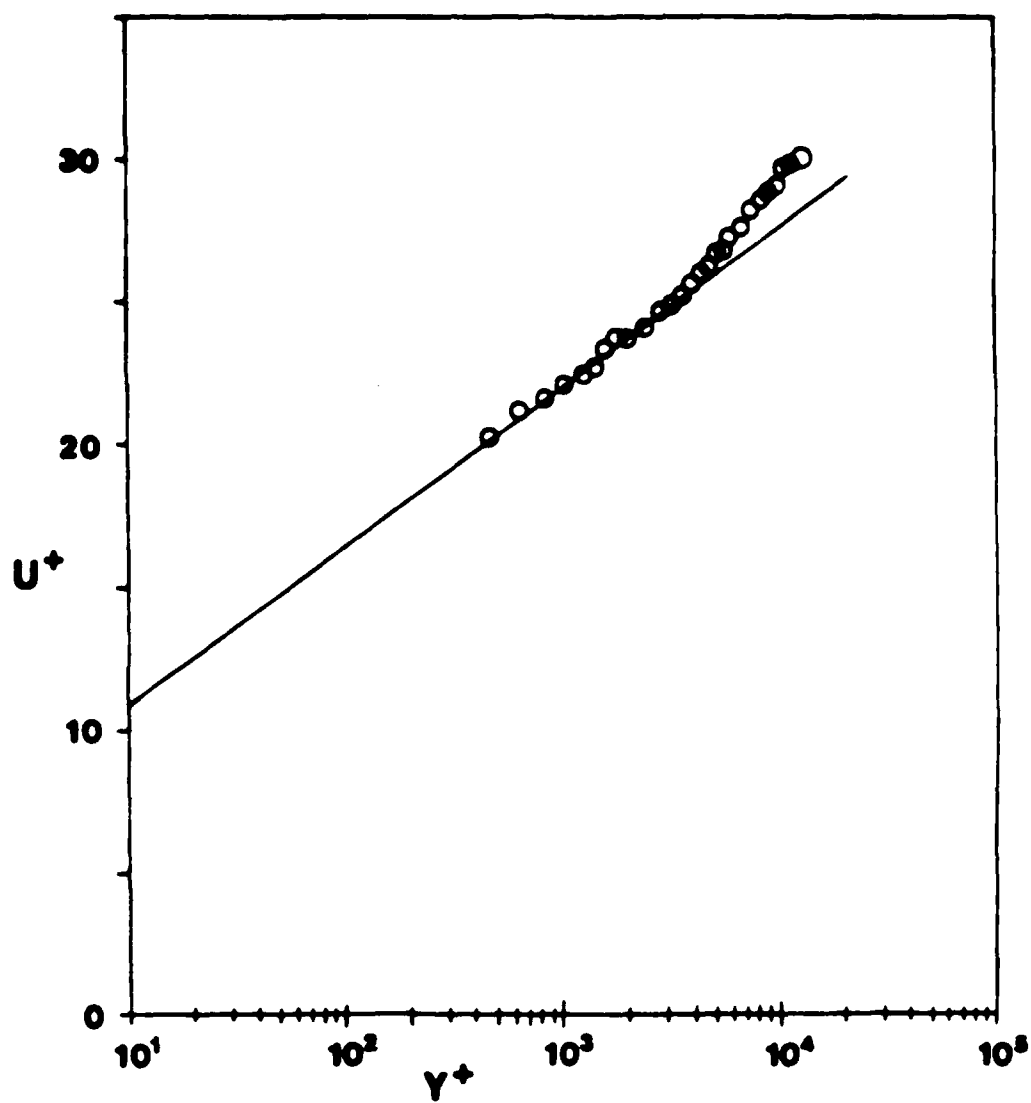


FIGURE 20.

Typical transformed velocity profile, fitted to the wall-wake law of Coles

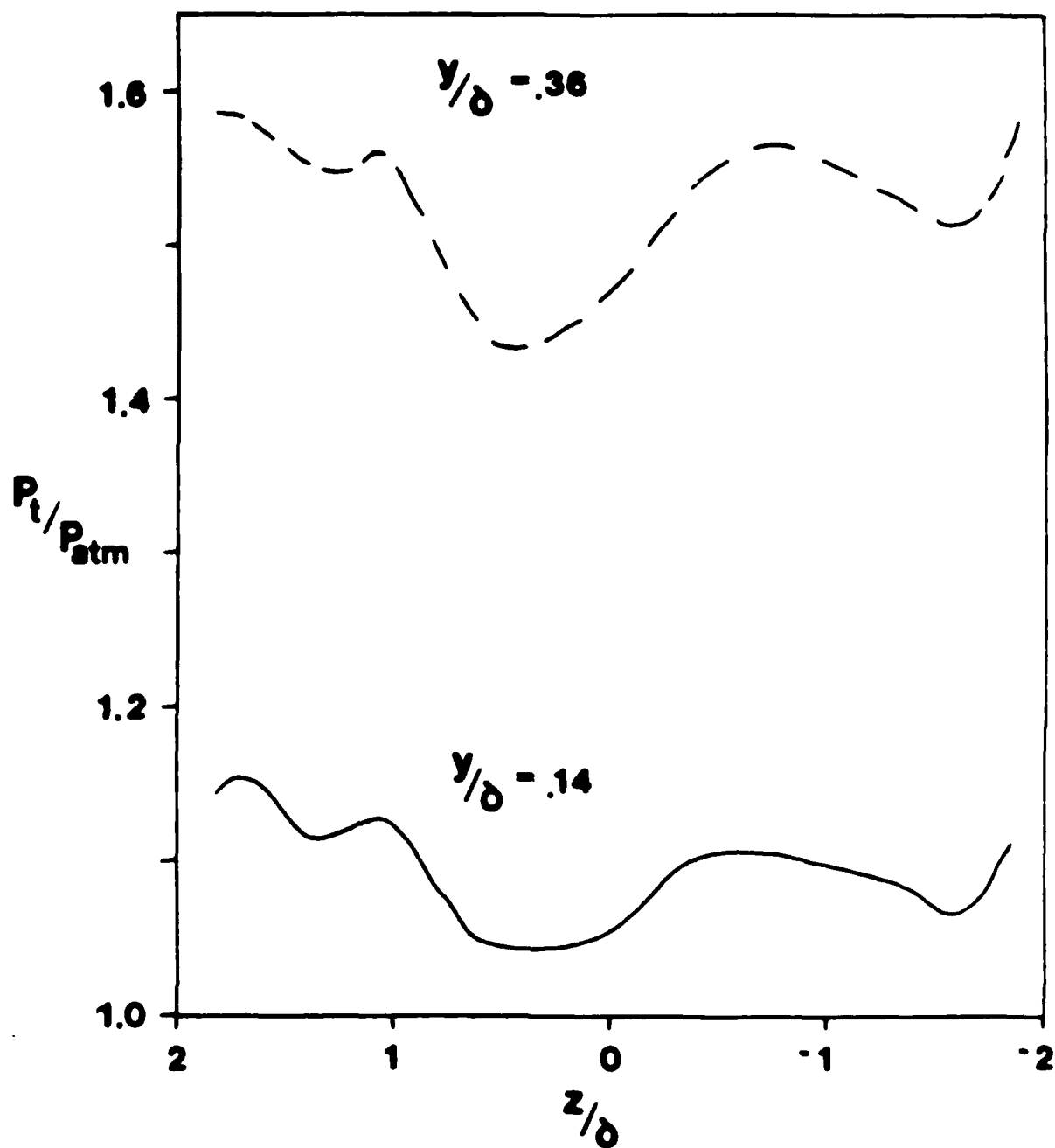


FIGURE 21.

Spanwise Pitot pressure distributions at $x = 18.5$ in., $y = 0.15$ and 0.4 in.

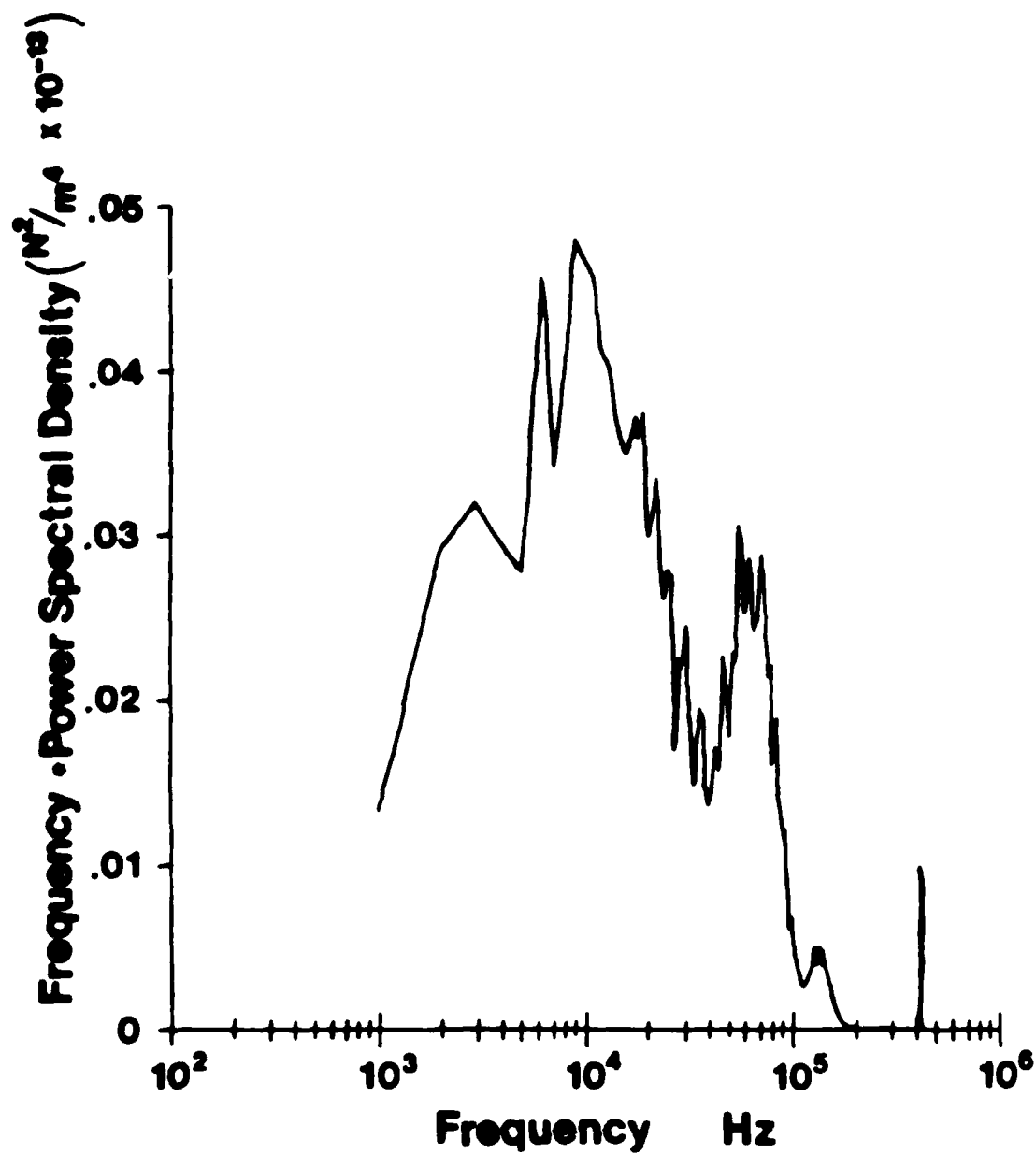


FIGURE 22

Typical measured wall pressure energy distribution

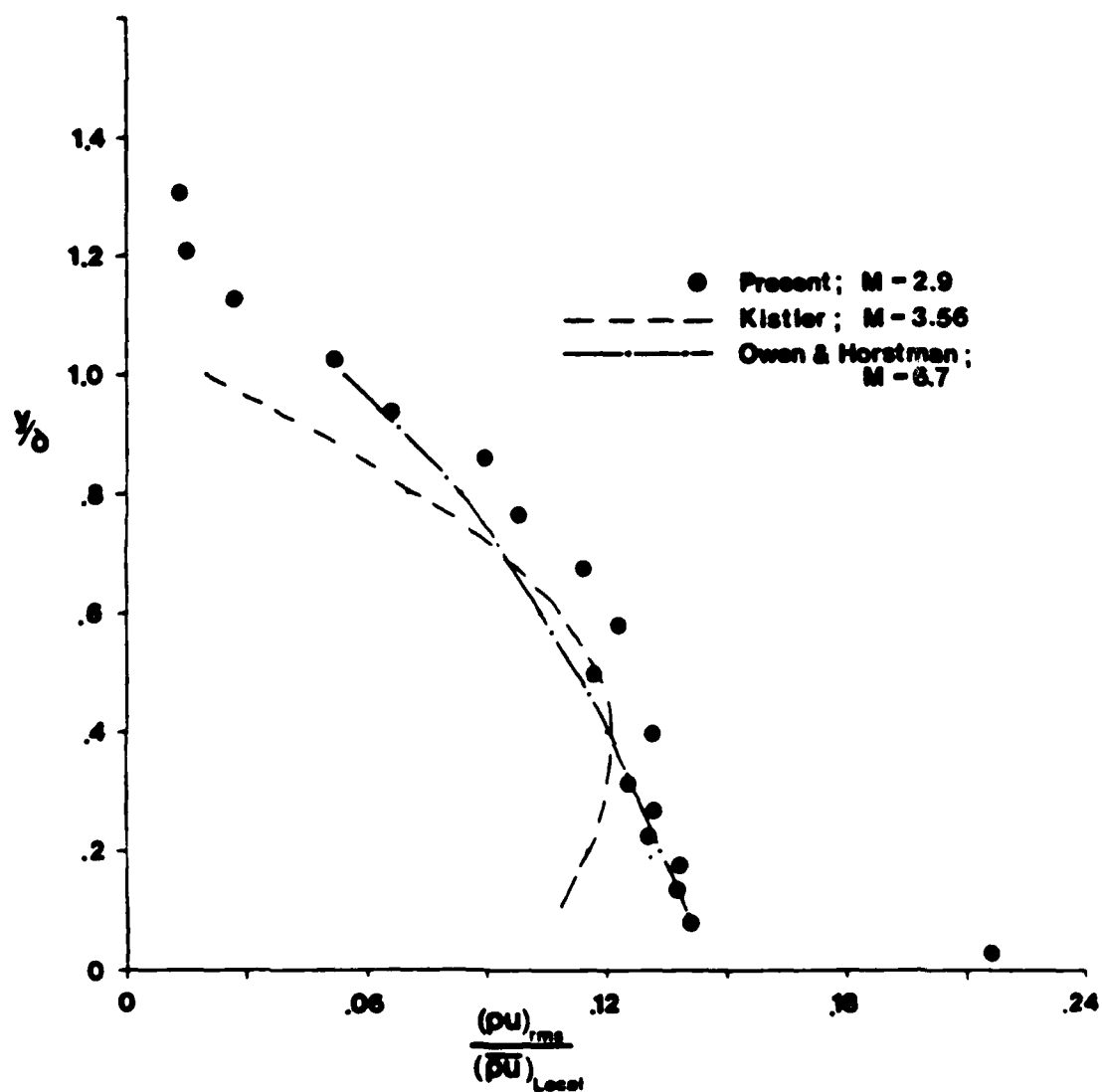


FIGURE 23. Typical r.m.s. mass-flow fluctuation level through the boundary layer

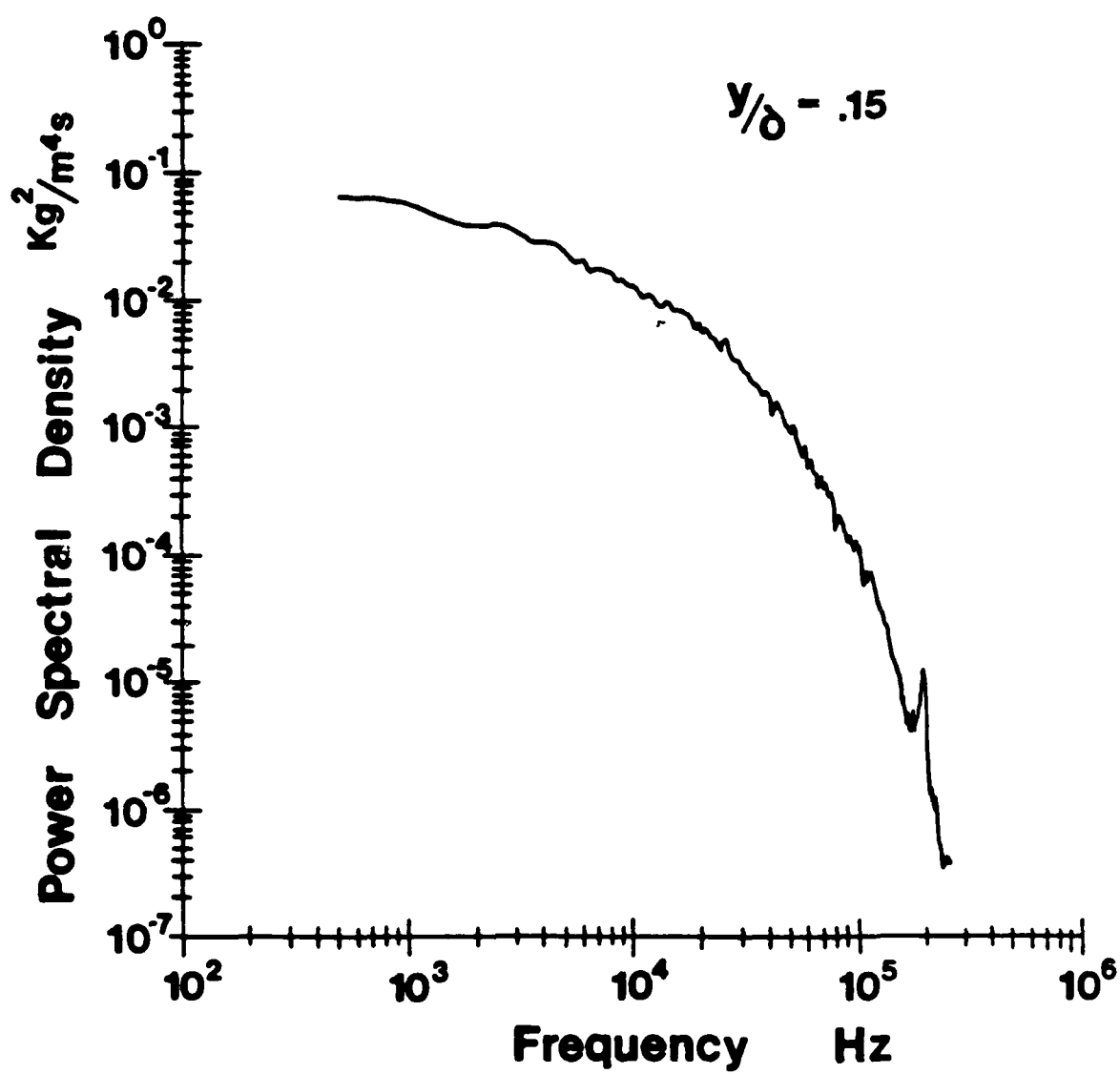


FIGURE 24.

Typical measured mass-flow fluctuation power spectral density distribution

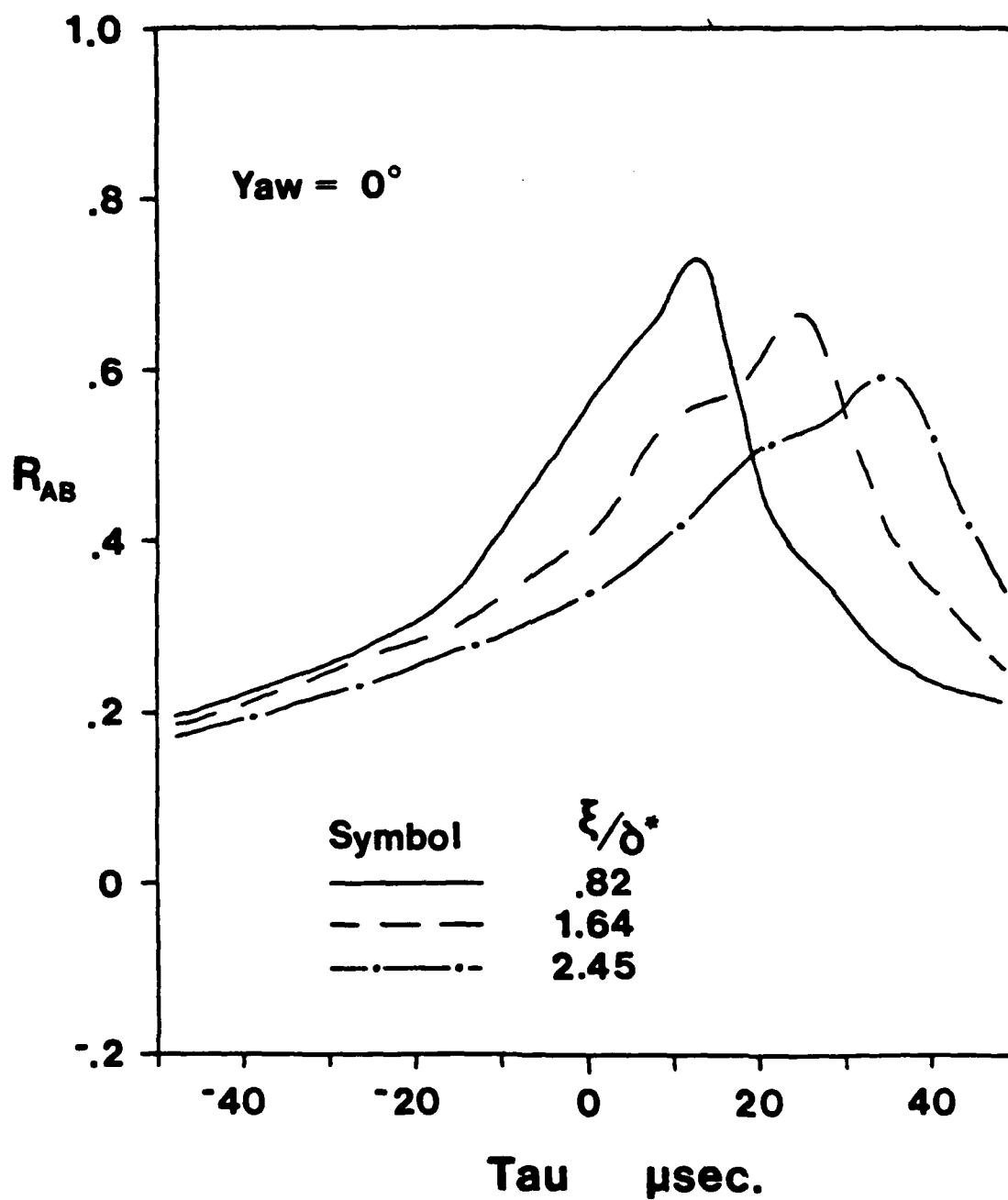


FIGURE 25a.

Space-time correlation of wall-pressure signals
at 0° yaw angle

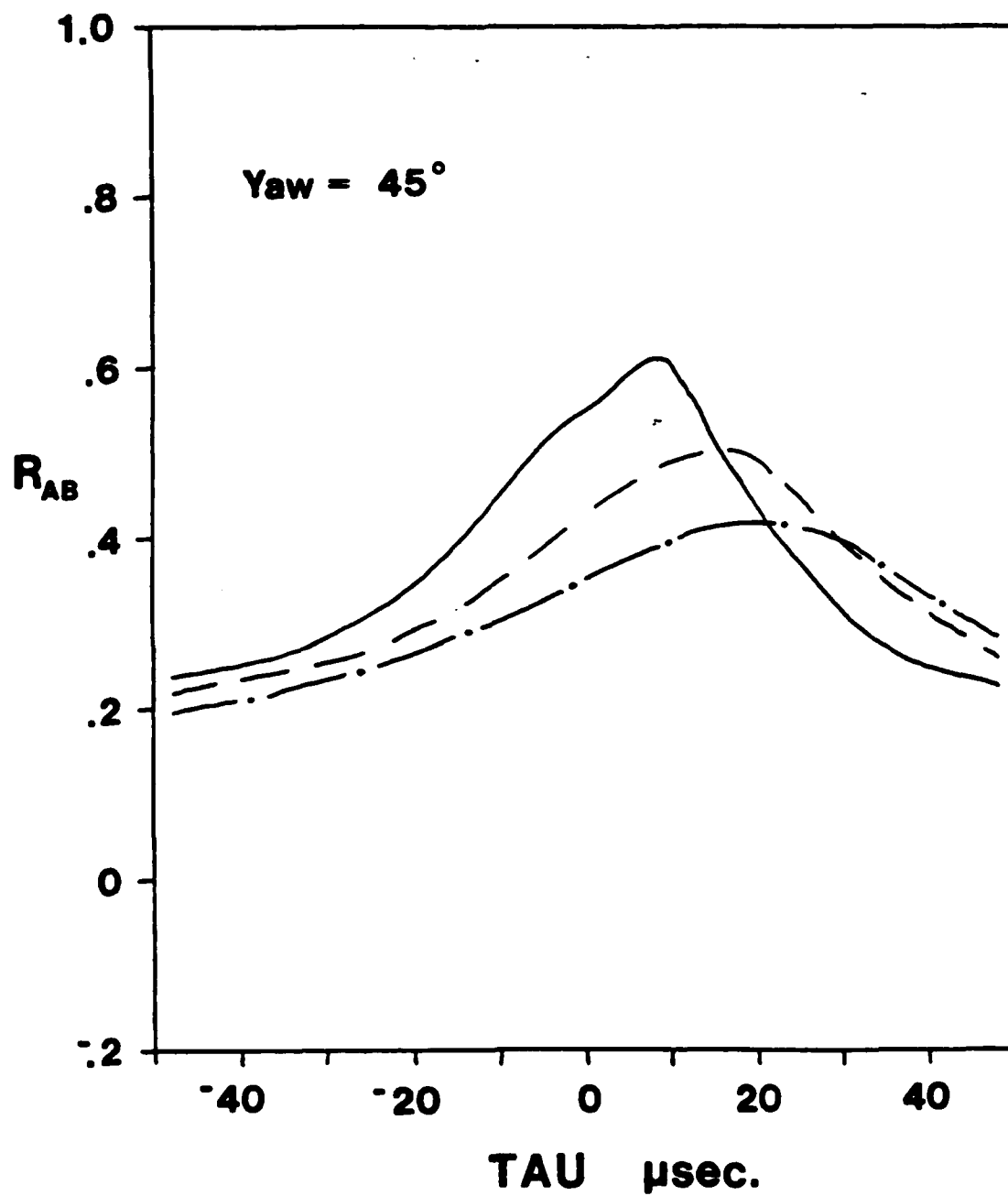


FIGURE 25b.

Space-time correlation of wall-pressure signals
at 45° yaw angle

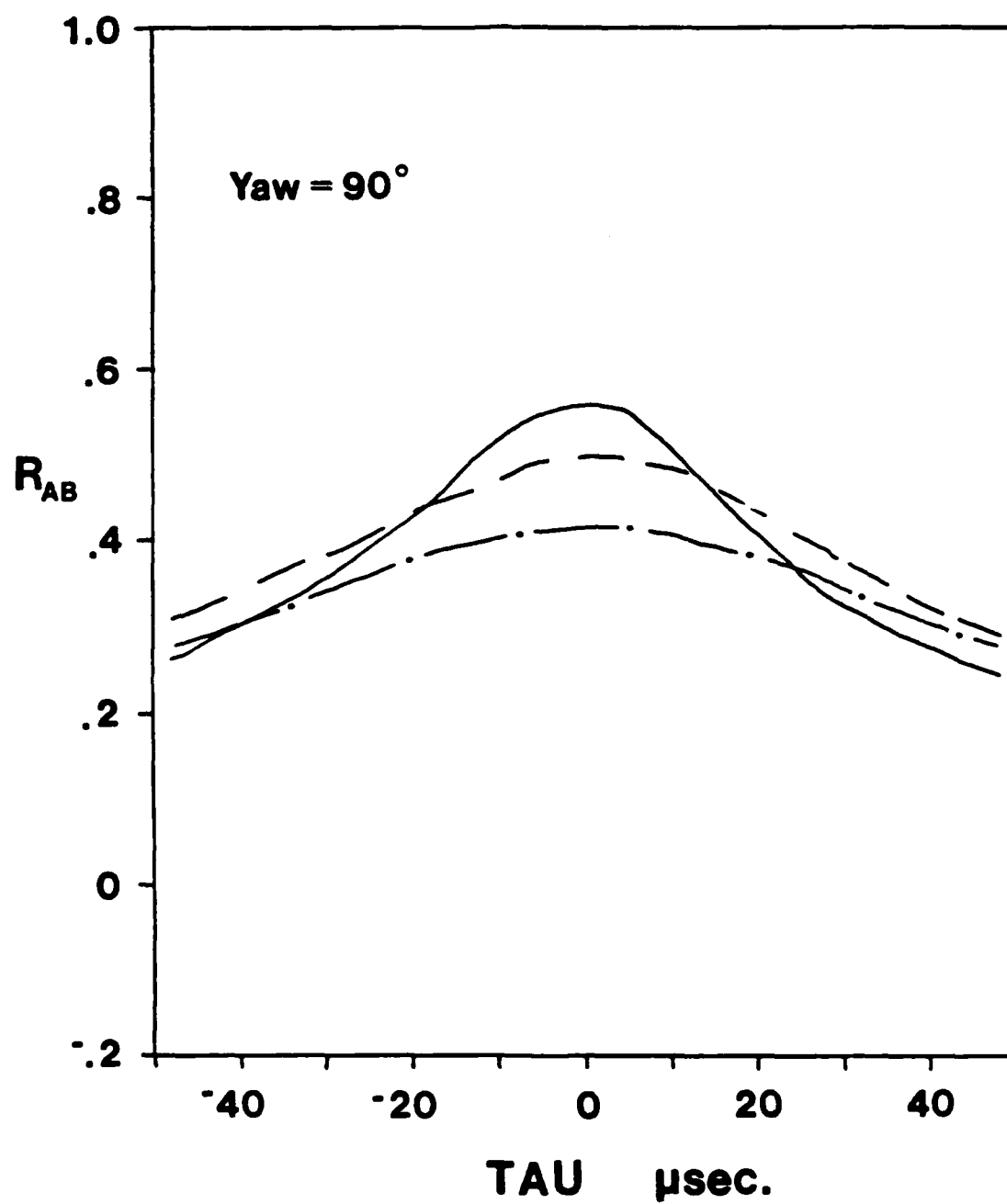


FIGURE 25c.

Space-time correlation of wall-pressure signals
at 90° yaw angle

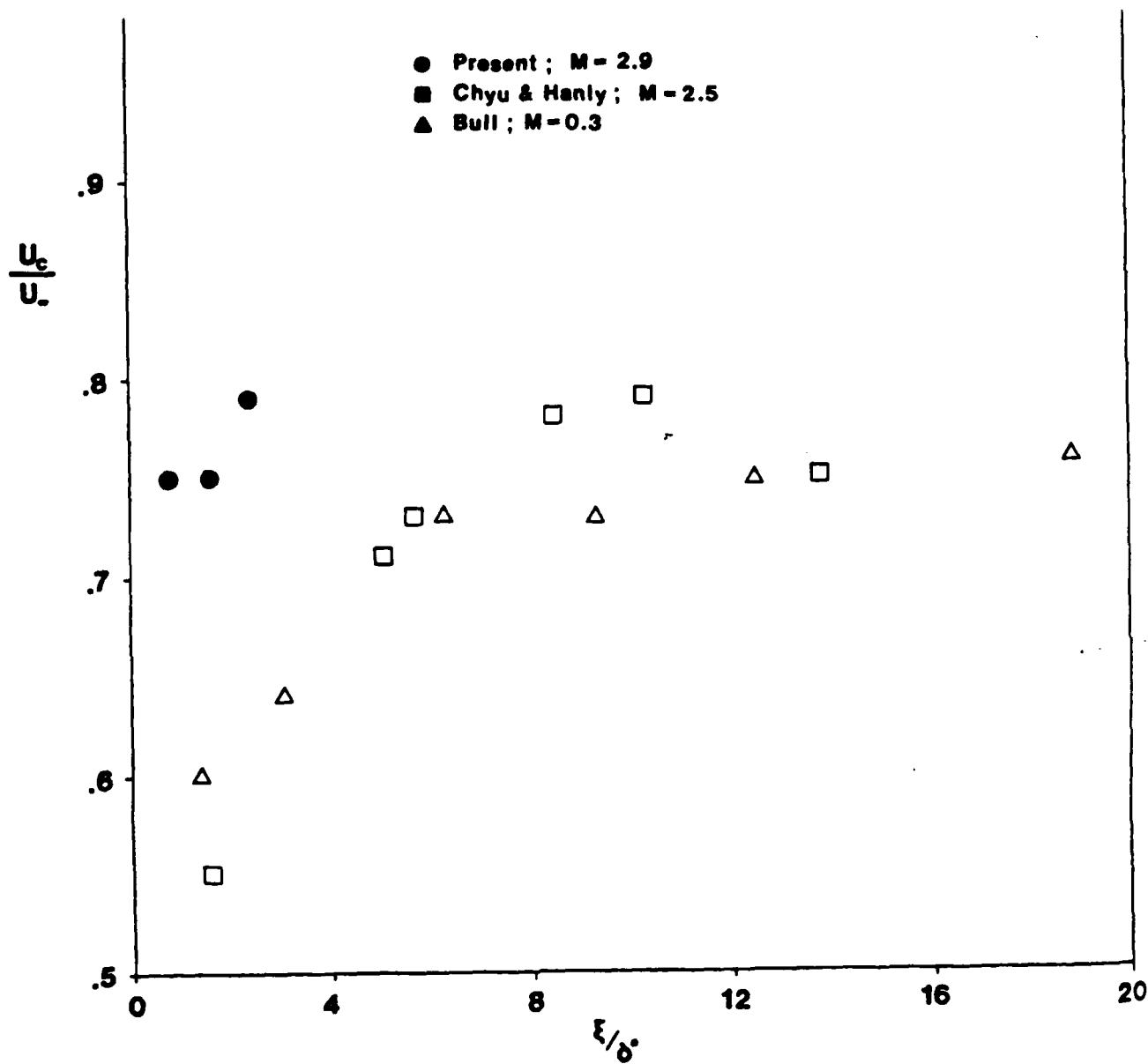


FIGURE 26.

Broad band convection velocities, deduced from wall-pressure signals

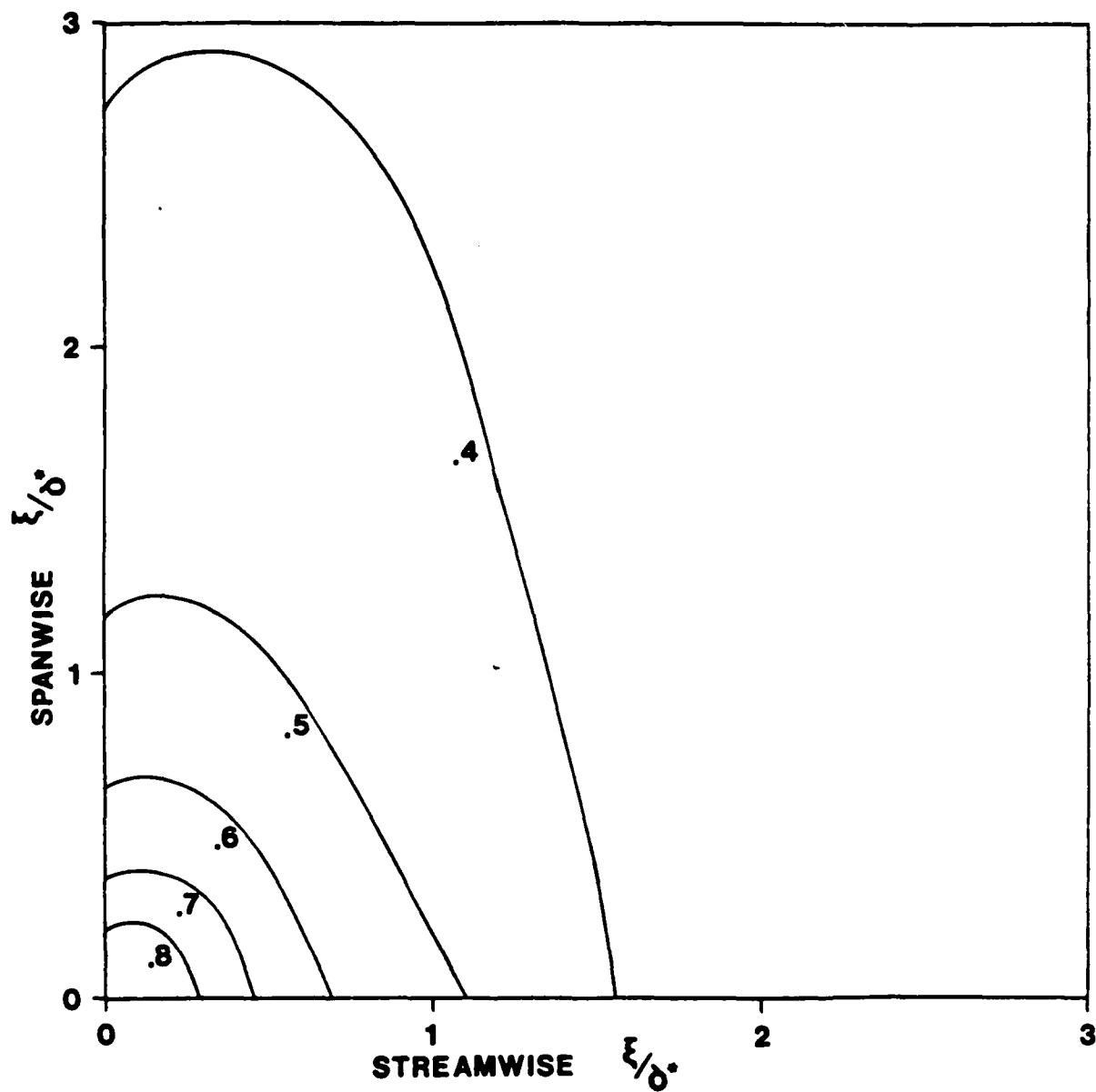


FIGURE 27.

Contour plot of equal space correlation maxima, deduced from wall-pressure signals

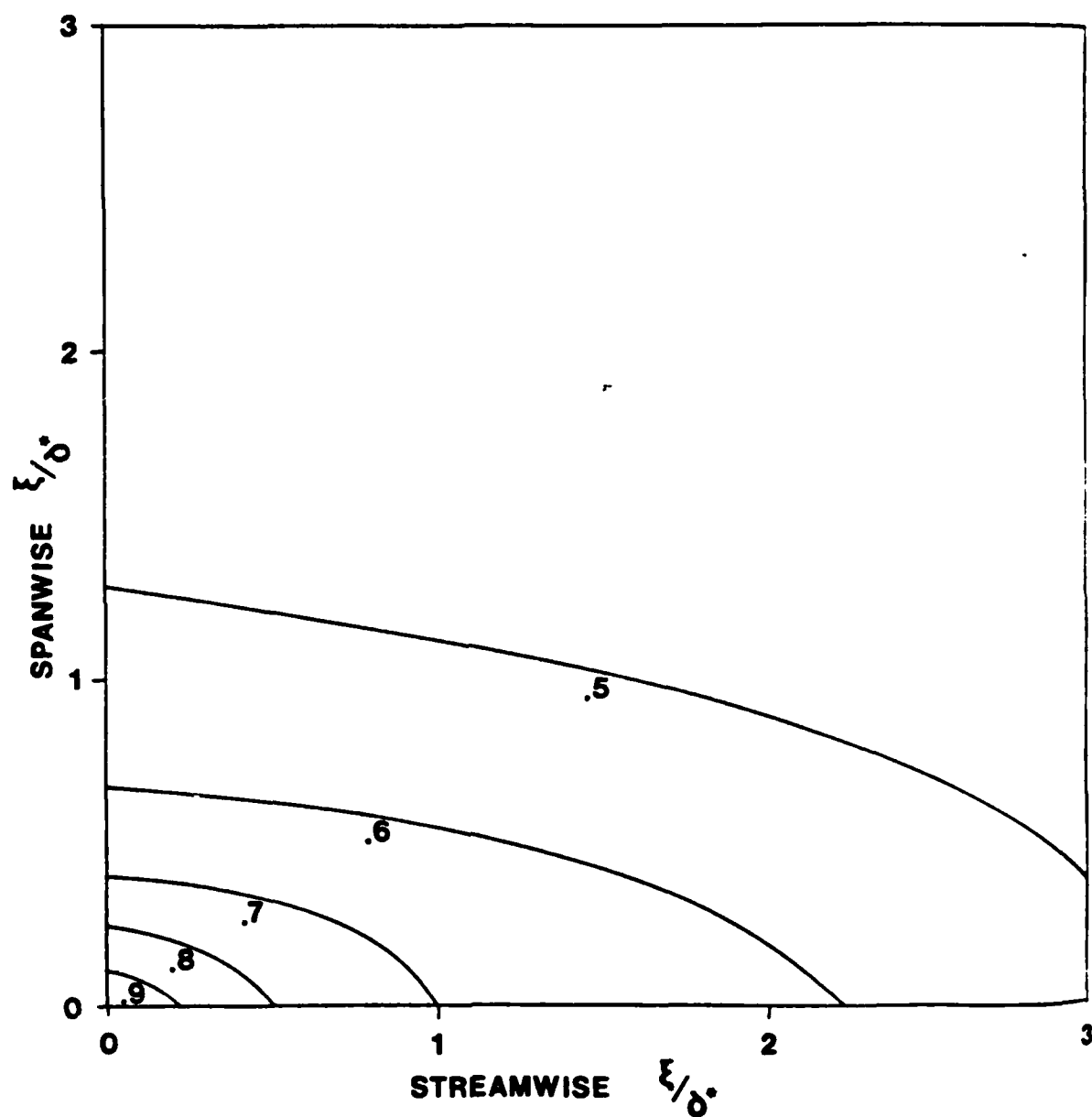


FIGURE 28.

Contour plot of equal space-time correlation maxima,
deduced from wall-pressure signals

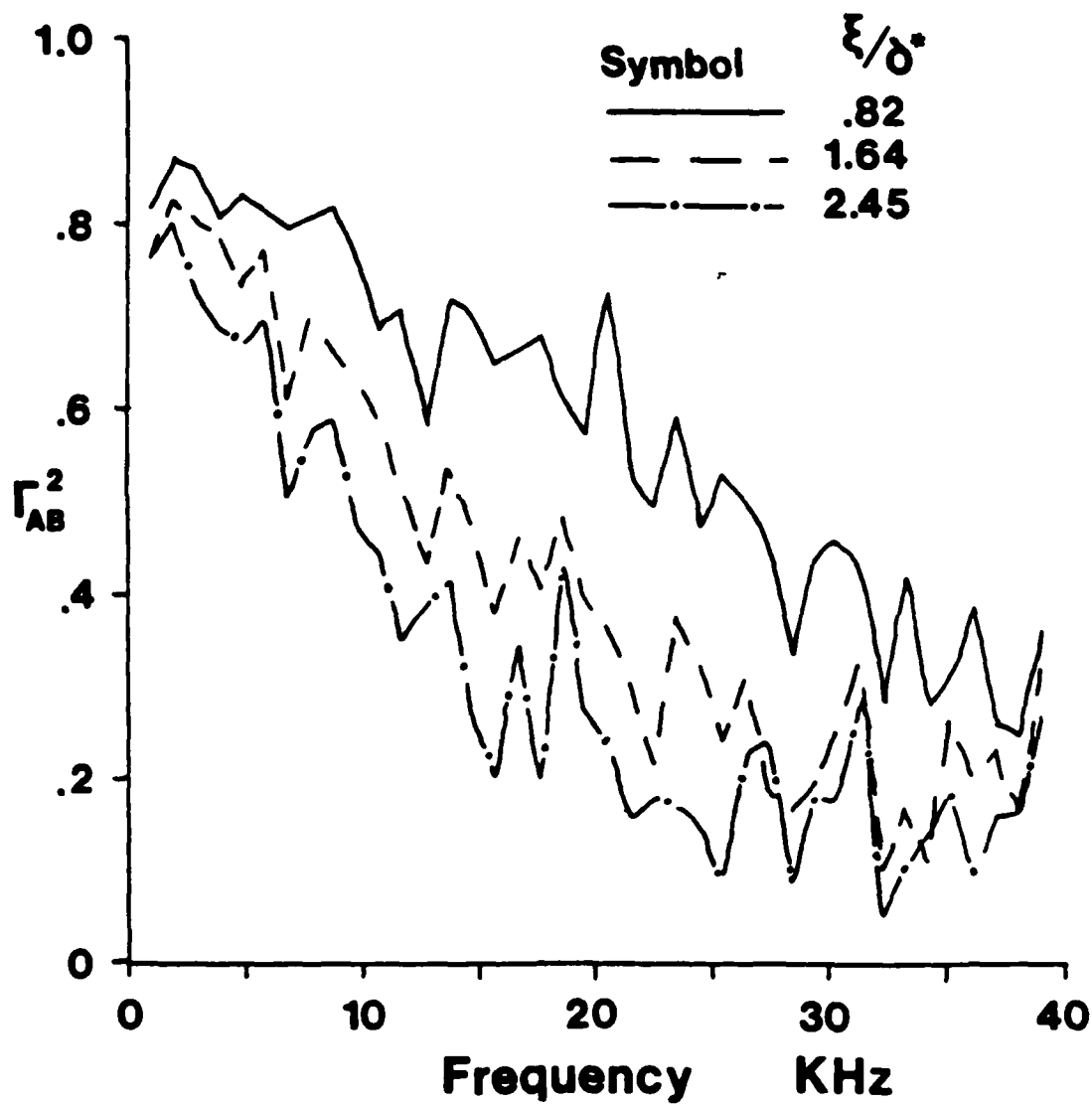


FIGURE 29. The computed wall-pressure coherence function

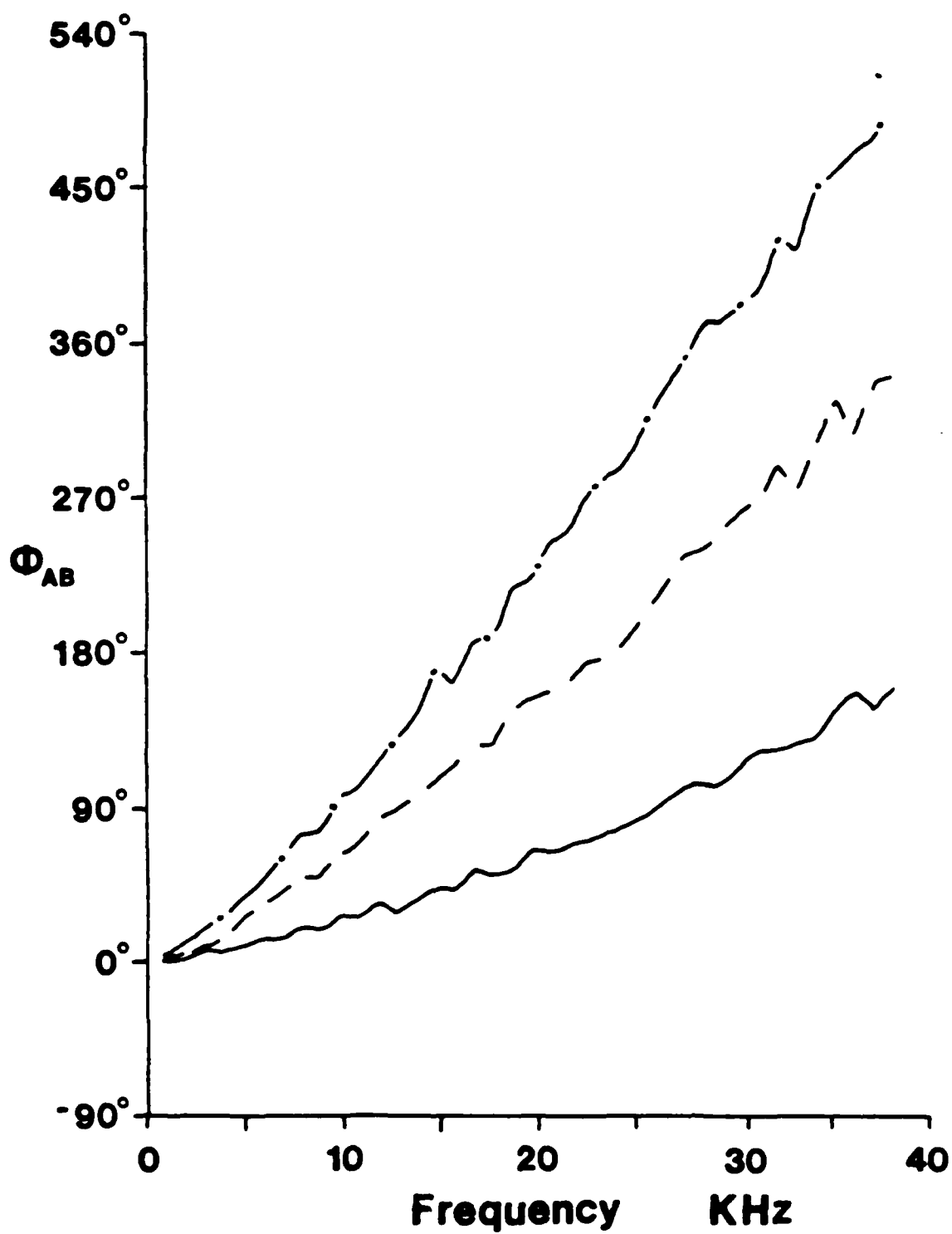


FIGURE 30.

The computed wall-pressure phase angle function.
See Figure 29 for legend

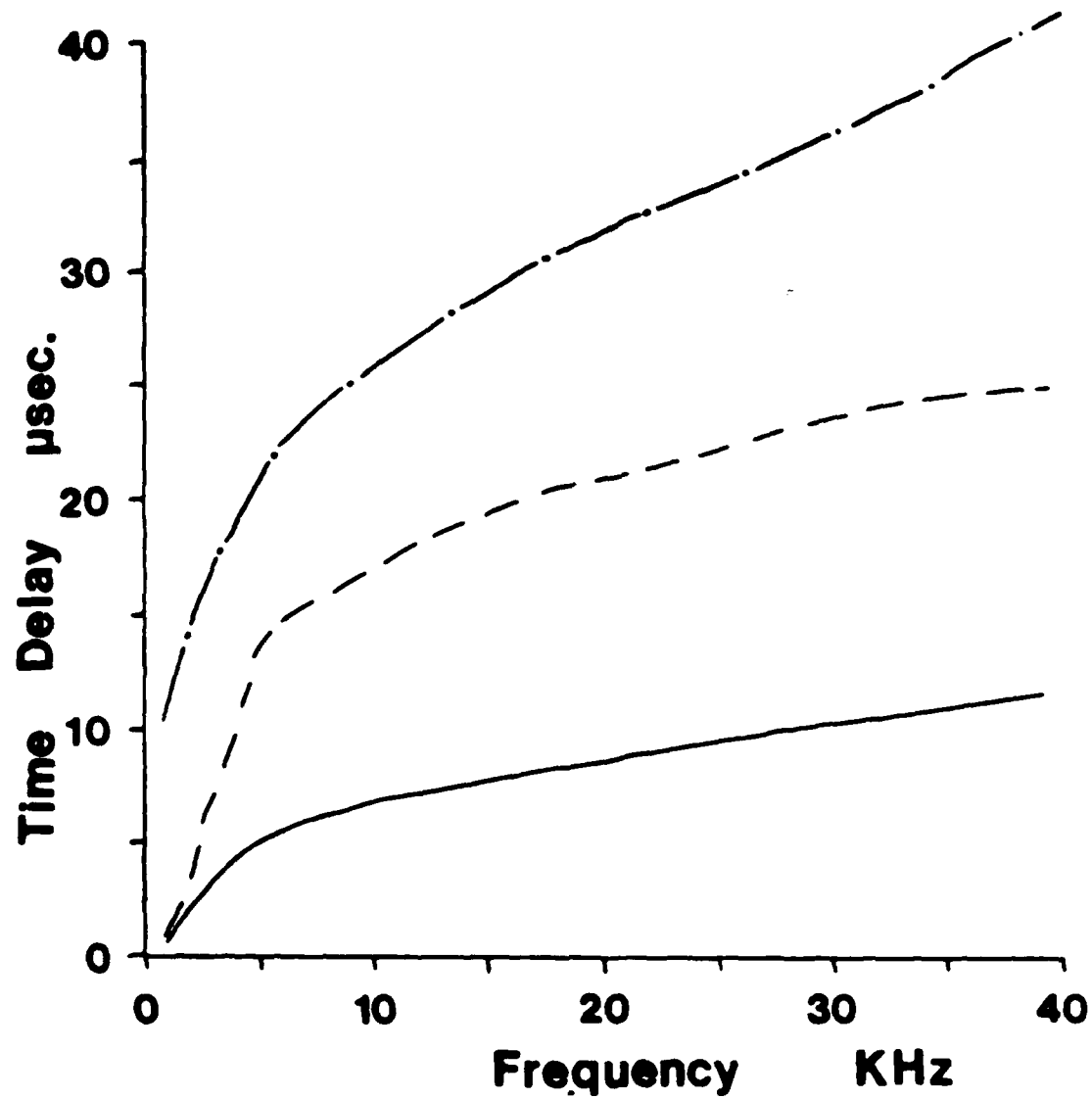


FIGURE 31.

The computed wall-pressure time-delay function.
See Figure 29 for legend

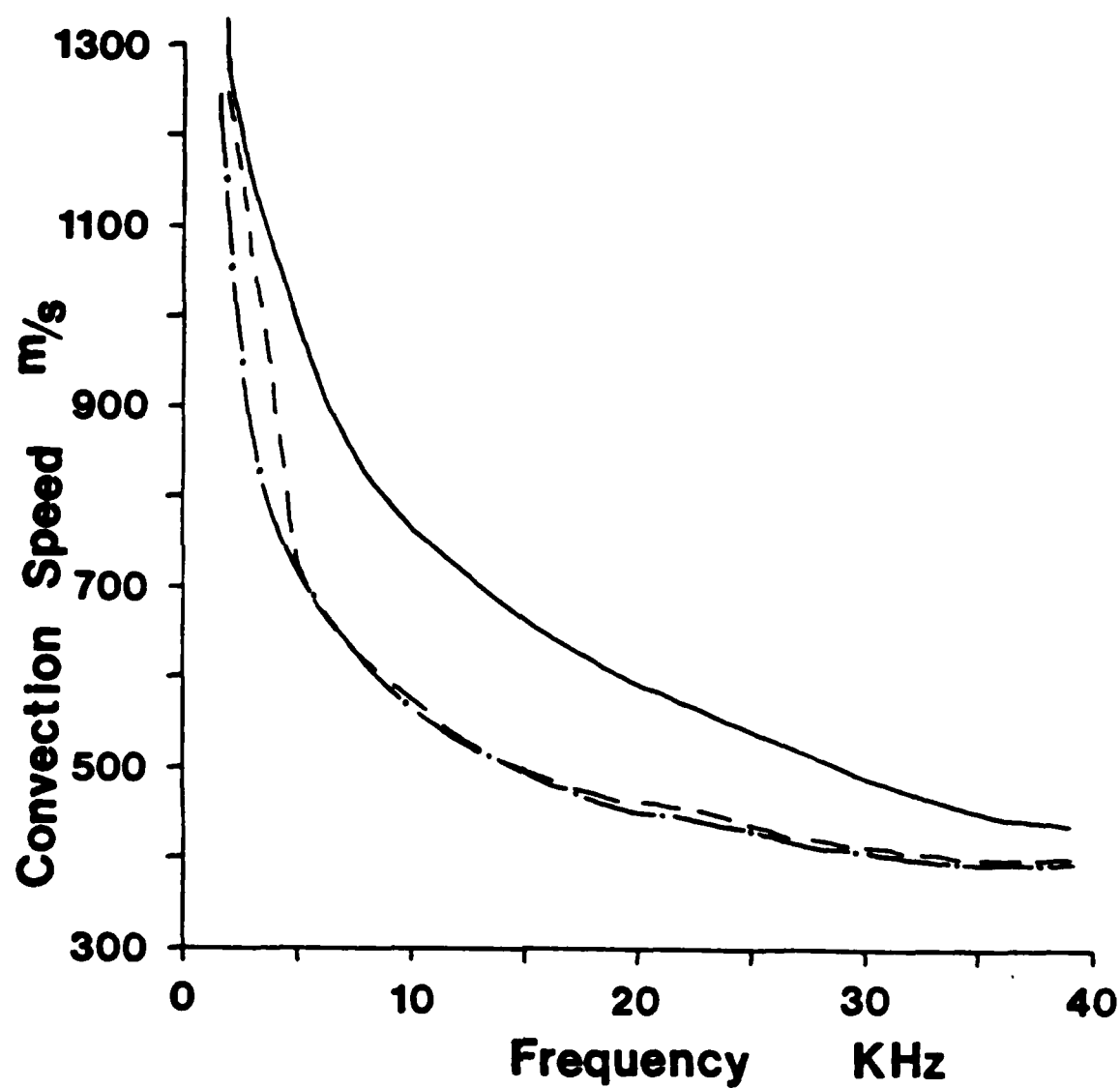


FIGURE 32.

The computed wall pressure convection speed function.
See Figure 29 for legend

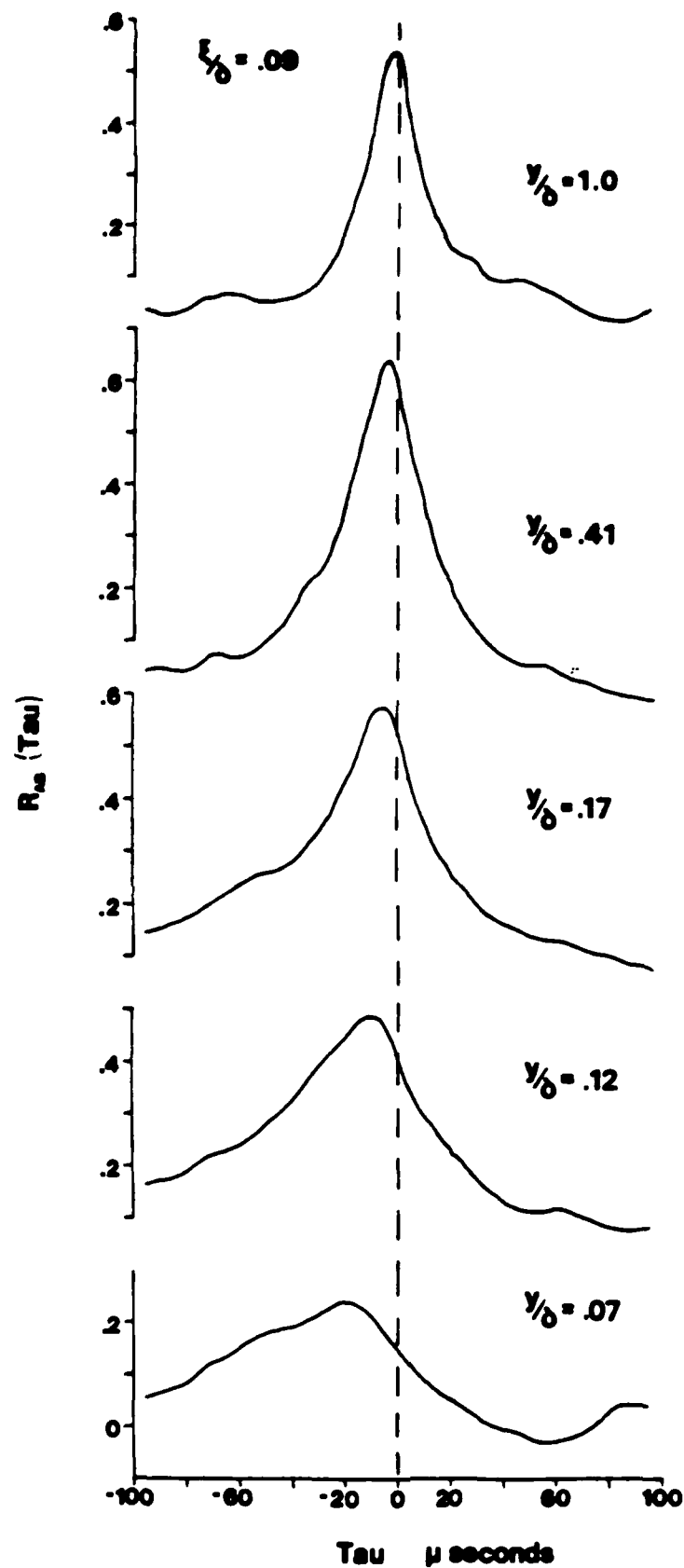


FIGURE 33.

The space-time correlation of mass-flow fluctuations throughout the boundary layer. Hot wire separation is 0.16

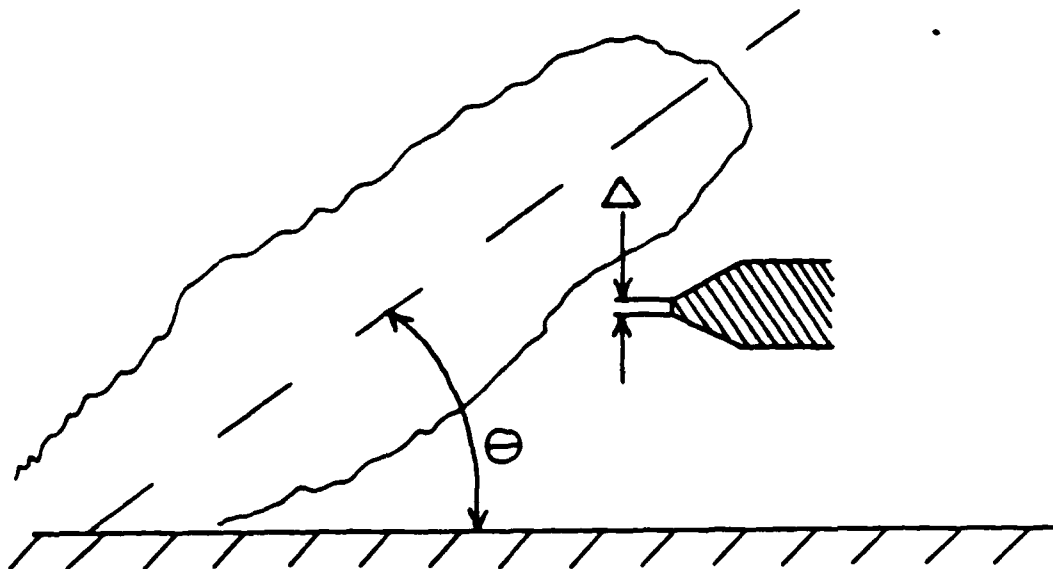


FIGURE 34a.

Sketch of a typical large-scale structure, inclined at an angle θ , passing a double wire probe

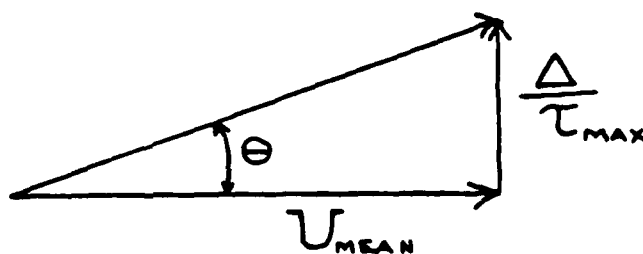


FIGURE 34b.

Diagram used to determine "structure angle "

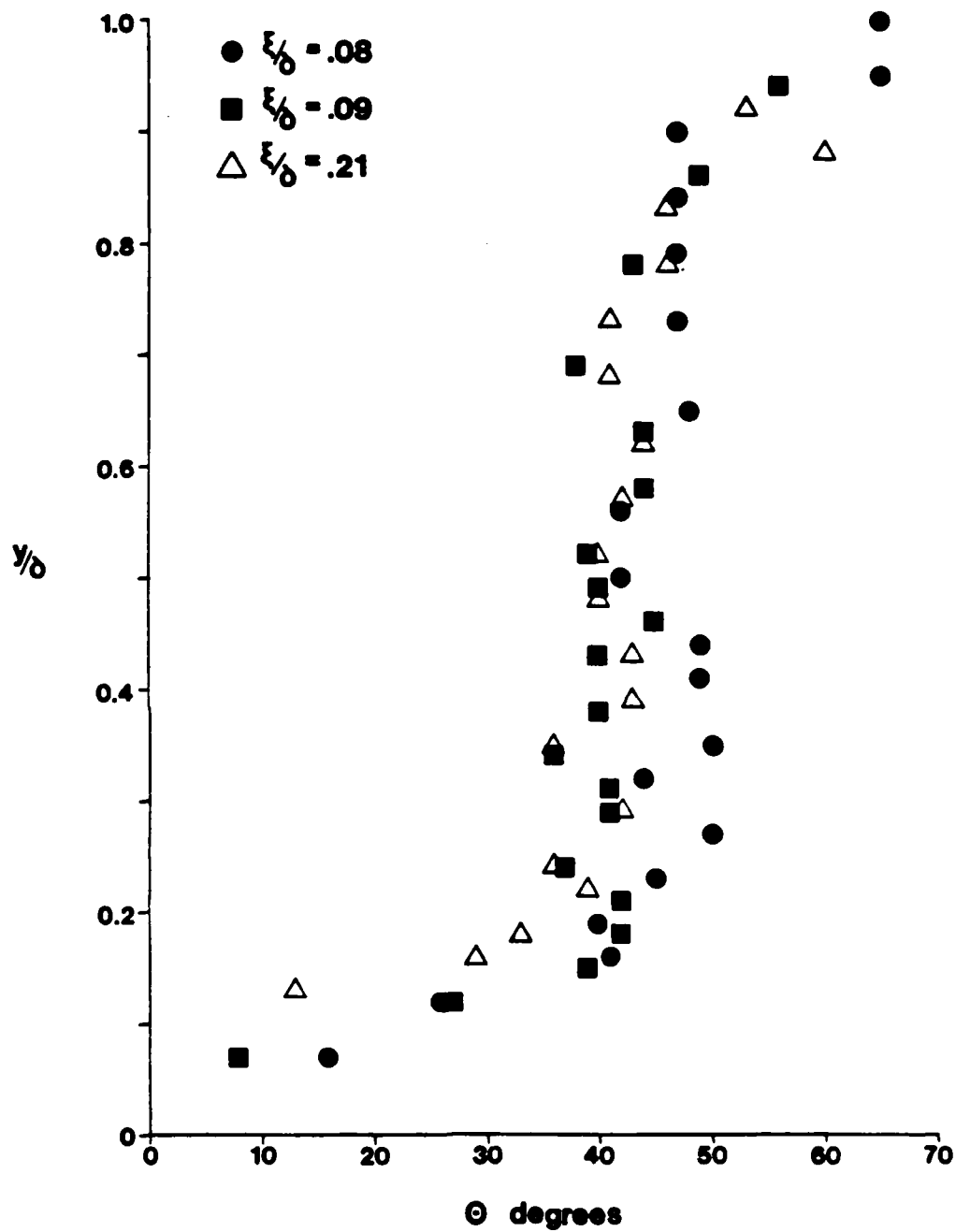


FIGURE 35.

Computed large-scale structure angle throughout the boundary layer for two different wire separation distances

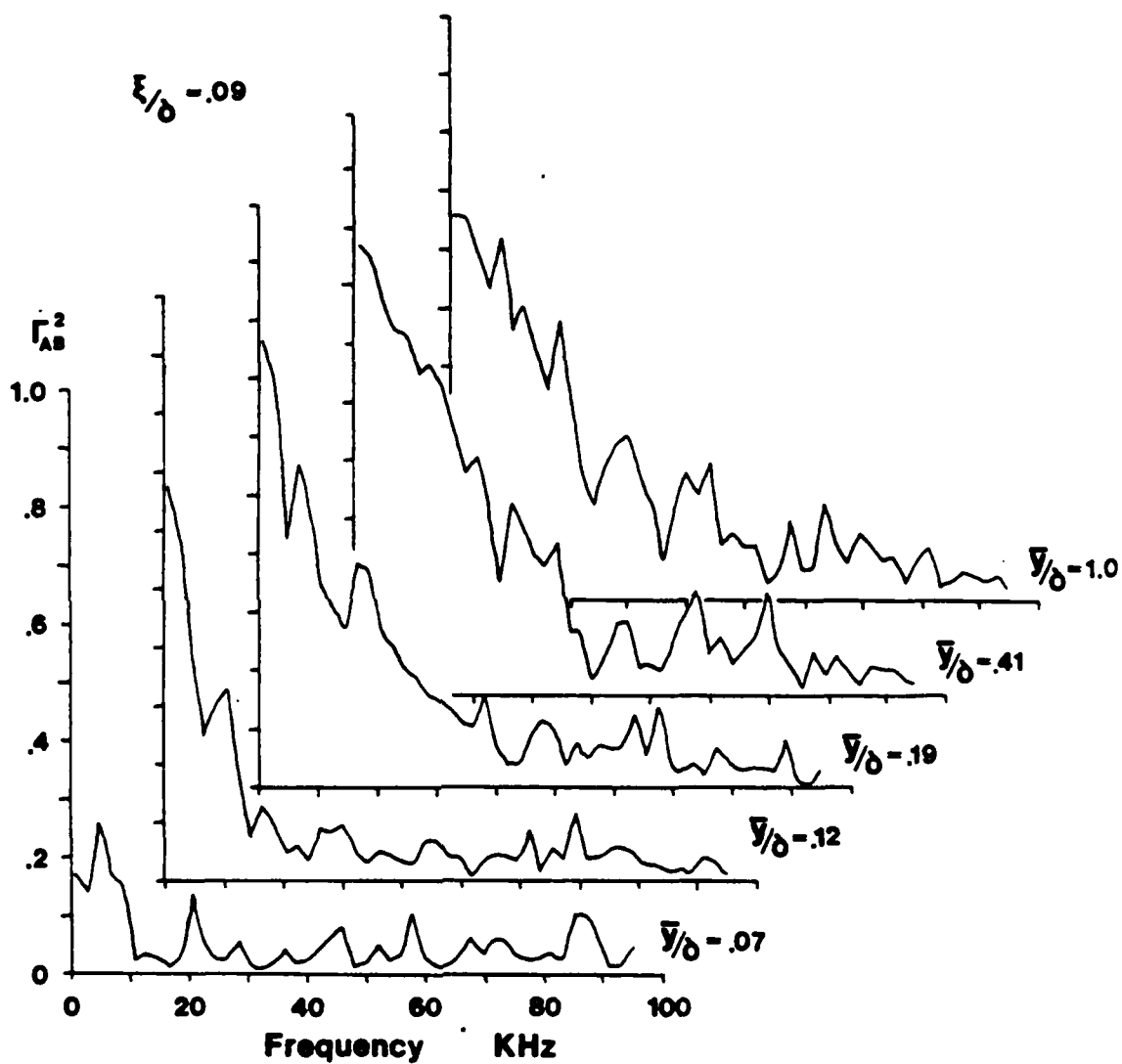


FIGURE 36.

Coherence function (through-out the boundary layer) for two fluctuating mass-flow signals separated by 0.09δ .

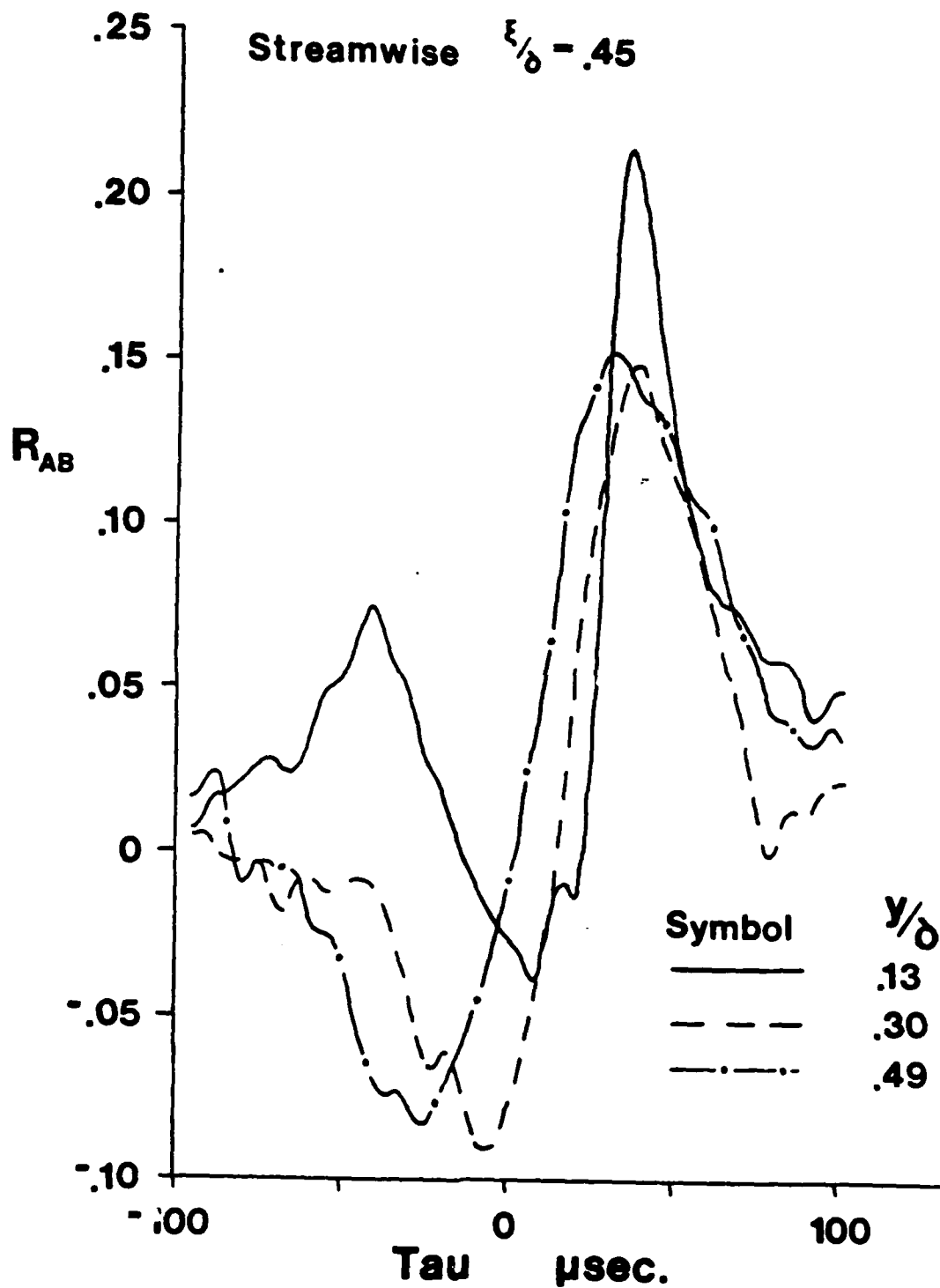


FIGURE 37a.

Space-time correlation between a wall-pressure signal and a mass-flow signal. Streamwise separation of 0.45 δ

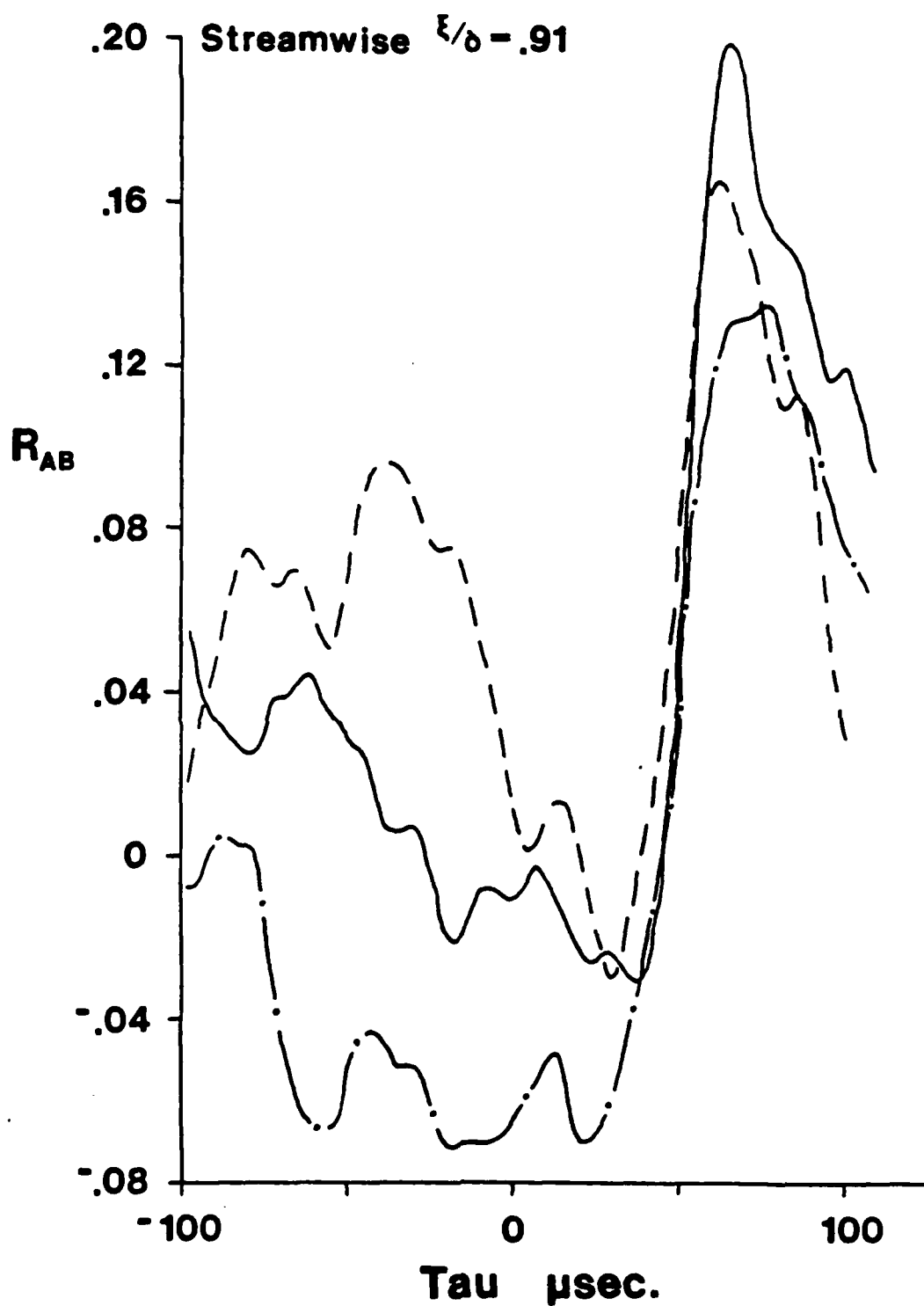


FIGURE 37b.

The same as Figure 37a; streamwise separation of 0.916

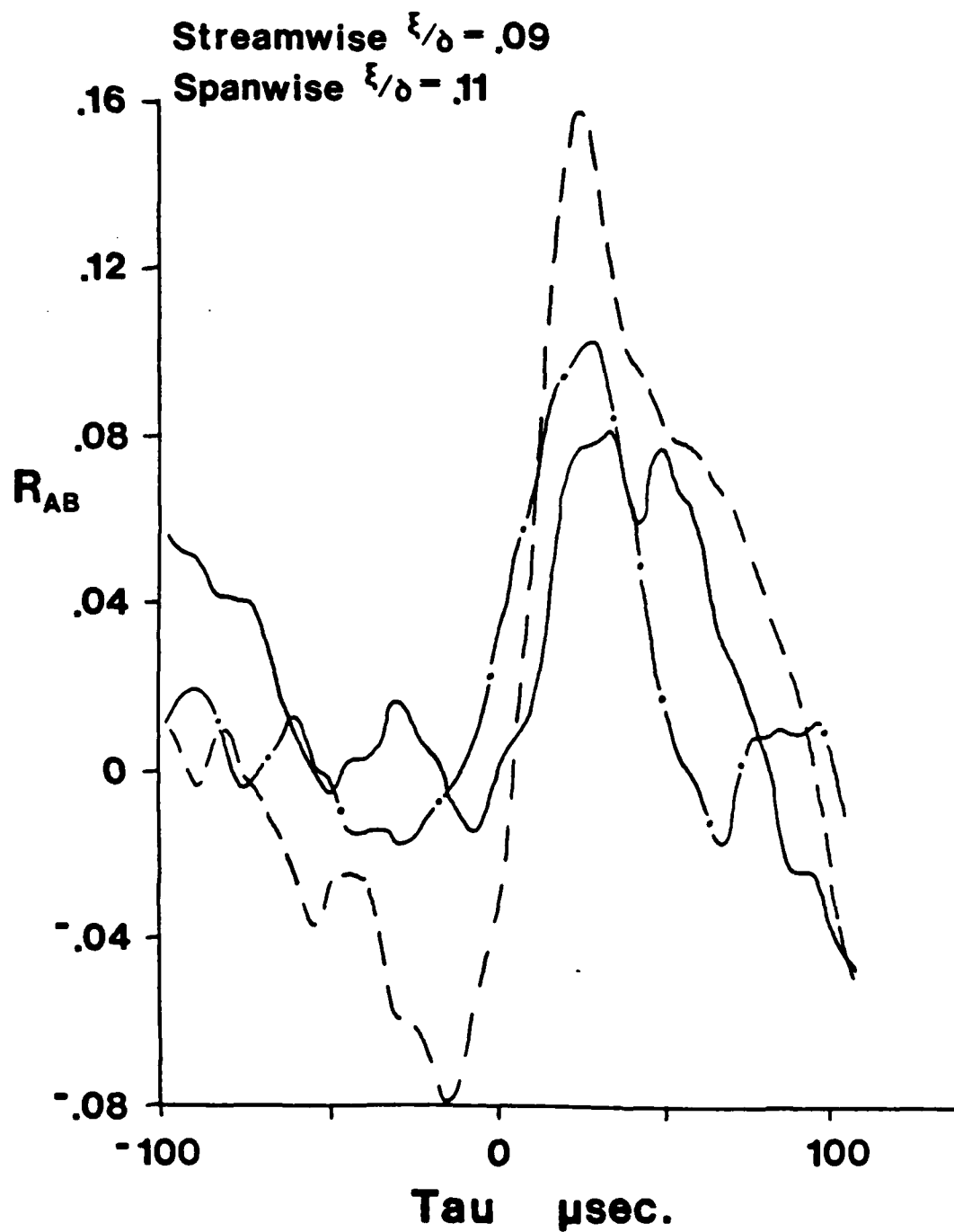


FIGURE 37c.

The same as Figure 37a; streamwise separation of 0.09 δ , spanwise separation of 0.11 δ

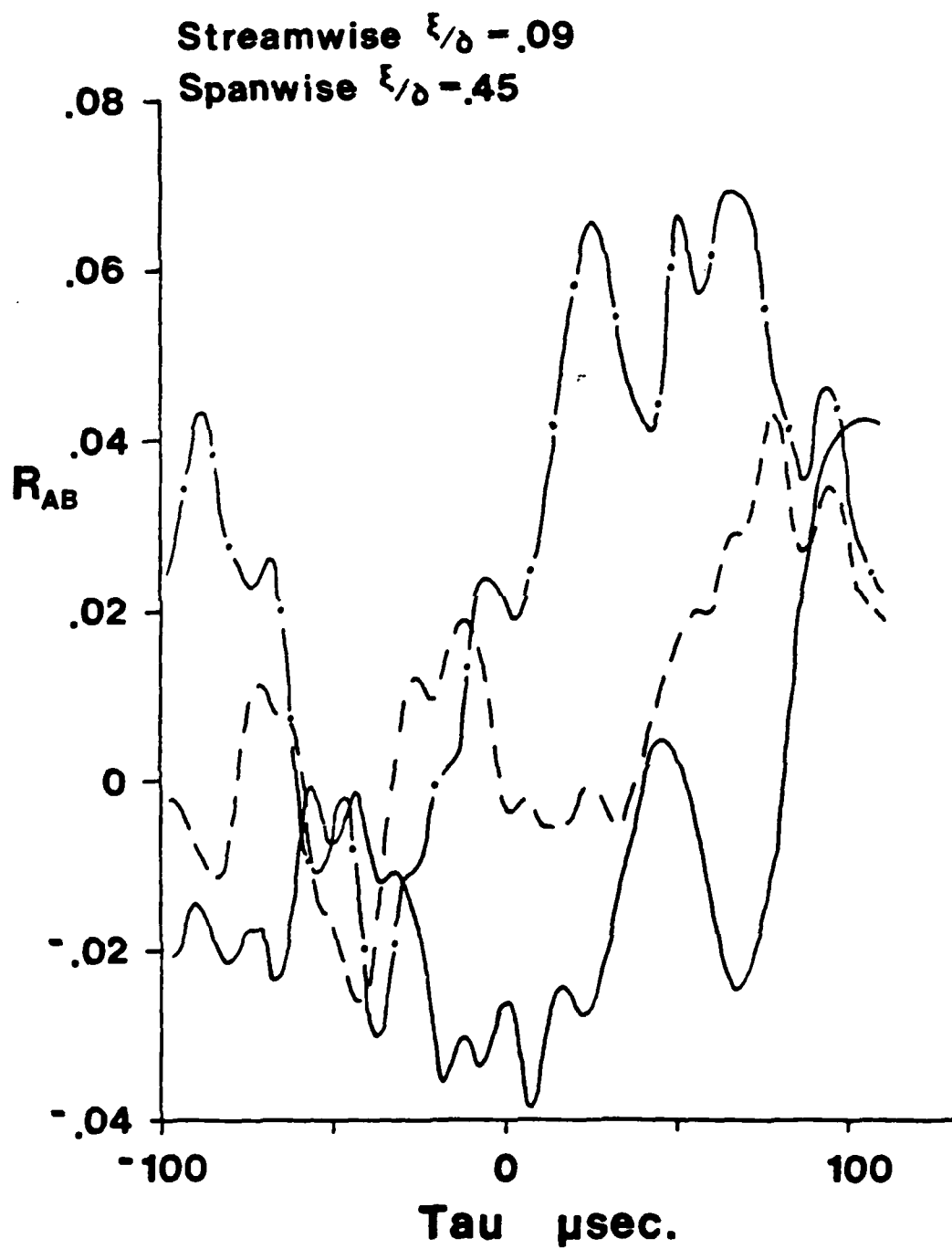


FIGURE 37d.

The same as Figure 37a; streamwise separation of 0.09 δ , spanwise separation of 0.45 δ

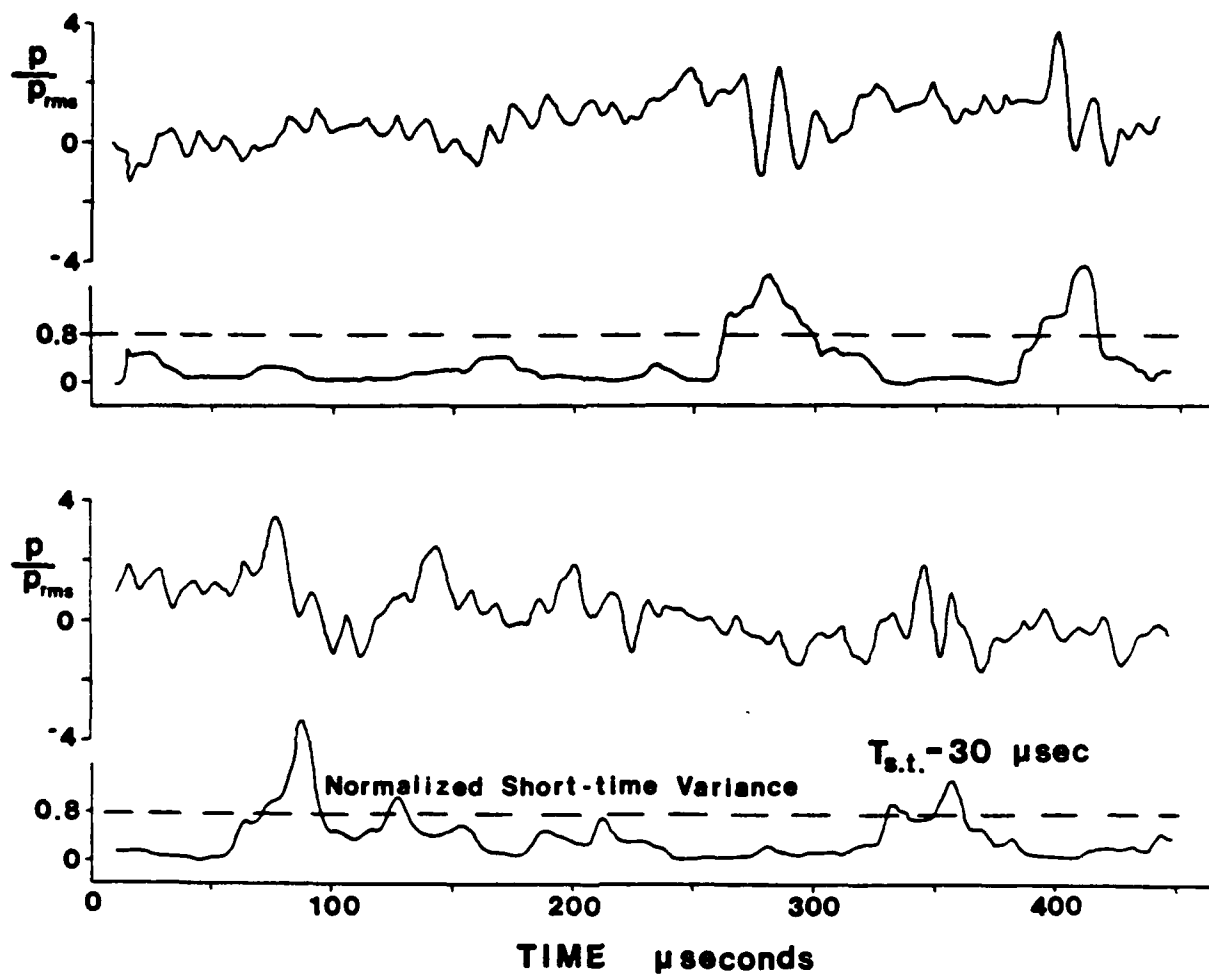


FIGURE 38. Instantaneous wall-pressure signal and its corresponding short-time variance

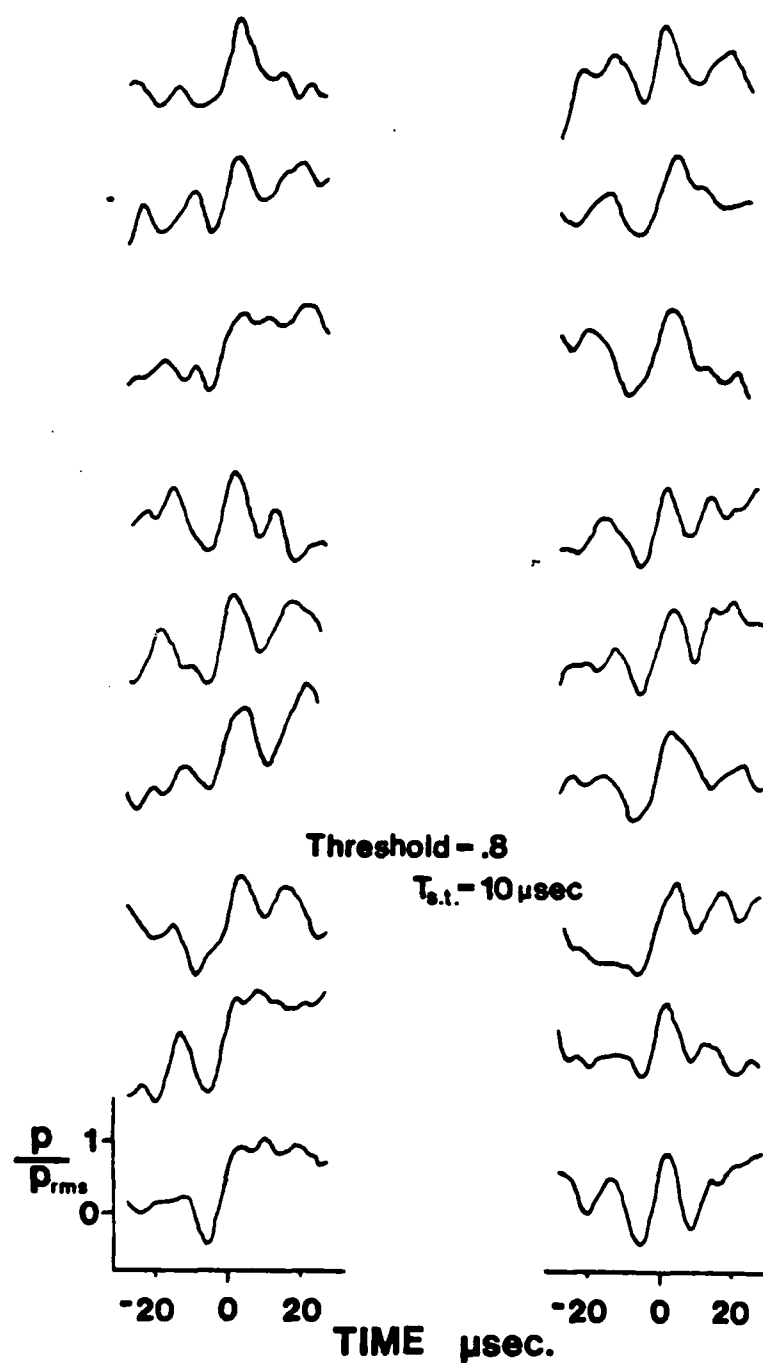


FIGURE 39.

Individual positive pressure events detected with the VITA technique

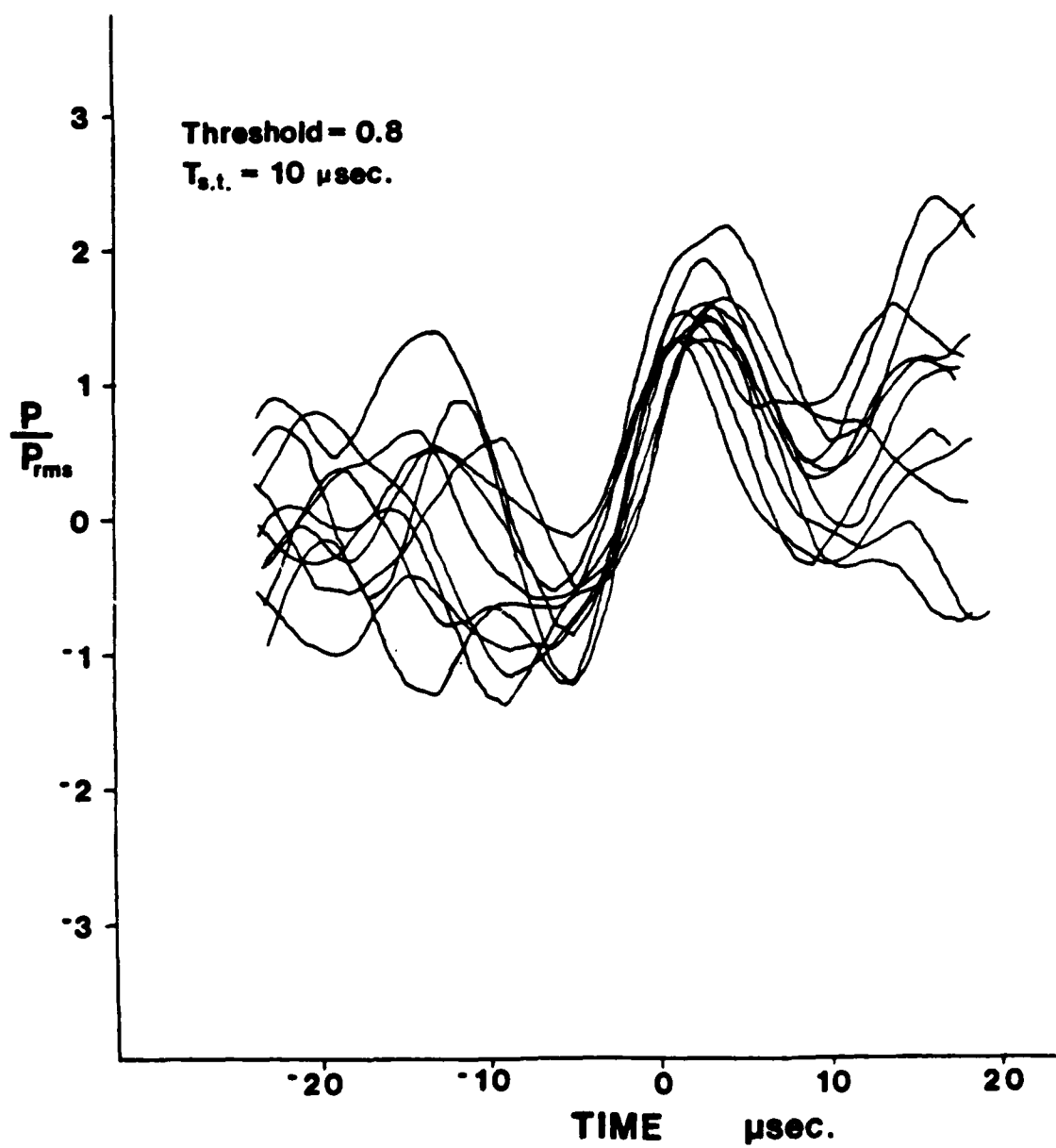


FIGURE 40. Superimposed individual positive pressure events

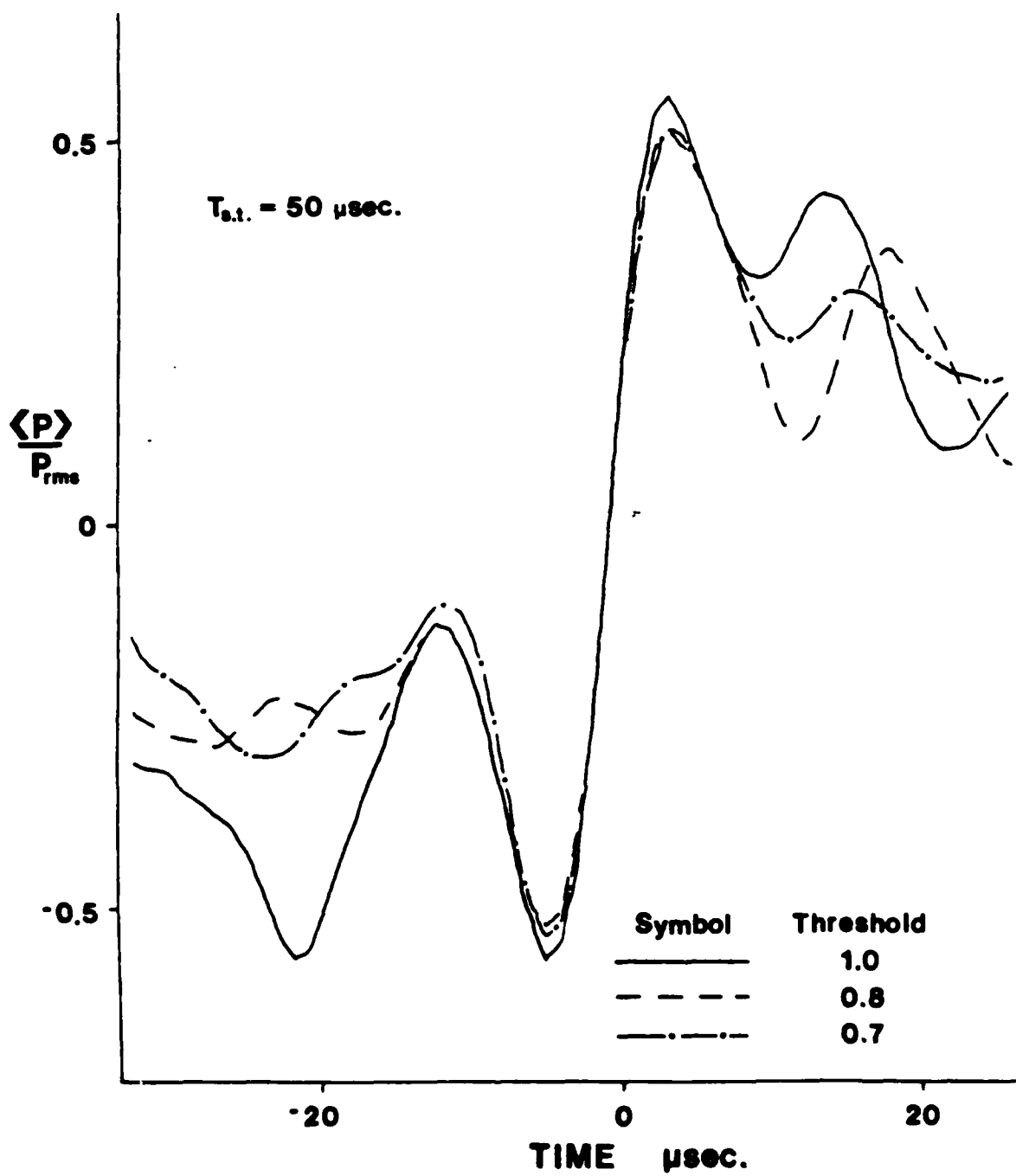


FIGURE 41.

Effect of the threshold level on the average positive pressure event

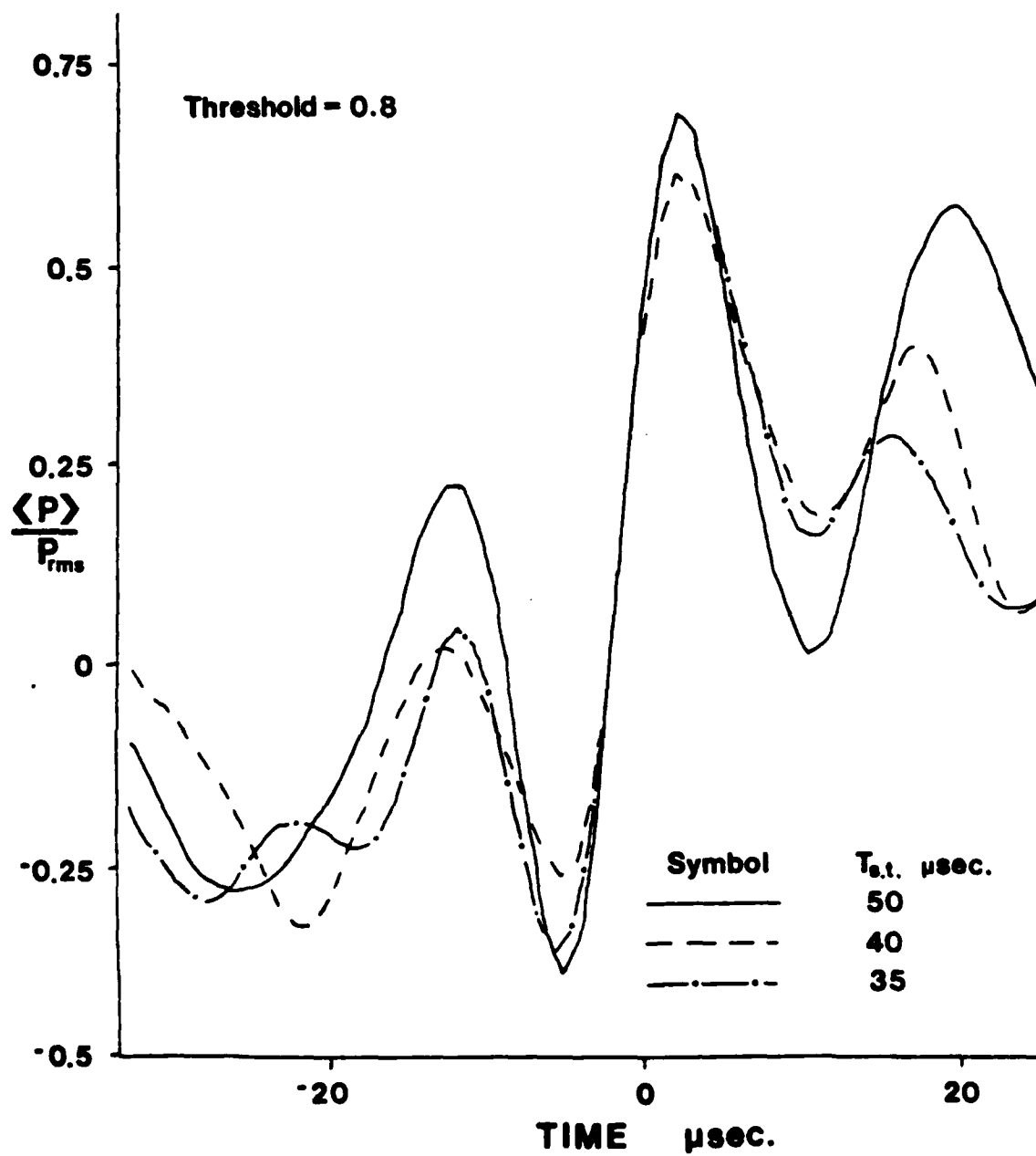


FIGURE 42.

Effect of the short-time variance period on the average positive pressure event

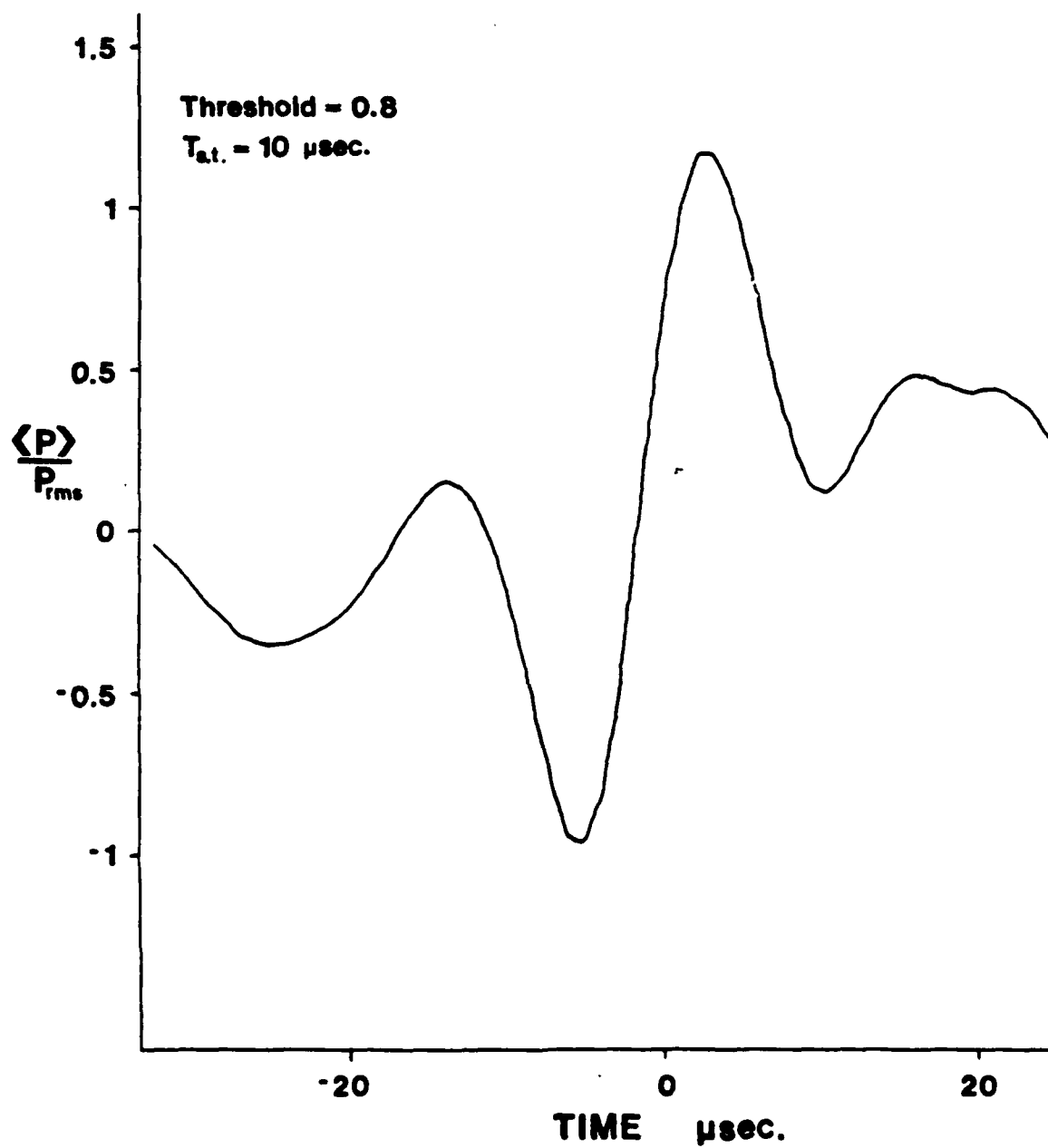


FIGURE 43. "Optimized" average positive pressure event

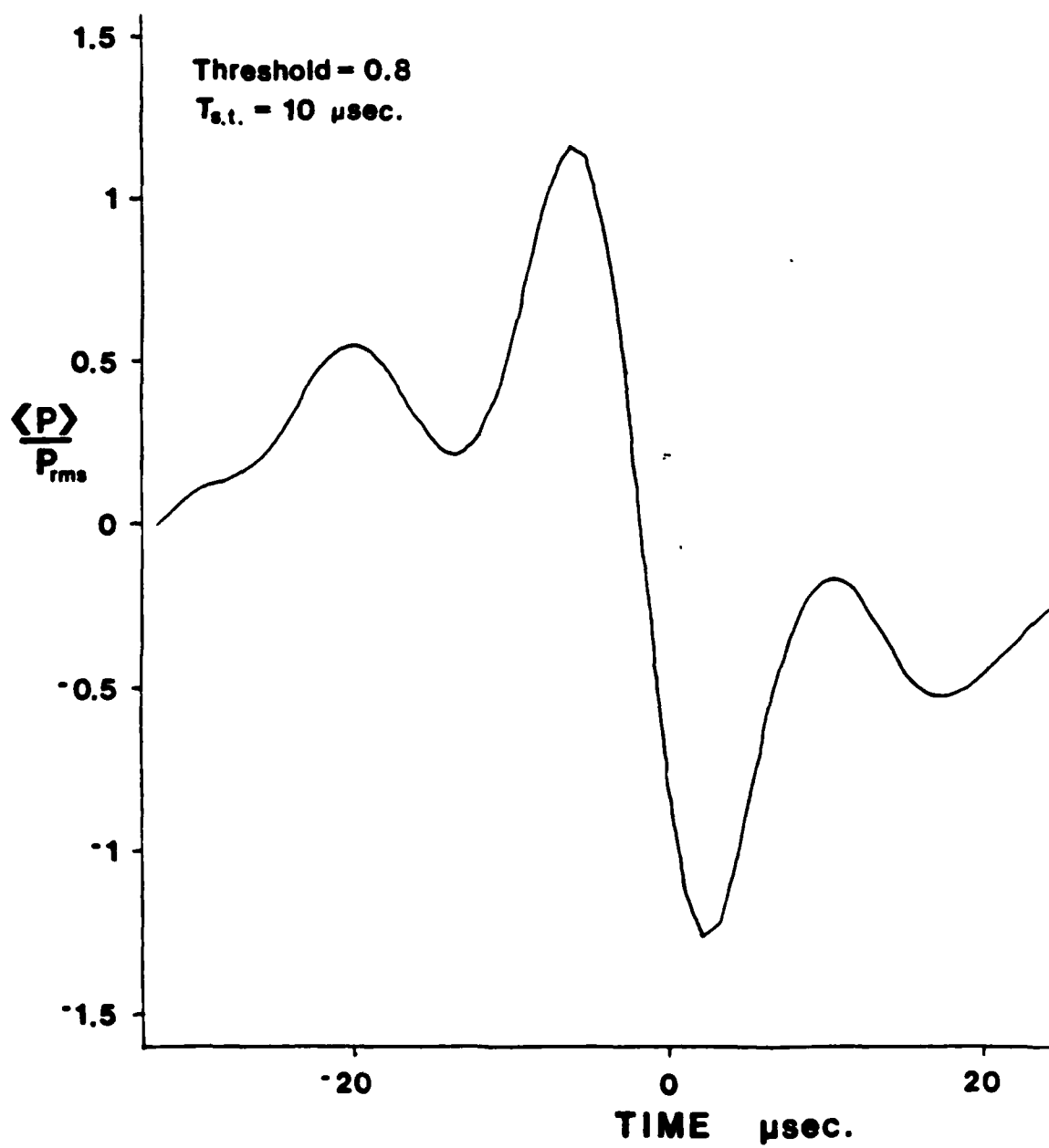


FIGURE 44. "Optimized" average negative pressure event

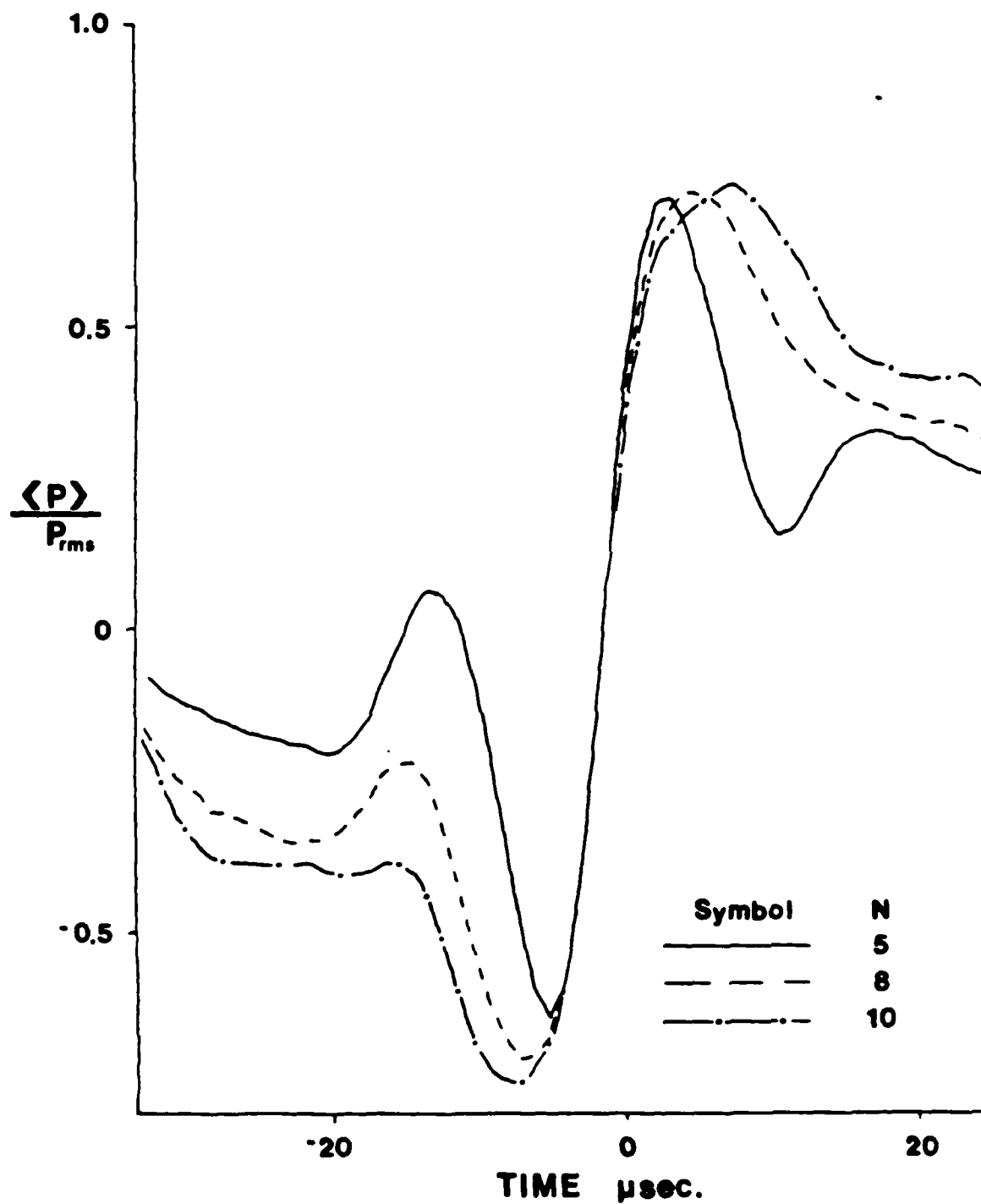


FIGURE 45.

Average positive pressure zerocrossing

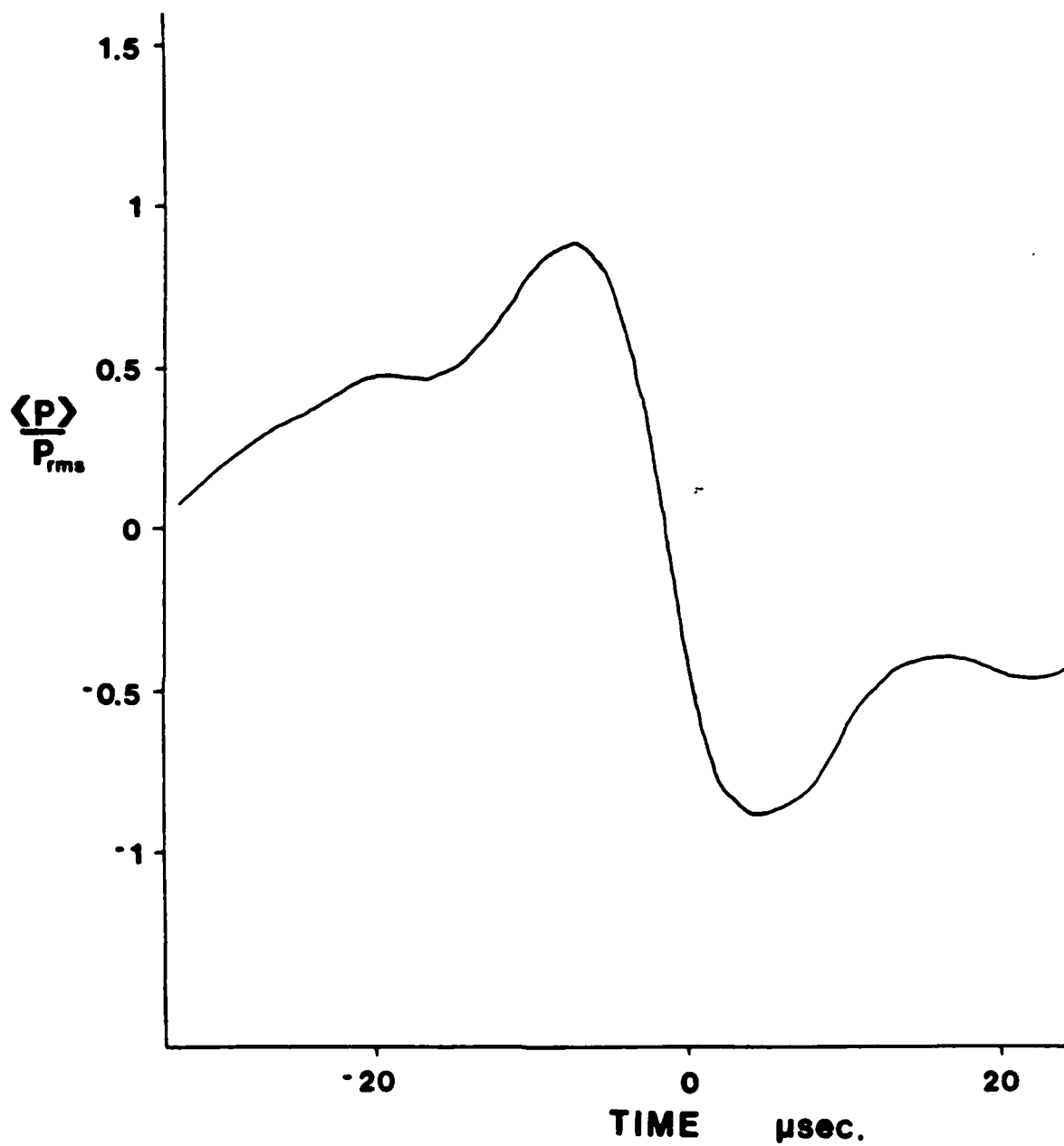


FIGURE 46. Average negative pressure zerocrossing

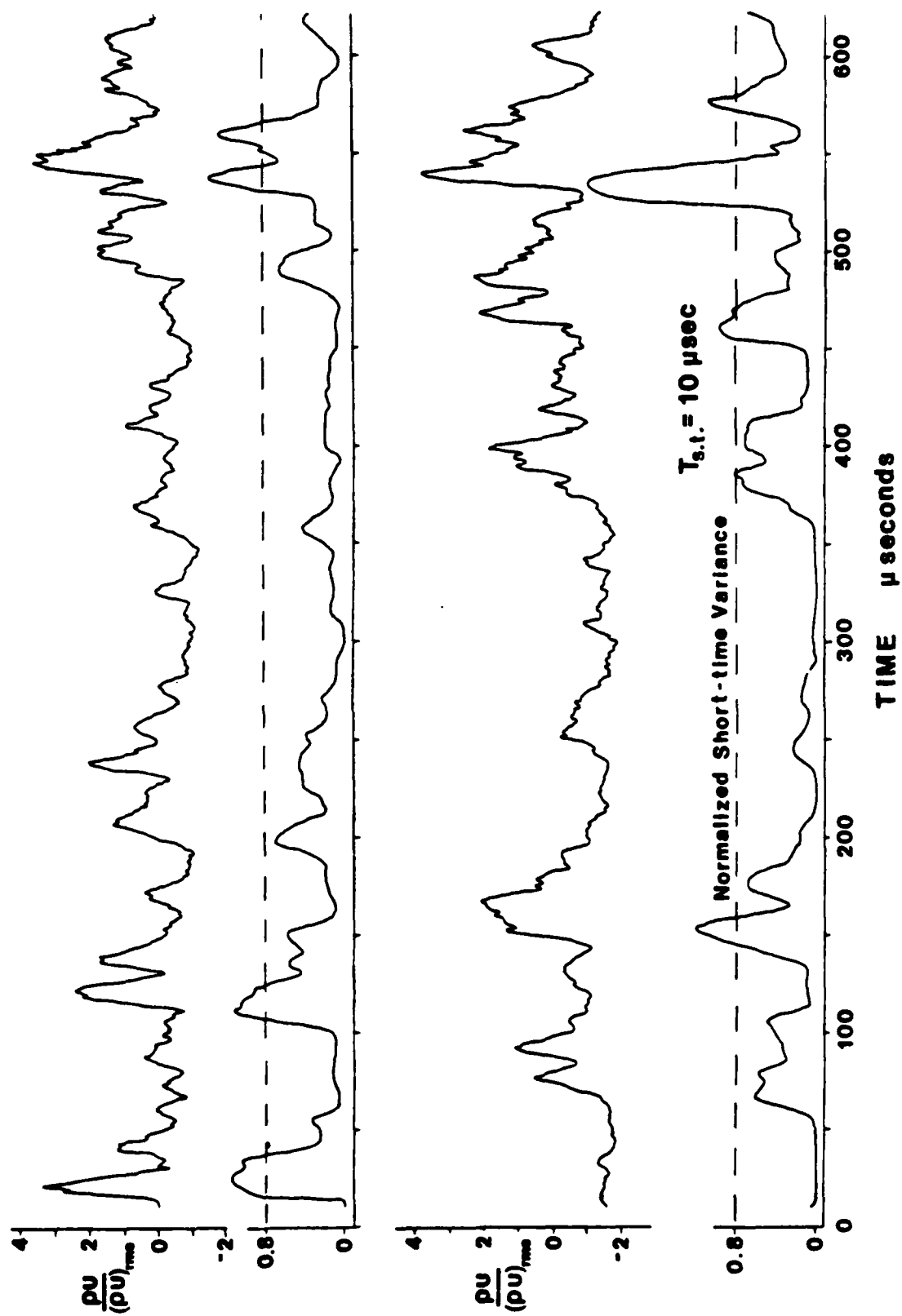


FIGURE 47. Instantaneous mass-flow signal and its corresponding short-time variance

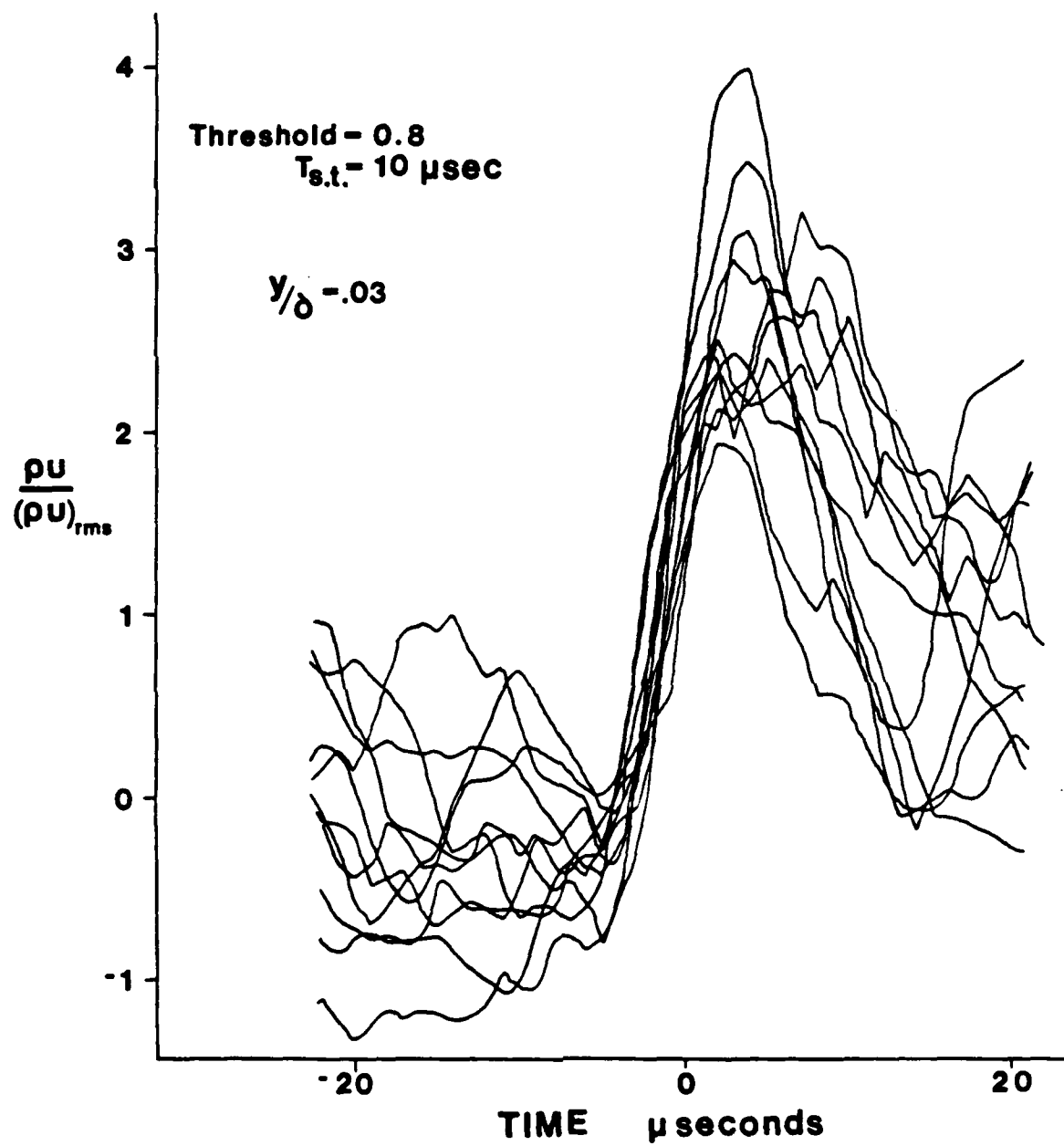


FIGURE 48. Superimposed individual positive mass-flow events

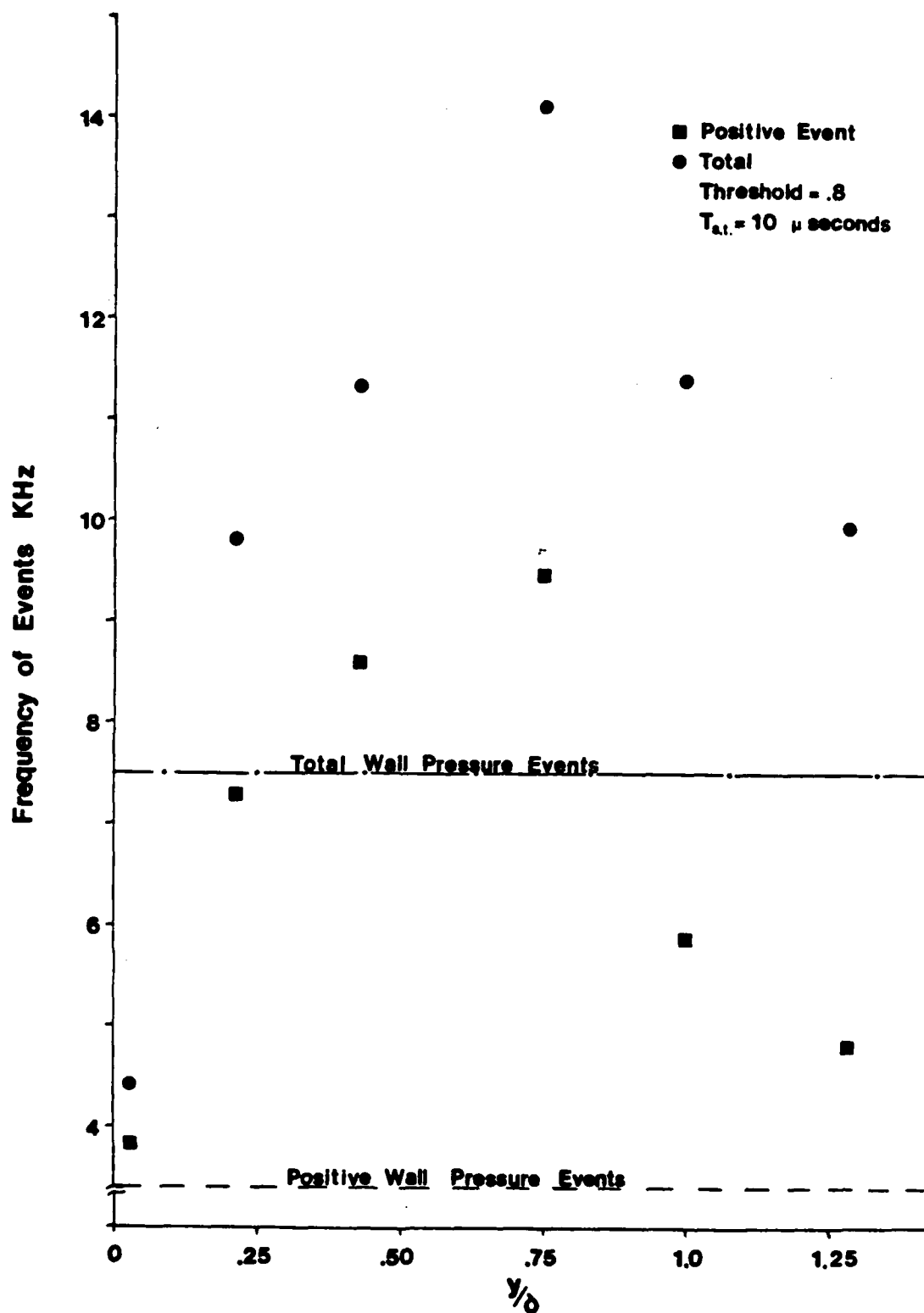


FIGURE 49.

Frequency of mass-flow events in the boundary layer

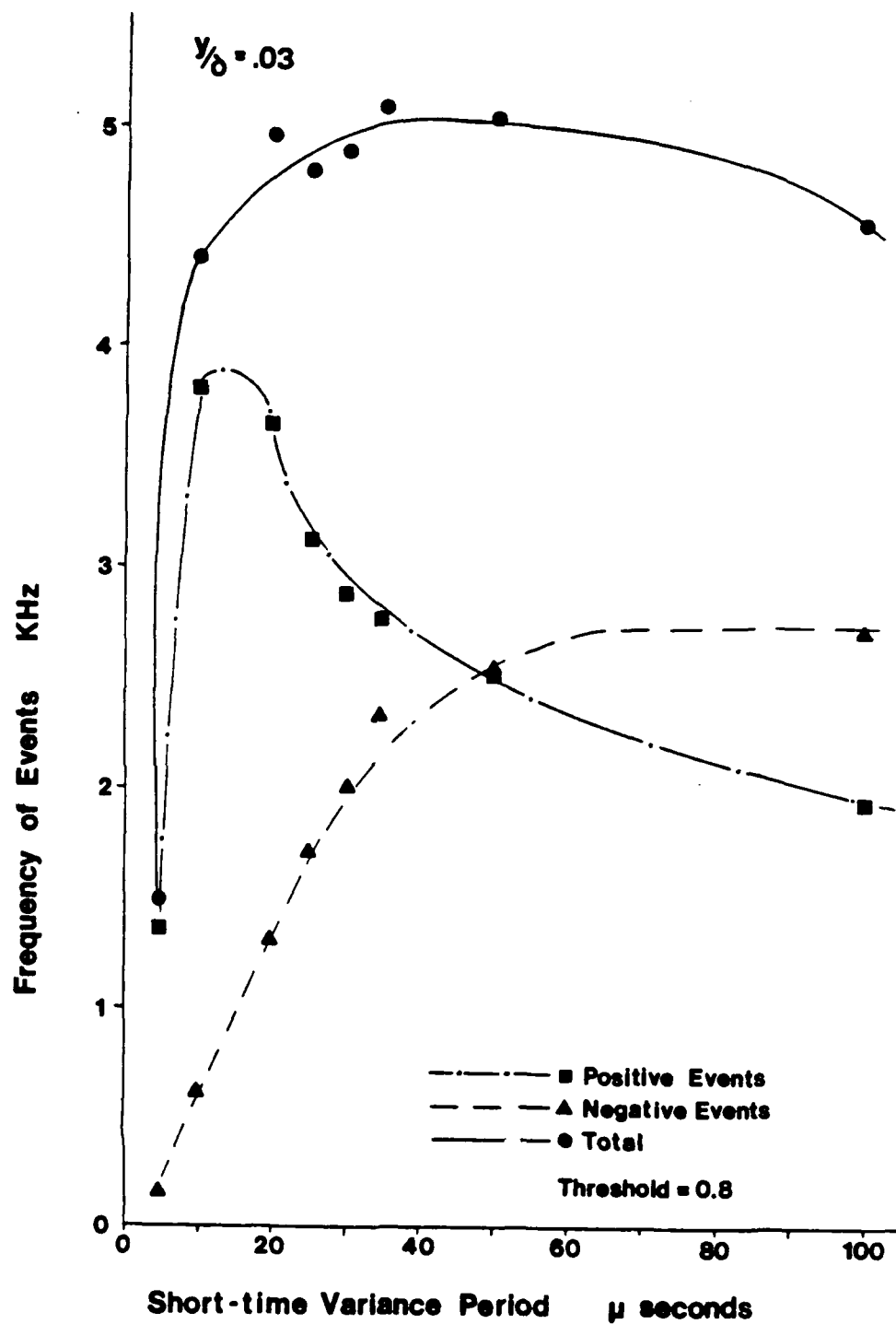


FIGURE 50.

Effect of the short-time variance period on the frequency of mass-flow events

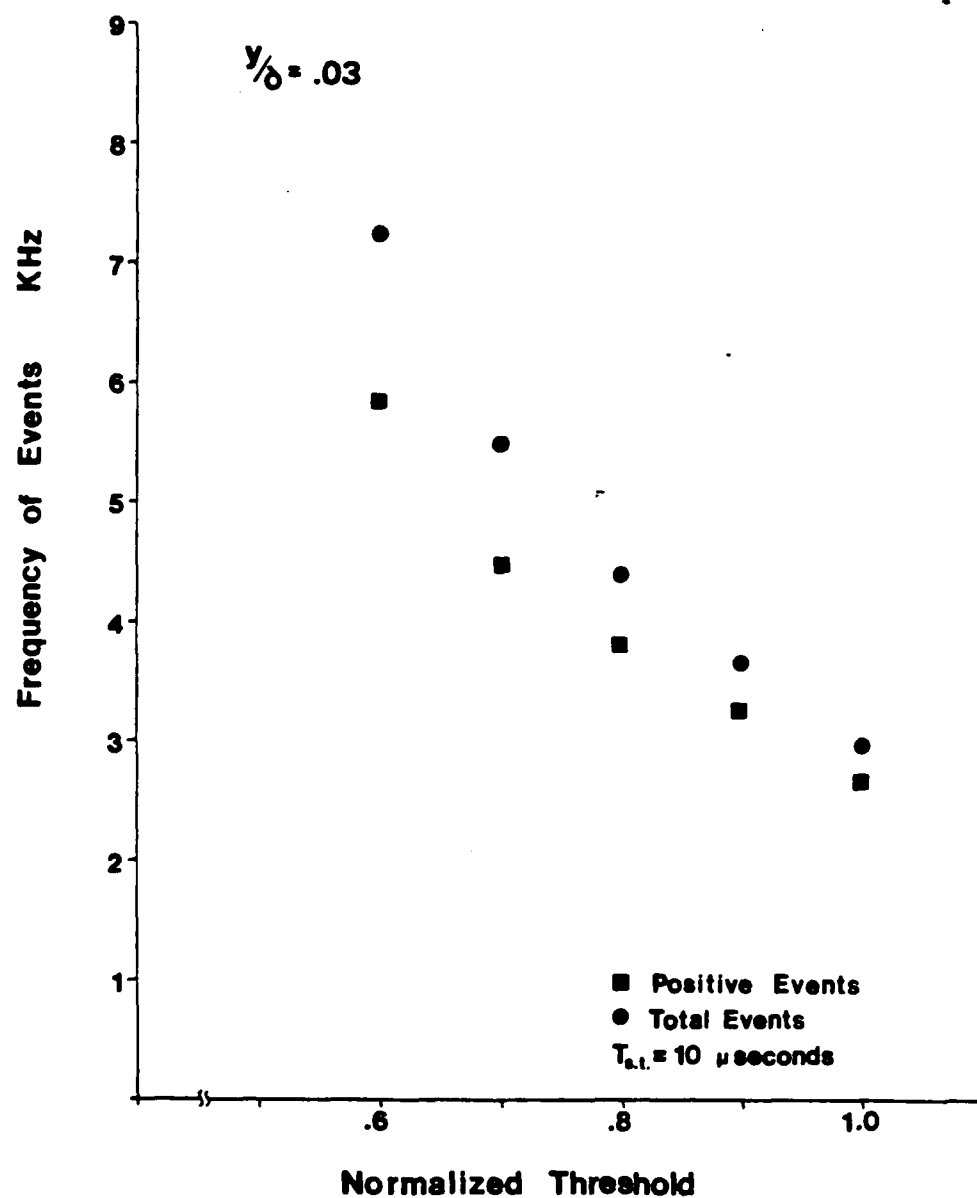


FIGURE 51.

Effect of the threshold level on the frequency of mass-flow events

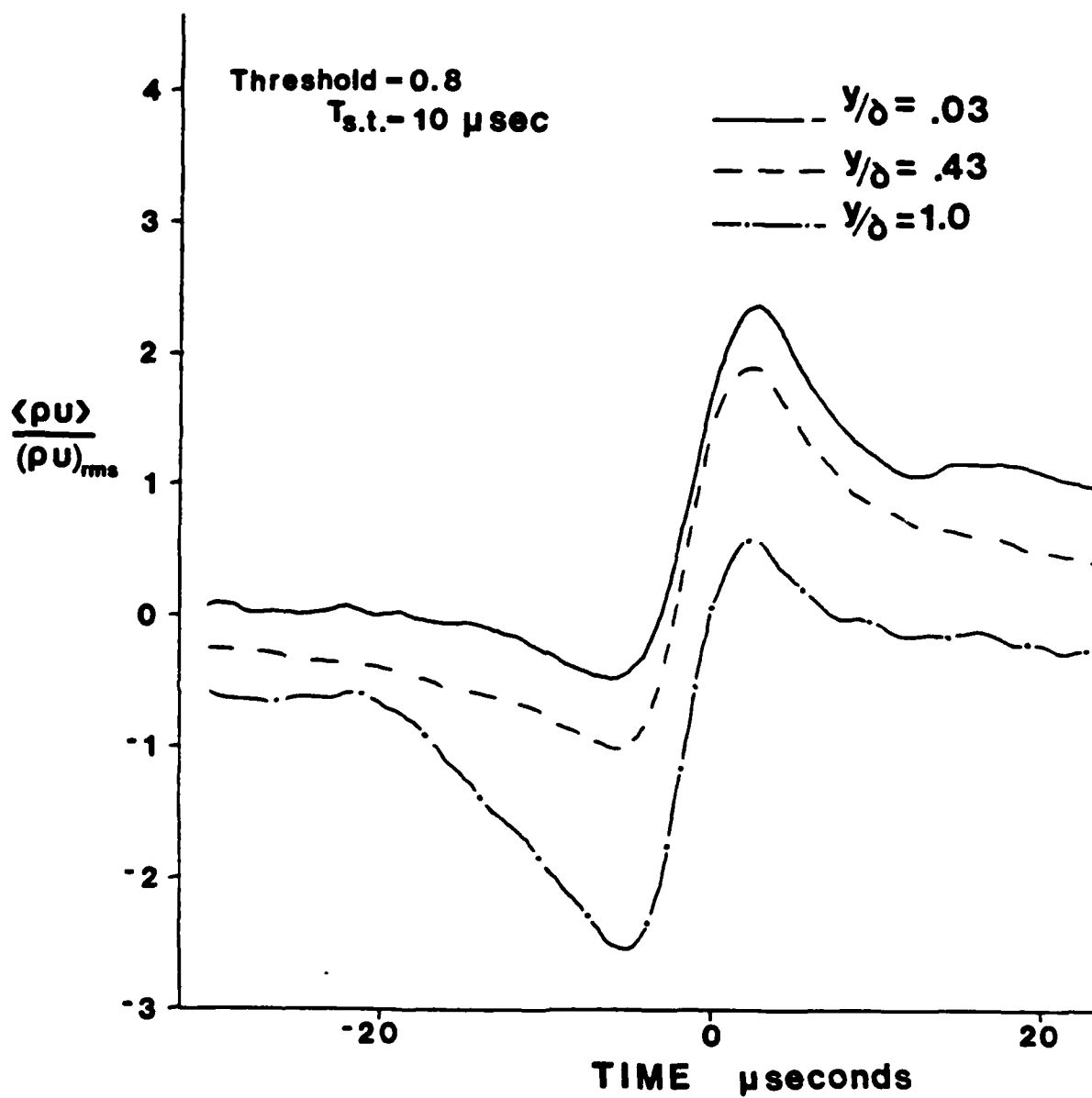


FIGURE 52. "Optimized" average positive mass-flow events at three points the boundary layer

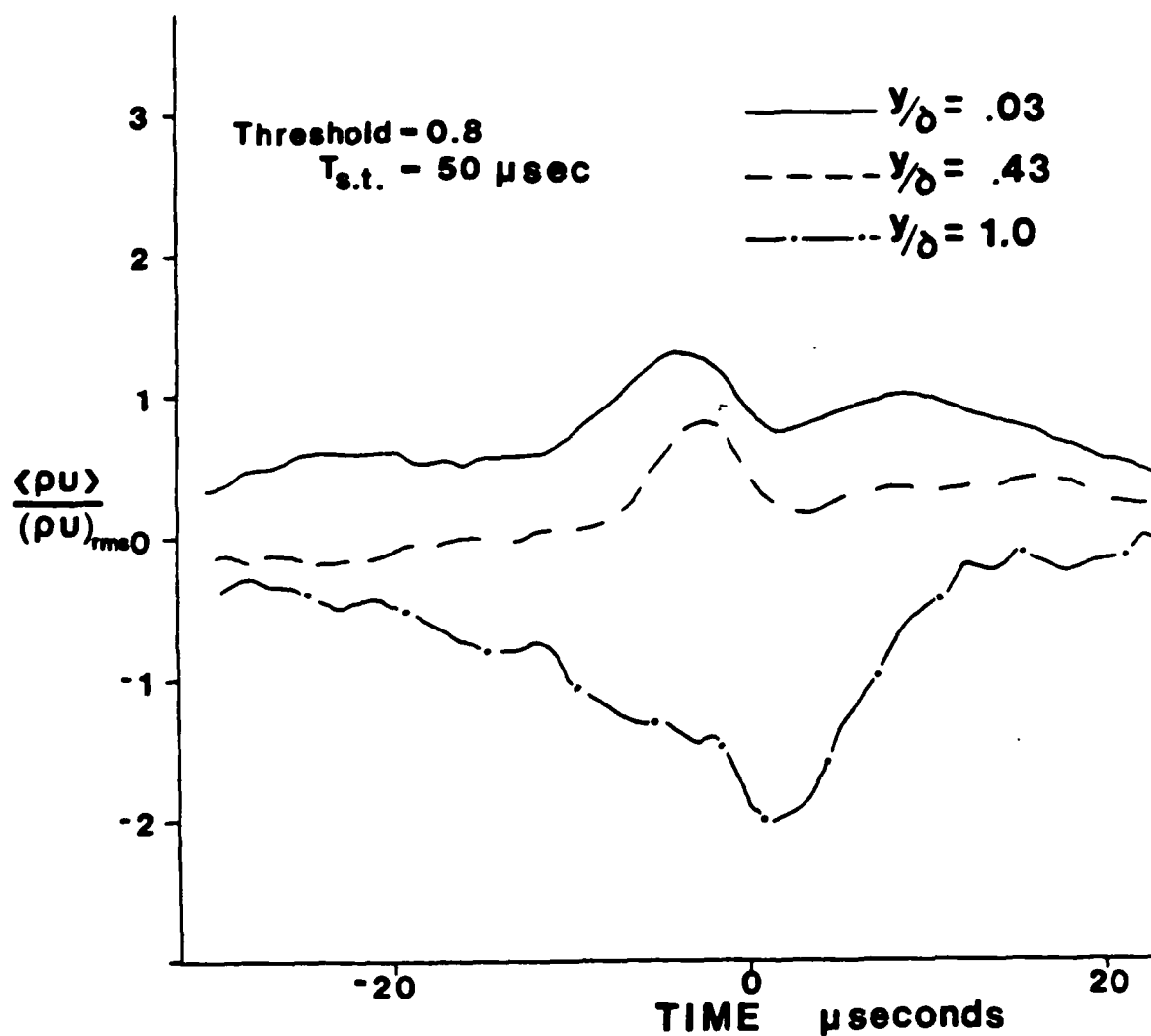


FIGURE 53.

"Optimized" average negative mass-flow events at three points through the boundary layer

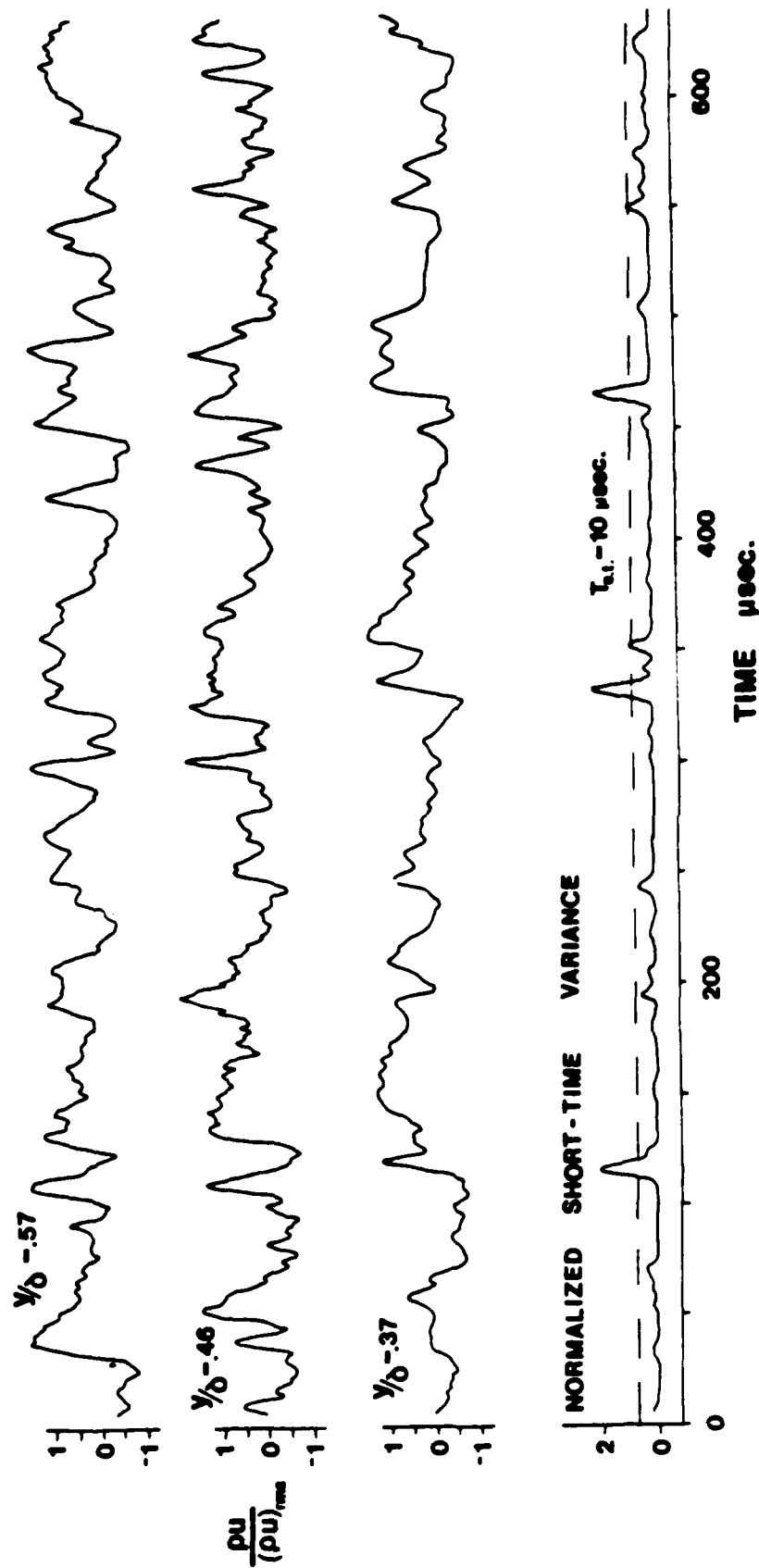


FIGURE 54. Three simultaneously measured, instantaneous mass-flow signals with their corresponding short-time variances

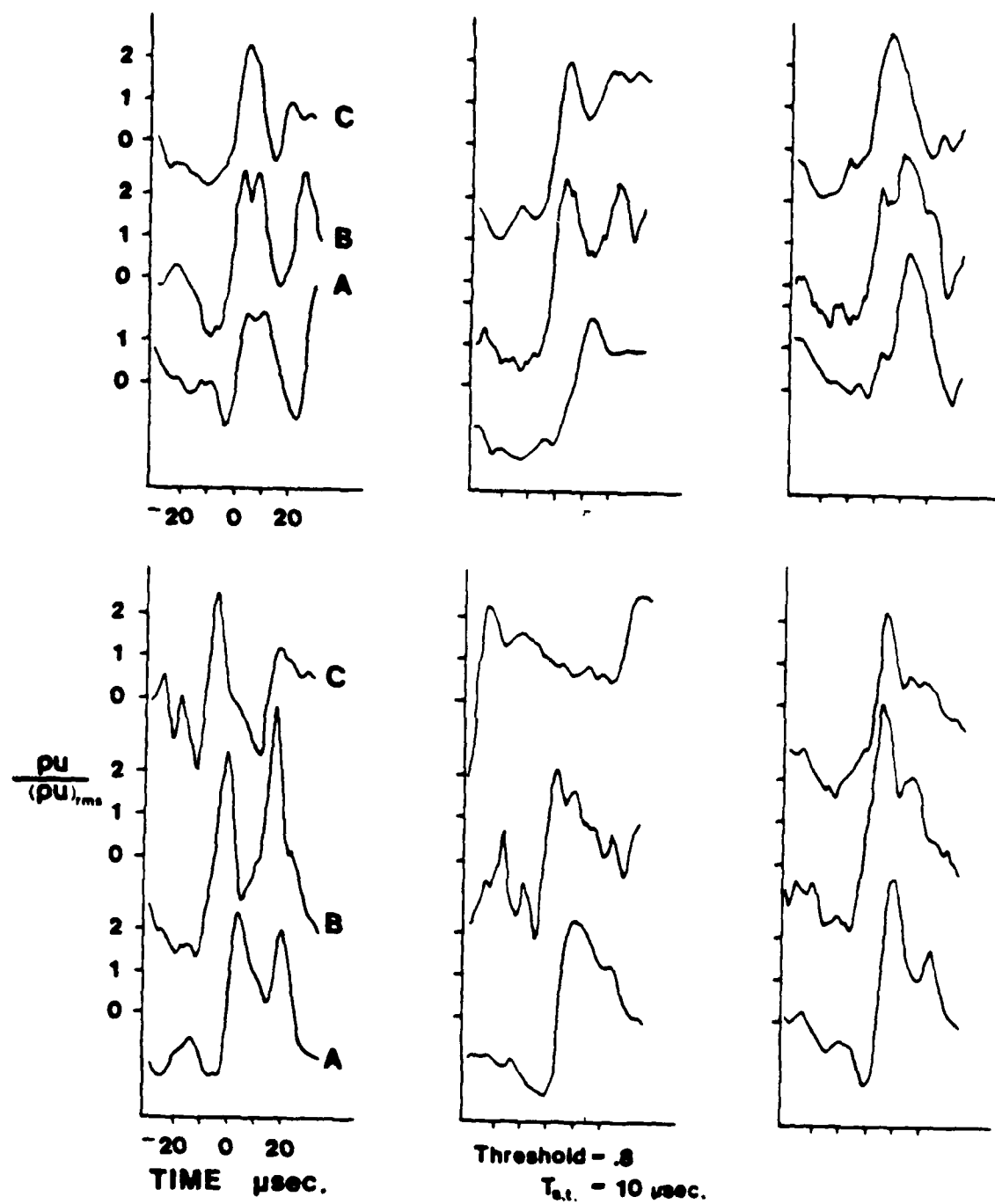


FIGURE 55.

Individual mass-flow events from the three-wire probe. Signals conditioned upon Wire B. Wires located at : A - $y/\delta = 0.37$; B - $y/\delta = 0.46$; C - $y/\delta = 0.57$

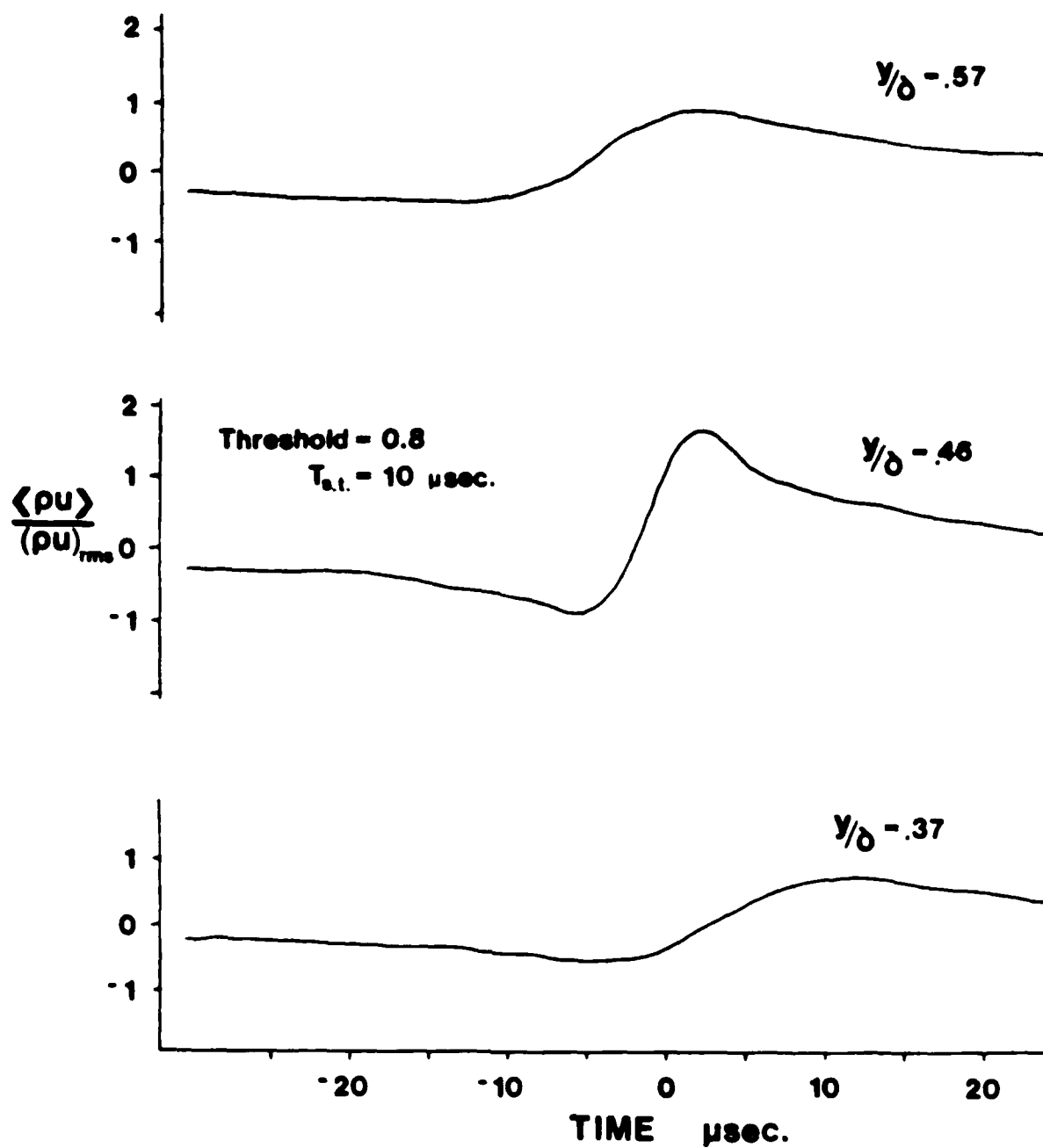


FIGURE 56.

"Optimized" average positive mass-flow events from the three-wire probe. Signals conditioned upon the middle wire

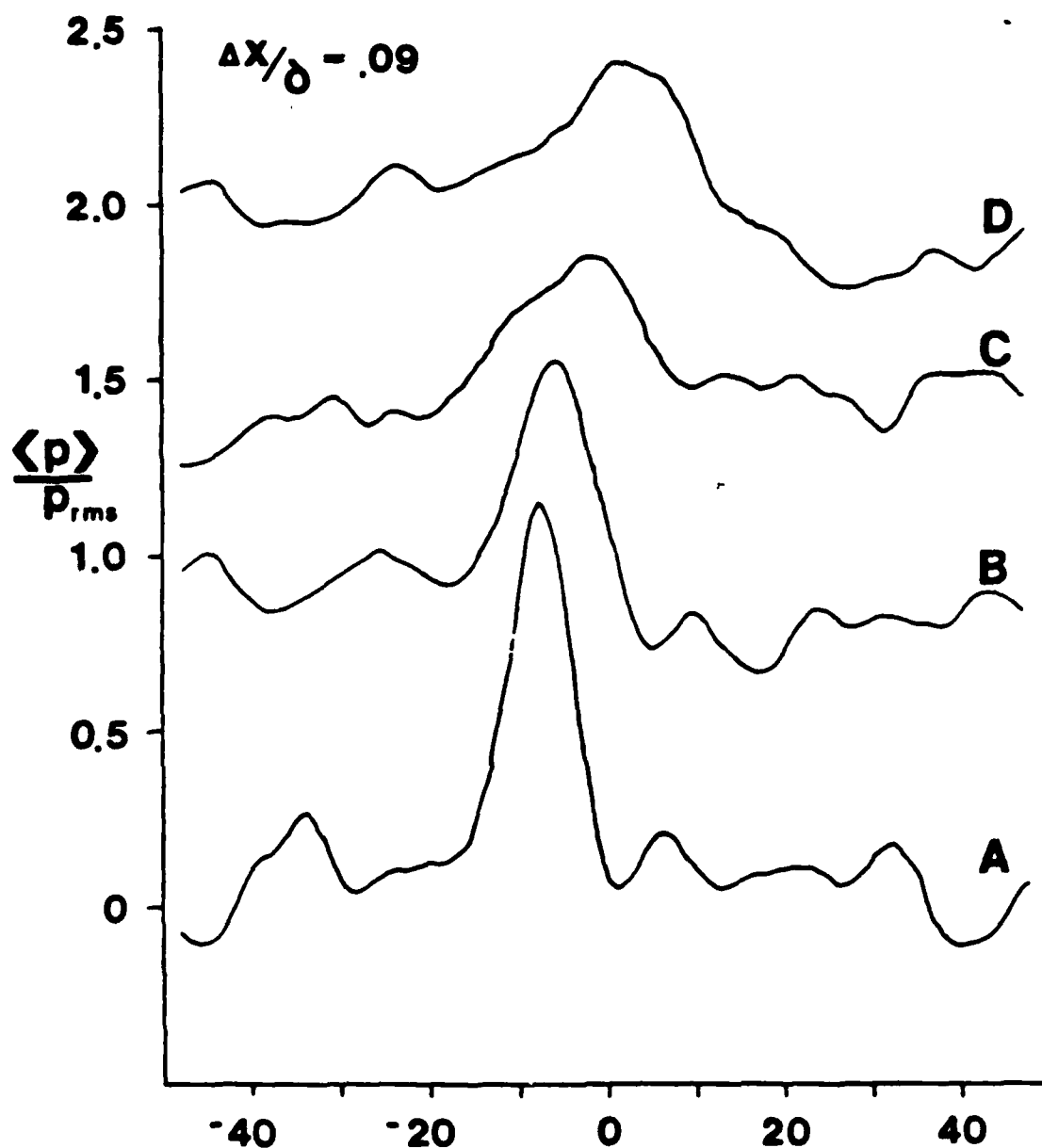


FIGURE 57.

Average positive pressure events conditioned upon mass-flow events from different locations in the boundary layer. The detection wire was located at: A) $y/\delta = 0.03$; B) $y/\delta = 0.13$; C) $y/\delta = 0.22$; D) $y/\delta = 0.30$

(a) Pressure transducer located 0.096 upstream of the hot-wire probe

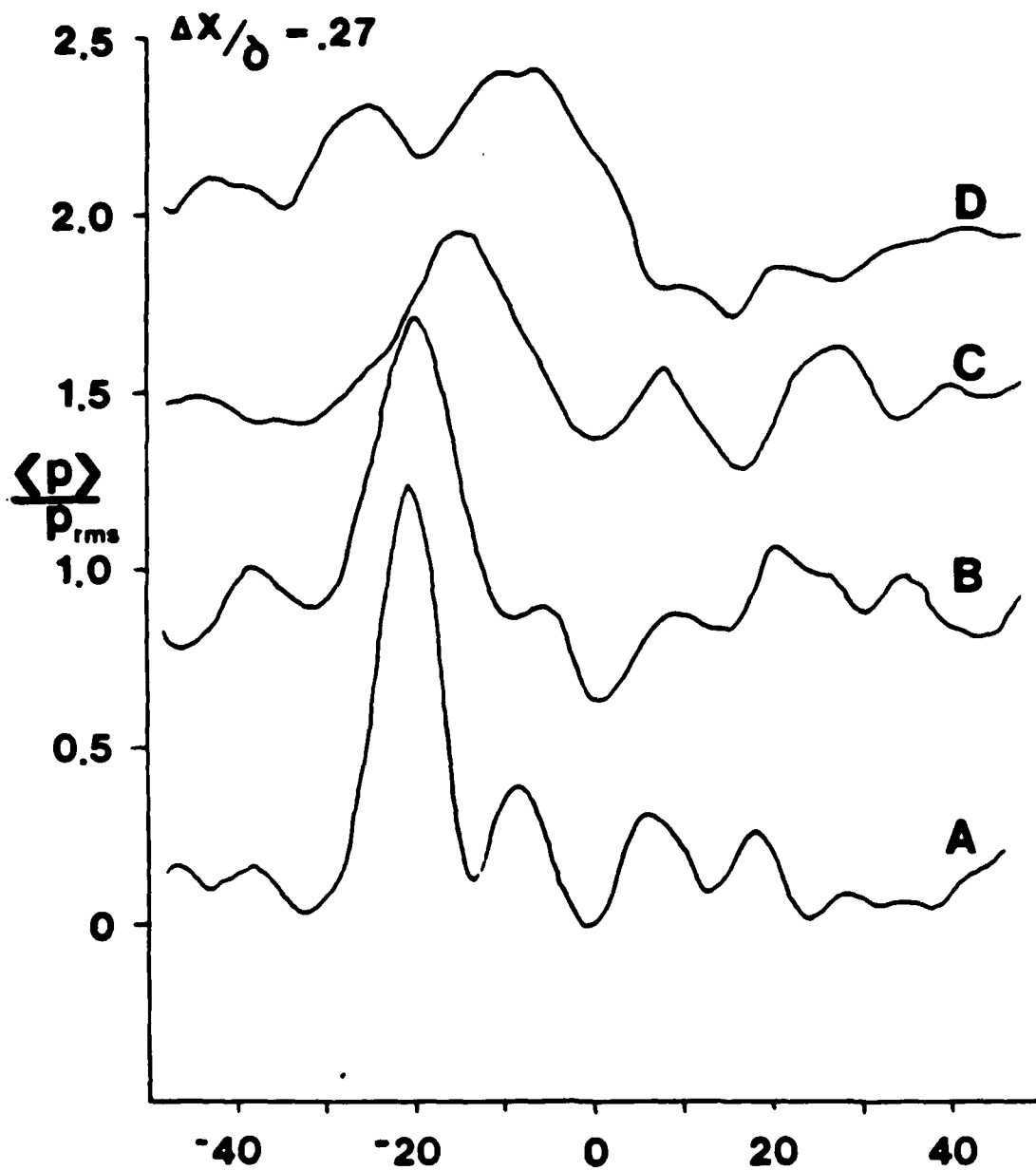


FIGURE 57 b

Pressure transducer located 0.276 upstream of
hot-wire probe

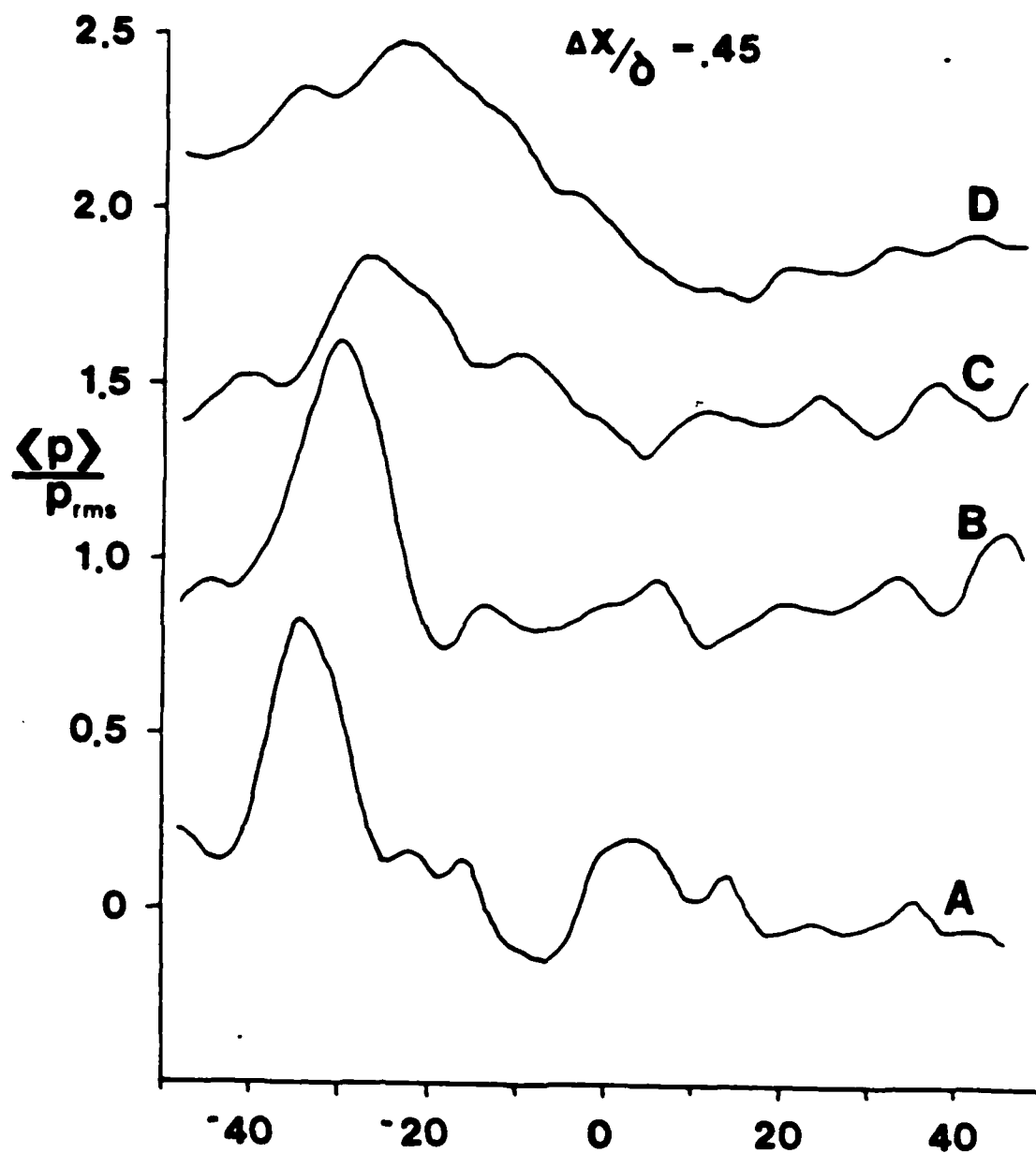


FIGURE 57 c

Pressure transducer located 0.45 δ upstream of the hot-wire probe

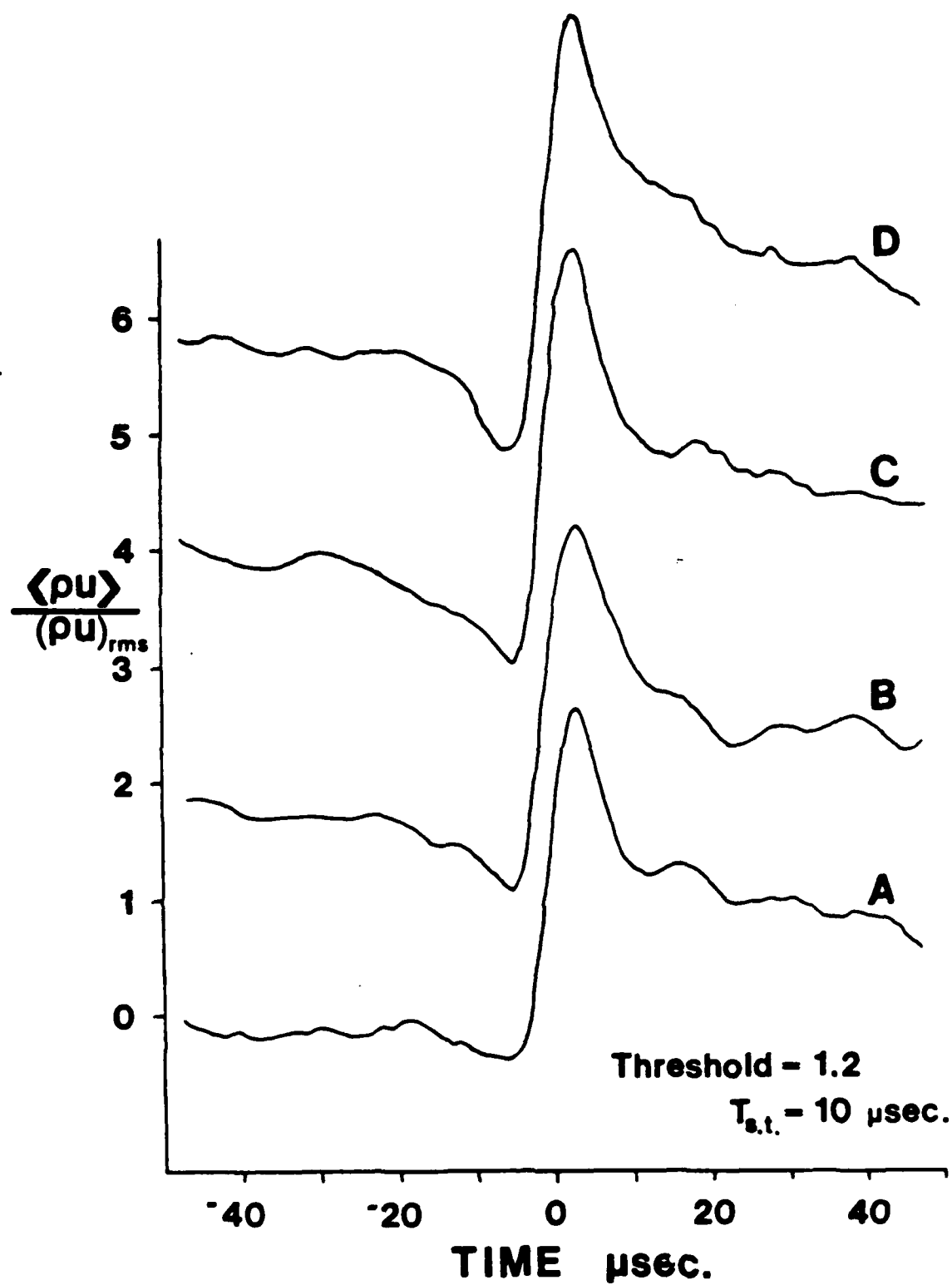


FIGURE 57 d

Average positive mass-flow events from which pressure events were detected

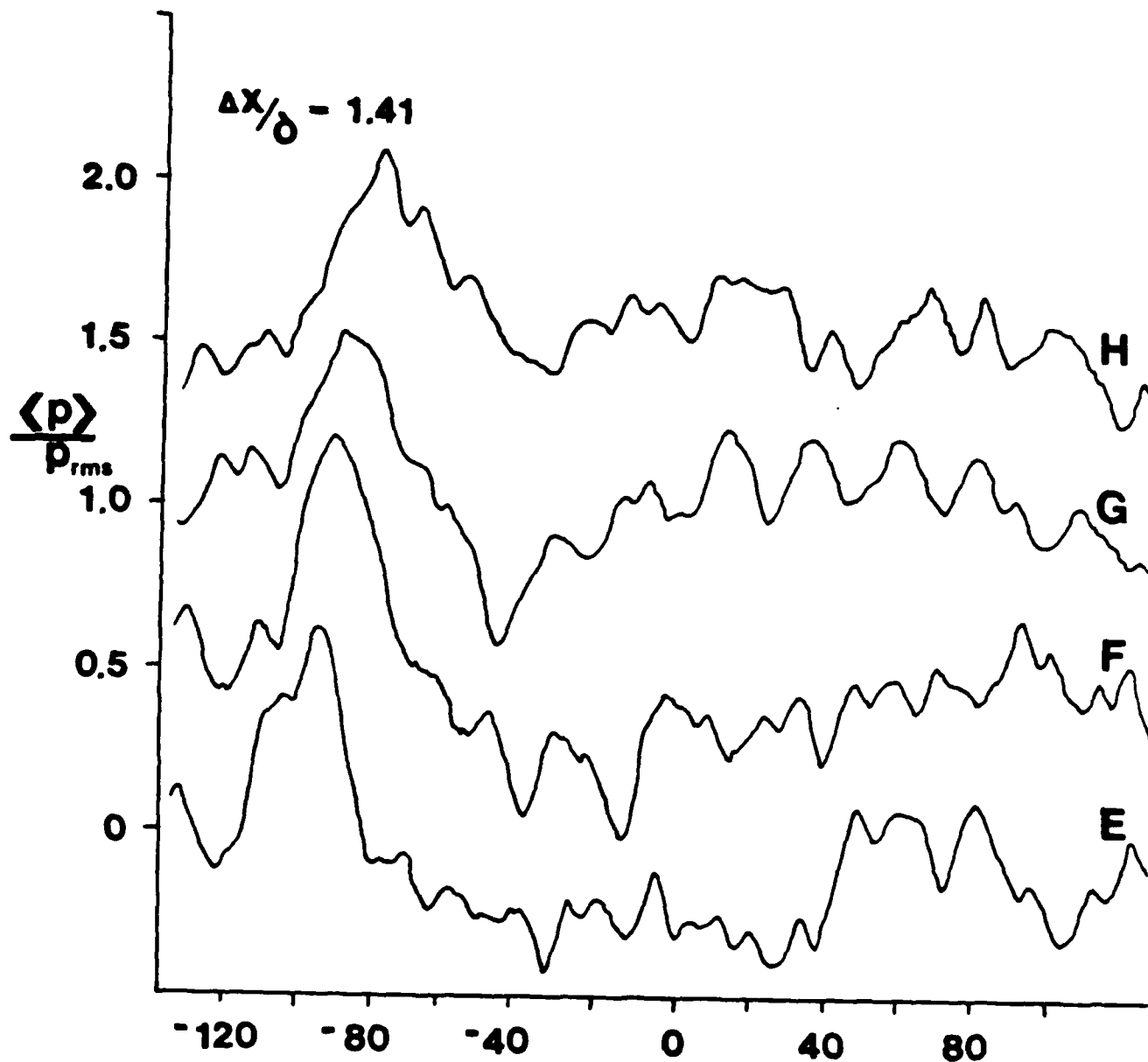


FIGURE 58.

Average positive pressure events conditioned upon mass-flow events from different locations in the boundary layer. The detection wire was located at:
 E) $y/\delta = 0.03$; F) $y/\delta = 0.12$; G) $y/\delta = 0.21$;
 H) $y/\delta = 0.30$

(a) Pressure transducer located 1.41 δ upstream of the hot-wire probe

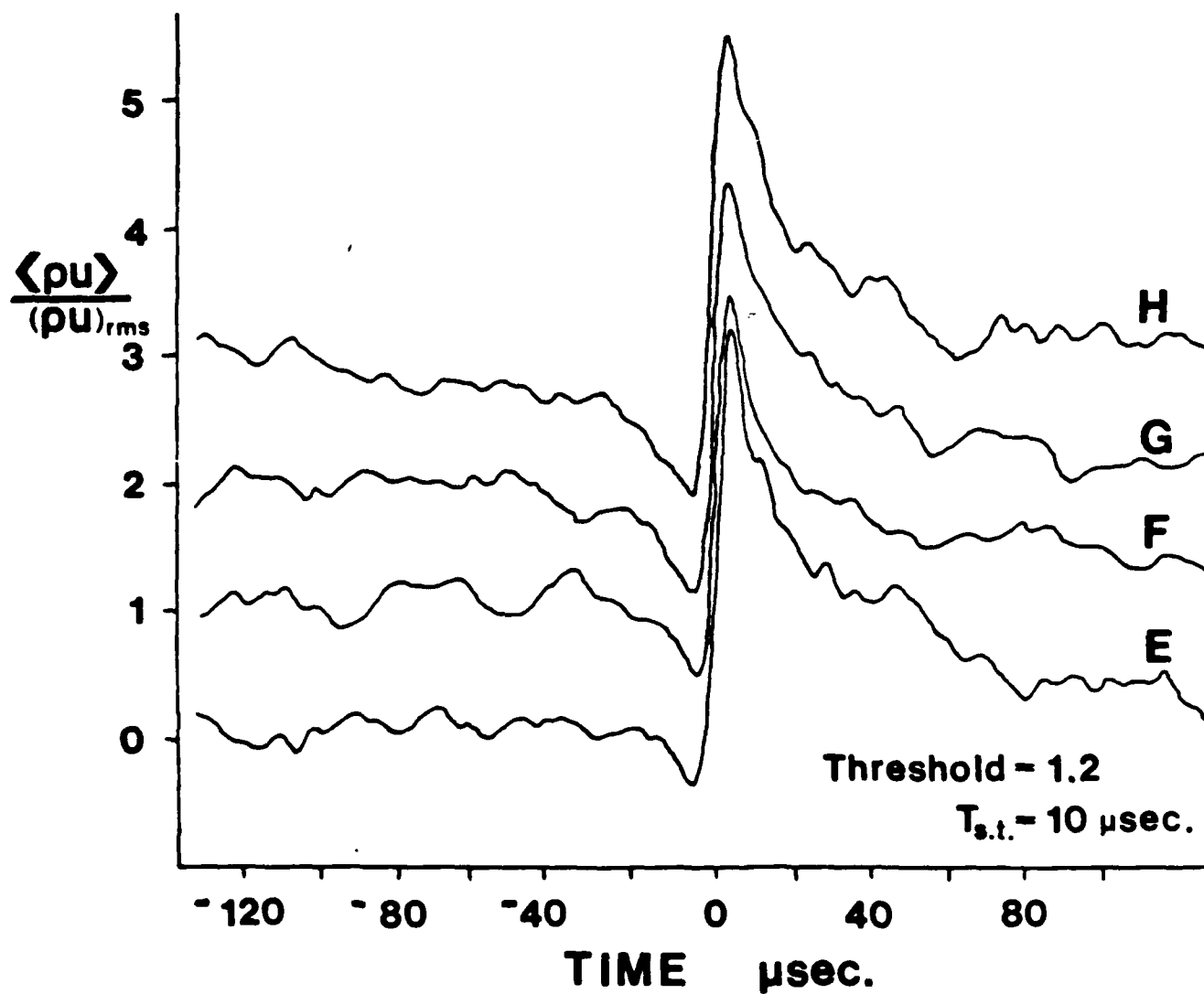


FIGURE 58 b

Average positive mass-flow events from which
pressure events were detected

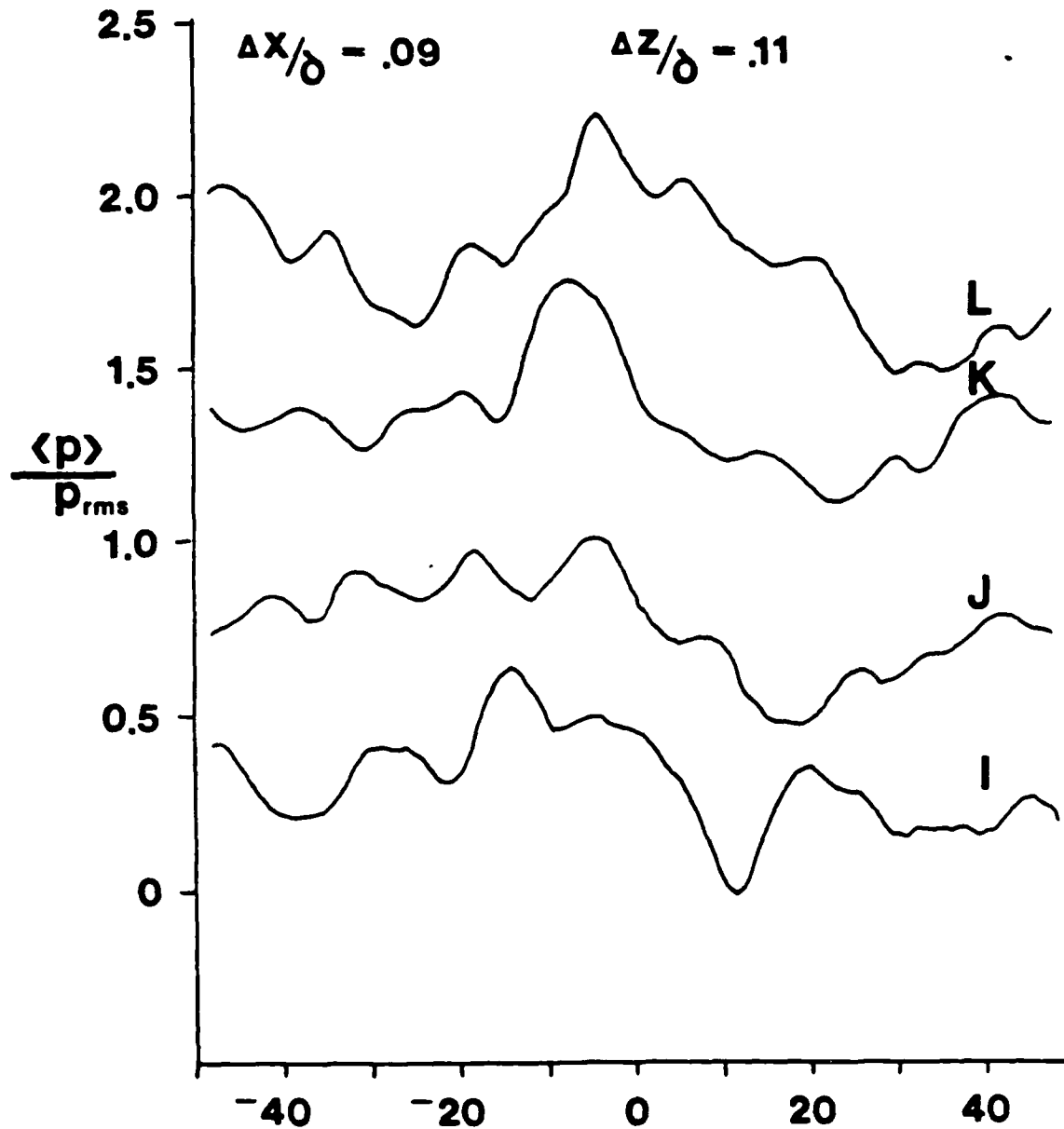


FIGURE 59.

Average positive pressure events conditioned upon mass-flow events from different locations in the boundary layer. The detection wire was located at:
 I) $y/\delta = 0.03$; J) $y/\delta = 0.08$; K) $y/\delta = 0.15$;
 L) $y/\delta = 0.20$

(a) Pressure transducer located 0.09δ upstream and 0.11δ laterally from the hot-wire probe

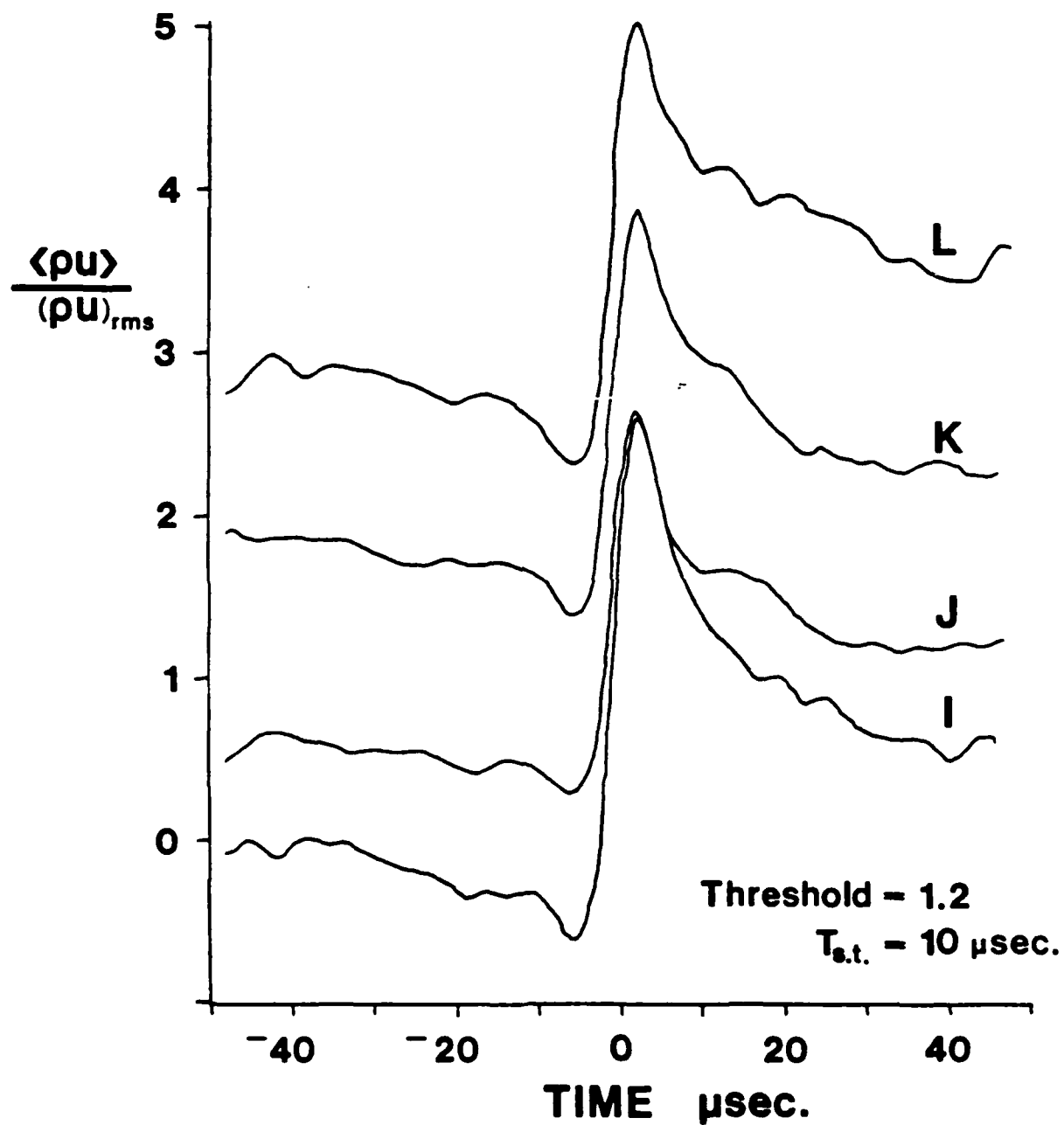


FIGURE 59 (b)

Average positive mass-flow events from which pressure events were detected.

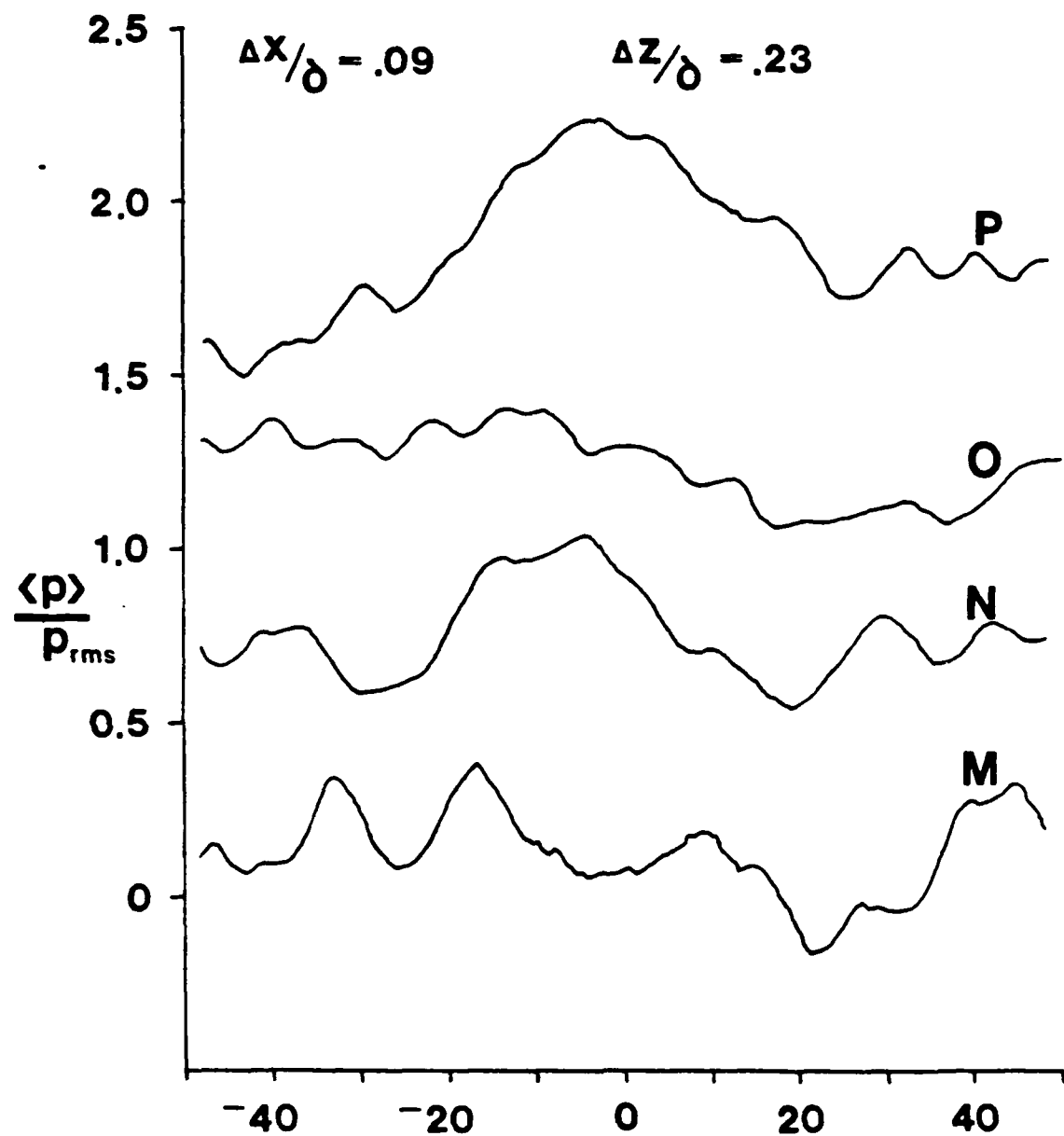


FIGURE 60.

Average positive pressure events conditioned upon mass-flow events from different locations in the boundary layer. The detection wire was located at: M) $y/\delta = 0.03$; N) $y/\delta = 0.08$; O) $y/\delta = 0.16$; P) $y/\delta = 0.23$

- (a) Pressure transducer located 0.09 δ upstream and 0.23 δ laterally from the hot-wire probe

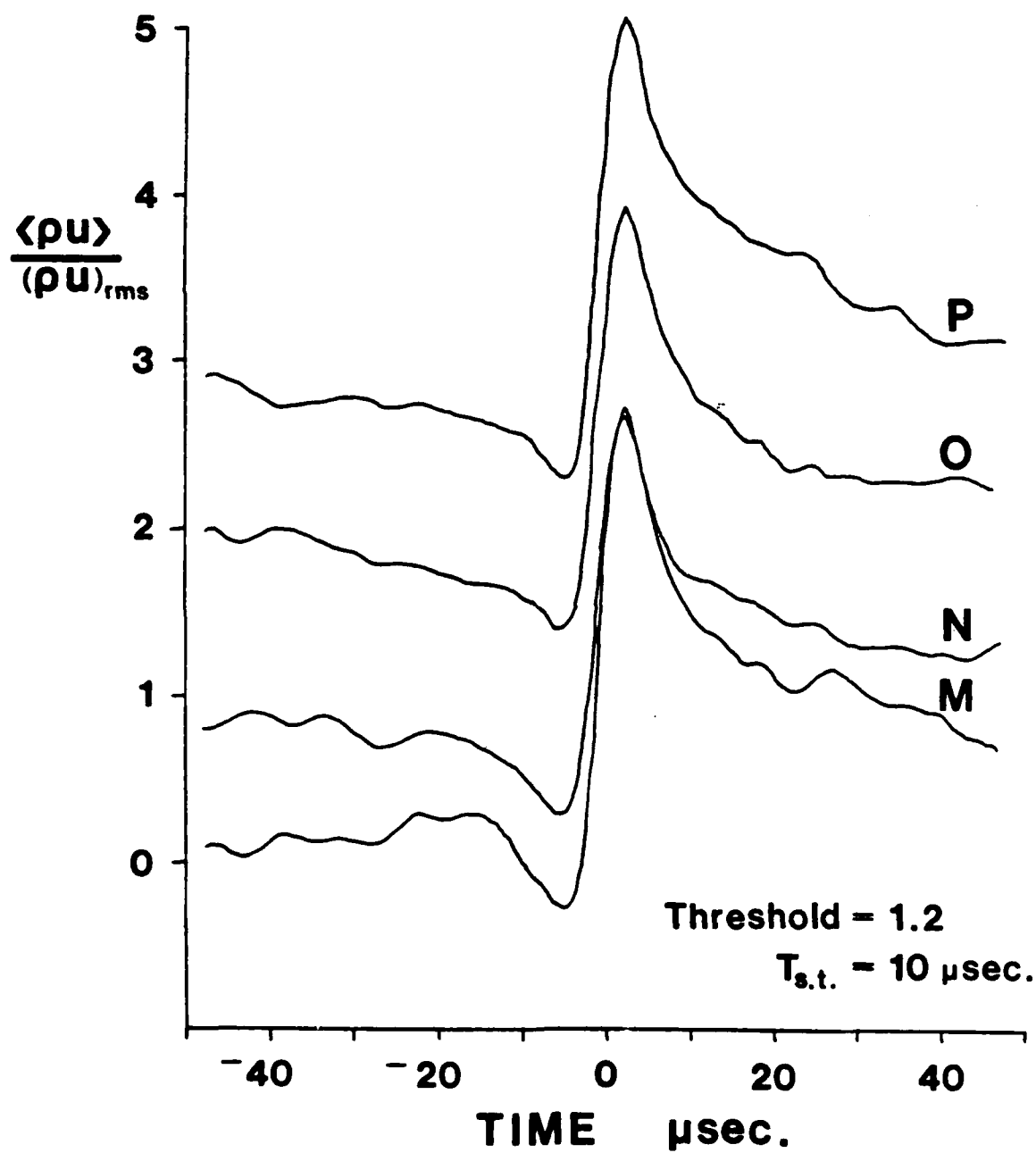


FIGURE 60 (b)

Average positive mass-flow events from which
pressure events were detected

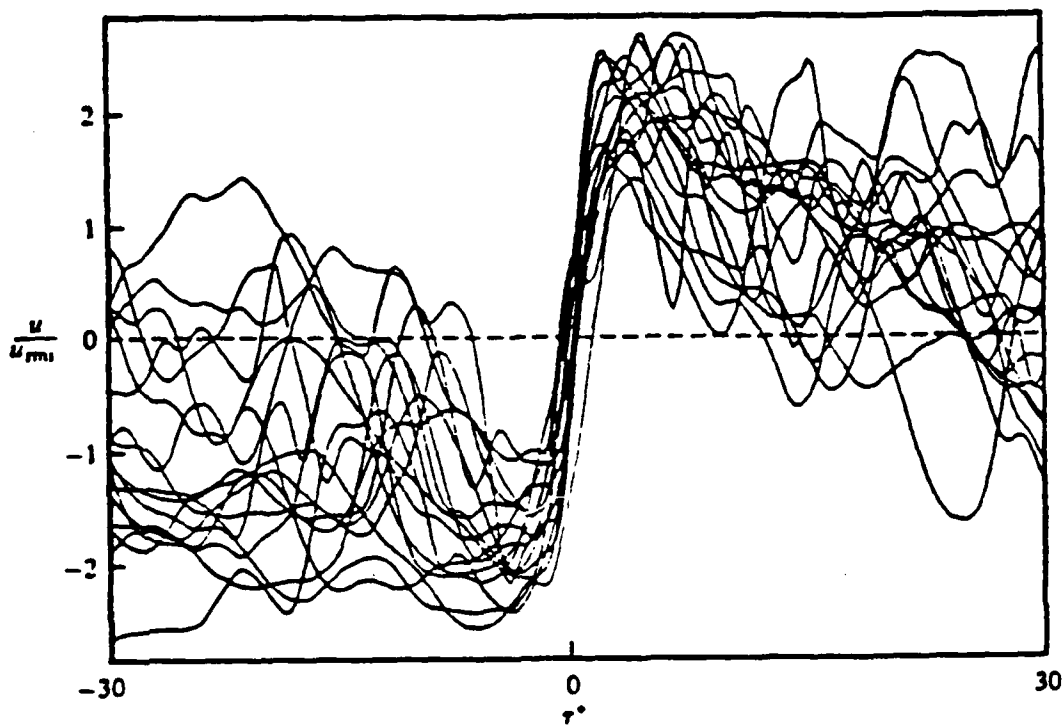


FIGURE 61.

Individual streamwise velocity events detected by the VITA technique at $y^+ = 13$ (Alfredsson and Johansson, 1982)

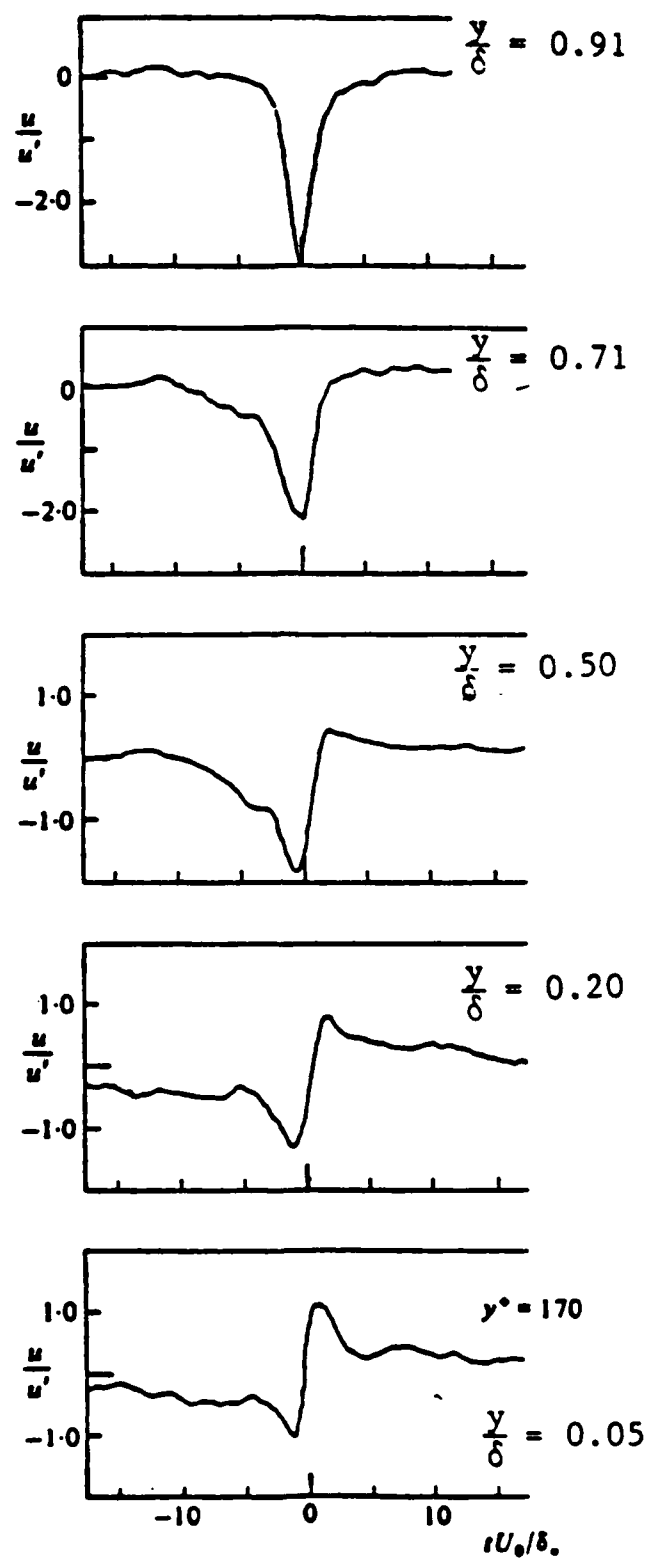


FIGURE 62.

Ensemble-average time histories of the conditionally sampled streamwise velocity. Detection is based on smoothed rectified high frequency u -component at each y -value (Thomas and Bull, 1983)

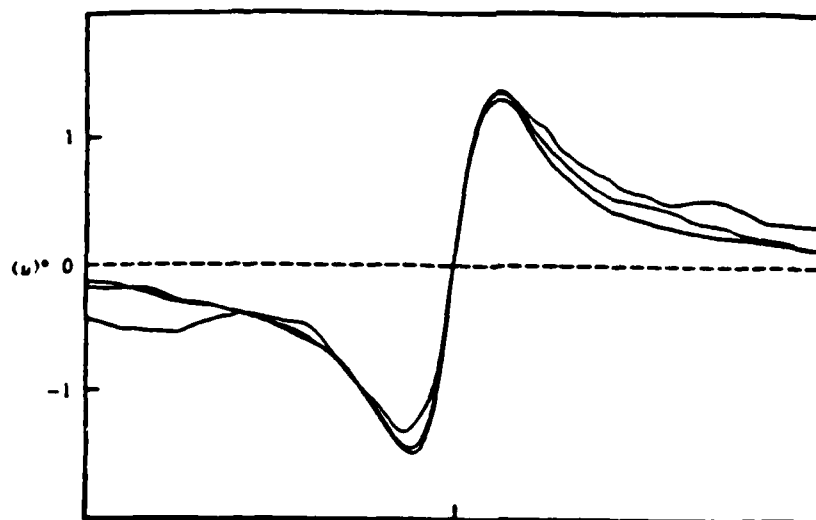


FIGURE 63. Positive VITA conditional averages of the streamwise velocity at $y^+ = 13$ (for three different threshold levels), normalized by $(K u_{rms})^{1/2}$ (Alfredsson and Johansson, 1982)

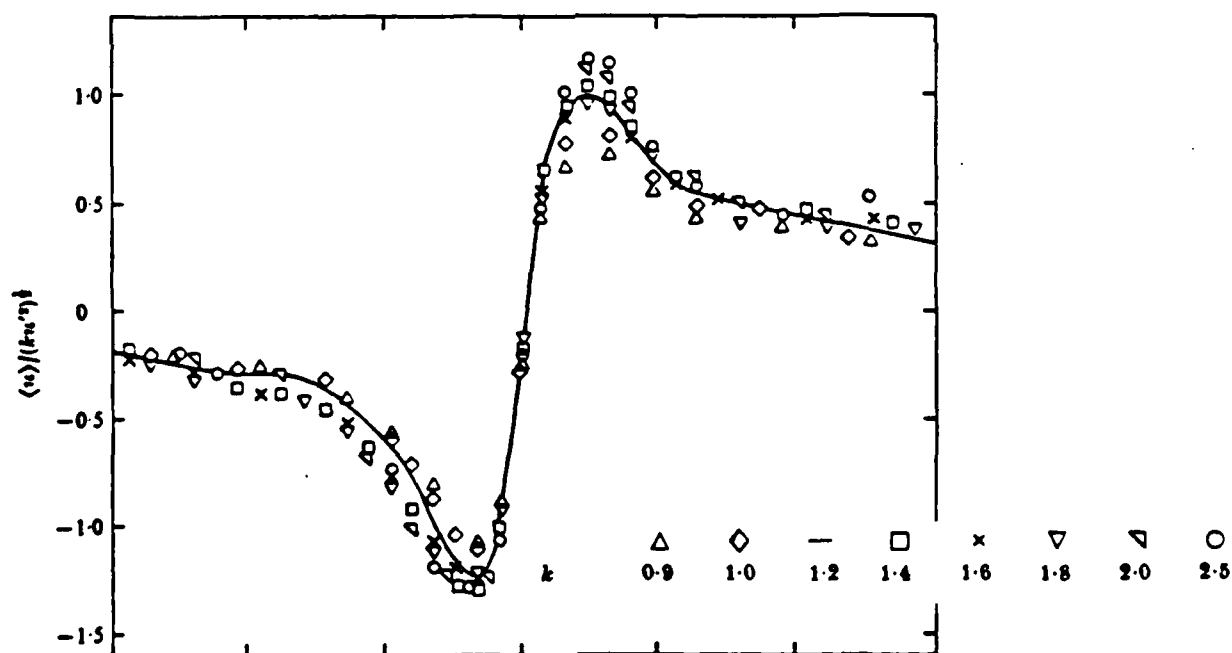


FIGURE 64. Positive VITA conditional average of streamwise velocity at $y^+ = 15$ with various threshold levels (Blackwelder and Kaplan, 1976)

M_∞	2.87
Re_∞/m	6.5×10^7
δ	28 mm
δ^*	6.2 mm
U_∞	565 m/s
$(\rho u)_\infty$	479 kg/m ² s
P_{wall}	3.34 p.s.i.
C_f	.00114

TABLE 1. Flow conditions on the tunnel centerline at $x = 18.5$ inches

Threshold	f^*	No. of Events
0.7	.18	90
0.8	.14	69
1.0	.09	44

TABLE 2. Effect of the threshold level on the number of pressure events

y/δ	Positive Events	Negative Events
	f^*	f^*
.03	.19	.13
.43	.43	.23
1.00	.29	.10

TABLE 3. Non-dimensionalized occurrence frequencies of "optimized" mass-flow events in the boundary layer

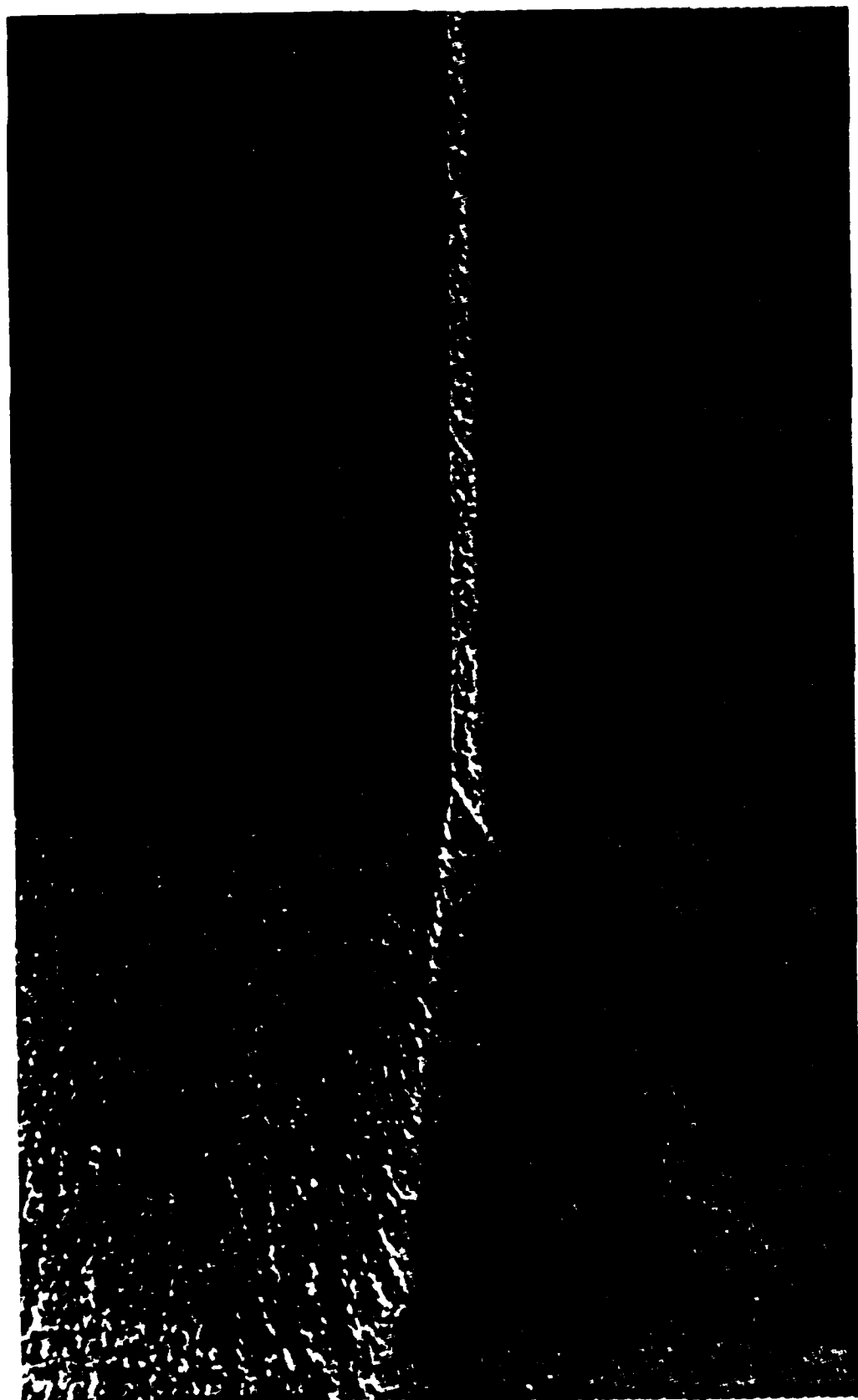


PLATE 1.

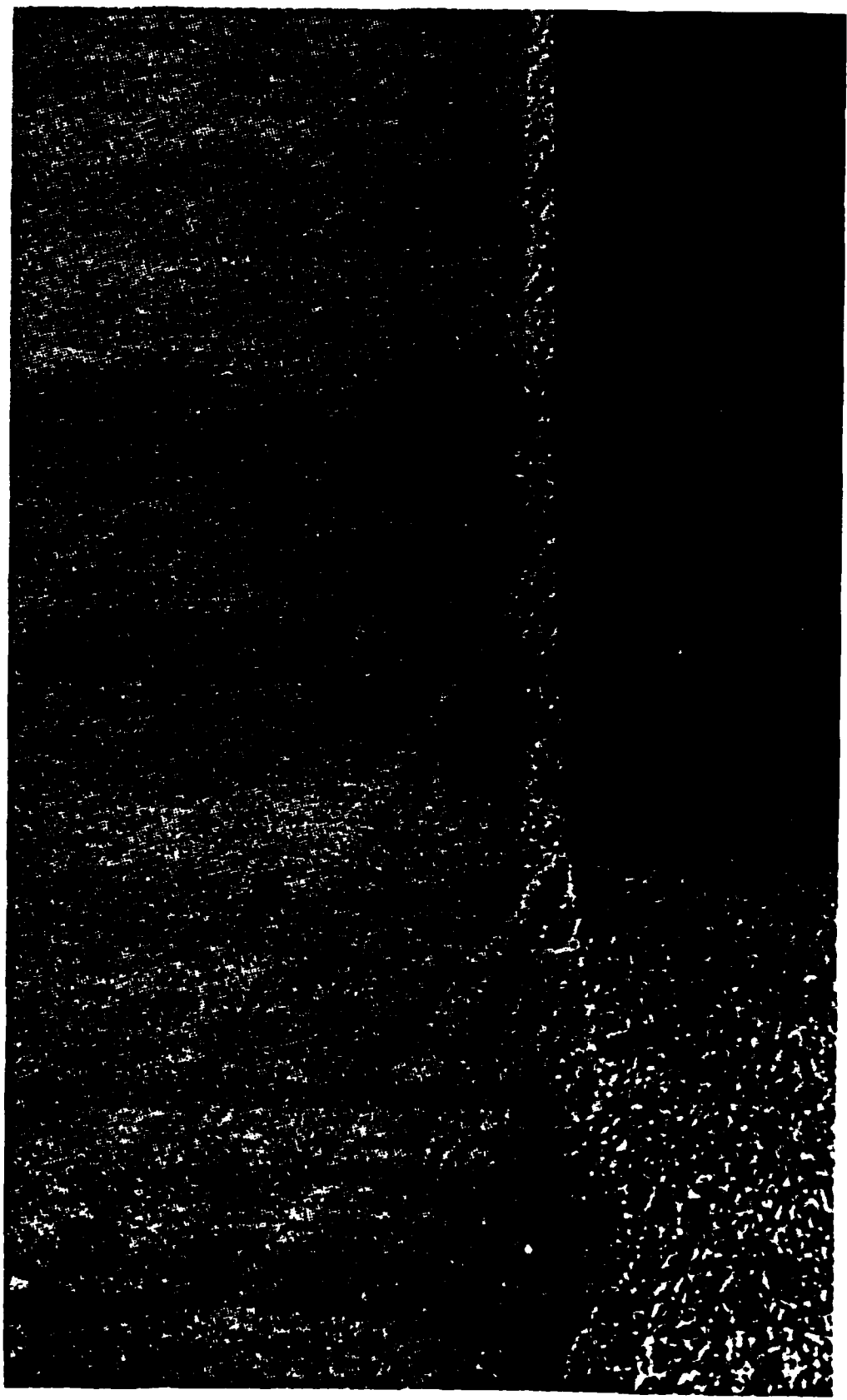


PLATE 2.

END

8-87

DTIC